

**Experimental and Modeling Studies of Thermal Barrier
Coating Failure under Isothermal Oxidation and Solid
Particle Erosion**

by

Samia Essa

A thesis submitted to the Faculty of Graduate and Postdoctoral Affairs in partial fulfillment of the requirements for the degree of

Doctor of Philosophy in Mechanical Engineering

Ottawa-Carleton Institute for Mechanical and Aerospace Engineering

Department of Mechanical and Aerospace Engineering

Carleton University

Ottawa, Ontario

June 2020

Abstract

Turbine blades used in industries are operated at high temperatures for maximum efficiency and power output. Commonly used nickel-based superalloys for these components exhibit deficiency in such a high temperature condition, therefore thermal barrier coatings (TBCs) have been developed, which can be applied on the nickel-based superalloy substrate via various deposition techniques, to reduce the temperature exerted on the substrate material.

In this research, the failure behavior of a TBC system that consists of an 8 wt% yttria partially stabilized zirconia (YSZ) top coat and CoNiCrAlY (Praxair CO-211) bond coat, deposited on nickel-based superalloy Inconel 718 substrate via atmospheric plasma spraying (APS) process, has been studied experimentally under isothermal oxidation loading and solid particulate erosion to have a better understanding of the failure mechanisms of the TBC system.

In the isothermal oxidation test, the TBC specimens are oxidized at 1050°C, 1100°C, and 1150°C in air condition for different exposure durations up to approximately 2000 h with cooling down the specimens in air to room temperature. The degradations of the APS TBCs, i.e., oxidation kinetics and crack evolution during isothermal testing, are monitored and systematically analyzed by means of scanning electron microscopy (SEM) and electron dispersive spectroscopy (EDS). A detailed examination of the oxide layer thickness is conducted on all TBC specimens, along with the characterization of the bond coat and thermally grown oxide (TGO). This is coupled with the examination of specimen cross-sections for cracking and signs of coating degradation. It is found that isothermal oxidation of the APS TBCS can result in significant Al-depletion of the CoNiCrAlY bond coat, which

leads to the formation of non-protective oxides on the top of the alumina layer (TGO), ultimately causing the delamination of the TGO layer. The growth kinetics of the TGO has been determined in order to obtain the activation energy for the TGO growth, which allows for the calculation of the TGO thickness as a function of the system temperature history. The trend in the TGO growth is found to follow the parabolic law with a value of activation energy consistent with the values reported in literature. Internal oxidation of the bond coat also occurs. Additionally, formation and propagation of cracks within the interface can result in complete spallation of the YSZ top coat from the bond-coated superalloy substrate.

The solid particle erosion behavior of as-deposited and aged APS TBCs is investigated at room temperature. The erodent material is 50 μm alumina, and the impact angles are 30°, 45°, 60°, and 90° at three particle impact velocities of 84 m/s, and 100 m/s, and 125 m/s. The effects of thermal aging on the erosion rate of the ABS TBCs are studied by testing the erosion resistance of the coatings that have experienced various heat treatments and comparing it to that of the ABS TBC in the as-received condition. Two different aging heat treatments are used, which are 1000°C and 1100°C for 24 h and 72 h. It is found that both heat treatments result in a decrease in the erosion rate of the aged APS TBCs when compared to the as-deposited APS TBC. The TBC microstructures and phase compositions are analyzed via SEM and X-ray diffraction (XRD). The erosion mechanisms of the APS TBCs are investigated by analyzing the cross-sectional and top surface microstructures of the eroded TBCs.

A temperature and exposure time-dependent interfacial fracture toughness model for TBCs has been proposed. The model characterizes the mode mixity of the stress field at the

interface between the top coat and bond coat, incorporates the Arrhenius equation to include temperature effect, and utilizes the microcrack formation theory, thus the microcrack density which is an exposure time dependent parameter in high temperature condition can be introduced to the model. The proposed model is applied to a TBC system, determining the model parameters by using the experimental data reported in literature. The interfacial fracture toughness is determined at selected mode mixity phase angles for the TBC system, showing the temperature dependence relation and the variation with exposure time at a given temperature.

Acknowledgements

I am very delighted to write this page. I greatly appreciate all the people who have provided me with tremendous help, support, and inspiration throughout my Ph.D. program. Their support is undoubtedly invaluable.

I owe my sincere gratitude to my supervisor, Professor Rong Liu, for her support, guidance, inspiration, and especially her patience throughout this research program. I would also like to express my gratitude to my co-supervisor, Dr. Kuiying Chen for all the advice, scientific discussions, and support during the entire project. He was always willing to provide support when I need help.

Thanks as well for all the members of our group and all my colleagues that helped me in my research, especially to Xiaozhou Zhang, Ding, Shawn, and Yinda for their direction and technical experience in the sample preparation and experiments.

I would like to extend my sincerest heart-felt thanks to my parents whose love and caring nature has made me the person that I am today. Their continues support and encouragement provided me with the will to persevere through times that seemed insurmountable.

I would like to express my sincere thanks and great appreciation to my Husband Ali Sbaei for his immeasurable and continuing support, and patience. Without his encouragement and support. I would not have been able to make it through my research and studies. This thesis is dedicated to him and my wonderful kids, Faruq, Qais, Khaled, and Omar.

Table of Content

Abstract.....	i
Acknowledgements	iv
Table of Content.....	v
List of Tables	x
List of Figures.....	xi
Acronyms	xvi
Nomenclatures.....	xvii
Chapter 1: Introduction	1
1.1 Background of the Research	1
1.2 Objectives of the Research	4
1.3 Tasks and Methodologies	6
1.4 Thesis Organization	9
Chapter 2: Literature Review.....	12
2.1 Thermal Barrier Coatings (TBCs)	12
2.1.1 Ceramic Top Coat.....	13
2.1.2 Bond Coat	19
2.1.3 Thermally Grown Oxide (TGO)	21
2.1.3.1 Formation of Protective Oxide Scale.....	23
2.1.3.2 Breakdown of Protective Oxide Scale	27
2.1.4 Superalloy Substrate	27
2.2 Failure Mechanisms of TBCs	28

2.2.1 Bond Coat Oxidation	30
2.2.2 Residual Stresses.....	32
2.2.3 Sintering of YSZ	34
2.2.4 Interdiffusion between Substrate and Bond Coat	35
2.2.5 Phase Transformation	36
2.2.6 Erosion of TBCs	38
2.2.7 Other TBC Failure Influence Factors	45
2.2.7.1 Effects of External Loading on the Failure Mode of TBCs.....	45
2.2.7.2 Effects of Substrate Curvature on the Failure Mode of TBCs.....	45
2.3 Interfacial Fracture Toughness of TBCs.....	46
2.3.1 Interfacial Cracking of TBCs.....	46
2.3.2 Evaluation of Interfacial Fracture Toughness.....	47
2.3.3 High Temperature Interfacial Fracture Toughness	53
2.4 Principles of Brittle Fracture Mechanics	56
2.4.1 Linear Elastic Fracture Mechanics.....	57
2.4.2 Interface Fracture Mechanics.....	59
Chapter 3: Experiments and Methodologies.....	64
3.1 TBC Specimens	64
3.1.1 TBC System and Materials	64
3.1.2 TBC Specimen Geometry and Microstructure	65
3.2 Isothermal Oxidation Testing	66
3.2.1 Test Focus	66
3.2.2 Test Plan.....	67

3.3 Solid Particle Erosion Testing	69
3.3.1 Test Objectives.....	69
3.3.2 Heat Treatment and Hardness Test.....	70
3.3.3 Testing Facility and Procedure	71
3.3.4 Data Collection	74
3.4 Microstructural Analysis.....	75
3.4.1 Metallographic Preparation.....	75
3.4.2 SEM and EDS Analyses	77
3.4.3 X-ray Diffraction	79
3.4.4 Image Analysis.....	79
3.4.5 GraphClick Software	80
Chapter 4: Results and Discussion of Isothermal Oxidation Test.....	81
4.1 Microstructure of TBC Specimen for Isothermal Oxidation Test	81
4.1.1 Cross-Sectional Morphology	81
4.1.2 Analysis of Elemental Concentration	83
4.2 Observation of the Failure under Isothermal Oxidation	85
4.3 Formation and Growth of TGO	87
4.3.1 Morphology and Composition of TGO.....	87
4.3.2 Internal Oxidation of Bond Coat.....	97
4.3.3 Oxidation Kinetics of TGO.....	104
4.4 Cracking and Failure.....	111
4.4.1 Crack Formation and Growth	111
4.4.2 Final Failure of TBCs	118

4.5 Concluding Remarks.....	125
Chapter 5: Results and Discussion of Solid Particle Erosion Test	129
5.1 Microstructure of TBC Specimen for Solid Particle Erosion Test	130
5.2 Erosion Rates	132
5.2.1 Variation of Erosion Rate with Impingement Angle	134
5.2.2 Variation of Erosion Rate with Particle Impact Velocity	135
5.3 Influence of Thermal Aging on Erosion Rate.....	136
5.3.1 Surface Morphology of Heat-Treated Specimens.....	137
5.3.2 Phase Transformation in Top Coat	138
5.3.3 Erosion Rates of Heat-Treated TBC Specimens.....	140
5.3.3.1 Effect of Coating Porosity on Erosion Rate.....	143
5.3.3.2 Effect of Coating Hardness on Erosion Rate	143
5.4 Erosion Mechanisms of TBCs	145
5.4.1 Surface Analysis of Eroded TBC Specimens	145
5.4.2 Cross-Sectional Analysis	148
5.5 Concluding Remarks.....	153
Chapter 6: Interfacial Fracture Toughness Model for TBC Systems.....	155
6.1 Investigation of TBC Failure	155
6.1.1 Failure Mechanism of TBCs	155
6.1.2 Fracture Toughness Assessment of TBCs	156
6.2 Theory of the Proposed Model	157
6.2.1 Critical Energy Release Rate	157
6.2.2 Formulation of Proposed Model	158

6.3 Determination of Model Parameters.....	163
6.4 Solution for Interfacial Fracture Toughness	165
6.5 Concluding Remarks.....	169
Chapter 7: Conclusions and Future Work.....	171
7.1 Summary of the Present Research	171
7.2 Conclusions from the Present Research.....	173
7.3 Significant Contributions.....	176
7.4 Future Work.....	178
References.....	180

List of Tables

Table 2.1 Chemical composition of Inconel 718 superalloy [11].....	28
Table 2.2 Chemical compositions (wt%) of Ni-based superalloys [65].	37
Table 3.1 Chemical compositions of the TBC materials.	64
Table 3.2 Isothermal test matrix of TBC specimens.....	69
Table 3.3 Erosion test Parameters.....	74
Table 3.4 Erosion test matrix.	75
Table 4.1 TGO thickness data from oxidation tests.....	104
Table 4.2 Experimentally determined parabolic rate constants for TGO growth in aged TBC specimens.	107
Table 5.1 Average erosion rates (mg/g) of the top coat in as-deposited TBC specimen.	133
Table 5.2 Average erosion rates (mg/g) of the top coats in heat-treated TBC specimens.	140
Table 6.1 Mechanical properties of the TBC system [94].	164
Table 6.2 Selected data of critical energy release rate versus mode mixity [94].....	164

List of Figures

Figure 1.1 Evolution of allowable gas temperature in gas turbines during last 50 years. The red lines show a progression of maximum allowable gas temperature in engines that could be achieved, which is highly increased by employing TBCs [5].....	2
Figure 1.2 An overview of the TBC system on a gas turbine blade [6].....	3
Figure 1.3 Schematic illustration of the TBC structure with coating dimensions shown on a turbine blade [4]	4
Figure 2.1 Schematic view of the structure and temperature distribution across a TBC system.	13
Figure 2.2 Thermal expansion coefficients and thermal conductivity of various materials [11].....	14
Figure 2.3 Phase diagram of yttria-stabilized zirconia system [13].....	15
Figure 2.4 Schematic diagram of an atmospheric plasma spray system (APS) [14].....	17
Figure 2.5 SEM microstructure of YSZ coating deposited with APS.	17
Figure 2.6 Schematic diagram of an electron beam physical vapor deposition (EB-PVD) system [14].....	18
Figure 2.7 SEM microstructure of YSZ coating deposited with EB-PVD [18].	19
Figure 2.8 Schematic illustration of three oxidation stages of TBC systems [33].....	23
Figure 2.9 Subscale thickness as a function of Al and O contents, also showing the hypothetical transition from internal to external oxidation [43].....	26
Figure 2.10 SEM microstructure in cross-section of a TBC system showing bond coat oxidation with developed TGO.....	32
Figure 2.11 Microstructure of EB-PVD top coat: (a) feathery shape of columns and (b) formation of necks [61].....	35
Figure 2.12 Identification of Ta+Ti-rich oxide at the bond coat surface with alloy 2 after exposure to 1150°C for 984 h with schematically showing the decohesion of the oxide by coalescence of voids around Ta+Ti-rich oxide particles [65].....	38
Figure 2.13 Erosion wear by solid particle impact [71].....	39
Figure 2.14 Typical erosion dependence on impact angle [71].....	40
Figure 2.15 Comparison of solid-particle erosion loss between different TBCs [79]....	43
Figure 2.16 TBC erosion rates under impact with 26 µm alumina particles at 982°C [80].	44
Figure 2.17 Comparison of erosion rate of Inconel 718 with or without TBC under impact with 26 µm alumina particles at 1093°C and 365.8 m/s [80].	44
Figure 2.18 Schematic illustration of Vickers indentation on a TBC system [90]	48
Figure 2.19 Interfacial crack in a TBC system under indentation: (a) geometry of interfacial crack and (b) schematic illustration of crack length [91].	49
Figure 2.20 Mixed-mode interfacial fracture testing method [87].....	52
Figure 2.21 Critical energy release rate varying with loading phase angle and interfacial crack roughness k value [94].	52
Figure 2.22 Critical energy release rate varying with mode mixity [95].....	53
Figure 2.23 Exposure temperature dependence of interfacial fracture toughness of TBCs [87].	55

Figure 2.24 Variation of interface stress intensity factor of TBCs with temperature [97].....	55
Figure 2.25 A summary of K_I versus K_{II} for mode I, mode II, and mixed mode fracture of plasma-sprayed ceramic TBC at 25°C and 1316°C in air , A and B distances from a load point [98].....	56
Figure 2.26 A crack in two-dimensional plane.....	58
Figure 2.27 Loading modes of cracked material [99].....	59
Figure 2.28 Generic configuration at the tip of an interfacial crack [101].	60
Figure 3.1 TBC specimen for isothermal oxidation test.....	65
Figure 3.2 TBC specimen for solid particle erosion test.....	65
Figure 3.3 SEM image in cross-section of the TBC specimen in as-deposited state.....	66
Figure 3.4 Lindberg Type (s) Box Furnace.....	68
Figure 3.5 Microhardness Tester Unit, Model SMT-X7 Dual Indenter.	71
Figure 3.6 Entire apparatus assembly of erosion test: (a) inert environment (compressed nitrogen gas); S.S. WHITE Airabrasive 6500 erosion chamber; and S.S. WHITE Airabrasive Micro-Blasting Jet Machine and (b) specimen nozzle and holder (Courtesy of S.S. WHITE Technologies Inc.).....	72
Figure 3.7 SEM image of erodent particles - Angular AccuBRADE-50 blend #3 alpha alumina powder.....	73
Figure 3.8 Secotom-10 Cutting Machine (Courtesy of Struers Co.).	76
Figure 3.9 MetaServ™ 250 Grinder-Polisher (Courtesy of BUEHLER® An ITW Company).....	76
Figure 3.10 TBC specimens mounted in epoxy resin for metallographic analyses after polishing.....	77
Figure 3.11 Tescan Vega- II XMU SEM/EDS Instrument.....	78
Figure 3.12 Bruker AXS D8 Discover Diffractometer.....	79
Figure 3.13 Cross-section microscopic images of the TBC sample for porosity analysis using Image J software: (a) SEM microstructure and (b) processed binary image showing pores.....	80
Figure 4.1 SEM microstructure of the TBC specimen for isothermal oxidation test in as-deposited state: (a) cross-section image at low magnification, (b) cross-section image at high magnification, (c) top coat and (d) bond coat.....	82
Figure 4.2 EDS analyses of CoNiCrAlY bond coat: SEM microstructure with selected points indicated, (b) EDS spectrum of alloy matrix (point 1) and (c) EDS spectrum of oxide particle (point 2).....	84
Figure 4.3 Macrograph of the failed TBC specimen after 1970 h isothermal tests at 1050°C.	85
Figure 4.4 Macrograph of failed TBC specimen (a) after 1500 h at 1100°C and (b) after 360 h at 1150°C isothermal test showing top coat spallation.....	86
Figure 4.5 SEM image of the oxidized TBC specimen showing a TGO formed at 1050°C for different exposure times.....	88
Figure 4.6 EDS analyses of the TGO in the specimen oxidized at 1050°C for 100 h: (a) SEM image showing the points investigated, (b) EDS spectrum of point 1 and (c) EDS spectrum of point 2.	90

Figure 4.7 SEM image of the TBC specimen oxidized at (a) 1100°C and (b) 1150°C for 200 h showing a TGO layer formed.....	92
Figure 4.8 SEM micrograph of developed TGO layer containing cracks after 200 h of exposure at 1150°C.....	93
Figure 4.9 EDS spectra of the TGO in the specimens oxidized at different temperatures for 200 h.....	94
Figure 4.10 SEM micrograph of the oxidized specimen showing porous and non-uniform TGO when oxides rather than alumina are present.....	96
Figure 4.11 SEM micrograph of the oxidized specimen showing poor adhesion between the top coat, the mixed oxides and alumina layer of the TGO, indicated by the arrows .	96
Figure 4.12 Internal oxides in the bond coat of the TBC specimen oxidized at 1050°C for 970 h: (a) SEM micrograph showing internal oxidation of bond coat and (b) EDS spectrum and elemental table of internal oxides.....	98
Figure 4.13 Internal oxides in the TBC specimen oxidized at 1050°C for 1970: (a) SEM micrograph showing internal oxidation of the bond coat and (b) EDS spectrum and elemental table of internal oxides.....	99
Figure 4.14 SEM micrographs of internal oxides in the bond coat of the TBC specimens oxidizes at 1100°C for (a) 700 h, (b) 970 h, and (c) 1500 h.....	101
Figure 4.15 SEM micrograph of internal oxides in the bond coat of the TBC specimen oxidized at 1150°C for 360 h.....	102
Figure 4.16 SEM micrograph of the specimen oxidized at (a) 1050°C and (b) 1100°C, showing multiple cracks inside thick TGO across detrimental oxides.....	103
Figure 4.17 Variation of TGO thickness with exposure time as a result of isothermal oxidation at high temperature.....	105
Figure 4.18 Plots for determination of K_p value for each oxidation temperature.....	107
Figure 4.19 Plot for determination of activation energy Q (- $\ln K_p$ vs $1/T$).....	108
Figure 4.20 Comparison in TGO thickness growing with exposure time at different oxidation temperatures between theoretically predicted values and experimentally measured data.....	109
Figure 4.21 Comparison of TBC failure times between theoretical prediction and experimental data.....	111
Figure 4.22 SEM examination of cracks in the top coat of the TBC specimen oxidized at 1050°C for (a) 100 h and (b) 360 h.....	113
Figure 4.23 SEM examination of cracks in the TBC specimen oxidized at 1050°C for (a) 200 h, (b) 970 h and (c) 1970 h.....	115
Figure 4.24 SEM examination of cracks in the TBC specimen oxidized at (a) 1100°C and (b) 1150°C.....	116
Figure 4.25 Crack sizes versus exposure time for the TBC specimen oxidized at 1050°C.....	117
Figure 4.26 Kinetic performance of the maximum crack length of the mixed crack during the TBC oxidation at different temperatures.....	118
Figure 4.27 SEM examination of the final failure of the TBC specimen oxidized at 1050°C for 1970 h: (a) and (b) failure path in top coat and (c) cracking within TGO.	121
Figure 4.28 SEM examination of the delamination crack in the TBC specimen oxidized at 1100°C for 970 h: (a) at low magnification and (b) at high magnification.	122

Figure 4.29 SEM examination of the final failure of the TBC specimen after 1500 h oxidation at 1100°C due to spallation of the ceramic top coat.....	123
Figure 4.30 SEM micrograph of the TBC specimen after oxidation at 1150°C showing spallation of the top coat	124
Figure 5.1 SEM micrograph in cross-section of the as-deposited specimen for solid particle erosion test.....	130
Figure 5.2 SEM surface morphology of the top coat in as-deposited state.	131
Figure 5.3 XRD diffraction pattern of the top coat in as-deposited condition.....	132
Figure 5.4 Erosion curve of as-deposited TBC specimen under solid particle erosion using 50 µm alumina at 30° impact angle and 84 m/s impact speed in room temperature.	133
Figure 5.5 Erosion rates of as-deposited TBC specimen tested with particle impact velocity 84 m/s at different particle impingement angles.....	134
Figure 5.6 Erosion rates of as-deposited TBC specimen tested at particle impingement angle 30° with different particle impact velocities.	135
Figure 5.7 Log – log plot of erosion rate against particle impact velocity for as-deposited TBC specimen tested at particle impingement angle 30°.	136
Figure 5.8 SEM surface morphology of the top coat thermally aged for 72 h at (a) 1000°C and (b) 1150°C.....	138
Figure 5.9 XRD pattern of the ceramic top coat in the TBC specimen aged for 72 h at (a) 1000°C and (b) 1150°C.....	139
Figure 5.10 Comparison in erosion rate of the TBC specimens aged at different temperatures for different times.....	142
Figure 5.11 Relative erosion resistance of heat-treated TBC specimens. The relative erosion resistance of as-deposited specimen was set to 0 %.	142
Figure 5.12 Microhardness of the top coat in the TBC specimens.	144
Figure 5.13 Erosion rate versus hardness of the APS top coat in the TBC specimens..	145
Figure 5.14 SEM eroded surface morphology of the top coat under solid particle erosion at impact angle of (a) 30°, (b) 45°, (c) 60°, and (d) 90°.	147
Figure 5.15 Cross–section microscopic images of as-deposited TBC specimen eroded at particle impact angle 30°: (a) at low magnification and (b) at high magnification.	149
Figure 5.16 Cross–section microscopic images of as-deposited TBC specimen eroded at particle impact angle 45°: (a) at low magnification and (b) at high magnification.	149
Figure 5.17 Cross–section microscopic images of as-deposited TBC specimen eroded at particle impact angle 60°: (a) at low magnification and (b) at high magnification.	150
Figure 5.18 Cross–section microscopic images of as-deposited TBC specimen eroded at particle impact angle 90°: (a) at low magnification and (b) at high magnification.	150
Figure 5.19 Cross–section microscopic images of eroded TBC specimen at impingement angle 30° and particle velocity 100 m/s: (a) at low magnification, (b) at high magnification. The specimen was previously heat-treated for 72 h at 1000°C.	152
Figure 5.20 Cross–section microscopic images of eroded TBC specimen at impingement angle 30° and particle velocity 100 m/s: (a) at low magnification, (b) at high magnification. The specimen was previously heat-treated for 72 h at 1150°C.	153
Figure 6.1 Variations of interfacial energy release rate with temperature for different mode mixites.....	166

Figure 6.2 Variation of crack density vs isothermal exposure time at 1050°C.	168
Figure 6.3 Variation of the interfacial energy release rate with exposure time at 1050°C.	168

Acronyms

TBC	Thermal Barrier Coating
APS	Atmospheric Plasma Spray
EB-PVD	Electron Beam Physical Vapor Deposition
CTE	Coefficient of Thermal Expansion
SPS	Suspension Plasma Sprayed
TGO	Thermally Grown Oxide
YSZ	Yttria Stabilized Zirconia
SEM	Scanning Electron Microscope
SSY	Small Scale Yielding
EDS	Energy Dispersive Spectroscopy
XRD	X-ray Diffraction
LEFM	Linear Elastic Fracture Mechanics
CTOD	Crack Tip Opening Displacement

Nomenclatures

K_{ca}	Interface Fracture Toughness
E	Young's Modulus
H	Hardness
F_c	Applied Force
c, a	Crack Length
G_e, J	Energy Release Rate
G_c	Critical Energy Release Rate
γ, γ_s	Surface Energy
ψ	Phase Angle
σ	Applied Stress
σ_{xy}, σ_{yy}	Stress Components
σ_c	Fracture or Critical Stress
K	Stress Intensity Factor
K_c	Critical Stress Intensity Factor
μ	Shear Modulus
ν	Poisson's Ratio
α, β	Dundurs Parameters
ε	Bimaterial Constant (Oscillation Factor)
r, l	Distance from the Crack
h, h_o	Oxide Thickness, Initial Oxide Thickness

K_p	Parabolic Rate Constant
t	Exposure Time
n_o	Oxidation Exponent
K_p	Parapolice Rate Constant
K_o	Oxidation Constant
T	Temperature
Q	Activation Energy
R	Universal Gas Constant
E_r	Erosion Rate
V	Particle Velocity
n_v	Velocity Exponent
r_p	Plastic Zone Size
δ_{ctod}	Crack Tip Opening Displacement
σ_y	Yield Strength
J_o, G_o	Maximum Plastic Deformation Work
J_s	Elastic Work
J_D	Plastic Dissipation Energy
b	Burgers Vector
γ_f	Stacking Fault Energy
h_p	Plastic Zone Size
ρ	Dislocation Density

U_{P-N}	(P–N) barrier Energy
K_B	Boltzmann Constant
G_D	Temperature Dependent Interfacial Fracture Toughness
ρ_c	Interfacial Microcrack Density
n, m	Linking Parameters

Chapter 1: Introduction

1.1 Background of the Research

Gas turbines are widely used for power production and aero-engine applications. In the power generation industry, there have been ongoing efforts to increase the working temperature of gas turbines in jet engines as it is directly linked to the efficiency and the performance of the engines [1]. The design and manufacturing of gas turbines have increased the service temperature to higher levels. However, the upper limit of the temperature has been determined by the tolerance of turbine blade materials, because as the temperature is driven to the higher levels, materials problems such as oxidation, creep, fatigue, loss of strength, corrosion are unavoidable [1]. Nickel-based superalloys with relatively high melting point (1260 - 1336°C) and good mechanical properties and resistance to high temperature inelastic deformation are commonly used as the base material for modern stationary gas turbines, which can be used at temperatures (~1700°C) [1], [2]. Further increase in turbine allowable temperature has been made possible by the development of thermal barrier coatings (TBCs), which are applied to the external surface of the turbine blades to protect the base material of the turbine blades against high temperature oxidation and corrosion. Thus, the lives of the hot sectional metal components can be extended by creating temperature drop across the coatings [3]. In combination with the internal cooling of the blades, TBCs provide a reduction of the substrate temperature, which makes the possibility of increasing the inlet temperature and/or decreasing the cooling air mass flow. As a result, higher gas temperatures can be used, which leads to improved efficiency and performance of aero-engines [3], [4]. **Figure 1.1** shows the evolution of the operation progression of Ni-based superalloy through the years due to the

improvement of their manufacturing, which leads to an advanced microstructure (single crystal) and different cooling techniques employed to cool the component at hot stages of the engines [5].

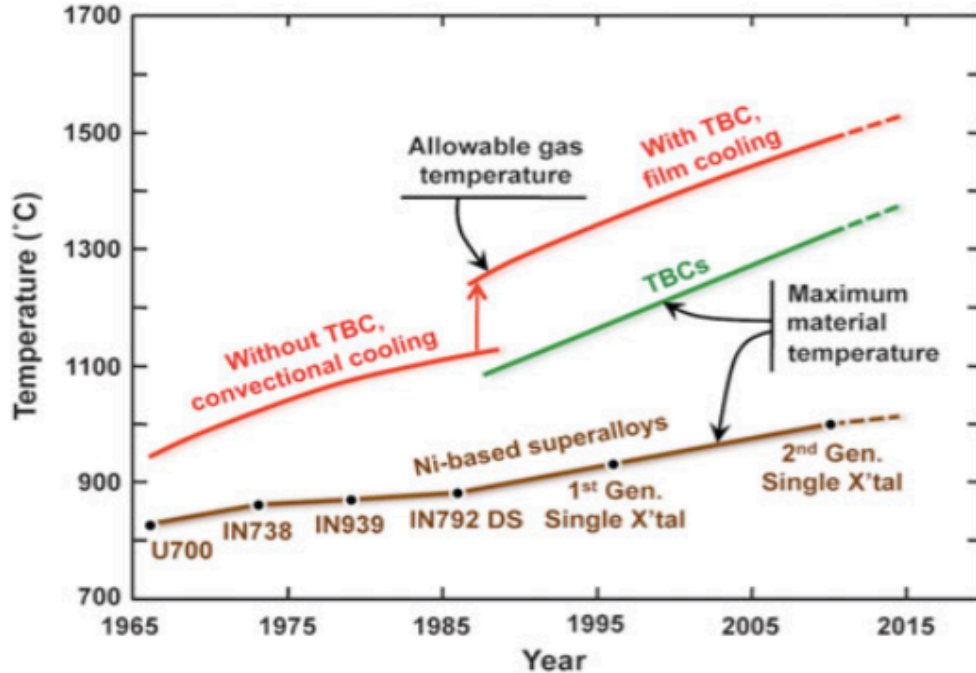


Figure 1.1 Evolution of allowable gas temperature in gas turbines during last 50 years. The red lines show a progression of maximum allowable gas temperature in engines that could be achieved, which is highly increased by employing TBCs [5].

The current state-of-the-art TBC systems consist of yttria-stabilized zirconia (YSZ) deposited either by atmospheric plasma spray (APS) or electron beam physical vapor deposition (EB-PVD) processes. The bond coat is platinum modified diffusion aluminide or MCrAlY bond coats. Single crystal Ni-based superalloys, which possess high strength at elevated temperatures, are usually employed as the substrates [4]. The typical structure of a TBC on a gas turbine blade is illustrated in **Figure 1.2** and **Figure 1.3**. Initially, in the as-deposited state, the TBCs are well-bonded to the substrate upon which they are

deposited. However, as the coating system is exposed to operating temperatures, its adherence degrades. Poor adhesion can lead to developing debonding or spallation of the coating, which is driven by thermal compressive stresses [4]. Therefore, there is a strong demand for developing more durable TBC systems. Although the failure mechanisms of TBC systems have been extensively studied, they are not yet fully understood due to the contribution of many factors to the failure. It is difficult to predict the lifetime of the coating systems accurately. Achieving higher gas turbine efficiency in the future requires better understanding of all factors that influence the TBC system integrity and service lifetime. To this end, further research in the failure of TBC systems is needed [4].

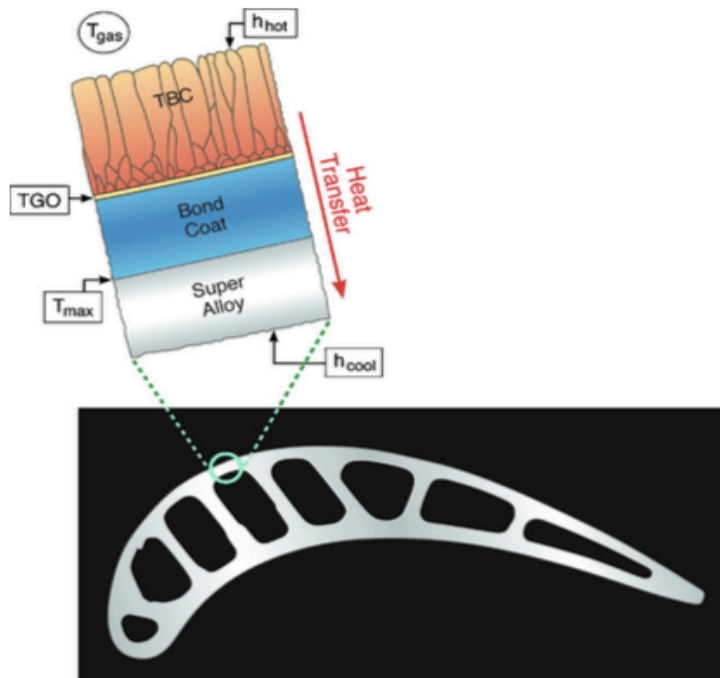


Figure 1.2 An overview of the TBC system on a gas turbine blade [6].

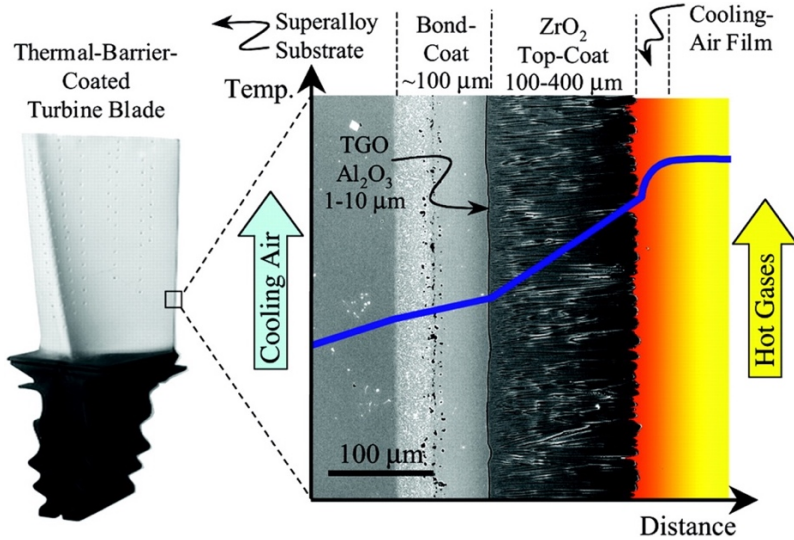


Figure 1.3 Schematic illustration of the TBC structure with coating dimensions shown on a turbine blade [4].

In addition to high temperature oxidation as the primary problem of TBCs, solid particle erosion while acknowledged as a problem has until recently been considered to be the secondary problem causing the failure of TBCs. Aero-engines may operate in dust-laden environments, which causes erosion problems to TBCs. Erosion may also arise due to inertial forces that cause particles, entrained within the gas stream, to deviate away from the gas streamlines, thus impacting the components within the gas flow [7]. The particulates generated inside the engine, such as carbon particles formed in the combustion process [8] and engine wear residues, for example, thermally spalled TBC from the combustor, can contribute significantly to the erosion damage of TBCs [9].

1.2 Objectives of the Research

As mentioned above, improving the design and manufacturing of TBCs to enhance durability needs better understanding the failure mechanisms of TBCs in the operating

conditions which involve high temperature oxidation and solid particle erosion. The lifetime of TBCs is strongly affected by many factors such as thermally grown oxide (TGO) growth, cracking at the top coat/bond coat interface due to induced stresses, ceramic top coat degradation by high temperature reactions, erosion with gas particles, and so on. When stresses develop mechanically or thermally in the coatings, they can generate cracks near the coating interface. With the propagation of these interfacial cracks, delamination of the coating occurs, leading to the final failure of the TBC. Interfacial fracture toughness is a measure of the stress field that governs the propagation of the cracks present in a TBC system so that accurate assessment of the interfacial fracture toughness of TBCs enables effectively predicting the service lifetime of TBCs.

The present research project was focused on the studies that contributed to the understanding of the APS TBC damage evolution and failure under high temperature oxidation and solid particle erosion so that the performance and durability of the TBC system can be improved. For this purpose, the research project was aimed at both testing and modeling efforts concerning the following aspects: (I) to investigate the oxidation behavior of the entire TBC system, with the focus on the changes in the microstructure of the top coat and bond coat at high temperatures as well as the interaction of the cracks generated in the top coat, TGO and bond coat as a result of high temperature oxidation, which would lead to the delamination of the coating, i.e., final failure of the TBC; (II) to evaluate the erosion performance of the APS TBC under solid particle impact and to address the failure mechanisms of the APS TBC system as a result of erosion damage; (III) to develop a high-temperature interfacial fracture toughness model for TBCs that can predict the fracture toughness of a given TBC at high temperatures based on the microcrack

formation theory and Arrhenius-type equation.

1.3 Tasks and Methodologies

Toward the research goals set, the entire research work can be divided into three parts: isothermal oxidation test, solid particle erosion test, and interfacial fracture toughness modeling of TBCs, which were implemented through the tasks detailed below. The TBC system that was studied in this research consisted of single crystal Ni-based superalloy Inconel 718 substrate, CoNiCrAlY (Praxair CO-211) bond coat and 8 wt% yttria partially stabilized zirconia (YSZ) top coat. The bond coat was deposited on the superalloy substrate with plasma thermal spray. The top coat was applied on the bond coat with atmospheric plasma spray (APS). Curtiss-Wright-US supplied all the TBC specimens.

Tasks in Part I — Isothermal oxidation test

- (1) Isothermal oxidation test was conducted in the TBC specimens to investigate the performance of the TBC at high temperatures. The tests were performed at 1050°C, 1100°C, and 1150°C in atmospheric condition for different time lengths up to approximately 2000 h, with cooling down the specimens in the laboratory air to room temperature.
- (2) Microstructure analysis was performed on the cross-sections of as-received TBC specimen and oxidized TBC specimens using scanning electron microscopy (SEM) with energy dispersive spectroscopy (EDS). The integrity of the coatings was examined after the TBC specimens were oxidation-tested at high temperatures.
- (3) The growth of the TGO was studied for the TBC specimens oxidized at the temperature

from 1050°C to 1150°C for different exposure times. The kinetics of the TGO growth was investigated by measuring the TGO thickness of the TBC specimens oxidized at 1050°C, 1100°C, and 1150°C for different time lengths. The TGO growth activation energy was determined and hence the TGO thickness could be determined as a function of the system temperature.

- (4) The detailed TGO structure and composition of the oxidized TBC specimens at different temperatures and exposure conditions were analyzed using SEM/EDS. The inhomogeneous feature of the TGO layer was investigated. The Al₂O₃ layer and mixed oxides such as (Ni, Cr, Co) oxides were identified within the TGO. The formation mechanisms and effects of the mixed oxides in the TGO were analyzed.
- (5) The internal oxidation of the bond coat was studied with SEM/EDS. The compositions of the formed oxides were analyzed. The oxide formation and distribution within the bond coat were examined with respect to oxidation temperature and exposure time.
- (6) Various cracks that developed in the TBC due to stresses or formation of oxides under the oxidation test conditions were analyzed. The features of each type of cracks including interfacial crack, internal crack, mixed crack, delamination crack, etc. and the interaction of these cracks were identified. The lengths of various cracks were measured in the TBC specimens oxidized at 1050°C, 1100°C, and 1150°C, for different times. The growth kinetics of the maximum crack which led to the delamination of the top coat was studied with respect to exposure time.

Tasks in Part II —Solid particle erosion test

- (1) In addition to top coat delamination, the degradation of top coat due to solid particle erosion may also cause the failure of TBCs. Therefore, solid particle erosion test was conducted on both as-deposited and aged TBC specimens to reflect the synergetic effect of thermal aging and solid particle erosion on the performance of the TBC under the actual working condition. The test was carried out at various particle impingement angles (30° , 45° , 60° , and 90°) on the top coat surface with particle impact velocities of 84 m/s, 100 m/s and 125 m/s at room temperature.
- (2) The erosion rate was evaluated for each of the as-deposited and aged specimens.
- (3) The effects of thermal aging on the erosion rate of the ABS TBC were studied by testing the erosion resistance of the ABS TBC that had received various heat treatments of the as-deposited specimen.
- (3) Possible damage mechanisms of the TBC specimens under solid particle erosion were explored thorough microstructural examination on the specimens before and after the erosion testing.

Tasks in Part III —Interfacial fracture toughness modelling

- (1) A temperature and exposure time dependent interfacial fracture toughness model for TBCs was developed based on the Arrhenius-type equation and microcrack density.
- (2) The mixed mode nature of the near-tip singularity field of the interface crack was analyzed.
- (3) The critical energy release rate for the propagation of the interfacial cracks in a TBC system was formulated in terms of the microcrack formation theory.

- (4) Crack tip opening displacement (CTOD) was used to measure the total growth of a microcrack at the coating interface in order to estimate the interfacial fracture toughness of TBC systems.
- (5) The proposed model was applied to a TBC system, determining the model parameters by utilizing the experimental data reported in literature. The interfacial fracture toughness was determined at selected mode mixity phase angles for the TBC system, showing the temperature dependence relation.
- (6) The exposure time-dependent interfacial fracture toughness at a specific temperature was obtained by incorporating the exposure time dependent microcrack density at a given temperature.

1.4 Thesis Organization

The entire research work presented in this thesis can be covered by seven chapters, as detailed below.

Chapter 1 is an introduction to this research, indicating the motivation and objectives of this research, tasks to be completed and methodologies to be used in this research, as well as the outline of this thesis.

Chapter 2 covers an extensive literature review of the fundamental concepts of TBCs and linear elastic fracture mechanics, as well as relevant studies to the present research. The theories of TBC structure, materials and deposition methods are reviewed. Other contents covered in this chapter include the failure mechanisms of TBCs, various influencing factors such as bond coat oxidation, the presence of residual stress, interfacial cracks, erosion of

top coat, etc., interfacial fracture toughness of TBCs at room temperature and at elevated temperatures.

Chapter 3 delineates the experiments and methodologies of this research. The details of the isothermal test and solid particle erosion test, including the testing facilities, process parameters, experimental procedures, data collection and analysis, etc., are described. The SEM/EDS experiments and equipment for the microstructural analyses of the as-deposited and aged TBC specimens, the eroded surface and cross-section morphology analyses of the TBC specimens after the solid particle erosion tests, are also covered in this chapter.

Chapter 4 reports the experimental results of the isothermal oxidation tests. The results include the SEM/EDS analyses of cross-section of the oxidized TBC specimens, focusing on the formation and growth of TGO, the development of oxidation kinetics equation for the TGO growth, internal oxidation of the bond coat, various cracks developed in the TBC specimens, cracking failure of the TBC specimens, and the spallation of the top coat.

Chapter 5 presents the results of the solid particle erosion tests, including the effects of particle impingement angle, particle velocity and thermal aging conditions on the APS TBC erosion rate as well as the possible failure mechanisms of the coating system under solid particulate erosion.

Chapter 6 presents the details of the proposed interfacial fracture toughness model for TBC systems, including the theory of the modeling, the formulation of the model, the determination of model parameters, and the evaluation of the interfacial fracture toughness for a TBC system using the proposed model. The distinct features of the proposed model

compared with the existing models for the interfacial fracture toughness of TBC systems and the limitations of the propose model are discussed.

Chapter 7 summarizes this research and delineates significant contributions and conclusions from this research. Future work for this research project is also recommended.

Chapter 2: Literature Review

2.1 Thermal Barrier Coatings (TBCs)

Thermal barrier coatings (TBCs) are protective coatings that are applied to the surfaces of metallic parts in the hottest section of gas-turbine engines. They enable the engines to operate at high temperatures without raising the base metal temperature when the cooling systems inside the hot section components are used and thus enhance the operating efficiency of the engines [4].

Due to the low thermal conductivity of the top-coat layer in TBCs, the substrate temperature can be decreased by some hundred degrees, as shown in *Figure 2.1*. Some ceramic materials, such as alumina, zirconia, etc., are usually chosen as the coating materials because they are thermally refractory and chemically inactive, they are well-suited for being used as high temperature protection barriers. TBCs with low thermal conductivity, phase stability, and high resistance to sintering, have ever increased demands [3], [10]. The porous and defect-rich microstructure of TBCs provides these highly desired properties [4]. Generally, TBCs consist of four major layers: (I) a ceramic top coat deposited on the bond coat, (II) a metallic bond coat deposited on the superalloy substrate, and (III) a thermally grown oxide (TGO) that forms between the bond coat and top coat when the coating is exposed to elevated temperatures, (IV) a super alloy substrate, as illustrated in *Figure 2.1*.

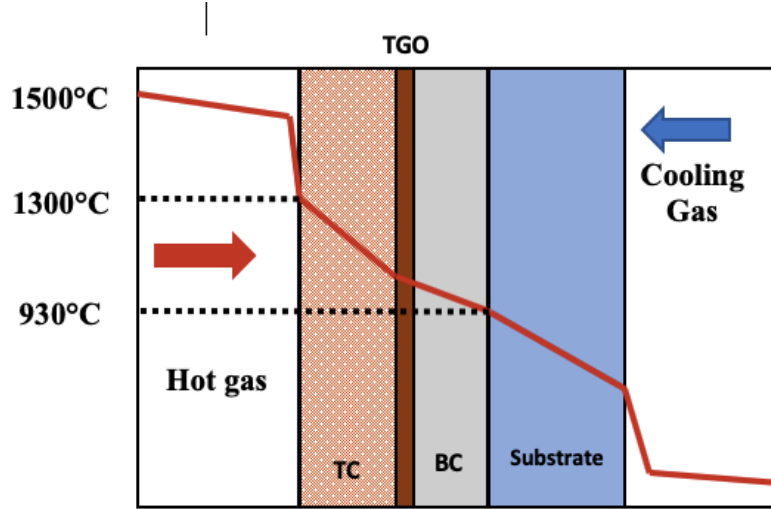


Figure 2.1 Schematic view of the structure and temperature distribution across a TBC system.

2.1.1 Ceramic Top Coat

The majority of TBCs in use today are ZrO_2 -based, having a composition containing about 8 wt% Y_2O_3 (8YSZ). The basic function of the top coat is to provide thermal insulation to the underlying layers. To achieve this objective, the ceramic top coat should possess the basic properties such as low thermal conductivity ($\sim 1 \text{ W.m}^{-1} \cdot \text{K}^{-1}$) to provide thermal insulation function, high melting point to keep the coating structure durable when in contact with hot gasses, high thermal expansion coefficient which helps relieve stresses induced due to the thermal expansion mismatch between the top coat ceramic layer and metallic bond coat layer [4], resistance to sintering, corrosion and oxidation, low density, and high strain tolerance in order to resist thermal shock during thermal cycles. Unlike other ceramics that are unstable at high temperatures due to their polymorph properties, YSZ material has a highly stable structure [11]. **Figure 2.2** presents thermal expansion

coefficients and thermal conductivity properties of different materials [11]. It can be seen that yttria stabilized zirconia has the desired combination of low thermal conductivity and high thermal expansion coefficient.

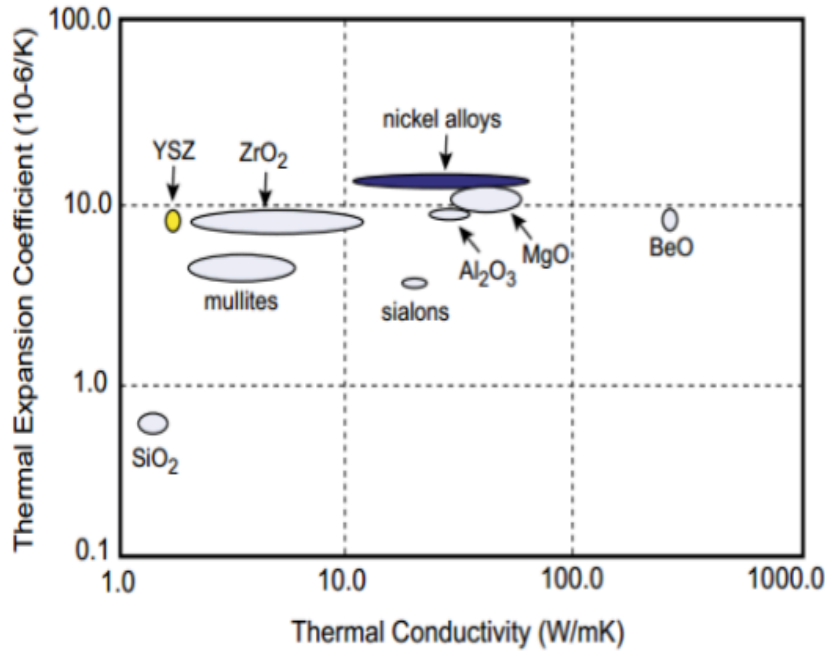


Figure 2.2 Thermal expansion coefficients and thermal conductivity of various materials [11].

Under equilibrium condition, the YSZ with 6 - 8 wt% yttria is stabilized to a tetragonal metastable phase t' , which is formed by rapid cooling during coating deposition. The metastable tetragonal phase decomposes into a high yttria content cubic phase (c) and a low yttria content equilibrium tetragonal phase (t) during engine operation. On cooling, the low yttria concentration tetragonal phase transforms into the monoclinic phase (m). The new monoclinic phase results in a volume increase by about 4% which in turn can lead to stress generation and cracking within the coating. While the minimum of 6% yttria is

required to stabilize the tetragonal phase of zirconia, a high fraction of yttria content can negatively impact the cyclic lifetime of the coating. It has been found that the content of 6 to 8 wt% gives the best compromise in properties [12], [13]. The phase diagram of the zirconia-yttria system in the composition range of interest for TBCs is shown in **Figure 2.3** [12].

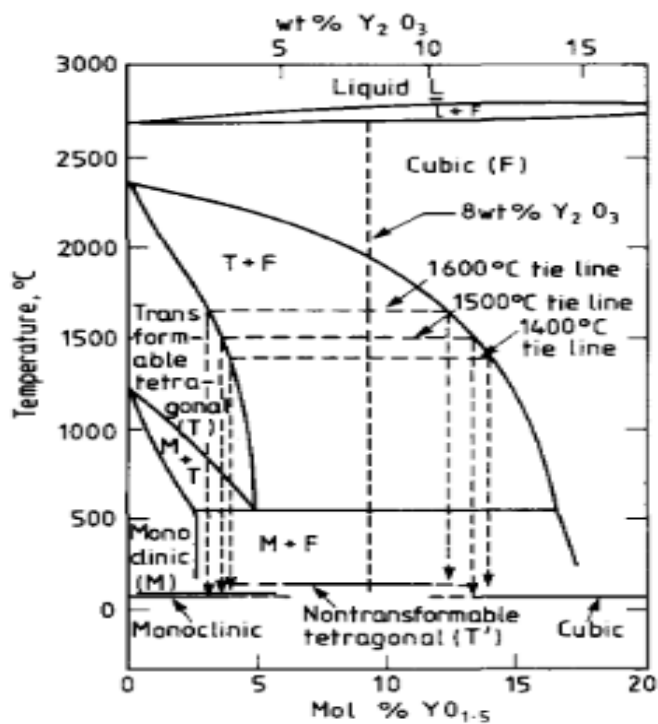


Figure 2.3 Phase diagram of yttria-stabilized zirconia system [13].

The ceramic top coat YSZ is typically applied over a bond coat and it can be deposited by one of the two common methods, atmospheric plasma spray (APS) and electron beam physical vapor deposition (EB-PVD), which result in different microstructures and characteristics. Atmospheric plasma spraying process (APS) produces TBCs by

introducing ceramic powders into a high-temperature plasma plume where they are melted into droplets and accelerated towards the bond coat surface [14], as illustrated in *Figure 2.4*. The molten droplets spread and form splats that are quickly quenched, resulting in the formation of a lamellar grain structure, which is a common feature of plasma sprayed TBCs, as shown in *Figure 2.5*. In one pass, several splats will be formed on the bond coat surface and the coating thickness can be increased by means of several passes. Unlike EB PVD top coat, a typical APS top coat is slightly thicker with a thickness about 300 to 600 μm . The coatings show layers of splats along with globular pores and microcracks between and within the individual splats. The structure and porosity of the resulting TBC depend mostly on particle velocity and temperature, which are controlled by spray parameters such as spraying distance and plasma power. The presence of these cracks and pores and their orientation normal to the heat flow reduce the thermal conductivity of the ceramic coating from $2.3 \text{ W m}^{-1}\text{K}^{-1}$ for a fully dense YSZ material to $0.8 - 1.7 \text{ W m}^{-1}\text{K}^{-1}$ [4], [15]. The low production cost of APS TBCs makes it attractive commercially. Nevertheless, due to the nature of growing microstructural defects parallel to the interface and undulating of the interface within APS TBCs, APS coatings have shorter cyclic lives than EB-PVD ones. Hence, they become a preferred choice for applications that operate in slightly lower temperature and fewer cycles such as in conventional power plant gas-turbine engines [4].

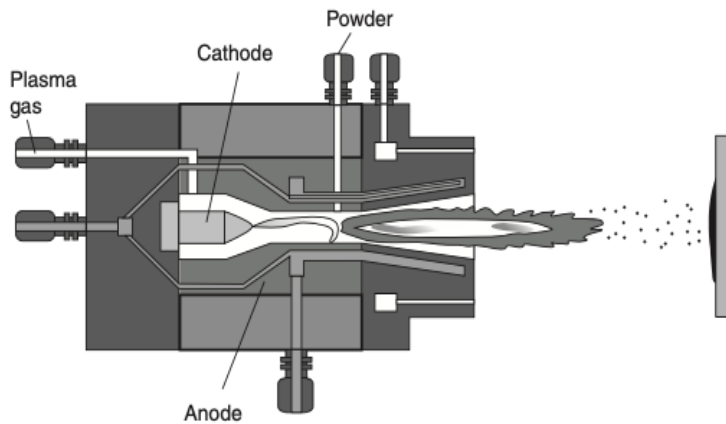


Figure 2.4 Schematic diagram of an atmospheric plasma spray system (APS) [14].

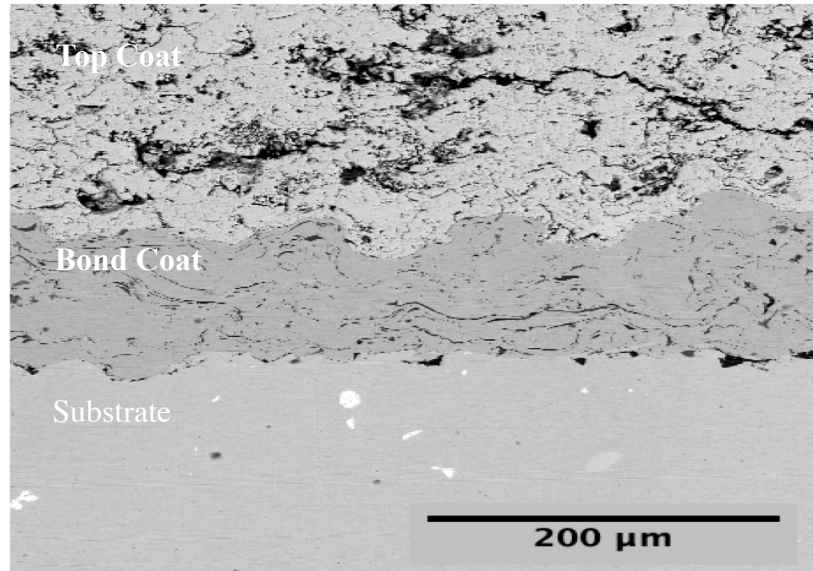


Figure 2.5 SEM microstructure of YSZ coating deposited with APS.

In the EB-PVD process, vapors are produced by heating the material with an electron beam and directed onto the preheated component [14], as illustrated in **Figure 2.6**. The vapor cloud condenses on the rotating component and forms the coating. In contrast to the TBCs

deposited by APS, EB-PVD TBCs have a columnar microstructure with nanometer-scale porosity and channels separating the columnar grains [16], as shown in *Figure 2.7*. The disconnected columns provide excellent strain tolerance and reduce thermal conductivity. Compared to APS TBCs described above, EB-PDV TBCs generally have longer thermal-cycling lives, but they are more expensive in production. As a result, EB-PVD TBCs are suitable for applications in aircraft engines, such as turbine blades [4], [17].

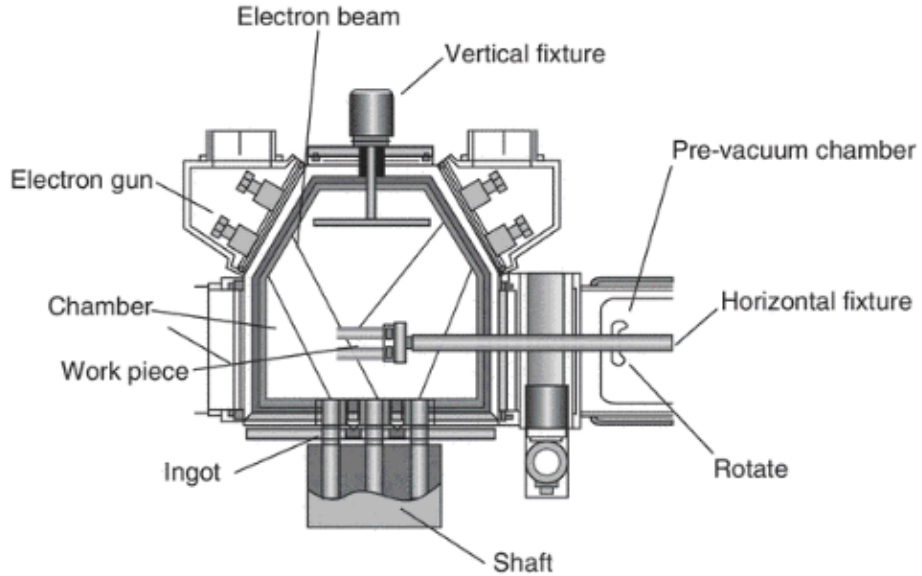


Figure 2.6 Schematic diagram of an electron beam physical vapor deposition (EB-PVD) system [14].

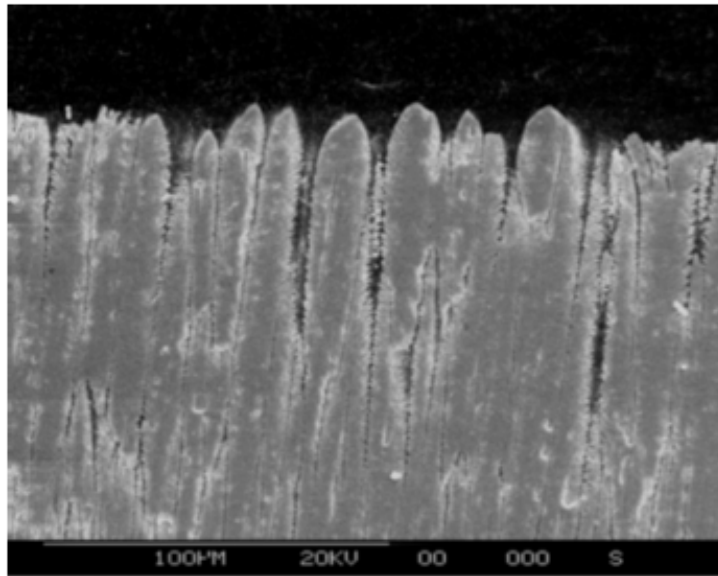


Figure 2.7 SEM microstructure of YSZ coating deposited with EB-PVD [18].

2.1.2 Bond Coat

The bond coat provides a number of functions to TBC systems. It provides adhesion of the ceramic top coat to the substrate, reduces the interface stresses induced due to a mismatch in thermal expansion coefficient between the top coat and substrate component, and protects the substrate from oxidation and corrosion by the formation of a slow-growing thermal oxide layer, i.e., TGO. Some of the basic properties of the materials used for the bond coat are resistant to inter-diffusion with the substrate and high creep strength with suitable ductility. The current state of the art TBC systems consists of MCrAlX and platinum modified diffusion aluminide bond coats, where M stands for metals, usually nickel (Ni), cobalt (Co) or iron (Fe) or a mixture of them and X = Y, Hf and/ or Si [19]. Typically used bond coat materials include a variety of MCrAlX alloy. Thermal spray

processes are usually used for the deposition of the MCrAlX bond coat. Nickel is added to enhance oxidation resistance while cobalt for corrosion and wear resistance [20]. Aluminum is added to the bond coat to act as a local Al reservoir to provide slow-growing α -alumina TGO during the TBC service condition, which can resist oxidation. The Al_2O_3 oxide is the preferable phase component of this layer, in the condition of oxidation above 900°C [11]. The addition of yttrium in MCrAlY mainly improves the adhesion of the bond coat by segregating to the bond coat/TGO interface and increases the oxidation resistance [21].

Diffusion aluminide coatings are fabricated either by pack cementation or chemical vapor deposition. The principle of both fabrication processes is the same where the coating develops by the reaction of gaseous aluminum halides with the substrate surface resulting in the formation of oxidation resistant NiAl phase. The adhesion of this coating is provided by elemental interdiffusion between the substrate and coating material.

In the case of platinum modified diffusion aluminide coatings, the NiPtAl bond coats are fabricated by electrodepositing a layer of Pt on the superalloy, followed by aluminizing process [22], [23]. Aluminide diffusion coatings have exhibited good protection against high temperature oxidation damage. The addition of Pt to the aluminide coating can enhance the scale adhesion, improve the oxidation resistance by further promoting selective oxidation of aluminum and stabilizing the interdiffusion between the bond coat and substrate [24], [25]. Moreover, it was reported that the oxide layer formed on the Pt-modified aluminide coating showed better adhesion in comparison to simple aluminide

coatings and was able to maintain an oxide layer with a higher amount of desirable α -alumina [26].

2.1.3 Thermally Grown Oxide (TGO)

The thermally grown oxide (TGO), typically alumina, is an oxidized scale formed at elevated temperatures on the bond coat as a result of oxidation. The oxidation is either because of diffusion of oxygen through the top coat towards the bond coat, where the new TGO growth occurs at the interface with the bond coat, or a result of outward diffusion of Al through the bond coat [27]. As mentioned in the previous section, the bond coat alloy is designed as a local aluminum reservoir so that alumina ($\alpha\text{-Al}_2\text{O}_3$) forms in preference of other oxides. Such a TGO has very low oxygen permeability so that its growth rate is low. Moreover, it provides an excellent diffusion, hindering further oxidation of the bond coat, and thus protects the substrate from oxidation [4], [11]. However, the establishment of pure alumina scale is not always possible due to mixed oxidation effects. When the TGO is formed, it grows and gets thicker, eventually imposes stresses on the interfaces of the TGO/bond coat and TGO/top coat. Therefore, TGO plays a significant role in the failure of TBC systems [28]. At some critical thickness of the TGO strains developed will be sufficient to drive crack formation at the interface, which is known as the critical strain energy [29], [30]. Most of the developed strains in an oxidizing TBC system can be dissipated by creep in the bond coat due to its high ductility at operating temperatures [31].

However, it has been reported that the stress relaxation via creep at the service temperatures is another factor thought to have a significant effect on the coating life, which causes high compressive stresses on the zirconia layer during cooling [30].

High temperature oxidation of TBCs can be explained by two processes, cyclic oxidation, and isothermal oxidation. The present research is focused on the isothermal oxidation of APS TBCs. As discussed above, at elevated temperatures bond coat oxidation leads to the formation and growth of the TGO scale at the bond coat/top coat interface. The formation of TGO is important for oxidation resistance. However, the breakdown of the protective scale might affect the integrity of TBCs. The characteristics of TGO such as growth rate, growth mechanisms, and TGO microstructure and its adherence to the bond coat and top coat are critical factors that determine the durability of TBC systems [32]. The oxidation of the bond coat can be divided into three stages, as shown in *Figure 2.8*, (I) a transient stage of simultaneous oxidation of all oxide-forming species in the bond coat, (II) a steady-state stage of formation and growth of a protective oxide scale, and (III) a breakaway stage of rapid oxidation and failure of TBC systems [33].

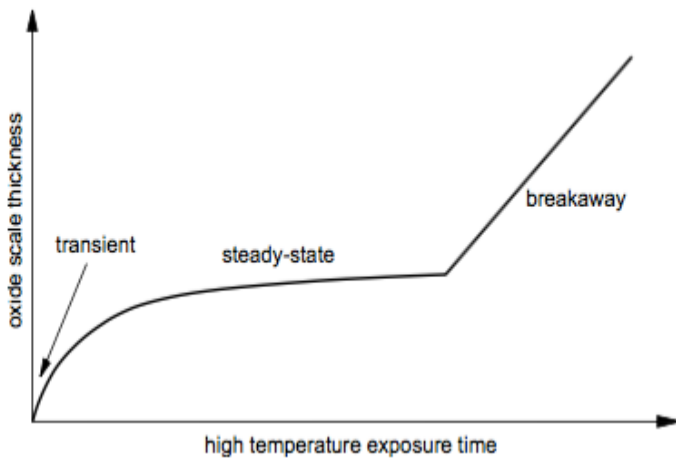


Figure 2.8 Schematic illustration of three oxidation stages of TBC systems [33].

2.1.3.1 Formation of Protective Oxide Scale

The transient stage is the stage of oxidation before a continuous oxide layer has formed on the metal surface. During this stage, more than one type of oxides form. Transient oxides include Cr_2O_3 , NiO , CoO , spinel type $(\text{Ni},\text{Co})(\text{Cr},\text{Al})_2\text{O}_4$ and various forms of alumina: γ , β , α - Al_2O_3 [35], [36], [40]. However, the transient stage is noticeably short, typically less than an hour for Ni-Cr-Al-Co systems oxidized at 1000 - 1200°C. The kinetic factors such as temperature, partial oxygen pressure, coating composition, and coating microstructure, play an important role during this stage and determine the composition of the transient oxides and whether a continuous scale of more thermodynamically stable oxides can be established or not. Low partial oxygen pressure, for example, may decrease the amounts of transient non-aluminum oxides and promote the formation of aluminum oxide [37]. The lower mechanical strength of these mixed oxides compared to alumina and the volumetric change associated with the transformation of the transient oxides to more

thermodynamically stable phases with continuous exposure to high temperatures can all contribute to the failure of TBCs. The formation of less stable oxides such as α -chromium or (Co, Ni) (Cr, Al) spinel is unfavorable because they are not as protective as alumina due to their high growth rate and porous structure. Moreover, it was reported that the TBC/spinel and TBC/ Cr_2O_3 interfaces can reduce the interfacial fracture resistance compared to the TBC/ Al_2O_3 interface and the transformation of Al_2O_3 into other mixed oxides as a result of aluminum depletion in the bond coat, which caused the TBC system to fail [38].

Following the transient stage comes the slower steady-state stage of the oxide growth during which a continues oxide layer is formed on the metal surface. From this point, the growth of the other metal oxides stops, and the oxidation rate becomes controlled by the diffusion rate of oxygen and metal ions through the oxide layer. The oxidation rate in this stage can be described by a power law as follows [33].

$$h = h_0 + (K_p t)^{\frac{1}{n_o}}, \quad n_o = 2 \sim 3 \quad (2.1)$$

where h is the thickness, or weight gain per area, of the formed oxide, h_0 is the thickness of the mixed oxides, K_p is the growth rate constant and t is the high temperature exposure time. The classical oxidation law is parabolic ($n_o = 2$) [39] but sub parabolic models ($1/n_o < 0.5$) are also in use [40], [41]. The oxides that are thermodynamically stable and exhibit low growth rate (lowering the diffusion rate through the oxide) are protective. Formation of such a protective oxide layer (alumina, chromia, or silica) is needed to obtain a long-term performance under oxidizing conditions [33], [40]. At high temperatures, aluminum oxide

is the most stable oxide at 1000°C compared to the oxides of the other major alloying elements.

In TBC systems oxidation can be either internal when the growth of TGO is controlled by the transport of oxygen towards the TGO/bond coat interface, or external by outward diffusion of Al ions towards the interface between the TGO and ceramic top layer [42]. The formation of an external oxide layer must be promoted in order to optimize the protective function, i.e., Al_2O_3 in a Ni-Cr-Al system. The amount of Al concentration in the alloy, oxygen partial pressure, the amount of solved O in the alloy, and the amount of other alloying elements are the most influential factors that affect the ability of the alloy to form external alumina. At a low fraction of Al, internal oxidation will occur if the diffusion of Al into the TGO/ceramic interface is slower than the diffusion of oxygen into the TGO/bond coat alloy interface and the aluminum will be oxidized internally due to high concentration of oxygen [43]. **Figure 2.9** shows the effect of Al concentration on the internal oxidation depth at 1000°C for different oxygen concentrations at the surface. It is revealed that the subscale thickness decreases with increasing Al and decreasing O in the alloy until the shift to external oxidation occurs [43].

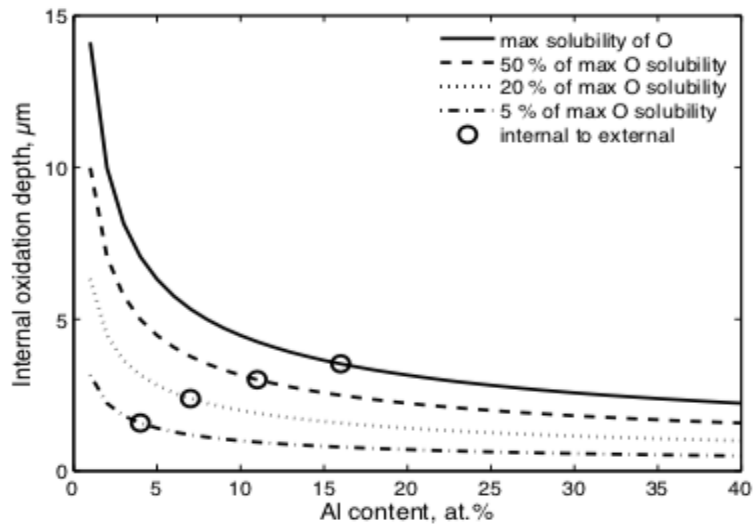


Figure 2.9 Subscale thickness as a function of Al and O contents, also showing the hypothetical transition from internal to external oxidation [43].

The oxidation kinetics of MCrAlY alloys is significantly affected by the presence of minor additions of reactive elements such as Y, Zr, or trace elements like Si, Ti, etc. These reactive elements are generally considered to improve the oxide scale adhesion, decrease the growth rate of oxides, and enhance selective oxidation in yttria-containing alloys [44], [45]. Although the mechanisms of how reactive elements improve adherence are not completely understood, a number of mechanisms have been proposed. First, reactive elements alter the oxide growth mechanism and reduce the outward diffusion of Al ions by segregating to Al_2O_3 grain boundaries, hence decrease spalling of the oxide by decreasing the lateral growth of the oxide [46]. Second, the presence of reactive elements at the alloy/oxide interface would improve the scale adhesion [47]. Third, reactive elements prevent sulfur from segregating at the alloy/oxide interface and weakening the adhesion by

trapping it at grain boundaries in the substrate [47], [48]. As a consequence, reactive element addition limits the formation of voids beneath the oxide scale [48].

A direct application of these effects can be seen by adding Y to MCrAl bond coat as reported by Tawancya and Abbasa [49]. Yttrium can alter the oxidation behavior of MCrAl alloy by various mechanisms. The presence of Y improved the mechanical adhesion of the α -Al₂O₃ scale to the coating by oxidizing into Y-rich oxide "pegs" within the scale. Moreover, the presence of Y in the solid solution in the TGO, and segregation of Y to the alumina grain boundaries could reduce the scale growth rate and improve its high temperature mechanical strength.

2.1.3.2 Breakdown of Protective Oxide Scale

The TGO will remain protective as long as the bond coat contains sufficient Al to ensure continuous protective layer. However, aluminum will be depleted through oxidation and interdiffusion during high temperature oxidation [40], [50]. After critical Al-depletion occurs, the oxygen partial pressure can reach a value, which is sufficiently high for the next stable oxide (chromia) to form and grow at the bond coat/top coat interface, causing an increase in the oxidation rate. The growth of unwanted oxides in the TGO can greatly accelerate the failure of the TGO because of their lower fracture toughness and increased mismatch in the coefficient of thermal expansion (CTE) [51]. This marks the onset of breakaway oxidation leading to the spallation or chemical failure of the TGO [52]

2.1.4 Superalloy Substrate

The substrate of TBC systems is the material intended to be protected at high temperature. The substrate material is typically nickel or cobalt-based alloy. Due to their enhanced

ability to maintain structural integrity and sustain high stresses in the service conditions and surface stability at high temperatures, superalloys are predominantly used in gas turbines. Turbine blades are exposed to high temperatures, high stresses, and rapid temperature changes during thermal cycles. Moreover, they are subjected to hot gases that cause the oxidation and corrosion of the component in the working conditions. Therefore, high corrosion and creep resistance as well as high fatigue strength are the basic properties that the substrate materials for gas turbine blade components should have. The nominal composition of a conventional Inconel 718 superalloy for the substrate material of TBCs is given in **Table 2.1**. The interdiffusion of the high concentration elements occurring at high temperature of operation has a pronounced influence on the spallation failure of TBCs [2], [11].

Table 2.1 Chemical composition of Inconel 718 superalloy [11].

Chemical Composition (wt%)								
Cr	Ni	Nb	Mo	Ti	Al	Cu	C	Fe
19	52.5	5.1	3.0	0.9	0.5	0.15 max	0.08 max	Bal.

2.2 Failure Mechanisms of TBCs

TBCs provide protection to the superalloy substrate from high temperature gasses. However, the beneficial effects obtained by using a TBC system strongly depend on the durability of the TBC system under different operation conditions. Many studies have been conducted to understand the failure mechanisms of TBC systems in order to be able to

improve their durability, but they are still not fully understood due to the complexity of TBCs, which comes from the multilayer structure of TBCs and highly coupled failure mechanisms. Many destructive processes have been identified to depend on temperature, oxidation time and the number of thermal cycles. The extreme difference in thermo-mechanical properties between the TBC and substrate creates thermal stresses at the TBC/substrate interface during the TBC high temperature service and/or in the manufacturing process [53], [54]. The evaluation of these individual effects on the coating's lifetime is complicated since they occur simultaneously, and multiple combinations are more likely to take place. The development of TBCs for high temperature applications requires a fundamental understanding of their failure mechanisms in order to prevent spallation of the coating from the substrate, which compromises the function of the coating. Researchers have found that the failure of TBCs generally follows a sequence of crack nucleation, propagation and coalescence events along or near the interface between the ceramic top coat and the metallic bond coat, which accumulate prior to the final failure by large scale buckling and spalling [53], [54]. It is generally believed that the failure process of TBCs starts in the earlier stages of TBC service, and some initial sites are generated during TBCs fabrication process. After a relatively short time in service, a granular pattern of cracking network formation can be observed on the TBC surface. These initial cracks propagate throughout the coating layer thickness and reach the coating/substrate interface.

Eventually, the separation between the coating and substrate would be more enough to cause large-scale buckling in edge delamination, leading to spallation of the coating [55]. Formation and propagation of these cracks are fundamental factors for developing failure of TBCs [56], therefore, reducing crack initiation, propagation, and coalescence would be a key factor to increase TBC durability.

2.2.1 Bond Coat Oxidation

The failure mechanisms of TBC systems also differ, depending on the underlying bond coat. Different failure mechanisms have been reported even for the same type of bond coat due to the pronounced effects of different fabrication procedures and composition on their properties. Bond coat oxidation has been recognized to be the most critical factor for TBC failure by causing spallation of the ceramic layer from the substrate. The functions of the bond coat are to enhance adhesion of the ceramic topcoat to the substrate and to provide oxidation and corrosion protection to the substrate metal. However, the oxidation of the bond coat can limit these functions, because under the service conditions it leads to the formation and development of TGO at the ceramic top/metal bond coat interface, as shown in *Figure 2.10*, which generates, in addition to the thermal stresses induced during cooling, high in-plane compressive stresses. Due to oxidation, significant out-of-plane tensile stresses that are the main driving force for crack formation, are induced at the top of the wavy interface. Failure usually occurs upon cooling because the thermal mismatch between the top coat, TGO, and bond coat generates additional in-plane compressive stresses [4], [42]. Therefore, the morphology, adherence, and stresses in the TGO are important issues in TBC durability evaluation and life prediction [42]. The growth of TGO scale is

controlled either by the transport of oxygen towards the TGO/bond coat interface, i.e., internal oxidation or by outward diffusion of Al ions towards the interface between the TGO and ceramic top layer, i.e., external oxidation. As a result, external oxidation can lead to the formation of β -depleted zone. Accordingly, other oxides such as chromia ((Cr, Al)₂O₃), spinel (Ni(Cr, Al)₂O₄), and nickel oxide (NiO), form along with the TGO layer in TBC systems. The formation of these oxides provides fast oxygen-diffusion paths and hence accelerates localized oxidation. Massive stresses due to the rapid local volume increase lead to consequent spallation and delamination of TBCs because crack initiation at these sites of TBC systems will eventually occur [4], [42], [57]. Generally, the failure of TBC systems mainly depends on the characteristics of the TGO layer. If this layer is composed of a continuous scale of Al₂O₃, it would serve as a diffusion barrier and repress the formation of other detrimental oxides during the extended thermal exposure in service, accordingly, favoring the protection of the substrate from further oxidation and improving the TBC system durability under working conditions [42].

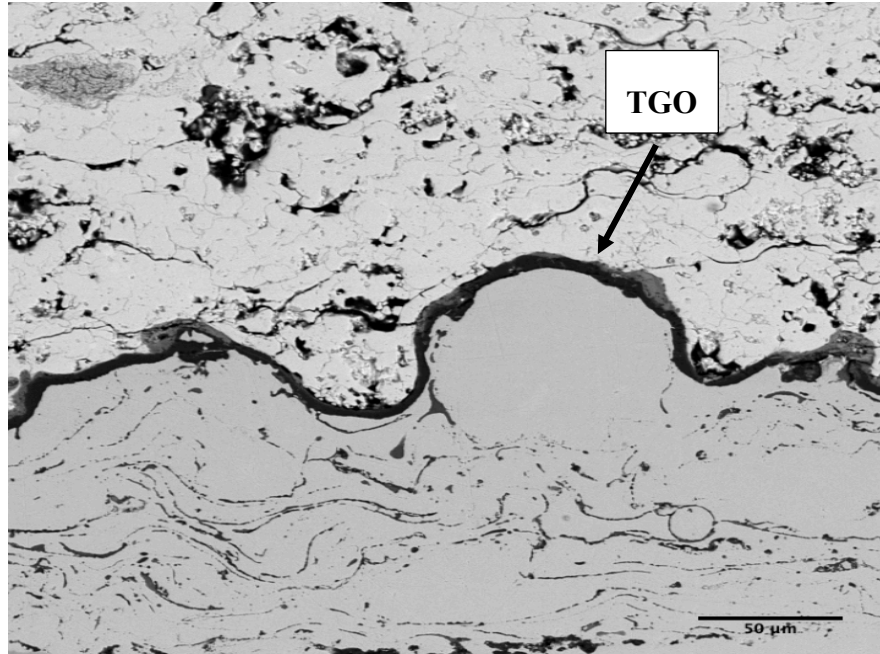


Figure 2.10 SEM microstructure in cross-section of a TBC system showing bond coat oxidation with developed TGO.

2.2.2 Residual Stresses

The residual stresses in TBCs have been extensively studied since they are one of the key factors affecting the functionality and durability of TBCs [34]. The performance of TBCs which is characterized by the lifetime under thermal cycling, the resistance to thermal shock, adhesion strength, erosion resistance, etc., is highly influenced by residual stresses in TBCs. Hence, the prediction of magnitude and distribution of residual stresses in TBCs is essential not only to understand the failure mechanisms of TBC systems but also to predict their service lives [34].

The residual stresses within TBC systems may arise from three main sources: (I) The stresses originated from the difference in coefficient of thermal expansion (CTE) of the

underlying materials and coatings upon cooling of TBCs, known as thermal stress or residual stress. Therefore, the thermal coefficient mismatch of different materials is the main reason for the large residual stresses induced in the coating. These stresses due to thermal mismatch are compressive in the ceramic coating at ambient temperature since the ceramic coating material has lower CTE than the other materials of TBCs [34]. Compressive thermal residual stresses can prompt crack initiation parallel to the coating interface and cause spalling inside the TBC system [54], [58]. (II) The stresses developed during the coating deposition process because of rapid solidification and contraction of the droplets deposited onto the bond coat [34]. The stresses induced in the condensed layer are tensile. In general, the stresses due to solidification are not significant as they are reduced by ongoing processes (stress relaxation). (III) During the growth of TGO, while thermal stresses are thought to be responsible for the eventual oxide scale failure in most cases, the growth stresses might play a significant role in the failure mechanisms of TBCs. The growth stresses might contribute indirectly to inducing oxide scale deformations resulting from the growth strain accommodation at oxidation temperature; this would eventually lead to a tougher oxide layer and consequently cause higher local tensile stresses upon cooling. They also contribute directly to imposing additional in-plane compressive stresses to the thermal stresses upon cooling, if they are not significantly relaxed during oxidation [28], [30]. The thermal and growth stresses are considered to be compressive stresses and the majority of them are generated at the interface upon cooling (thermal mismatch stress). The growth stresses are considered to be negligible on a flat surface. However, it has been shown that imperfections such as undulations on the coating surface can be considered as defect generators [30]. Out-of-plane stresses are generated at the flanks of asperities within

the TGO and top coat as a result of uneven growth of the oxides, and cracks can be nucleated as soon as the stress level rises to a critical point [51]. These cracks grow and coalesce with increased exposure to high temperatures; finally leading to the spallation of the ceramic top coat. The residual stresses in TBC systems are directly affected by bond coat properties. Depending on the type of bond coat, TGO will have different morphologies and thickness, which influence the residual stress state [59]. Generally, after several thermal cycles, the damages in TBCs are related to the residual stresses developed from the coating deposition process, thermal mismatch of the material constituents, the oxidation of the bond coat, complex shape of the ceramic/metal interface, and the redistribution of stresses via creep, plastic deformation, and cracking resistance [59].

2.2.3 Sintering of YSZ

When TBCs are exposed to oxidizing gasses and the external temperature reaches 1200°C, sintering which is one of the temperature driven phenomena takes place [4]. Sintering adversely affects the durability of the ceramic top coat. In general, there are two effects associated with sintering. A decrease in the volume fraction of the defects, partial healing of cracks and a reduction in porosity, lead to the increase in stiffness, and thereby decrease the compliance of the ceramic top coat, which directly influences the stress distribution in TBC systems. On the other hand, these changes also cause the increase in thermal conductivity of the top coat, resulting in an increase of bond coat surface temperature and consequently, the enhancement of creep and bond coat oxidation [4], [60].

For APS YSZ top coat the change of microcrack morphology (healing) starts at 900°C. At higher temperatures, above 1200°C, the reduction of porosity occurs due to the increase of the contact area between spraying splats [4]. EB-PVD ceramic coatings have a columnar

structure with channels between the individual columns [60]. The individual columns should in principle not be in contact at high temperatures in order to accommodate thermal expansion mismatch stresses. However, due to the feathery shape contact sites exist and sintering “necks” are formed, as shown in **Figure 2.1**. The resulting coating will have higher stiffness with reduced strain tolerance and thermal insulation capability [61].

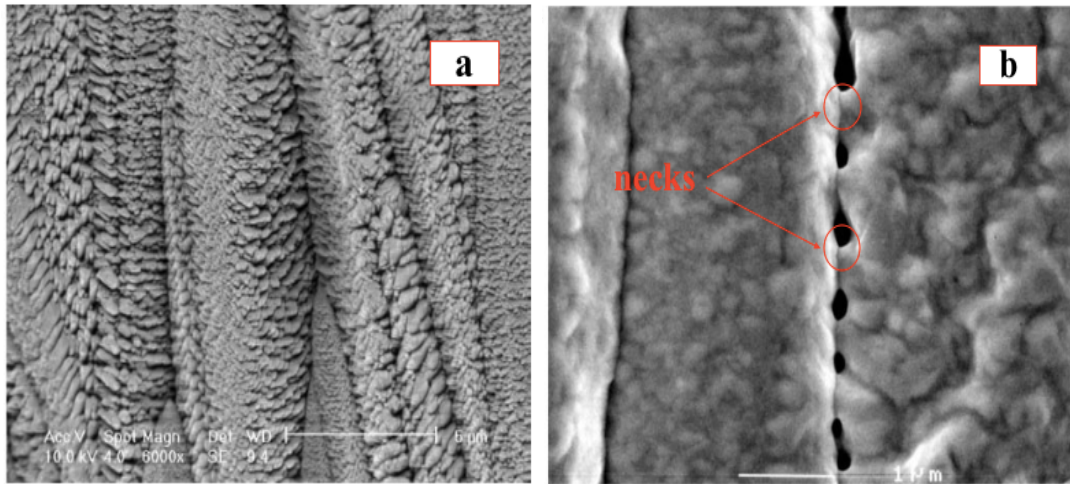


Figure 2.11 Microstructure of EB-PVD top coat: (a) feathery shape of columns and (b) formation of necks [61].

2.2.4 Interdiffusion between Substrate and Bond Coat

The thermal cycling of TBC systems promotes interdiffusion of various elements between the bond coat and the underlying superalloy substrate matrix. The Al content in the bond coat becomes lower and lower due to the inward diffusion of Al in the substrate (depletion of β -phase in favor of γ' -phase) during the service of TBCs. In addition, outward diffusion of some elements of the substrate such as chromium, titanium, or cobalt might also occur [60]. The interdiffusion between Ni-base superalloys and MCrAlY bond coat can lead to the formation of detrimental phases such as σ (sigma)-phase, Laves phases, brittle carbides,

voids, and porosity [62]. However, the effects of such interdiffusion on TBC failure are not well defined. The changes in the compositions of the bond coat layer and the substrate through interdiffusion can have a profound influence on the spallation failure of TBCs [4].

2.2.5 Phase Transformation

Phase transformation can occur in the ceramic top coat of TBCs during thermal aging. This transformation leads to volume changes that induce stresses within the coating. Consequently, spalling of the coating might occur. Moreover, the mechanical properties of the coating such as strain compliance, sintering capabilities, and thermophysical properties will also be affected [63]. It was reported that the yttria-rich islands at the TGO/top coat interface of an EB-PVD TBC system locally impeded zirconia uptake of the scale during the TBC deposition process, causing the formation of an "off-plane" alumina-zirconia mixed zone textured perpendicular to the TGO/top coat interface. Also, during prolonged isothermal/cyclic oxidation the increase of chromium diffusion through the TGO scale changed the mixed zone into a reaction zone introducing a morphological instability of the mixed zone/top coat interface due to solutioning of the -Pt on two single-crystal Ni-base superalloys with the chemical compositions given in *Table 2.2* at the high temperature of 1150°C found that the decohesion between the TGO and bond coat occurred, which was the failure mode of the coating system for both alloys. This was suggested to correlate with the formation of Ti-rich and/or Ti+Ta-rich oxide particles near the oxide/bond coat interface, which degraded the adherence of the TGO [65], as shown in *Figure 2.12*. It was also revealed that the constrained phase transformation in the oxide occurred if the TBC was deposited prior to completion of the phase transformation in the alumina. There existed a critical thickness of TGO above which interface separation would

occur if the phase transformation in the oxide was incomplete before TBC deposition [66]. Phase transformation may also take place in the bond coat of TBCs. As reported [67], before thermal cycling, the structure of as-fabricated bond coat was present as a long-range ordered B2 β -phase, but after thermal cycling to ~28 % of the cyclic life, the phase of the bond coat transferred into Ni-rich L1₀ martensite (M) from its original B2 structure. This transformation was reversible and occurred under heating and cooling in each cycle. XRD measurements and analyses on the TBC specimens at high temperatures showed that the phase transformations produced about 0.7 % transformation strain. These phase transformations have detrimental effects on the durability of TBC systems.

Table 2.2 Chemical compositions (wt%) of Ni-based superalloys [65].

Element	Ni	Co	Cr	Al	Ti	Ta	W	Re	Mo	Hf
Alloy 1	Bal.	9.5	6.2	5.5	1.0	6.5	6.5	2.9	0.6	0.1
Alloy 2	Bal.	9.5	6.2	5.5	0.3	8.5	6.5	6.0	0.6	0.1

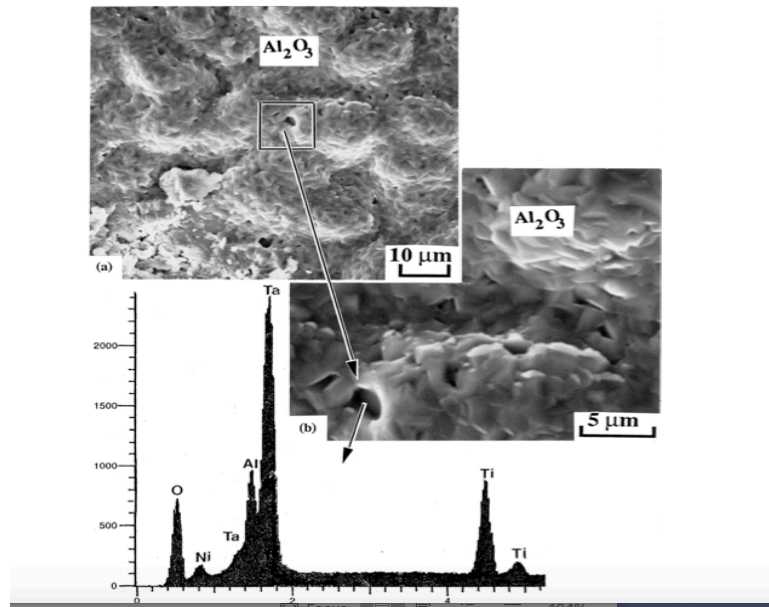


Figure 2.12 Identification of $Ta+Ti$ -rich oxide at the bond coat surface with alloy 2 after exposure to $1150^{\circ}C$ for 984 h with schematically showing the decohesion of the oxide by coalescence of voids around $Ta+Ti$ -rich oxide particles [65].

2.2.6 Erosion of TBCs

Aero-engines operating in dust-laden environments often encounter solid particle erosion problems. Various particulates generated within the engine such as carbon particles formed from the engine combustion process and wear debris of engine components may also cause the erosion of the TBC on the turbine blades. Therefore, erosion-based failures also play an important role in the service life of TBCs under environmental conditions. In TBCs, better erosion resistance of the ceramic top coat is highly desirable as it has a direct influence on the TBC performance.

Erosion is described as a degradation of the surface as a result of mechanical interaction of the material surface with solid particles, which can occur in the atmosphere or be induced by the spalling of the surface material [68]. In aero engines the particle impact results in

material removal that can put the turbine at risk. In aerospace applications, TBCs are subjected to airborne particles, making the solid particle erosion an important failure mode of TBCs [69], [70]. A schematic diagram of erosion wear by solid particle impact is shown in *Figure 2.13* [71]. The damage related to erosion is primarily dependent on the microstructure and properties of the target material. Moreover, impingement particle size, particle velocity, impact angle, and temperature among others have the most significant effects on the erosion rate of both APS and EB-PVD TBCs [72]. *Figure 2.14* shows the dependence of erosion on the impact angle. Recently, Nicholls et al. demonstrated that EB-PVD deposited TBCs possess better erosion resistance compared to APS TBCs due to their columnar microstructure [18]. However, EB-PVD is a comparatively expensive process with lower deposition rates than APS.

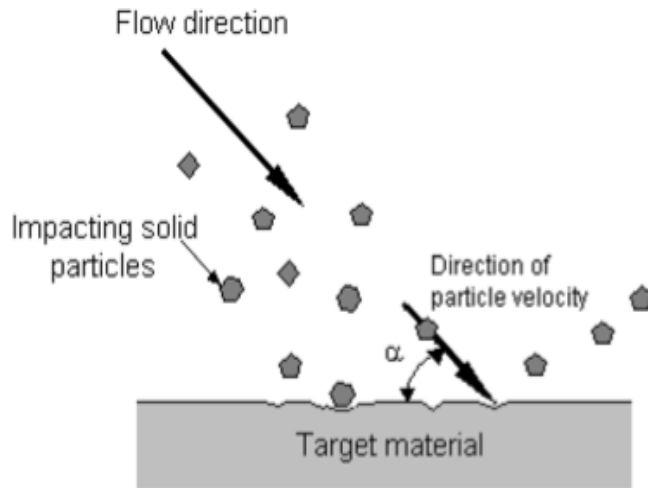


Figure 2.13 Erosion wear by solid particle impact [71].

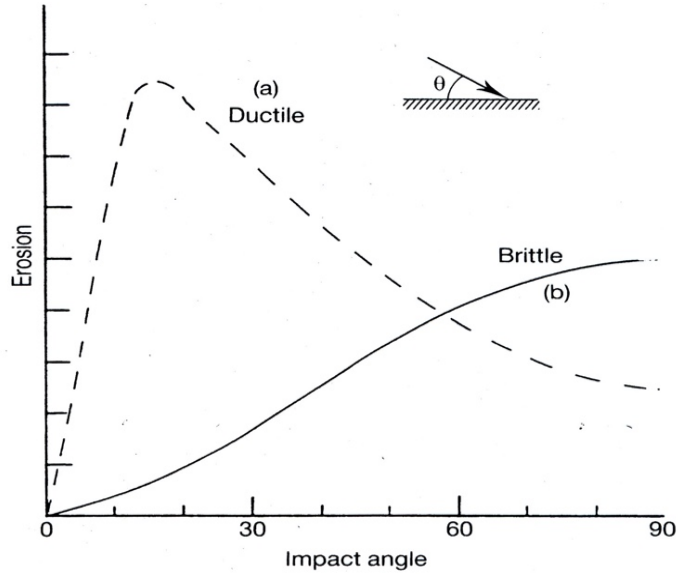


Figure 2.14 Typical erosion dependence on impact angle [71].

There are two types of damage induced by solid particles in the erosion of TBCs: One is foreign object damage (FOD) when the top coat is removed down to the bond coat. This damage generates local hot spots where the substrate could be severely damaged. Cracks can then be initiated and propagate from these hot spots leading to the whole TBC spallation. The other is erosion thinning, where the ceramic coating thickness is locally reduced by wear. The substrate remains protected but at a lower level and oxidation rates then increase locally in this case [73], [74]. It has been reported that TBCs are more susceptible to erosion than fully dense ceramics because the coating microstructures contain many cracks [73].

Erosion mechanisms of APS and EB-PVD coatings differ significantly because of their different microstructures. Eaton and Novak [75] in their work distinguished three different types of solid particle erosion of APS TBCs. In first type, impacting particles produce

mainly indentations on the surface (low erosion rates), in the second type of mechanism, the impact promotes crack nucleation in the impact area and crack propagation through and around individual splats (medium erosion rates). In the third type, crack propagation through pores and cracks, which are typical of the APS microstructure, promoting erosion of clusters of splats (tunneling) (high erosion rates). For EB-PVD coatings, the columnar structure is responsible for the damage modes different from that of bulk ceramic materials and APS coatings. Wellman and Nicholls [76] described three possible erosion damage modes for EB-PVD TBCs. Mode I: when small particles impact on EB-PVD TBC surface at a sufficiently low speed, the top 20 μm of the individual columns are cracked due to impact (near surface cracking/lateral cracking). Mode II: with intermediate particle size and momentum, a shallow thin layer zone forms by multiple impacts. Successive impacts induce stress concentrations at the intersection of the dense and columnar regions, which cause portions of the dense layer to detach from the underlying columns. Mode III: when particles with high momentum (high speed large particles) impact on the EB-PVD TBC, most of the kinetic energy is absorbed by plastic deformation and densification bending. Deformation is accompanied by kink bands around the perimeter of the plastic zone. These bands intersect the TGO and initiate delamination cracks that extend outward from the impact center, parallel to the coating interface (foreign object damage) [77].

Erosion rate is used to distinguish the two main types of erosion processes: ductile and brittle. During the ductile erosion process, for ductile materials, the surface damage develops predominantly by plastic deformation, such as cutting, extrusion, adiabatic, shear, and forging. During the brittle erosion process, particle impact produces different types of cracks and chipping, with negligible plastic deformation. However, ductile and brittle

erosion of materials could occur simultaneously, the ratio of them depending on impact angle and material properties [72].

The response of the erosion rate of ED-PVD top coat to the reduction of the coating thickness through to the bond coat was investigated under a range of different impact conditions. The different damage mechanisms were identified and related to the size and impact velocity of the impacting particles. It was found that at temperatures above 800°C the coating can accommodate a large degree of plastic deformation, while at room temperature there was a greater degree of cracking. Also, the erosion rate was reduced with a decrease in the column diameter, but aging caused an increase in the erosion rate, depending on the aging temperature and time [78]. The erosion behavior of suspension plasma spray (SPS) EB-PVD and APS YSZ-based TBCs with APS CoNiCrAlY bond coat was studied at room temperature. The erodent material was 50 µm alumina. The impact angles were 15 degree and 90 degree. The erosion tests demonstrated that for all the TBC specimens 15 degrees impact angle caused larger erosion volume loss than normal impact angle and SPS EB-PVD TBCs exhibited better erosion resistance than APS TBCs. Between the two microstructures of YSZ top coat, the columnar-segmented microstructure was better than columnar-grown microstructure in resistance to solid particle erosion [79], as presented in *Figure 2.15*. The erosion behavior of TBCs on Inconel 718 substrate was also investigated with a combined experimental and computational approach. The experiments were performed using alumina particles to determine the erosion rates and particle restitution characteristics under different impact conditions. It was shown that the erosion rates rose with increasing impingement angle, impact velocity, and temperature, as illustrated in *Figure 2.16*. Inconel 718 alloy with or without TBC exhibited different

erosion performance, as shown in *Figure 2.17*, the latter had a turning point on the erosion rate curve (about 20 degrees impingement angle) where the erosion rate started to decrease with impingement angle. This was attributed to the ductile feature of Inconel 718 alloy, which made the erosion mechanism change at the critical impingement angle [80].

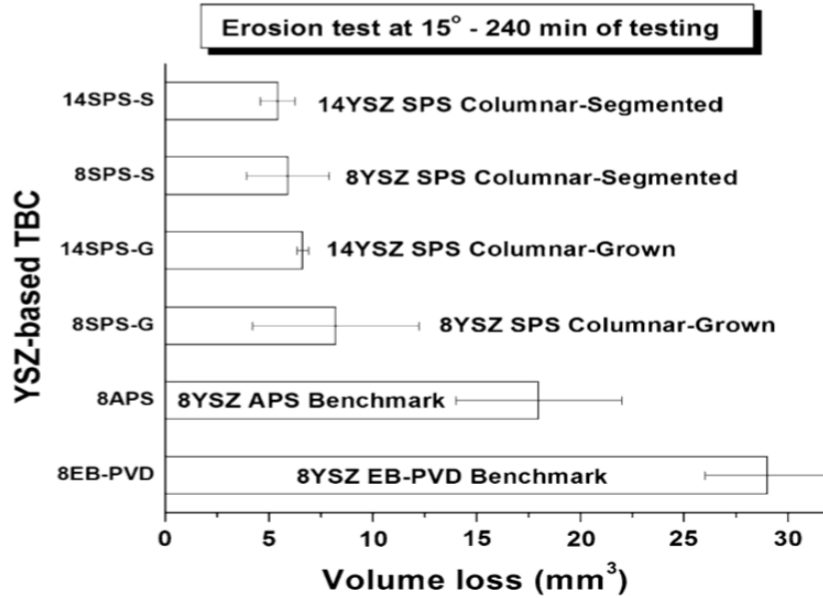


Figure 2.15 Comparison of solid-particle erosion loss between different TBCs [79].

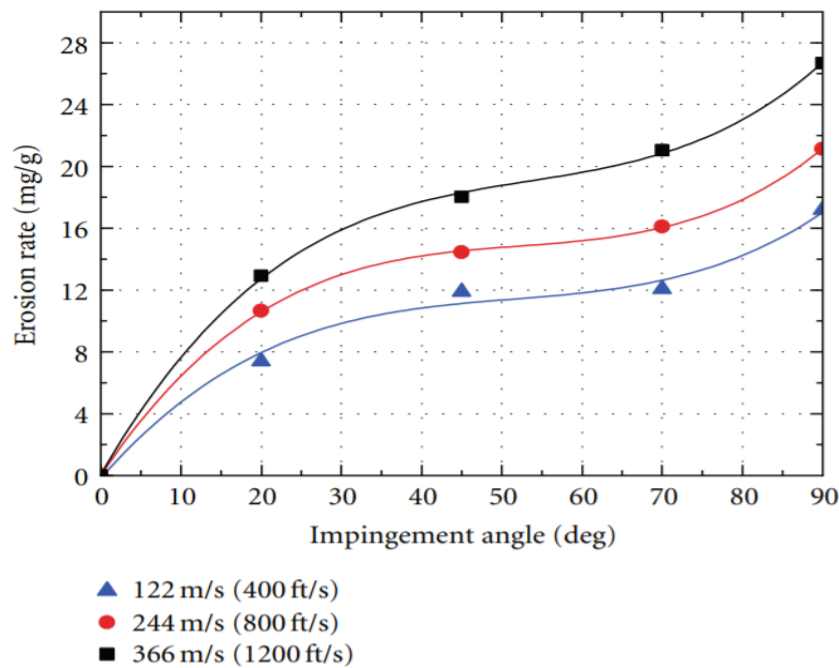


Figure 2.16 TBC erosion rates under impact with $26 \mu\text{m}$ alumina particles at 982°C [80].

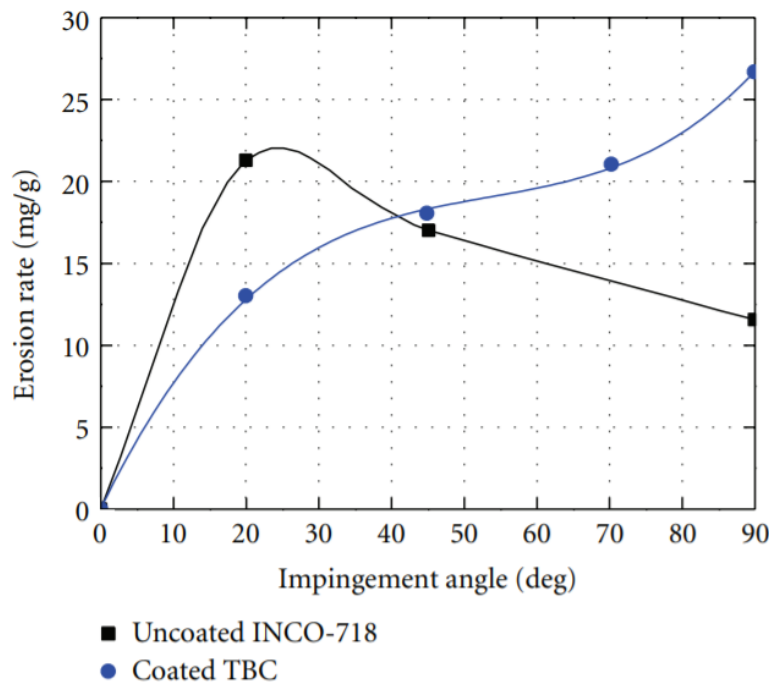


Figure 2.17 Comparison of erosion rate of Inconel 718 with or without TBC under impact with $26 \mu\text{m}$ alumina particles at 1093°C and 365.8 m/s [80].

2.2.7 Other TBC Failure Influence Factors

2.2.7.1 Effects of External Loading on the Failure Mode of TBCs

The components in the hot sections of gas turbine engines experience severe cyclic thermal and mechanical loads and hence, their lives are limited by the severity of these thermomechanical loads. Tzimas et al. [81] studied the failure of TBC systems under thermomechanical tests that simulated the cyclic mechanical loading with cyclic temperature gradients. They found that TBCs failed by cracks that started at the bond coat/TGO interface and penetrated through the bond coat into the substrate. When the load was reduced the lifetime of the coating increased and the cracks leading to failure moved to the top coat.

2.2.7.2 Effects of Substrate Curvature on the Failure Mode of TBCs

The geometry of a real turbine blade and vans is characterized by a degree of curvature, concave or convex. The substrate curvature influences the thermal/residual stress distribution within the layers of TBC systems thus affecting the energy release rates associated with interface delamination and crack propagation during the spallation of the coatings. Liu et al. [82] determined the stress distribution in the top coat near the interface with different interface morphologies to characterize the failure modes of TBCs from the stress distribution. They found that the substrate curvature affected the splats deposition behavior and therefore altered the microstructure of various locations accordingly, which led to the redistribution of residual stresses in both top coat and Bond coat. Moreover, the cracks into top coat promoted the critical failure of the TBC and this failure was enhanced for the top coats with convex curvatures.

2.3 Interfacial Fracture Toughness of TBCs

2.3.1 Interfacial Cracking of TBCs

The main function of TBCs is to protect the engine component in high temperature environments. However, when stresses develop mechanically or thermally in the coatings, they can lead to crack initiation near the TBC interface. The interfacial crack initiated from small defects near the TBC interface propagates parallel or close to the top coat/bond coat interface. After a certain time of service, the coating layer can delaminate, leaving the underneath layers in unprotected state [83]. In both APS and EP-PVD TBCs, interfacial fracture is aided by interfacial toughness degradation due to fatigue and segregation of undesirable elements, for example, sulfur, to the interface [4]. During the TBC spallation, debonding of the coating layer from the substrate or cracking within the coating layer typically occurs, which leads to the failure of the entire coating system. From the preventing mechanical failure point of view, increasing the bonding strength directly benefits the durability and reliability of TBCs. Moreover, the bonding strength is an essential parameter utilized to predict the lifetime of TBCs. Therefore, selecting a suitable and reliable measurement technique to gauge the bonding strength plays a key role in identifying and quantitatively calibrating coating integrity, such as fatigue lifetime and failure strength evolution and assessment [84].

One of the widely accepted measurements of coating bond strength is debonding stress from the tensile adhesion test specified in ASTM C63379 [85]. Although the average debonding stress is simple to obtain, it discounts the fact that TBCs are full of defects such as pores and cracks. It is agreed that the presence of defects will create stress concentrations and lower the debonding stress. Obviously, such bond strength measurement does not

account for intrinsic defects in the coatings. Therefore, for more reliable results, the fracture toughness approach which accounts for interior coating defects is recommended as a conservative measurement for the debonding characteristics of TBCs [84]. Interfacial fracture toughness of TBCs is a critical factor that affects the durability of the coatings. Recently, it has received significant interest as one of the most design parameters that control the selection of the coating materials and assess the coating durability.

2.3.2 Evaluation of Interfacial Fracture Toughness

Many methods have been developed to measure the interfacial fracture toughness of TBCs, for example, barb pullout, double cantilever beam [86], three-point or four-point bending, scratch [86], Raman spectroscopy, X-ray diffraction, indentation, etc. Tensile fracture test using a sandwich type- Chevron-notched TBC specimen was conducted to measure the interfacial fracture toughness of TBCs [87]. An effective method can be chosen, based on test applicability, the cost of conducting the test, and the difficulties in implementation of the adequate test, to evaluate the interfacial toughness of TBCs. Indentation techniques have been widely used to determine the fracture toughness of brittle bulk materials such as ceramics [86]. The simplicity and flexibility for material evaluation are the features of general indentation testing. Indentation perpendicular to the coating surface is one of the proposed tests to measure the interfacial fracture toughness. The test was first proposed by Drory and Hutchinson to measure the interfacial adhesion of a diamond-coated aluminum alloy [88]. Their work was based on two assumptions: (I) The film was in a state of biaxial compressive stress, (II) Linear elastic fracture occurred under mode II condition and the thickness of the film deposited was small so that it did not affect the substrate delamination induced by the indentation. Based on their work, Visinonta et al. developed the procedures

for using the Rockwell-type indentation test to measure the fracture toughness of TBC systems [89]. The indenter used in the test was Rockwell Brale C indenter. The coating material was penetrated by the indenter; thus, compressive radial strains were induced in the substrate which was driven by the elastic-plastic deformation of the substrate. These compressive strains were transferred to the top coat layer and eventually delamination of the coating occurred. By the measurements of the indent, delamination radii, and coating thickness, toughness can be determined [89]. By far, Vickers indentation is the most widely used indentation test method for evaluating the fracture toughness of TBCs. The assessment of the fracture toughness can be achieved directly from the indent cracks that are induced by a pyramidal Vickers indenter. The TBC sample is indented exactly at the coating/substrate interface, as shown in *Figure 2.18* [90].

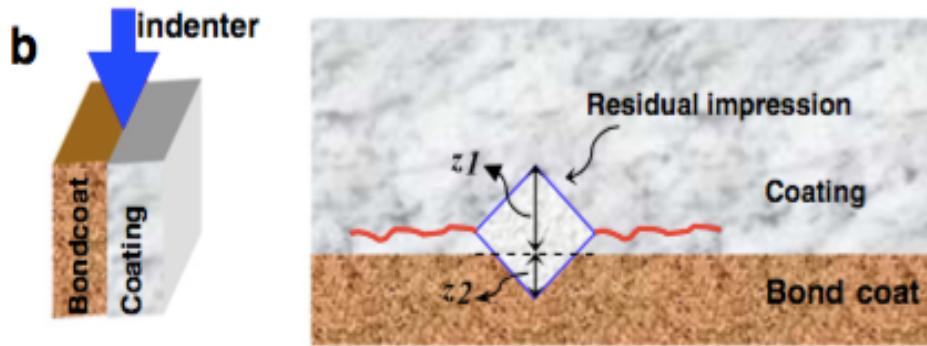


Figure 2.18 Schematic illustration of Vickers indentation on a TBC system [90].

In the indentation test, an interfacial crack develops at the corners of the indent and propagates along the interface with increasing the applied load. The total half crack length c , shown in *Figure 2.19 a*, is half of the diagonal of the indentation mark a plus the length

of the radial crack which starts at the corner of the indentation mark or impression, as indicated in **Figure 2.19 a**. When the crack length is plotted as a function of the applied load in a bi-logarithmic scale, a linear relationship (called the crack curve) is achieved for a given substrate and coating thickness [91]. Similarly, the relationship between the half diagonal length of the impression, and the applied force is linear, as shown in **Figure 2.19 b**. The intersection between the line of the half of the diagonal and the line of the crack length is the critical point for failure, as indicated in **Figure 2.19 b**. The coordinates of the points are the critical load F_c and the corresponding critical crack length c . The apparent interfacial fracture toughness is calculated by using these coordinates of the critical point [91], [92].

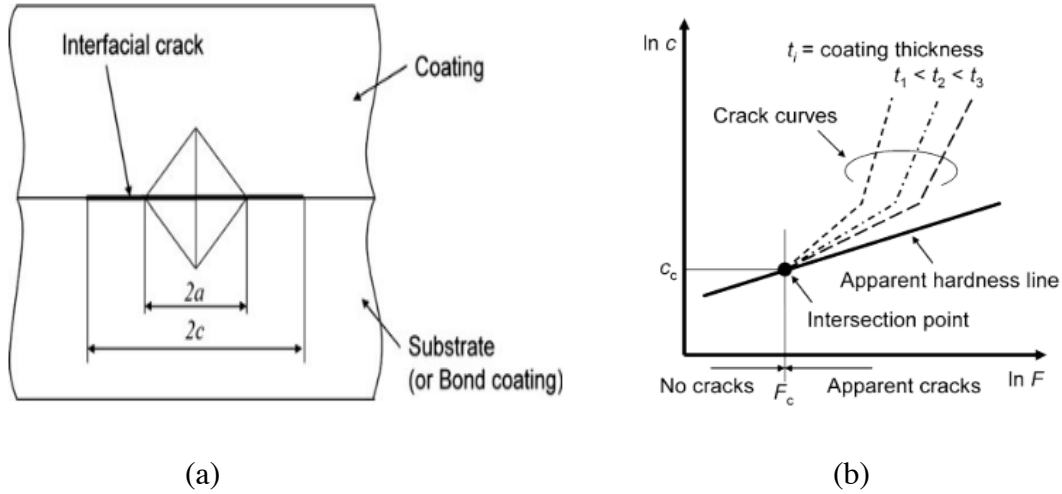


Figure 2.19 Interfacial crack in a TBC system under indentation: (a) geometry of interfacial crack and (b) schematic illustration of crack length [91].

Lesage et al. [92] proposed the following equation to gauge the apparent interface fracture toughness K_{Ca} .

$$K_{ca} = 0.015 \left(\frac{E}{H} \right)_I^{1/2} \frac{F_c}{C a_c^{3/2}} \quad (2.2)$$

$$(E/H)_I^{1/2} = \frac{(E_s/H_s)^{1/2}}{1 + (H_s/H_c)^{1/2}} + \frac{(E_c/H_c)^{1/2}}{1 + (H_c/H_s)^{1/2}} \quad (2.3)$$

where E_i is Young's modulus, H_i is the hardness, and subscripts s and c refer to substrate and coating respectively. These techniques are simple and useful in engineering. However, the interfacial fracture toughness obtained via these techniques can differ greatly between tests. For instance, it has been found that the interfacial fracture toughness obtained in a shear-type test is approximately 100 J/m^2 , while that obtained in a tensile type fracture test is only 38 J/m^2 . This can be attributed to the defects in the ceramic coating, as suggested in [87]. On the other hand, from the interfacial fracture mechanics point of view, the discrepancy can be attributed to the different loading modes. For example, the Vickers indentation fracture test belongs to mode I (loading normal to the interface). Four-point bending interfacial fracture test is based on mode II type loading (shear loading along the interface). The common disadvantage of these testing methods is that they can only be used to test the interfacial fracture toughness within a limited range of mode mixity. It has been found experimentally that the mixed mode condition significantly influences the test results of the interfacial fracture toughness of TBCs [87]. The complex process of actual TBC delamination makes it difficult to conduct a fracture test since the mixed-mode nature of the crack tip singularity at the coating interface must be considered [84]. In general, the mixed-mode delamination beam test is widely used to measure the fracture toughness of

bi-material interfaces under mixed loading conditions. Typically, the interface fracture energy increases with the phase angle of loading ψ [93], which is the amount of relative shearing to opening mode loading experienced at the crack tip. Therefore, the interface toughness measured in mechanical tests depends on the method used. Basically, the loading in the test method should be similar to the loading experienced by the coating in actual service conditions [83].

Arai et al. [94] developed an improved interfacial fracture test method with measuring the mixed-mode interfacial fracture toughness of TBCs over a range of mode mixity. The proposed method was based on the peeling of the coating from the substrate due to compressive loading to the coating edge, as a shear loading, and slinging loading such as a beam bending, as normal loading, as illustrated in **Figure 2.20**. A yttria-stabilized zirconia (YSZ) coating which was thermally sprayed on Ni-based superalloy was tested using this method. The determined energy release rate G for an interfacial crack in a TBC varying with phase angles ψ is shown in **Figure 2.21**. It is obvious that the critical energy release rate has strong phase angle dependence. It varies approximately from 15 to 100 Jm⁻² with the mode mixity range $50^\circ < \psi < 90^\circ$.

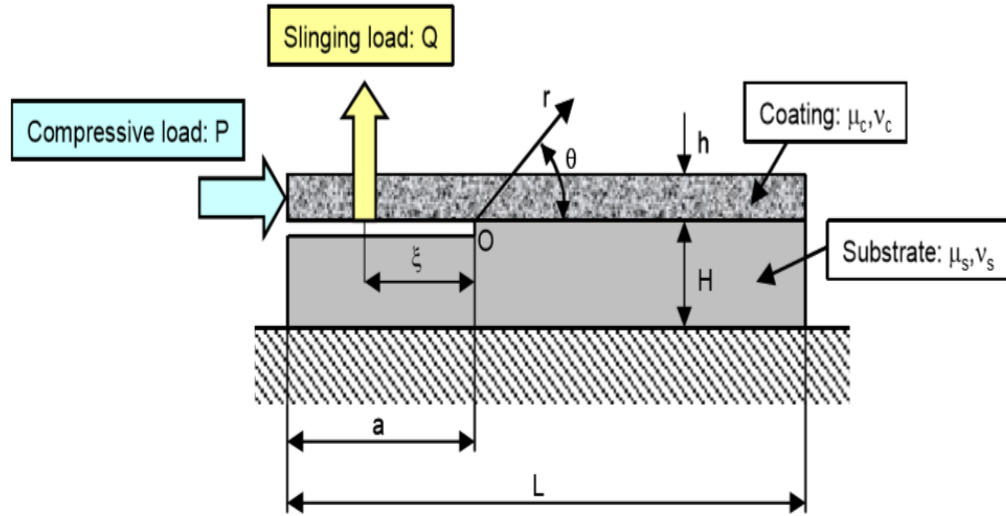


Figure 2.20 Mixed-mode interfacial fracture testing method [87].

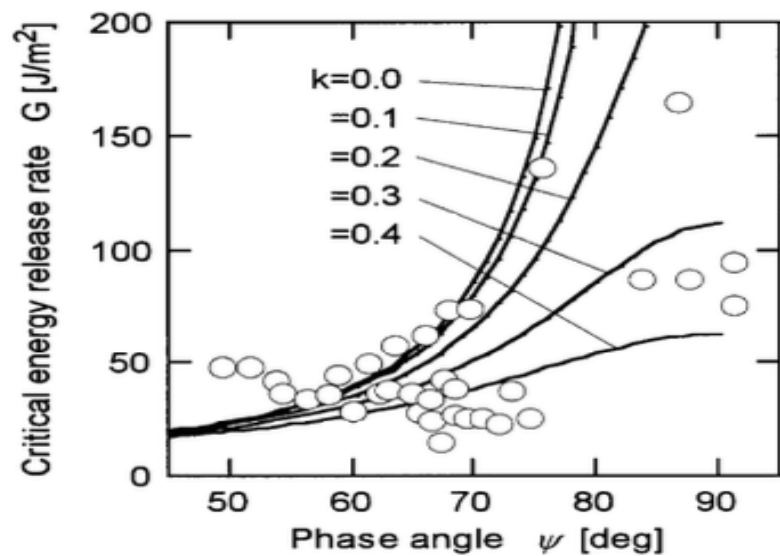


Figure 2.21 Critical energy release rate varying with loading phase angle and interfacial crack roughness k value [94].

Deng et al. [95] developed a mixed-mode test method to evaluate the interfacial fracture toughness of TBCs over a wide range of mode mixity. Their results shown in **Figure 2.22** reveal the dependence of the critical energy release rate on mode mixity. The measured critical energy release rate in their work varies from 13 to 85 J.m⁻² with mode mixity range $-12.7^\circ < \psi < 76.5^\circ$. The differences in critical energy release rates between these tests may be attributed to many factors such as the difference in properties of each layer and the interface, the difference in surface roughness and stress at the interface, etc.

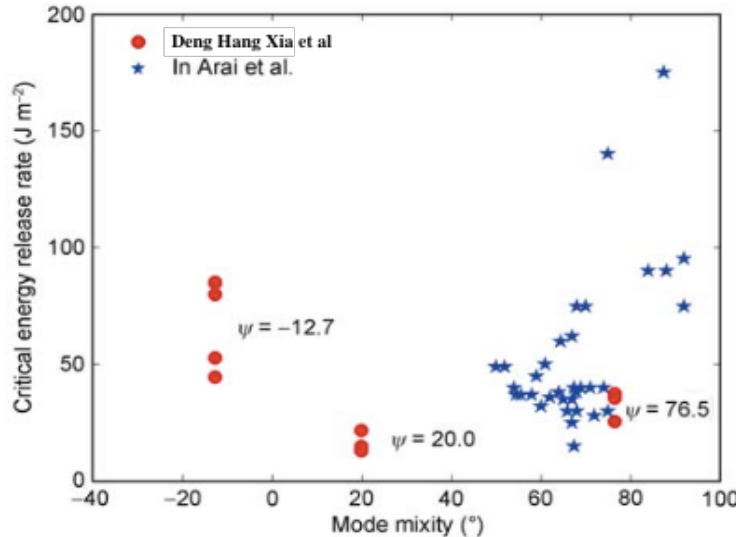


Figure 2.22 Critical energy release rate varying with mode mixity [95].

2.3.3 High Temperature Interfacial Fracture Toughness

It is well known that TBCs are designed to function at high temperatures and prevent the substrate from excessive heating, erosion, and corrosion during the operation [4]. It has been reported that the relatively low fracture energy of the coating in the plane at and near the interface is a limiting factor encountered in TBCs. One of the most significant failure

modes of TBCs observed in service is cracking at the top coat/TGO or TGO/bond coat interfaces. These cracks are initiated due to thermally or mechanically stresses induced during the actual operation. As a result, buckling, delamination, and spallation damage develops in the coatings. These destructions critically affect the function and life expectancy of TBCs and hence the high-temperature fatigue life [30], [87], [96]. Various efforts have been made to determine the fracture toughness of TBCs, as discussed above, however, these experiments were mainly conducted at room temperature. The damage evolution process of TBC systems needs more detailed observations at high temperatures. Interfacial fracture toughness data are rarely available in literature for elevated temperatures, although the mechanical properties of the coatings at high temperatures are crucial for TBCs. There are no standard and effective experimental methods that can be used to assess the interfacial fracture toughness of TBCs under thermal-mechanical loading conditions.

Arai et al. [87] investigated the influence of high temperature exposure on TBC interface. Their results revealed that the fracture toughness of TBCs has a strong dependency on exposure temperature and it increases with exposure temperature, as shown in *Figure 2.23*. However, a decrease in interfacial fracture toughness with an increase in temperature was also reported by Wu et al. [97]. They conducted uniaxial tensile tests on TBCs at high temperatures. Their results revealed that the interface strength of the coatings at high temperatures decreased as the temperature increased, as illustrated in *Figure 2.24*. The fracture behavior of plasma sprayed ceramic TBCs under the loading of modes I and II were determined at 25°C and 1316°C in asymmetric four-point flexure [98]. It was found that the values of the fracture toughness K_I and K_{II} were decreased by 15% and 11%,

respectively, when the temperature was increased to 1316°C, as depicted in *Figure 2.25*. Therefore, it is necessary to further study the temperature-dependent fracture toughness of TBCs with the consideration of mode mixity. This can help assess one of the most common failure modes, cracking at the interface of TBC systems.

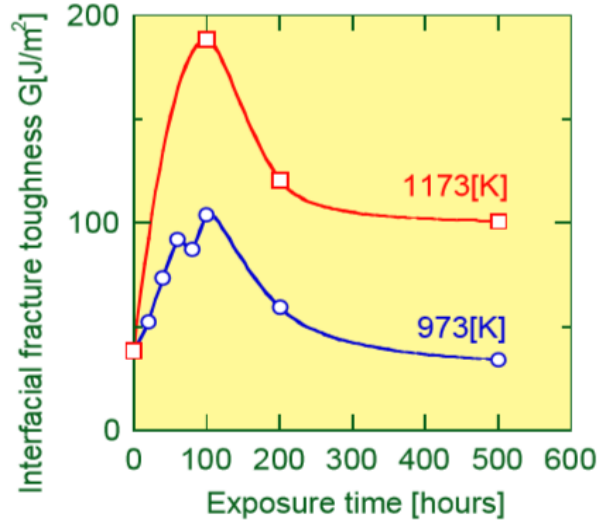


Figure 2.23 Exposure temperature dependence of interfacial fracture toughness of TBCs [87].

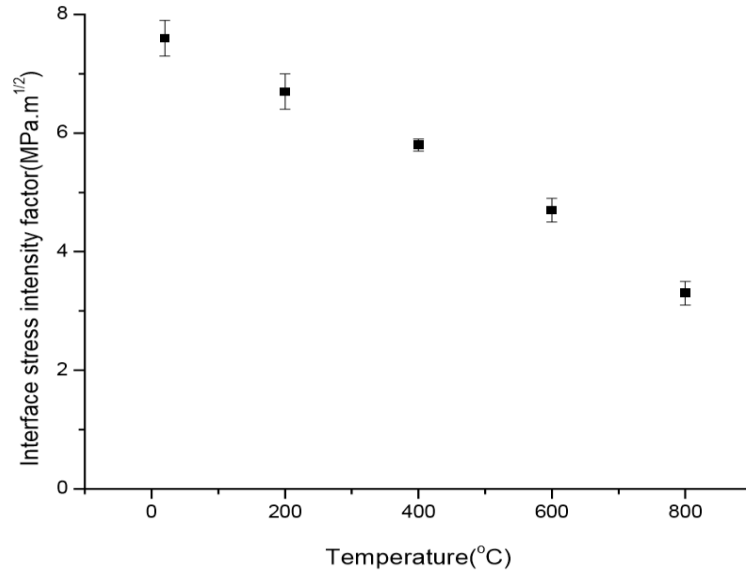


Figure 2.24 Variation of interface stress intensity factor of TBCs with temperature [97].

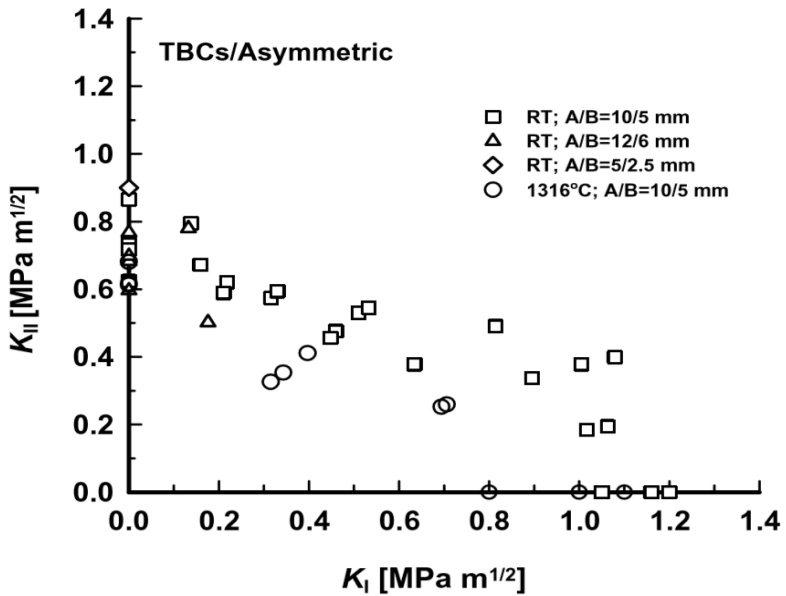


Figure 2.25 A summary of K_I versus K_{II} for mode I, mode II, and mixed mode fracture of plasma-sprayed ceramic TBC at 25 °C and 1316°C in air , A and B distances from a load point [98].

2.4 Principles of Brittle Fracture Mechanics

Fracture toughness is an important property of materials that describes the stress required to propagate a pre-existing crack within the materials. This is particularly important for a TBC system because its microstructure has a high content of pores and cracks that can act as stress concentrations. TBC systems can fail as soon as the stress required to propagate the crack reaches a critical value. As discussed above, the delamination of TB Cs is located in the essentially brittle ceramic material or along the interfaces between brittle ceramics. To implement the approach to the fracture toughness of TBCs, it is necessary to understand the fundaments of linear elastic fracture mechanics (LEFM).

2.4.1 Linear Elastic Fracture Mechanics

Griffith in [99] related the fracture in brittle materials to small defects such as cracks, which act as stress concentrators. The balance between the energy released rate associated with crack growth and the energy absorbed in creating a new surface determines the crack stability. For the unstable extension of the crack, the rate of strain energy release per unit area of the crack extension G_e is greater than or equal to the rate of increase in surface energy. For a two-dimensional crack shown in *Figure 2.26*, the applied stress σ is related to the Young's modulus E of the material, the crack length a , and the surface energy γ :

$$\sigma = \sqrt{2E\gamma/\pi a} \quad (2.4)$$

Therefore, the fracture stress or critical stress in the presence of a crack having a size $2c$ is given as

$$\sigma_c \geq \sqrt{2E\gamma/\pi a} = \sqrt{EG_c/\pi a} \quad (2.5)$$

where $G_c = 2\gamma$ which represents the surface energy required per unit new crack area and is designated as the crack resistance R . It follows that the energy release rate G_e must be greater than G_c before crack growth occurs. Hence, the fracture condition can also be written as

$$G_e \geq G_c \quad (2.6)$$

The Griffith approach uses an energy balance and does not consider the details of the structure of the crack tip.

Another common approach leads to a concept known as stress intensity factor K that is related to the fracture toughness of the material. Stress intensity factor is a local

parameter, which is used in fracture mechanics to describe the magnitude of stress at some coordinate ("stress intensity") near the tip of a crack, caused by a remote load. Fracture will occur when the stress intensity factor at the crack tip reaches a critical value. The critical intensity stress factor is related to the G_c by the equation [99], [100]:

$$K_c = \sqrt{G_c E} \quad (2.7)$$

Hence, the fracture of the material is governed by either critical stress intensity factor K_c , or critical energy release rate G_c .

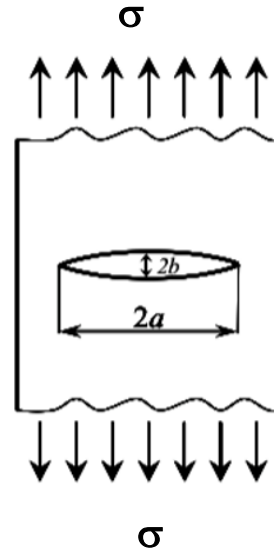


Figure 2.26 A crack in two-dimensional plane.

There are three distinguishable basic modes of failure with respect to the applied load [99], [100], as illustrated in **Figure 2.27**:

Mode I - Opening mode, where tensile stress acts perpendicular to the plane of the crack. Depending on the thickness of the solid body, two different stress states in the crack tip field may take place [99]:

- State of plane stress can be represented by a thin plate loaded in its plane with real values of σ_x and σ_y stress, and σ_z stress is zero.
- State of plane strain occurs when strain components ε_x and ε_y are larger than zero but the strain in z direction is zero.

Mode II - Sliding mode, where shear stress acts perpendicular to the crack tip.

Mode III - Tearing mode, where a shear stress acts parallel to the crack front.

These modes are indicated in G and K by the subscripts I, II or III.

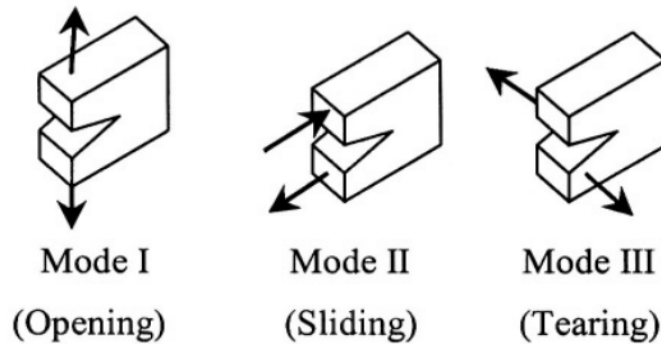


Figure 2.27 Loading modes of cracked material [99].

2.4.2 Interface Fracture Mechanics

The near crack-tip field at an interface is characterized by the mixed mode singularity field.

Due to the mismatch of material properties between two adjoining materials, the crack tip field contains shear loading even under far-field tension. A pure mode I or mode II stress

does not exist for an interface crack approach, therefore, it is important to have parameters to define the magnitude of the mismatch [98].

Consider an interface crack between two homogeneous isotropic and linearly elastic solids with material 1 below and material 2 above having shear moduli μ_1 and μ_2 , Poisson's ratio ν_1 and ν_2 respectively, as illustrated in **Figure 2.28**.

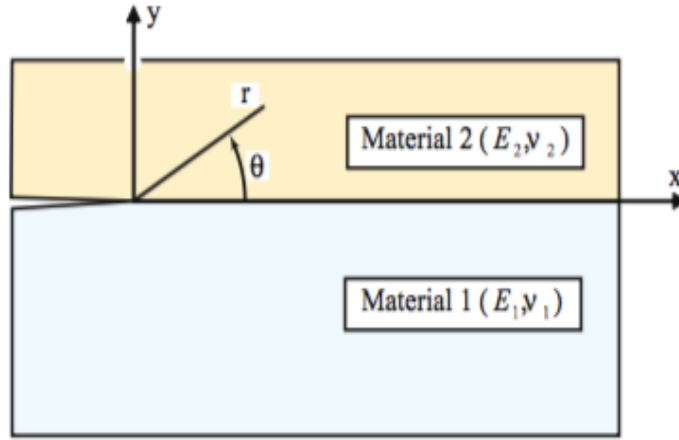


Figure 2.28 Generic configuration at the tip of an interfacial crack [101].

The bimaterial elastic properties that govern plane strain interface crack fields are Dundurs parameters given by

$$\alpha = \frac{\bar{E}_1 - \bar{E}_2}{\bar{E}_1 + \bar{E}_2}, \quad \beta = \frac{\mu_1(1 - 2\nu_1) - \mu_2(1 - 2\nu_2)}{2\{\mu_1(1 - \nu_2) + \mu_2(1 - \nu_1)\}} \quad (2.8)$$

where $\bar{E}_i = \frac{E}{1 - \nu_i^2}$ for plane strain and $\bar{E}_i = E$ for plane stress. In the above equation, parameter α measures the mismatch of the bimaterial system while β measures the mismatch of the bulk moduli. When $\alpha = 1$, the lower material is rigid, and when $\alpha = 0$,

no mismatch exists. Similar implication exists for β [103], [104]. The bimaterial constant (oscillation index) is given by

$$\varepsilon = \frac{1}{2\pi} \ln \left[\frac{1-\beta}{1+\beta} \right] \quad (2.9)$$

It explains the differences between the linear elasticity solution for the interfacial crack in comparison to the cracks in homogeneous materials. When the two materials have same elastic constants, $\mu_1 = \mu_2$, and $\nu_1 = \nu_2$, the constant ε vanishes, and the singular field around the tip of a crack at the interface is analogous to that around the tip of a crack in homogeneous materials. A larger ε indicates more severe oscillatory singularity near the crack tip [102]. Williams [104] revealed that the singular field around the interfacial crack tip was not square-root singular, but it took a new form. This prediction implied that there was an oscillation of stresses and displacements near the crack tip. When the crack tip was approached, the interpenetration of the crack surfaces occurred, which was not physically feasible. However, this was explained later by Rice [105]. The oscillatory solution given by Williams was considered valid in K -annulus, the small region close to the crack tip where the singular field was dominant, outside the nonlinear contact zone [105]. In the K -annulus region, the stress acting on the interface at a distance r ahead of the crack tip can be written in the compact complex form,

$$\sigma_{yy} + i\sigma_{xy} = \frac{K}{\sqrt{2\pi r}} r^{i\varepsilon} \quad (2.10)$$

where r is the distance from the crack tip, σ_{yy} is the mode I tensile opening stress, σ_{xy} is the mode II shear stress, $K = K_1 + iK_2 = K_I l^{i\varepsilon} = |K| e^{i\psi}$, is the complex stress intensity factor at the interface, and l is an arbitrarily chosen reference length, ψ is the mode mixity

of $Kl^{i\varepsilon}$, and K_1 and K_2 are determined based on the reference length $r = l$ [101]. Since the characterizing reference length always needs to be defined, the stress field in Eq (2.10) can be written as follows

$$\sigma_{yy} + i\sigma_{xy} = \frac{K_1 + iK_2}{\sqrt{2\pi r}} \left(\frac{r}{l}\right)^{i\varepsilon} \quad (2.11)$$

The parameter l is the characteristic length based on which the crack length or the plastic zone size is defined [105].

The fracture of bimaterial interface can be expressed in terms of two parameters. The first parameter is fracture energy and it can be assessed based on the energy release rate G_e [93], which is the reduction of the potential energy of the body associated with crack extending in the unit area. It characterizes the load amplitude and can be expressed in terms of complex K as [101]

$$G_e = \frac{1}{2} \left(\frac{1}{\bar{E}_1} + \frac{1}{\bar{E}_2} \right) \frac{|K^2|}{\cosh^2(\pi\varepsilon)} \quad (2.12)$$

where $|K^2| = K_1^2 + iK_2^2$ and $\cosh^2(\pi\varepsilon) = \frac{1}{1-\beta^2}$. Crack propagation will not occur unless the energy release rate reaches a critical value, i.e., the fracture toughness of the bimaterial system.

The second parameter is the loading phase angle, ψ , which measures the degree of the mixity of shear to opening experienced by the interface crack surface. The higher the shearing load (mode II), the larger the phase angle, and the higher the expected toughness value are. For homogeneous materials, the phase angle of loading can be described simply

in terms of either the opening and shear stresses or the mode I and mode II stress intensity factors:

$$\psi = \tan^{-1} \left(\frac{\sigma_{xy}}{\sigma_{yy}} \right) = \tan^{-1} \left(\frac{K_2}{K_1} \right) \quad (2.13)$$

When bimaterial interface is concerned with $\beta \neq 0$, the definition becomes more complicated. Since the stress must be observed at a point $r = l$ away from the crack tip, the phase angle can be defined as [102]

$$\psi = \tan^{-1} \left(\frac{\sigma_{xy}}{\sigma_{yy}} \right)_{r=l} = \tan^{-1} \left(\frac{Im|Kl^{i\varepsilon}|}{Re|Kl^{i\varepsilon}|} \right) \quad (2.14)$$

The concepts of interface fracture reviewed in this section are valid for all mixed mode fracture problems. An interfacial crack is exposed to mixed mode conditions and propagates in mixed mode when its fracture path is on the interface. Even if the crack is located not exactly on the interface, its fracture resistance can still be characterized based on interfacial fracture mechanics as long as the distance between the crack path and the interface is less than the crack length [94].

Chapter 3: Experiments and Methodologies

In the present study, the TBC system was studied under an isothermal and erosion testing regime. After the tests, the TBC specimens were prepared and examined using SEM/EDS/XRD in order to address the failure mechanisms due to oxidation of the bond coat at high temperatures (isothermal oxidation test) and also to gain more understanding about the failure of the TBC linked to the ceramic top coat itself (solid particle erosion test).

3.1 TBC Specimens

3.1.1 TBC System and Materials

The coating system tested in the present study was deposited on a single crystal Ni-base superalloy Inconel 718. A typical composition of this alloy is given in **Table 3.1**. CoNiCrAlY bond coat, Praxair CO-211, Co-32Ni-21Cr-8Al-0.5Y, was applied on the substrate by atmospheric plasma spraying. The top coat was atmospheric plasma sprayed (APS) 8 wt% Yttria partially stabilized zirconia with a typical 15 - 16% porosity. All TBC specimens were supplied by Curtiss-Wright-US.

Table 3.1 Chemical compositions of the TBC materials.

TBC Constitute	Elemental Content (wt%)								
APS YSZ Top Coat	ZrO ₂	Y ₂ O ₃							
	Bal.	8							
CoNiCrAlY Bond Coat	Co	Ni	Cr	Al	Y				
	Bal.	32	21	8	0.5				
Inconel 718 Superalloy Substrate	Ni	Cr	Nb	Mo	Ti	Al	Cu	C	Fe
	52.5	19	5.1	3.0	0.9	0.5	0.15	0.08	Balance

3.1.2 TBC Specimen Geometry and Microstructure

For isothermal oxidation test the TBC specimen was a circular disc having 25.4 mm diameter and 3.2 mm thickness, as photographically shown in the *Figure 3.1*.

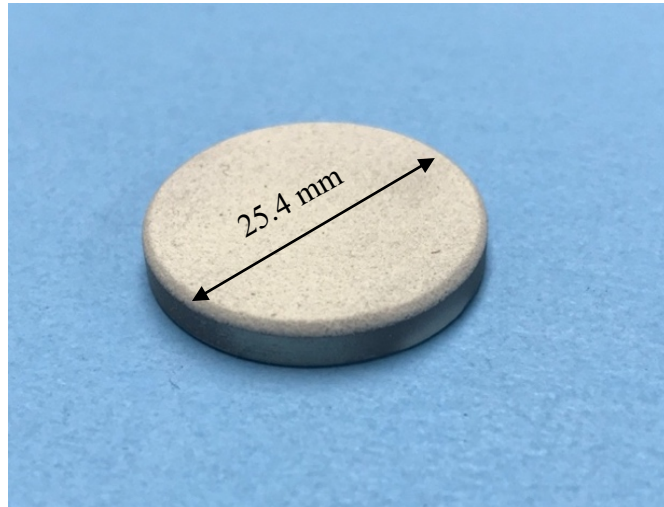


Figure 3.1 TBC specimen for isothermal oxidation test.

The specimens used for solid particle erosion test were rectangular blocks of $45 \times 25.4 \times 2$ mm, as photographically shown in *Figure 3.2*.

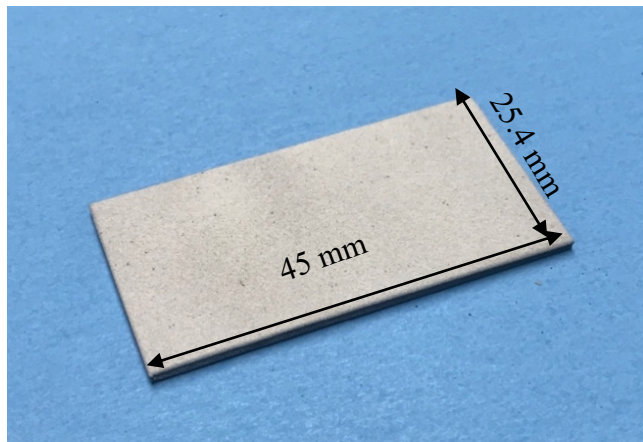


Figure 3.2 TBC specimen for solid particle erosion test.

Figure 3.3 shows the typical microstructure of the TBC system in the as-deposited condition. The cross-section microscopic image displays the three layers, substrate, bond coat, and top coat. The APS top coat layer is about $254 \pm 5.9 \mu\text{m}$ thick. The thickness of the bond coat is approximately $111.70 \pm 3.9 \mu\text{m}$.

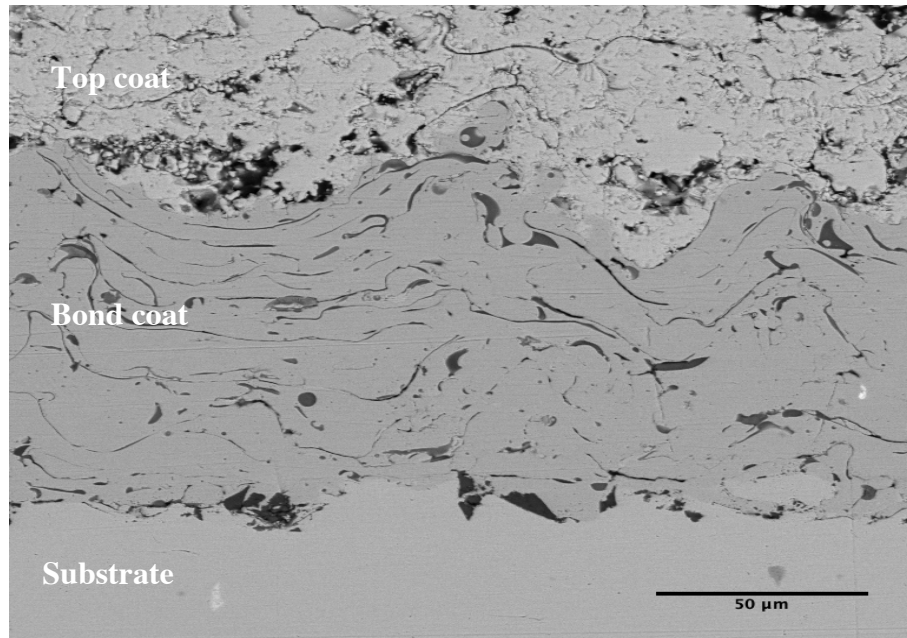


Figure 3.3 SEM image in cross-section of the TBC specimen in as-deposited state.

3.2 Isothermal Oxidation Testing

3.2.1 Test Focus

High temperature components in gas turbines experience complex thermal and mechanical loading during a typical operation cycle. Under the base-load operating conditions, isothermal exposure at high temperatures is one of the major life-limiting factors of TBCs. Isothermal oxidation test as a one-load component testing method with high temperature exposure activates bond coat oxidation of TBCs and the associated diffusion processes and

phase changes as well as the increase in stiffness of the coating due to sintering.

In the present research, an extensive study was made for the growth of the TGO as this is thought to be one of the detrimental factors that affect the coating life in service. Therefore, it is important to identify the growth kinetics of the TGO over time at high temperatures. Also, one of the proposed failure mechanisms in TBCs is the nucleation and growth of microcracks. Therefore, investigation of cracks and study of cracking behavior of TBCs under isothermal testing were another main task of the present research. This would be implemented by examining the cross-sections of the TBC specimen tested at different temperatures for evidence of these cracks and relating the location of the cracks to any microstructural or topographical features.

3.2.2 Test Plan

The isothermal oxidation experiments of the TBC specimens were carried out at temperatures of 1050°C, 1100°C, and 1150°C in the laboratory atmosphere for up to approximately 2000 h in order to compare their oxidation kinetics and any damage to the coatings caused during the oxidation process. The selection of these three temperatures for oxidation test was based on two considerations. One was the capacity of the furnace available for this research, the other was that although the real operating temperature of present and future gas turbine engines is higher than 1150°C, the oxidation mechanisms of the TBC materials would be similar at high temperatures between 1000°C and 1700°C. The focus of the present research was on investigating the oxidation kinetics of the TBC at high temperatures through oxidation tests at 1050°C, 1100°C, and 1150°C, from which the oxidation behavior of the TBC at other temperatures can be predicted.

The tests were performed using a Lindberg type (s) box furnace, shown in *Figure 3.4*. The furnace was preheated to the set temperature before the TBC specimens were inserted. The detailed test plan is given in *Table 3.2*. For each test, after the set test time, or after the failure had occurred, the specimens were removed from the furnace and allowed to cool in laboratory air to room temperature before being prepared for examinations to compare their oxidation kinetics and damage to the coatings caused during the oxidation process.



Figure 3.4 Lindberg Type (s) Box Furnace.

Table 3.2 Isothermal test matrix of TBC specimens.

Sample No.	1	2	3	4	5	6
1050°C						
Time (h)	100	200	360	700	970	1970 Failure

Sample No.	7	8	9	10	11	12
1100°C						
Time (h)	100	200	360	700	970	1500 Spallation

Sample No.	13	14	15	16	17	18
1150°C						
Time (h)	100	200	360 Spallation			

3.3 Solid Particle Erosion Testing

3.3.1 Test Objectives

As discussed previously, TBCs used in gas turbines exhibit two major categories of failure: one is based on oxidation [30], [106], and the other is due to the impact of projectiles ingested into the gas stream [107], [77]. Erosion-caused failures have an important impact on TBCs in environmental conditions. Solid particle erosion can be deemed as a crucial problem in many engineering components, including jet turbines and steam systems. Erosion can lead to aerospace component failure under the presence of dust storms, volcanic ashes, and ice articles in atmospheric conditions [68].

The major purpose of this study was to investigate the solid particle erosion behavior of the APS YSZ top coat by examining the mechanisms of solid particle erosion of the APS TBCs under a range of different impact conditions and testing the effects of thermal aging on the erosion rate of the APS coating. Surface and cross-sectional analyses were

performed using SEM in conjunction with the erosion test to gain more understanding about the failure mechanisms of TBCs linked to the ceramic top coat durability.

3.3.2 Heat Treatment and Hardness Test

To investigate the influence of thermal aging on the erosion resistance of the APS TBC system, some of as-deposited TBC specimens were isothermally heat-treated at 1000°C and 1150°C for 24 h and 72 h. Before the erosion test. Certainly, higher temperatures and longer aging times would be better to represent the actual engine operating conditions, but a slightly lower temperatures and shorter aging times were used in order to maintain the bond coat/substrate integrity of the TBC specimens. The heat treatment tests were conducted in air condition (laboratory atmosphere) using a Lindberg type (s) box furnace, shown in *Figure 3.4*. The furnace was preheated to the set temperature before the TBC specimens were inserted.

The erosion rate of the APS top coat in TBCs may also be governed by other factors such as the hardness and rupture strength of the coating material, etc. To relate the erosion resistance of the top coat with its hardness, Vickers microhardness test was carried out on the top coat in cross-section of the TBC specimens in as-deposited state and in heat-treated condition, using a Microhardness Tester Unit, Model SMT-X7 Dual Indenter, shown in *Figure 3.5*. The measurement of hardness was made along the total thickness of the coating in cross-section. An average of five measurements made at different locations of the coating was taken as the final hardness value.

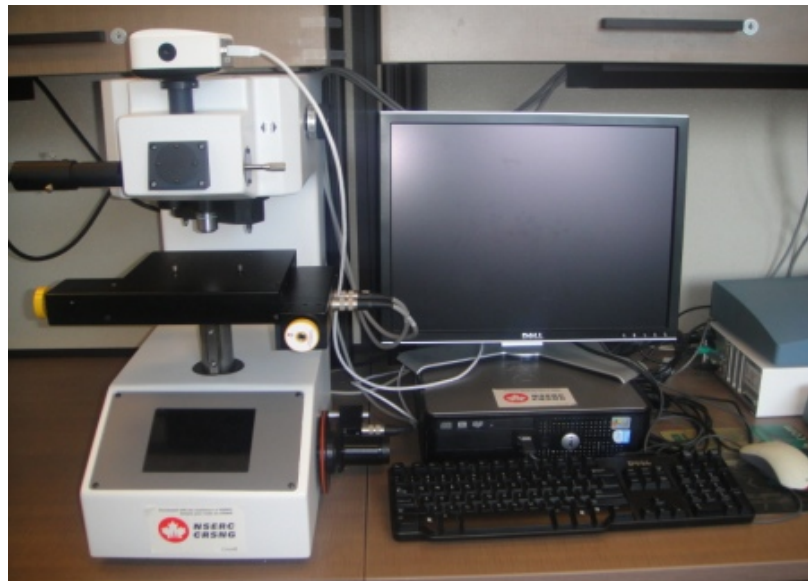
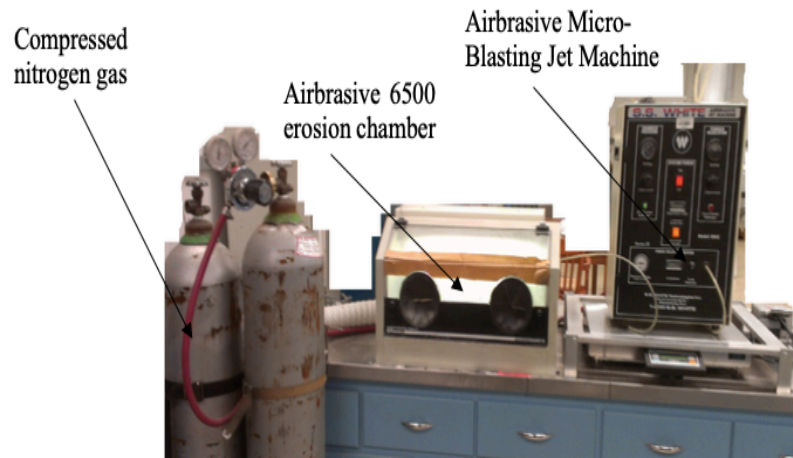


Figure 3.5 Microhardness Tester Unit, Model SMT-X7 Dual Indenter.

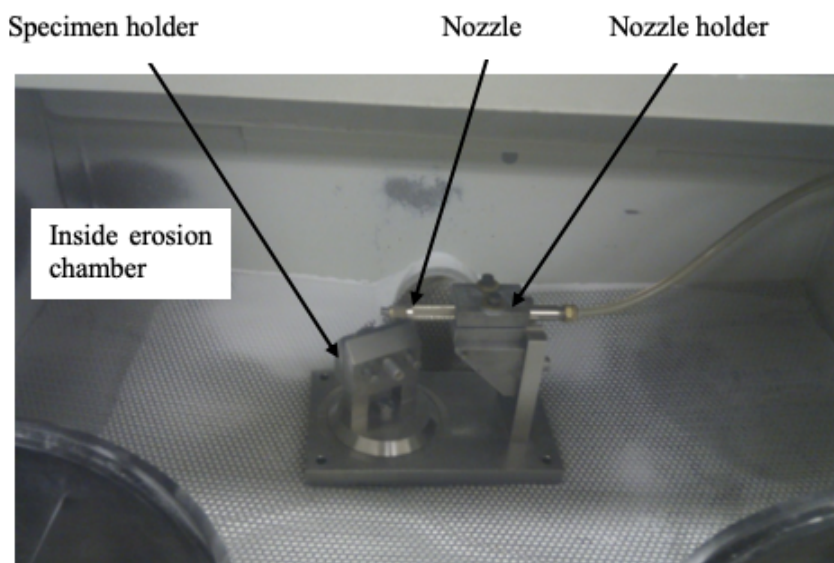
3.3.3 Testing Facility and Procedure

The erosion test equipment used in this study was an S.S. WHITE Airabrasive jet machine.

The test was conducted in an inert environment at room temperature. The entire apparatus consisted of five different sections: an S.S. WHITE Airbrasive Micro-Blasting Jet Machine; an S.S. WHITE Airbrasive 6500 erosion chamber, a specimen and nozzle holder; an inert environment used to accelerate the erodent (abrasive) particles; and a nozzle to feed erodent particles, as shown in ***Figure 3.6***.



(a)



(b)

Figure 3.6 Entire apparatus assembly of erosion test: (a) inert environment (compressed nitrogen gas); S.S. WHITE Airbrasive 6500 erosion chamber; and S.S. WHITE Airbrasive Micro-Blasting Jet Machine and (b) specimen nozzle and holder (Courtesy of S.S. WHITE Technologies Inc.).

The erodent particles used in this study was angular in shape, as shown in *Figure 3.7*. The product was commercial AccuBRADE-50 blend #3 alpha alumina powder with an average particle size of 50 μm , supplied by S.S. WHITE Technologies Inc. The particles were carried by static pressure and accelerated along the nozzle with the distance between the nozzle head and the tested specimen set to 50 mm during the erosion test process. The erosion tests were performed at various particle impingement angles (30° , 45° , 60° , and 90°) on the top coat surface to better investigate the erosion mechanism of the TBC under solid particle impact. The impingement angle was easily adjusted by rotating the specimen holder. An adjustable pressure differential introduced across the nozzle established the particle velocity. During testing, the voltage controller was adjusted to a value of 4 V, which could achieve a particle flow rate of 0.7 g/min for three particle impact velocities of 84 m/s, 100 m/s and 125 m/s. All the test parameters used in this study are summarized in *Table 3.3.*

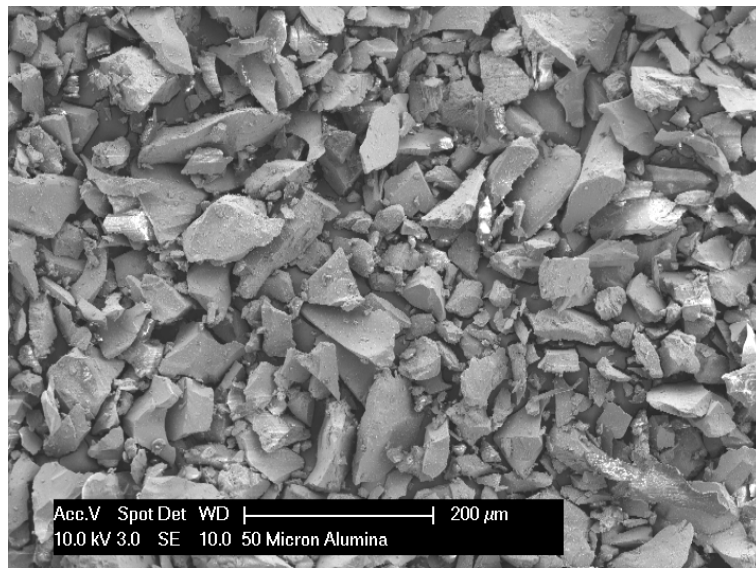


Figure 3.7 SEM image of erodent particles - Angular AccuBRADE-50 blend #3 alpha alumina powder.

Table 3.3 Erosion test Parameters.

Erodent Particle	Average Particle Size (μm)	Nozzle Distance (mm)	Temperature (°C)	Transport Medium
Aluminum Oxide	50	50	20	Compressed nitrogen gas

3.3.4 Data Collection

Each TBC specimen was weighed before erosion testing and then mounted into the specimen holder after it was adjusted to the desired impingement angle, see *Figure 3.6 b.* Thus, the TBC specimen was exposed to the particle stream for 1.5 min as a test duration. The specimen then was removed from the holder and reweighed. At least 6 measurements were performed on each specimen or until the coating was penetrated. The weight loss of the specimen and the mass of erodent grit used were determined for each run of the test with an accuracy of 0.0001g. The same process was repeated three times on different testing spots of a specimen. This was done to minimize experimental errors involved for each testing condition. The weight loss of the specimen was plotted against the cumulative erodent weight. The erosion rate was then evaluated as the slope of the linear best fitting of the experimental data. The detailed test plan is given in *Table 3.4.*

Table 3.4 Erosion test matrix.

Specimen	Test Duration (min)	Impingement Angle (degree)	Particle Velocity (m/s)
As deposited TBC	1.5	30, 45, 60, 90	84, 100, 125
Aged TBC at 1000°C for 24 h and 72 h	1.5	30	100
Aged TBC at 1150°C for 24 h and 72 h	1.5	30	100

3.4 Microstructural Analysis

3.4.1 Metallographic Preparation

For both oxidation and erosion tests, after tested and cooled to room temperature, the TBC specimens were first cold-mounted in epoxy resin in order to avoid additional damage to the coatings which could have been caused by sectioning. Once the resin had set, sectioning perpendicular to the top surface was done using a precision diamond saw (Secotom-10 Cutting Machine), shown in *Figure 3.8*. The transfer sections were then remounted in epoxy, with cut face exposed, to ensure that the specimens remained flat for the duration of the preparation. Once the resin had set; the specimens were ground to 1200 grit using wet SiC abrasive paper and subsequently polished using diamond suspension down to 0.5 μm finish on a MetaServ™ 250 Grinder-Polisher (BUEHLER® An ITW Company), shown in *Figure 3.9*. The TBC specimens mounted in epoxy resin for metallographic analyses after polishing are shown in *Figure 3.10*.



Figure 3.8 Secotom-10 Cutting Machine (Courtesy of Struers Co.).



Figure 3.9 MetaServ™ 250 Grinder-Polisher (Courtesy of BUEHLER® An ITW Company).

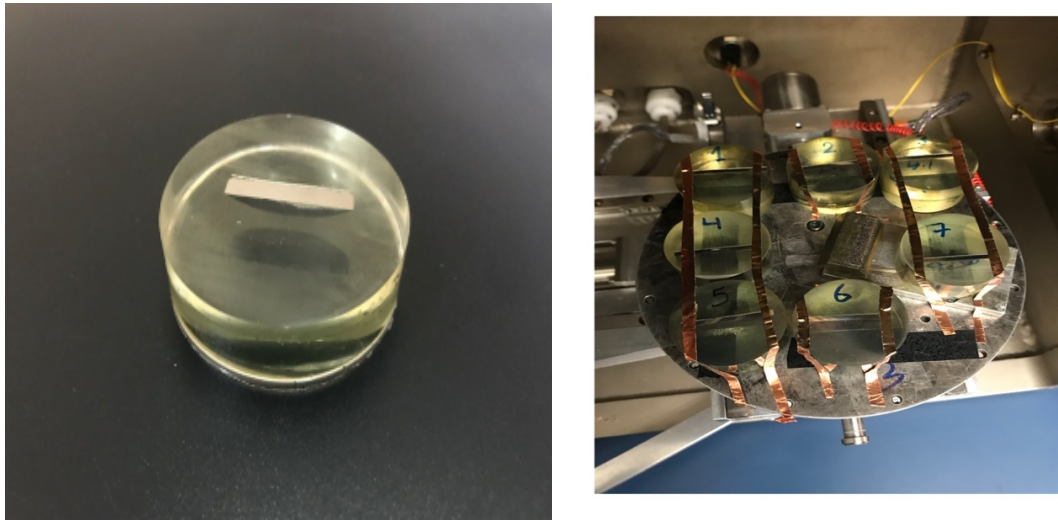


Figure 3.10 TBC specimens mounted in epoxy resin for metallographic analyses after polishing.

3.4.2 SEM and EDS Analyses

After the metallographic preparation of the specimens, the SEM and EDS analyses were carried out on each of the isothermal-tested and erosion-tested specimens to evaluate the damage evolution using a Tescan Vega-II XMU SEM equipped with Oxford X-ray detection systems, shown in *Figure 3.11*. A thin layer of carbon or gold coatings of approximately 10 nm was applied to the specimen surface using a Q150T Plus - Turbomolecular pumped coater, prior to examination via SEM for discharging the electric field and accomplishing good quality images.

For the oxidation-tested TBC specimens, an extensive study was made on the growth of the TGO formed between the bond coat and the top coat because it was thought to be one of the crucial factors affecting TBC life in service. The growth kinetics of the TGO over

time at high temperatures was investigated. Seven images at least of the section through the coating were obtained at regular intervals across each specimen. The measurements of approximately ten TGO thickness data were taken from each image where the TGO kept its integrity and continuousness. This gave a total of at least 70 measurements for each specimen. The average TGO thickness and standard deviation were then calculated for each specimen. Moreover, elemental concentrations were investigated at selected locations of the bond coat and TGO with EDS. Furthermore, since the nucleation and growth of microcracks were proposed as one of the important failure mechanisms of TBCs under high temperatures, examining cracks, including location, orientation, and size, in the coatings of the oxidized TBC specimens was also the focus of these SEM/EDS analyses.

For the erosion-tested ABS TBC specimens, eroded surfaces and polished cross-sections were examined under SEM.

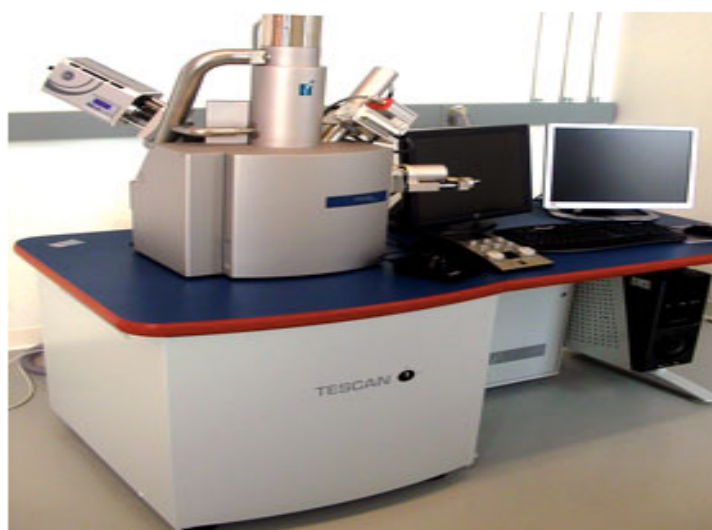


Figure 3.11 Tescan Vega-II XMU SEM/EDS Instrument.

3.4.3 X-ray Diffraction

X-ray diffraction analysis using a D8 Discovery, Brucker AXS D8 diffractometer, shown in *Figure 3.12*, was performed to evaluate the phase compositions of the TBC specimens in as-deposited state and heat-treated condition. The XRD 2θ parameter varied in the range from 10° to 120° for each measurement.



Figure 3.12 Bruker AXS D8 Discover Diffractometer.

3.4.4 Image Analysis

Further microstructural evaluation was performed with a commonly used technique, known as Image J analysis. Image J is open source software and one of the most commonly used programs for image processing. In the present study, the software was used to measure the TGO thickness in order to quantify the TGO growth. The crack lengths in the specimens oxidized at different temperatures were also measured using Image J software. Moreover, it was utilized to measure the porosity of the coating in as-deposited condition and in the heat-treated state. It was done by importing the cross-sectional image into the software (Image J) to crop the measurement region (coating section). Afterword, the threshold was adjusted to separate pores from the background. The background was converted into the

black pixel, and the pores were converted into white pixels, as shown in **Figure 3.13**. The process of selecting the appropriate range of white pixels was done to ensure that only voids were sampled. The analysis was repeated at least three times for each image to ensure accurate.

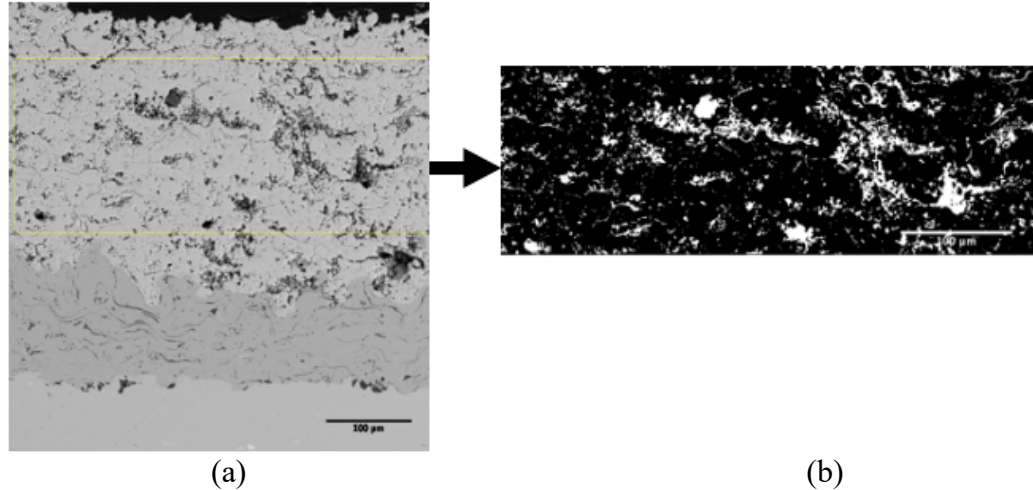


Figure 3.13 Cross-section microscopic images of the TBC sample for porosity analysis using Image J software: (a) SEM microstructure and (b) processed binary image showing pores.

3.4.5 GraphClick Software

GraphClick software is a graph digitizer which allows to automatically retrieve the original x and y coordinates from a scanned graph or chart. The software was used to obtain the critical energy release rate data from the results given by Deng et al. [95] in the modeling of interfacial fracture toughness for TBCs.

Chapter 4: Results and Discussion of Isothermal Oxidation Test

A series of isothermal oxidation experiments at 1050°C, 1100°C, and 1150°C were carried out in order to evaluate the bond coat oxidation kinetics and damage evolution. The development of the TGO thickness and crack evolution were monitored for the specimens after specified exposure time at high temperatures. The microstructure of the APS TBC specimens was examined using SEM to record the evolution of the different layers as a function of oxidation time and temperature. The as-deposited specimen was also analyzed with EDS to determine the approximate compositions of each layer in the coating specimen.

4.1 Microstructure of TBC Specimen for Isothermal Oxidation Test

4.1.1 Cross-Sectional Morphology

Figure 4.1 shows a typical microstructure in cross-section of the APS TBC specimen for isothermal oxidation test in as-deposited condition. The YSZ top coat is densely adherent to the bond coat without visible interfacial oxidation and the bonding between the top coat and the bond coat appears good. No cracks or spallation are observed along the interface between the YSZ top coat and the bond coat (*Figure 4.1 a and b*). However, the typical feature of plasma sprayed YSZ microstructure can be observed in this APS TBC specimen, showing porosity between the splats, microcracks, and lamellae boundaries (*Figure 4.1 c*). The microstructure of the CoNiCrAlY bond coat in the as-deposited specimen appears homogeneous but contains small intergranular gaps and interlamellar porosity (*Figure 4.1 d*), which is common for APS coatings. The rough surface and sharp-edged morphology of the bond coat can be recognized in the cross-section image of the TBC specimen,

characterized by the rugged interface between the top coat and bond coat, which is required for good mechanical adherence of APS TBCs [108] .

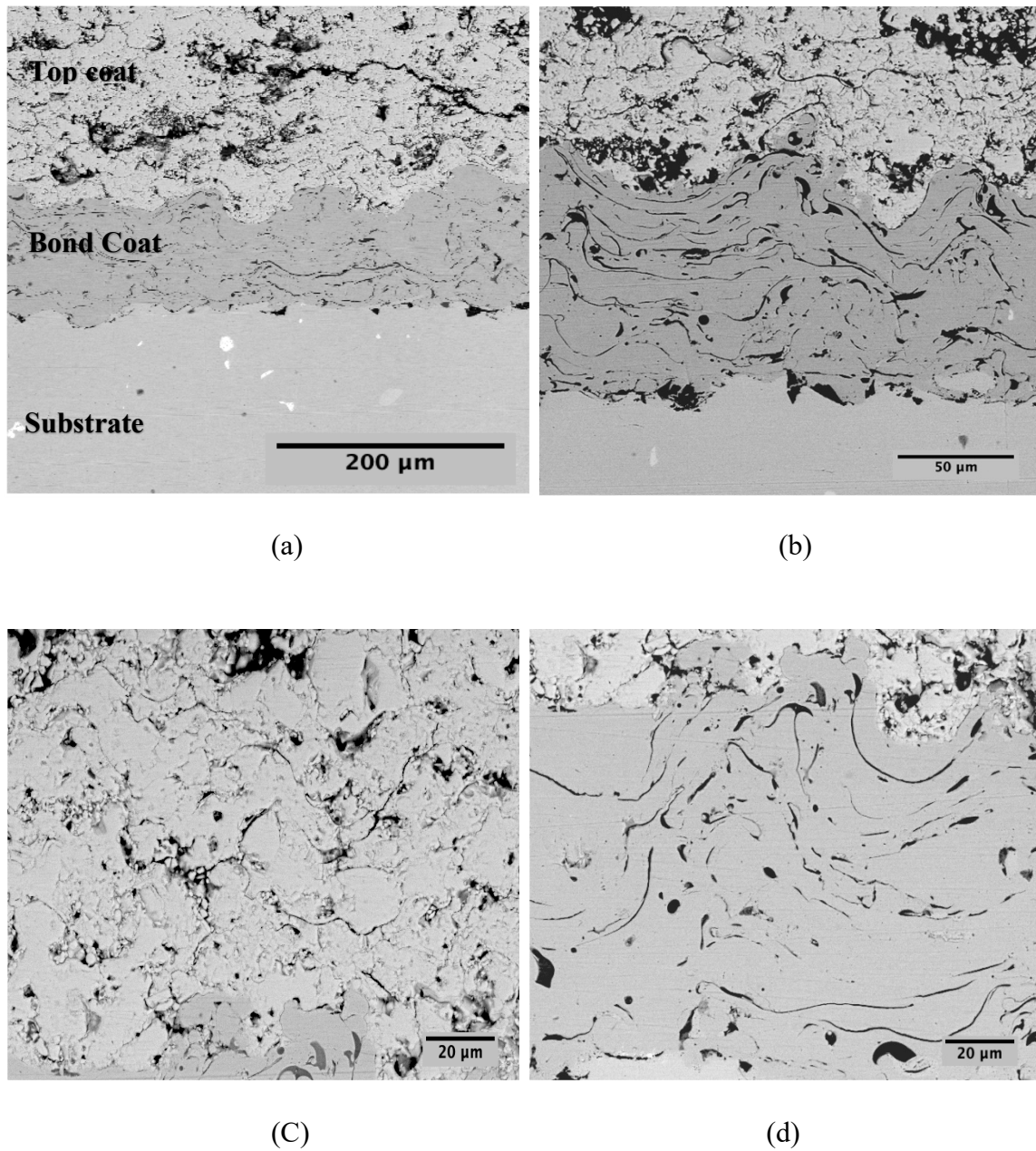


Figure 4.1 SEM microstructure of the TBC specimen for isothermal oxidation test in as-deposited state: (a) cross-section image at low magnification, (b) cross-section image at high magnification, (c) top coat and (d) bond coat.

Pores and cracks with various sizes and morphologies are inherent features of thermally sprayed coatings, which are generated during the deposition process and entrapped between the splats. Incomplete contact between contiguous splats and the presence of unmelted particles resulted in the formation of large globular pores [109]. It was suggested that during the spraying process molten particles were landed on a rough surface, coalesced with each other and froze to form a coating. Surface tension prevented liquid splats from completely filling crevices in the substrate, forming pores [110]. Oxidation of CoNiCrAlY can occur at high temperatures, which may also be one of the pore sources. The formed oxides can be the sites for pore formation [111]. It is apparent that the porosity of the bond coat is lower than that of the top coat, as compared between the SEM microstructures in **Figure 4.1 c** and **Figure 4.1 d**. The difference can be attributed to the material features of ceramic and metal. During the thermal spray process, the in-flight particles were melted in the plasma flame. Since the ceramic material of the top coat has higher melting point than the metallic material of the bond coat, the relatively low level of porosity in the CoNiCrAlY bond coat could be related to the lower melting degree of the deposited particles than those in the YSZ top coat during the coating deposition processes.

4.1.2 Analysis of Elemental Concentration

EDS was utilized to characterize the chemical composition of as-deposited CoNiCrAlY bond coat as shown in **Figure 4.2**. The measured amounts of the alloying elements agreed with those of the data provided from the CoNiCrAlY powder supplier. High Co and Ni concentrations were identified in the CoNiCrAlY matrix indicated by point 1. Oxide particle indicated by point 2 contained mainly Al_2O_3 with minor Cr element. It was found that element Y was absent from the metallic matrix and enriched in the oxide particles. It

is known from chapter 2 that element Y is usually added to the bond coat of TBCs to enhance the alumina scale adherence. The absence of this element in the metallic matrix of the bond coat of the as-deposited TBC specimen could be attributed to the oxidation Y in the coating deposition process, which had limited its positive effect in the bond coat.

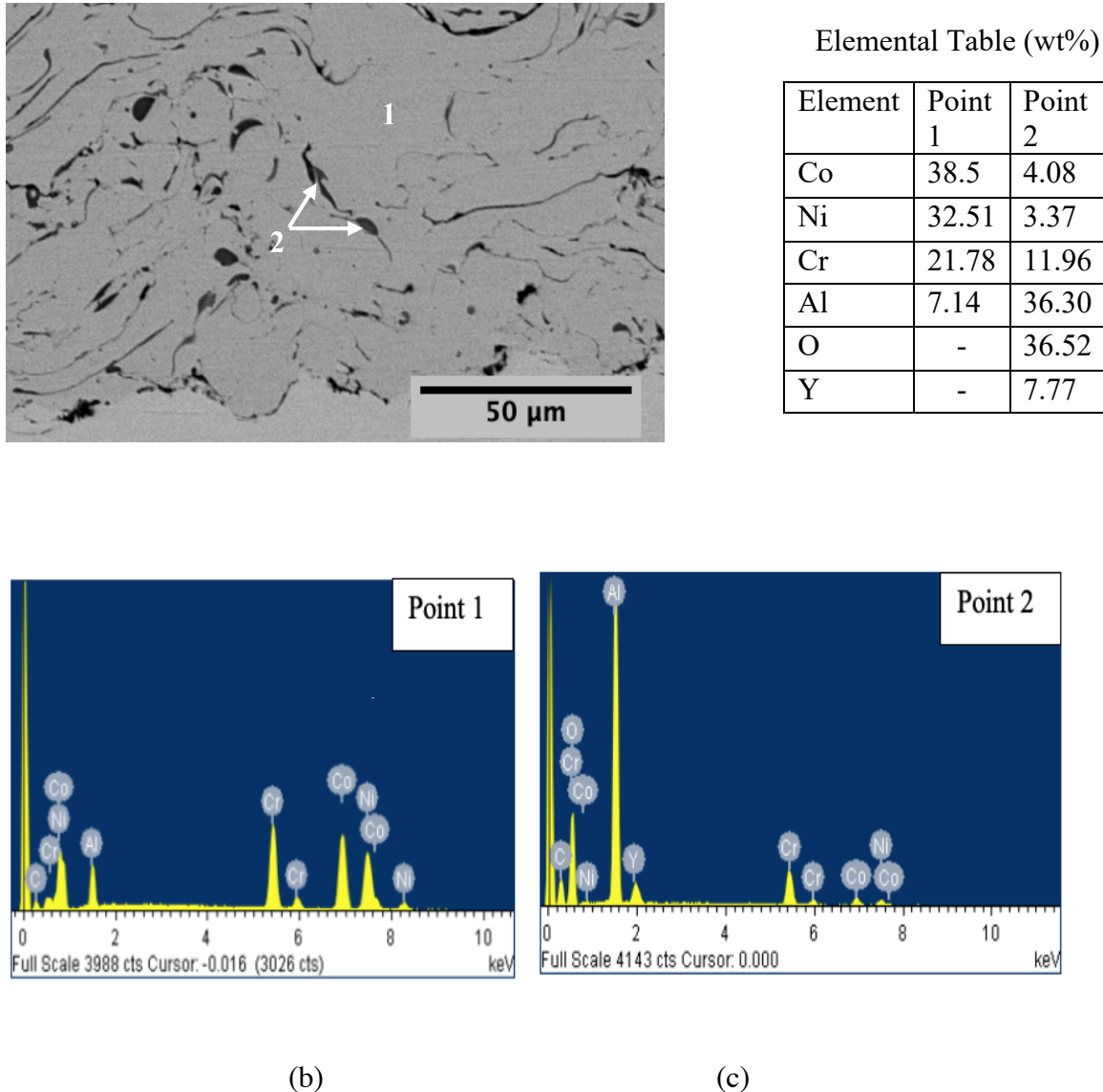


Figure 4.2 EDS analyses of CoNiCrAlY bond coat: SEM microstructure with selected points indicated, (b) EDS spectrum of alloy matrix (point 1) and (c) EDS spectrum of oxide particle (point 2).

4.2 Observation of the Failure under Isothermal Oxidation

The TBC failure was determined by conducting an isothermal test on the TBC specimen at 1050°C, 1100°C, and 1150°C until failure of the coatings had occurred. Visual observations of the TBC specimens were made periodically after a specified time to inspect the macroscopic failure. The failure of the TBC specimen tested at 1050°C accrued after 1970 h exposure time (20% failure criterion was taken). The specimen exhibited a macroscopic failure starting from the edge of the top coat layer with the remaining coating layer still attached, as shown in *Figure 4.3*. Additionally, the surface of the spalled top coat was cracked, but most part of the top coat remained on the fracture surface, suggesting that the failure occurred within the top coat layer.



Figure 4.3 Macrograph of the failed TBC specimen after 1970 h isothermal tests at 1050°C.

At 1100°C, no macroscopic failure was observed over the exposure time. However, after 1500 h exposure time complete spalling of the coating had occurred, as shown in *Figure*

4.4. The generated residual stresses, which resulted from the combination of TGO growth and the thermal mismatch of coating materials, were considered to be one of the main reasons for APS TBC spallation.

Complete spallation had also occurred when the TBC specimen was oxidized at 1150°C for 360 h and then cooled down to ambient temperature. The specimen did not show any sign of macroscopic or complete spallation initially as soon as it was cooled down, but after a short time at room temperature, the YSZ top coat layer had completely spalled off. Generally, the exposure time at a high temperature until failure decreased with increasing the exposure temperature.

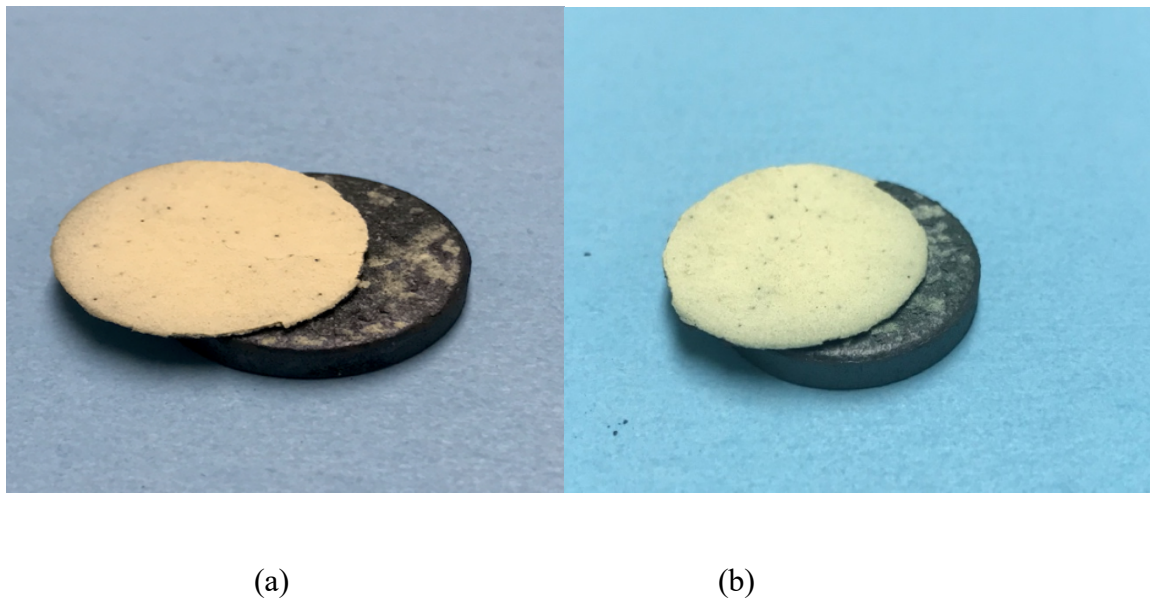


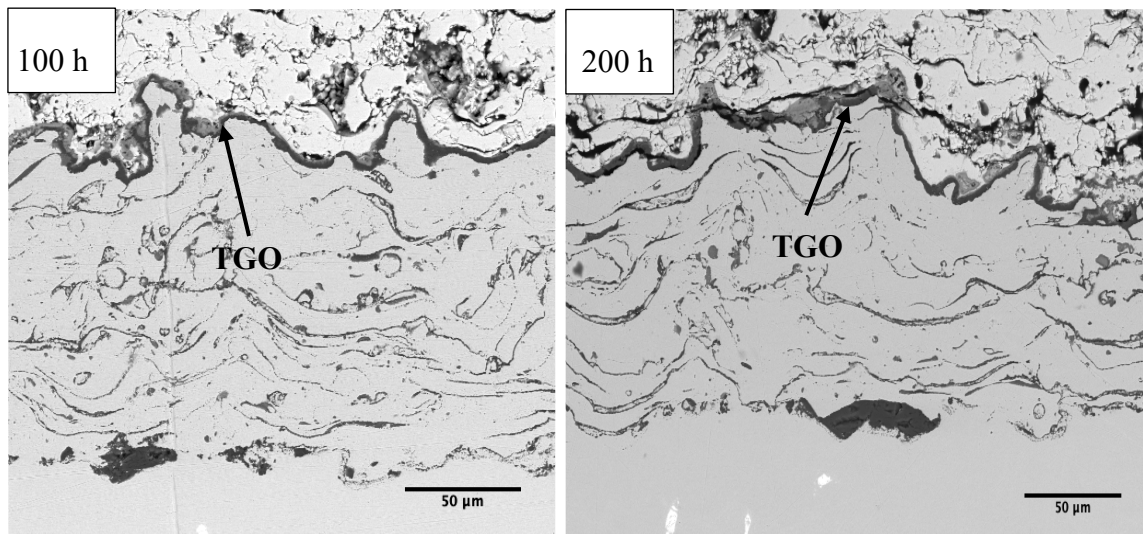
Figure 4.4 Macrograph of failed TBC specimen (a) after 1500 h at 1100°C and (b) after 360 h at 1150°C isothermal test showing top coat spallation.

4.3 Formation and Growth of TGO

4.3.1 Morphology and Composition of TGO

The development of TGO thickness and the crack evolution in the TBC specimens were systematically studied at different temperatures for various exposure durations. Microstructural examination was conducted on the polished cross-sections of the oxidized specimens as a function of exposure time using SEM/EDS.

After isothermal oxidation, an oxide layer (TGO) was formed at the top coat/bond coat interface, which was a critical factor influencing the service lifetime of TBCs. The growth of TGO influenced the lifetime of the TBC significantly due to the induction of mechanical stresses which depended on the oxide growth. *Figure 4.5* reveals the development of the TGO layer and microstructural changes in the specimens after different exposure times at 1050°C. The examinations in the cross-sections of the oxidized TBC specimens showed that the TGO layer was formed in the bond coat and it grew in thickness with increasing oxidation temperature and exposure time.



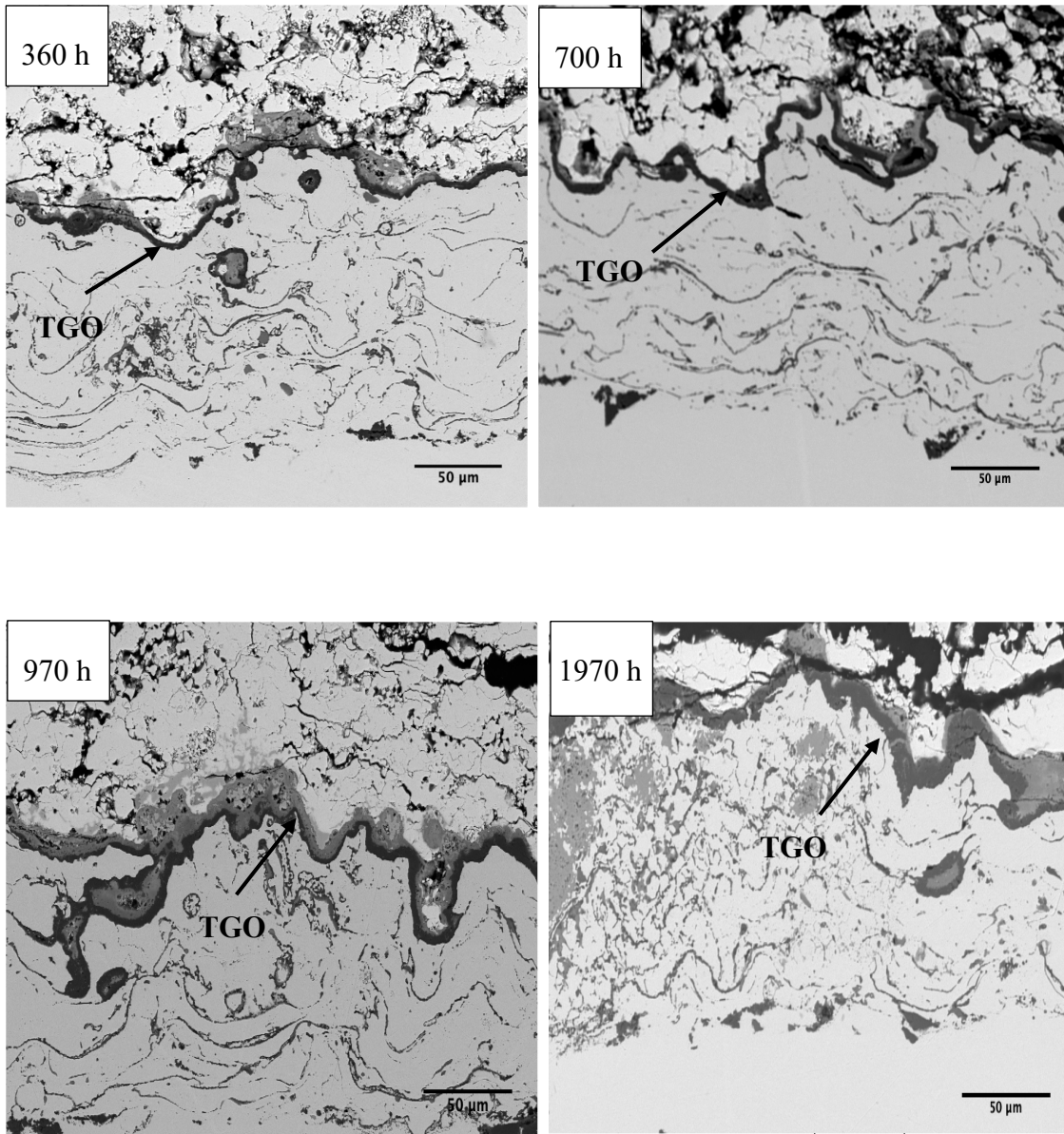
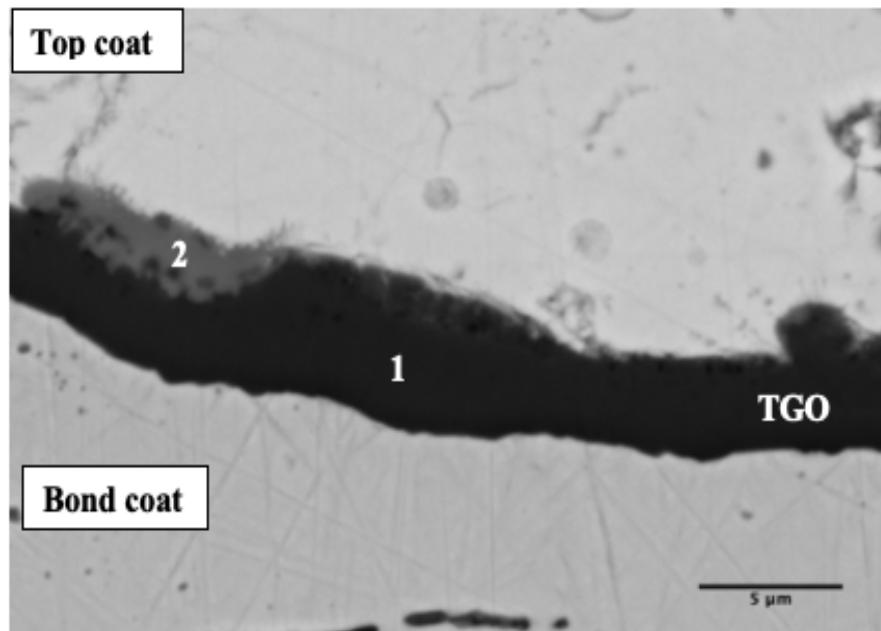


Figure 4.5 SEM image of the oxidized TBC specimen showing a TGO formed at 1050°C for different exposure times.

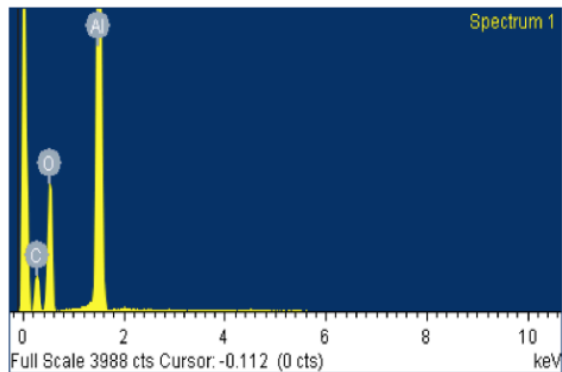
A thin layer of TGO scale of about 2.65 μm thick formed after 100 h time exposure at 1050°C. Also, as shown in **Figure 4.5 a**, the inhomogeneous image contrast indicates that the TGO oxide layer does not contain exclusively Al_2O_3 , but other oxides such as (Ni, Cr, Co) oxides which are found in a few regions between the oxide layer and the ceramic top

coat, as a result of the diffusion of Ni and Cr atoms from the bond coat into the top of the TGO during the oxidation process [57].

The examination of the TGO with EDS revealed a high percentage of Al and O elements (*Figure 4.6 b*) in the inner dark contrast region, indicated by point 1 in *Figure 4.6 a* and the outer grey contrast region indicated by point 2 in *Figure 4.6 a* consisting of O, Al, Cr, Co, and Ni elements, as detailed in *Figure 4.6 c*.



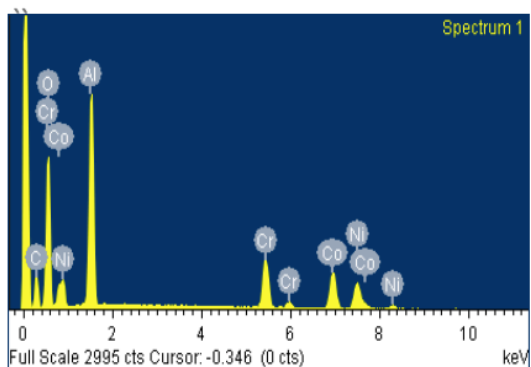
(a)



Elemental Table (wt%)

Element	1050°C
O	48.68
Al	51.32

(b)



Elemental Table (wt%)

Element	1050°C
O	35.01
Al	23.28
Cr	12.08
Co	16.27
Ni	13.36

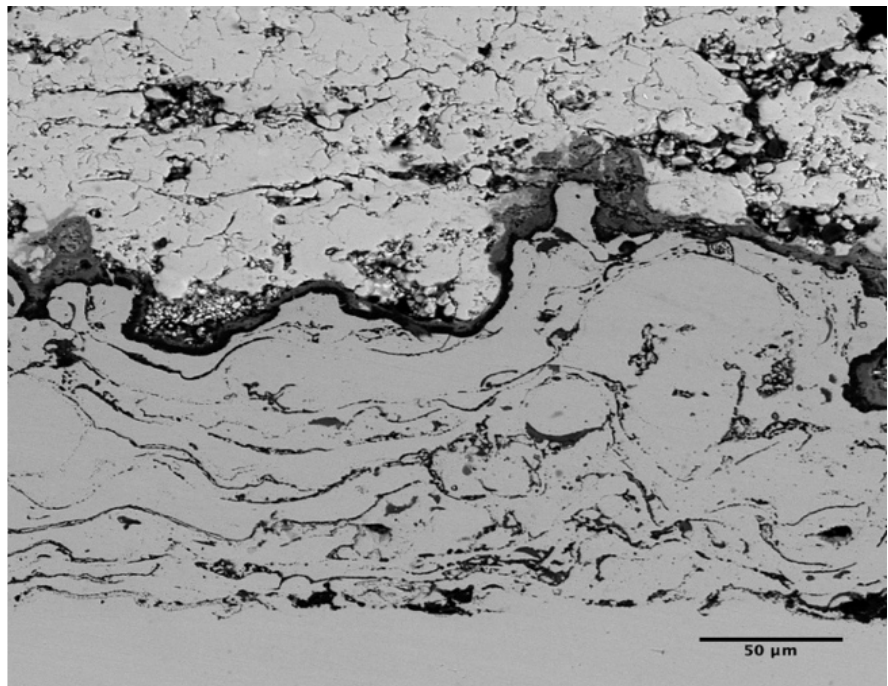
(c)

Figure 4.6 EDS analyses of the TGO in the specimen oxidized at 1050°C for 100 h: (a) SEM image showing the points investigated, (b) EDS spectrum of point 1 and (c) EDS spectrum of point 2.

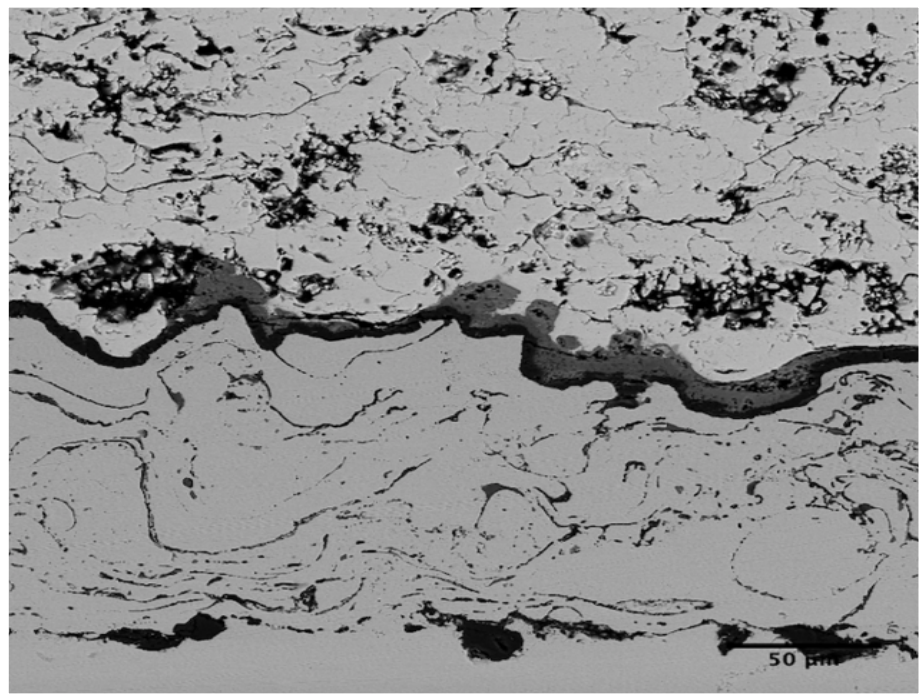
After 200 h of exposure, the thickness of the TGO oxide layer increased to 3.77 µm, as shown in **Figure 4.5 b**, and it contained increasing amounts of the mixed oxides, such as chromia, and/or spinel, distinguishable by phase contrast in SEM image and confirmed with the EDS analysis. It was observed that the TGO layer became thicker in further oxidation stages, 11.28 µm for 1970 h of exposure, and the mixed oxides and spinels grew

rapidly. The increase in the oxide scale thickness during the oxidation process would be accompanied with the generation of stresses at the top coat/bond coat interface. When these stresses were large enough beyond the strain tolerance of the TBC, the delamination of the coating would eventually occur [27]. The formation of mixed oxides rather than alumina can be attributed to the depletion of the Al in the bond coat which indicated the Al-depleted phase.

The interface SEM microstructures of the oxidized specimens after 200 h of exposure at 1100°C and 1150°C are shown in **Figure 4.7**. The oxidation behavior of the TBC specimens oxidized at 1100°C and 1150°C was similar to that at 1050°C, but the TGO layer was obviously thicker and the rate of oxide formation was higher at these temperatures. The TGO scales showed an obvious double-layer structure with the outer layer consisting of mixed oxides and the inner layer containing mainly Al₂O₃, as revealed by the EDS analysis. The thickness of the TGO at 1100°C after 200 h exposure increased and reached 6.11 μm and 9.45 μm at 1150°C, compared to 3.77 μm at 1050°C.



(a)



(b)

Figure 4.7 SEM image of the TBC specimen oxidized at (a) 1100°C and (b) 1150°C for 200 h showing a TGO layer formed.

The formation of the TGO layer and subsequent thickening of the oxide layer resulted in the development of out-of-plane stresses at the interface, which promoted cracking within the vicinity of the interface. With increasing the time of exposure, these stresses increased as the TGO became thicker, thus led to the propagation of microcracks and subsequent the failure of the coating. **Figure 4.8** shows the delaminated top coat/TGO interface in the TBC specimen oxidized at 1150°C for 200 h.

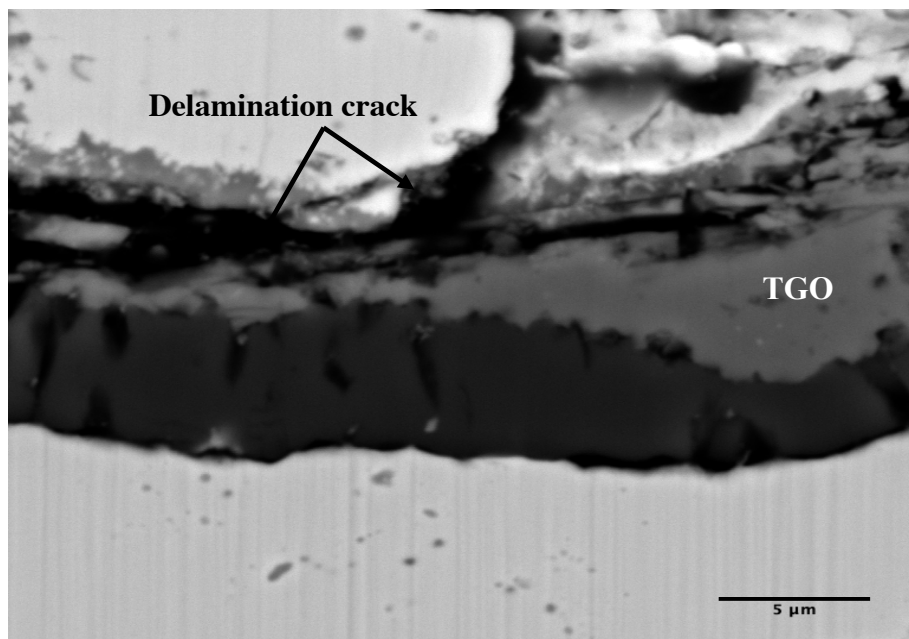


Figure 4.8 SEM micrograph of developed TGO layer containing cracks after 200 h of exposure at 1150°C.

The characteristics of the oxide formation showed a similarity in all the specimens oxidized at different temperatures and there was no remarkable change in the microstructural compositions when the TBC specimens were oxidized at different temperatures. **Figure 4.9** shows the chemical compositions of the mixed oxides after 200 h exposure at different temperatures, examined with EDS. Although the variation in element concentrations of the

TGO existed between the TBC specimens oxidized at different temperatures, the constituents of the TGO in all the specimens were the same. Moreover, it was found that for short oxidation time, the TGO was mostly alumina. With increasing the exposure time, the thickness of the mixed oxide layer became similar to or exceeded that of the alumina layer.

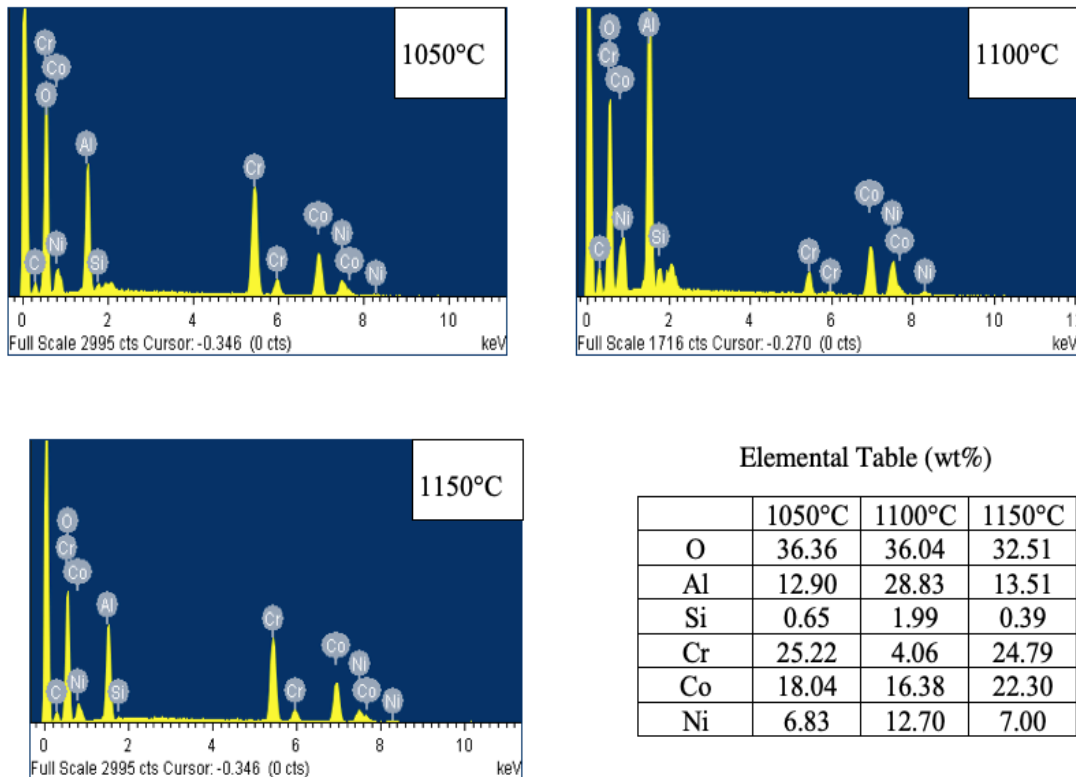


Figure 4.9 EDS spectra of the TGO in the specimens oxidized at different temperatures for 200 h.

The TGO growth was associated with Al depletion mainly from Al-rich β -phase in the bond coat. As a result, Al-depleted zone would form underneath the oxide layer. Al concentration measured with EDS in the bond coat decreased from 7.14 wt% in the as-deposited specimen to 2.67 wt% in the specimen oxidized at 1050°C for 970 h, as revealed

by the EDS measurements. At 1150°C Al concentration in the bond coat was about 2.08 wt% after only 100 h oxidation test and then decreased to 1.64 wt% after 360 h of oxidation.

Al depletion in the bond coat was considered as one of the mechanisms that contributed to the TBC system failure because it can result in the formation of mixed oxides rather than the protective alumina scale. As well known, alumina is impermeable to oxygen so that it can protect the bond coat from further oxidation once it forms. However, when Al-depleted phase was formed in the bond coat due to Al consumption, the oxidation rate of the bond coat would increase because the Cr, Co and Ni elements in the bond coat became more reactive and diffused outward, thus oxidized to form nonprotective Cr_2O_3 , CoO , and NiO oxides, which led to the formation of spinels [112]. As shown in *Figure 4.10*, with Al depletion occurring, the TGO became porous and had nonuniform morphology, which made it preferable sites for crack initiation due to the stress concentration in the vicinity of the pores. Additionally, growing of these oxide phases led to increased volume, consequently, the localized stresses that generated cracks or spallation of the ceramic layer would be induced [77]. Moreover, it was found that the interfaces between the mixed oxide layer, top coat, and alumina scale became weak and resulted in poor adhesion between these interfaces which could be considered as a source of weakness as demonstrated in *Figure 4.11*. Therefore, the availability of Al within the bond coat or even in the substrate will determine the nature of formed oxides and the ability of the alumina-based TGO scale to grow and hence the performance of the TBC system at high temperatures.

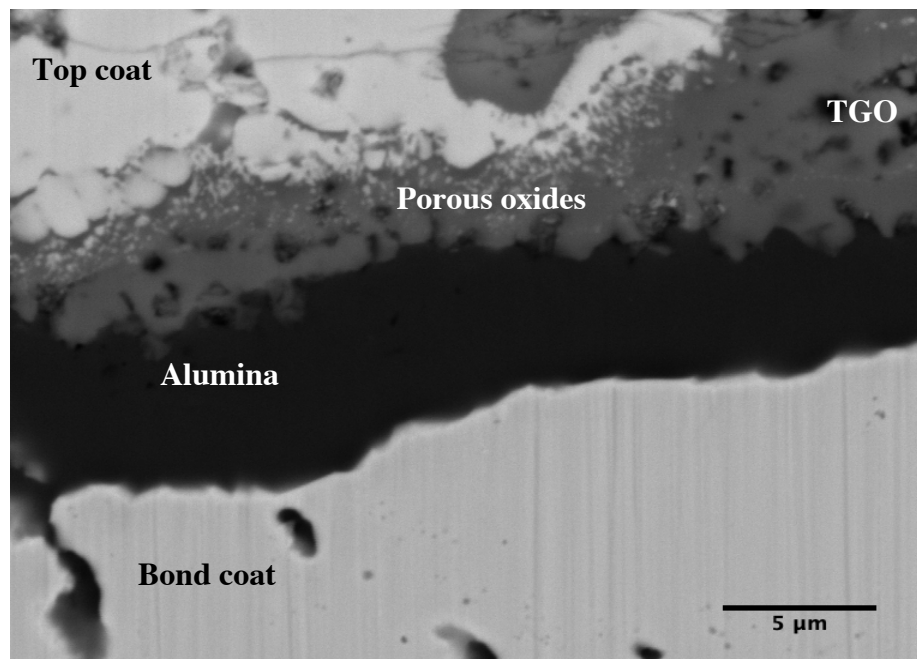


Figure 4.10 SEM micrograph of the oxidized specimen showing porous and non-uniform TGO when oxides rather than alumina are present.

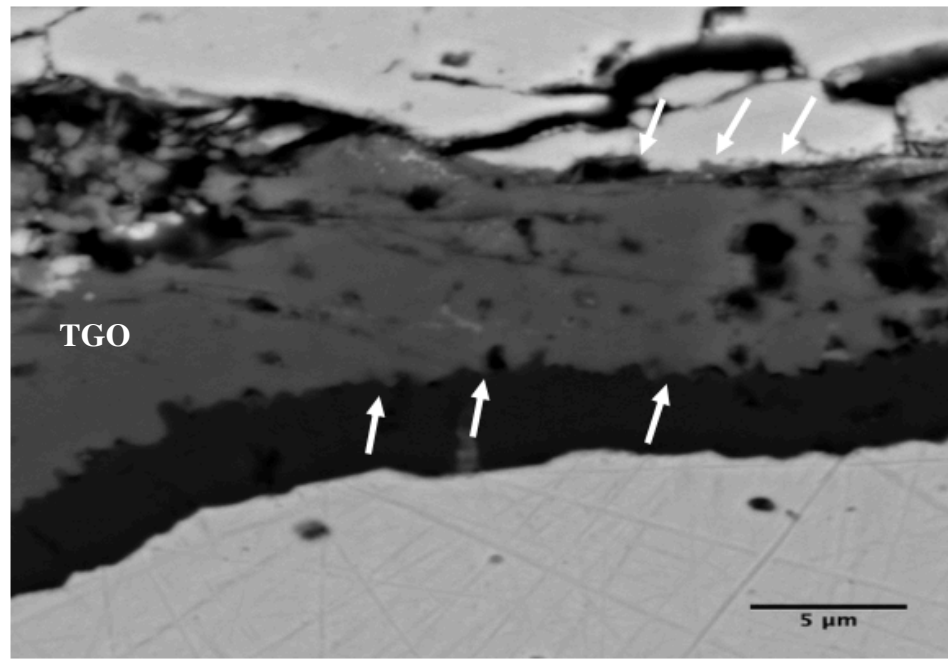
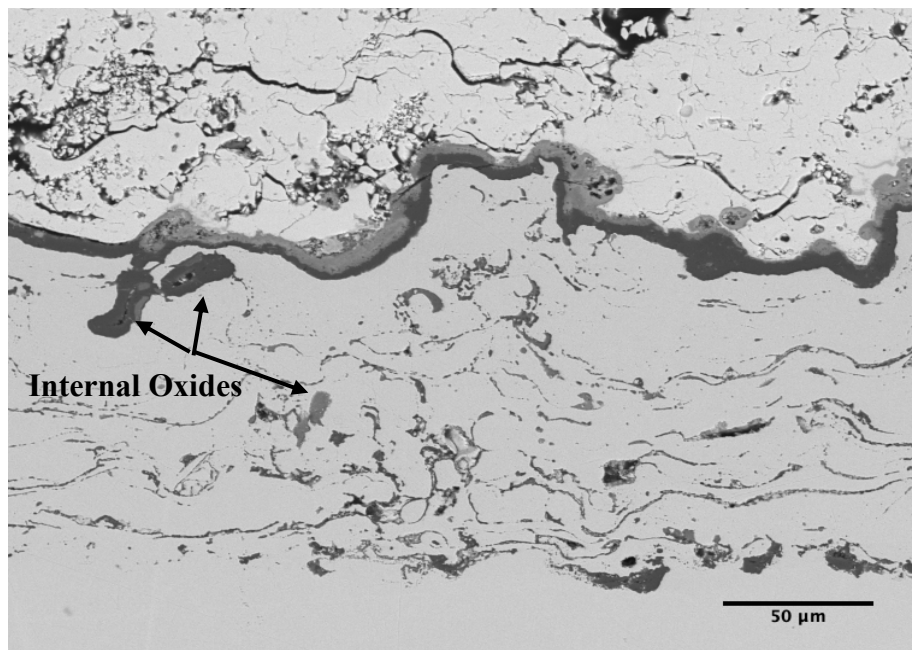


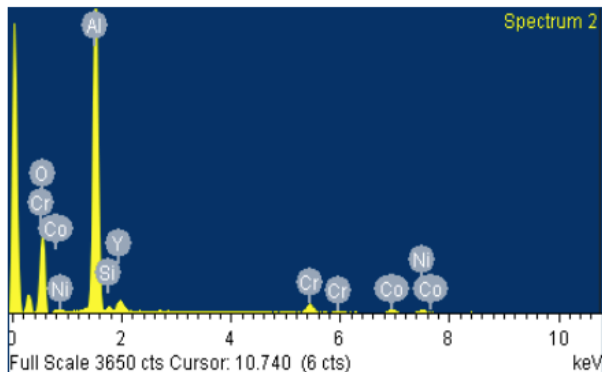
Figure 4.11 SEM micrograph of the oxidized specimen showing poor adhesion between the top coat, the mixed oxides and alumina layer of the TGO, indicated by the arrows .

4.3.2 Internal Oxidation of Bond Coat

The metallurgical examinations of the oxidized specimens showed the presence of internal oxidation of the bond coat after long-term exposure at high temperatures. There was a large variation in oxidation behavior in terms of inwardly growing oxides. The formation of internal oxides can be attributed to the penetration of oxygen through the microcracks formed in the TGO or through interconnected porosities inside the TGO and the bond coat. It was found that the amount of internal oxidation increased with exposure time. A typical microstructure of the bond coat at the early stage of internal oxidation in the specimen oxidized at 1050°C for 970 h is shown in *Figure 4.12 a*, along with the average compositions of the oxides determined with EDS (*Figure 4.12 b*). The oxides were found consisting of mainly alumina, which was formed due to the reaction of the Al cations with oxygen that penetrated the internal TGO interface, with a small amount of yttrium oxides, as confirmed by the EDS analysis.



(a)



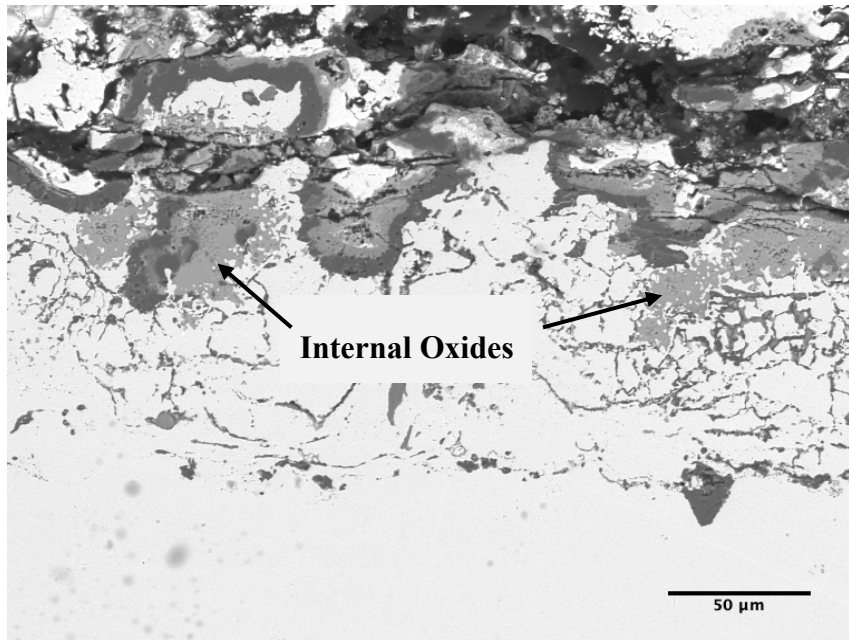
Elemental Table (wt%)

Element	Wt%
O	49.5
Al	42.0
Si	1.01
Cr	3.64
Co	2.99
Ni	2.93
Y	5.92

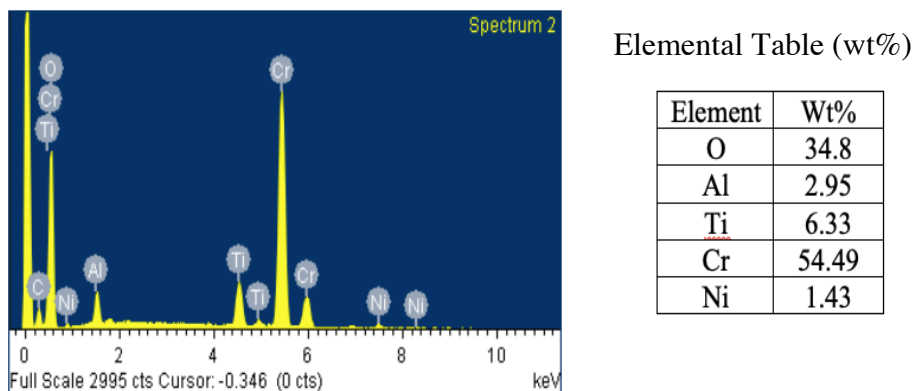
(b)

Figure 4.12 Internal oxides in the bond coat of the TBC specimen oxidized at 1050°C for 970 h: (a) SEM micrograph showing internal oxidation of bond coat and (b) EDS spectrum and elemental table of internal oxides.

With increasing the exposure time, as a result of Al depletion and oxygen ingress to the bond coat through the top coat as well as the interface cracking, the effect of internally grown oxides was more pronounced after the TBC specimen was oxidized for 1970 h at 1050°C, as shown in **Figure 4.13 a**. The islands of inward growing Cr₂O₃ can be observed and this was confirmed by the EDS analysis (**Figure 4.13 b**). However, the TGO layer was still visible and could be distinguished.



(a)

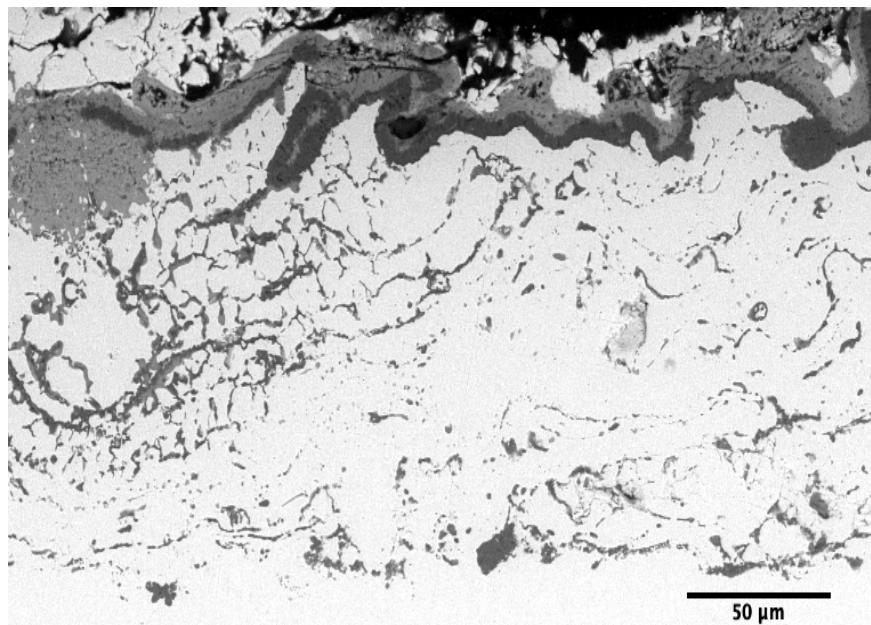


(b)

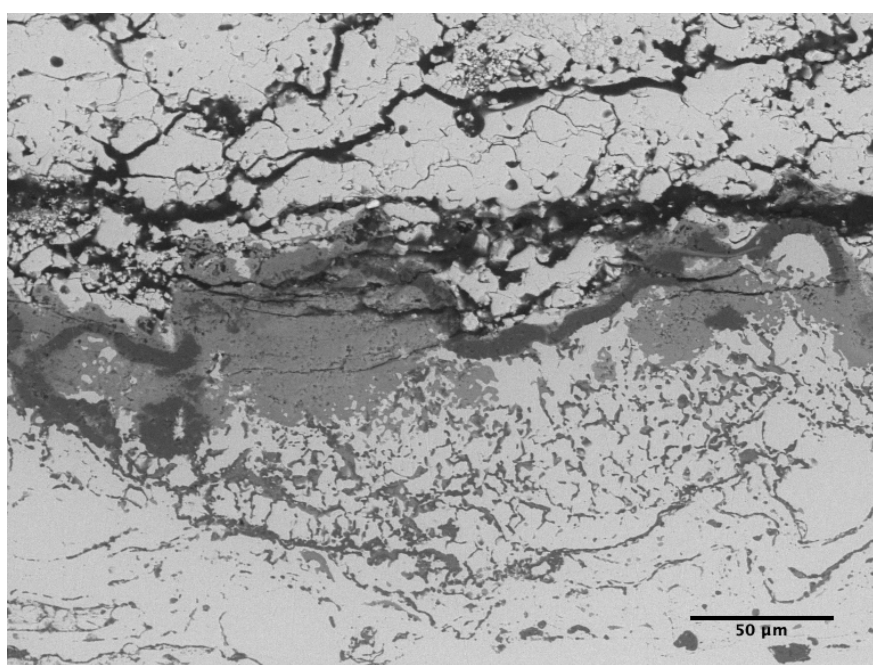
Figure 4.13 Internal oxides in the TBC specimen oxidized at 1050°C for 1970: (a) SEM micrograph showing internal oxidation of the bond coat and (b) EDS spectrum and elemental table of internal oxides.

Moreover, it was found that as the exposure temperature was increased, the inwardly grown oxides were observed at earlier stage of exposure time, as shown in **Figure 4.14**. It was

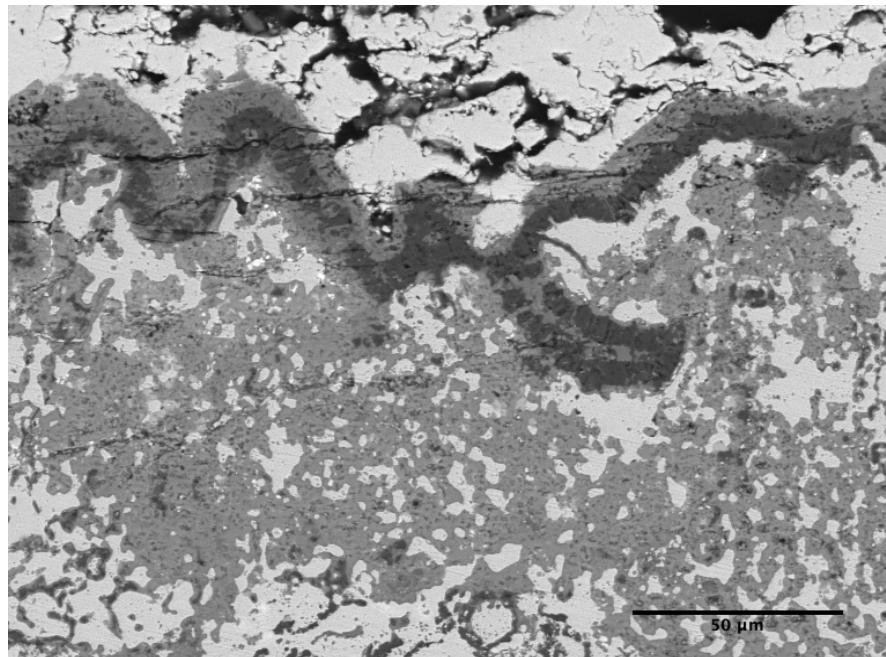
obvious that the internal oxides started to form at 700 h of exposure as the temperature was raised to 1100°C.



(a)



(b)



(c)

Figure 4.14 SEM micrographs of internal oxides in the bond coat of the TBC specimens oxidizes at 1100°C for (a) 700 h, (b) 970 h, and (c) 1500 h.

At oxidation temperature of 1150°C, internal growing oxides of the bond coat were observed after only 360 h of exposure and the distinction between the TGO layer and inward growing oxides became difficult in some areas, as shown in **Figure 4.15**. It can be concluded that internal oxidation of the bond coat started at earlier stage of oxidation as the exposure temperature was increased and the amount of internal oxides increased with increasing exposure temperature and time.

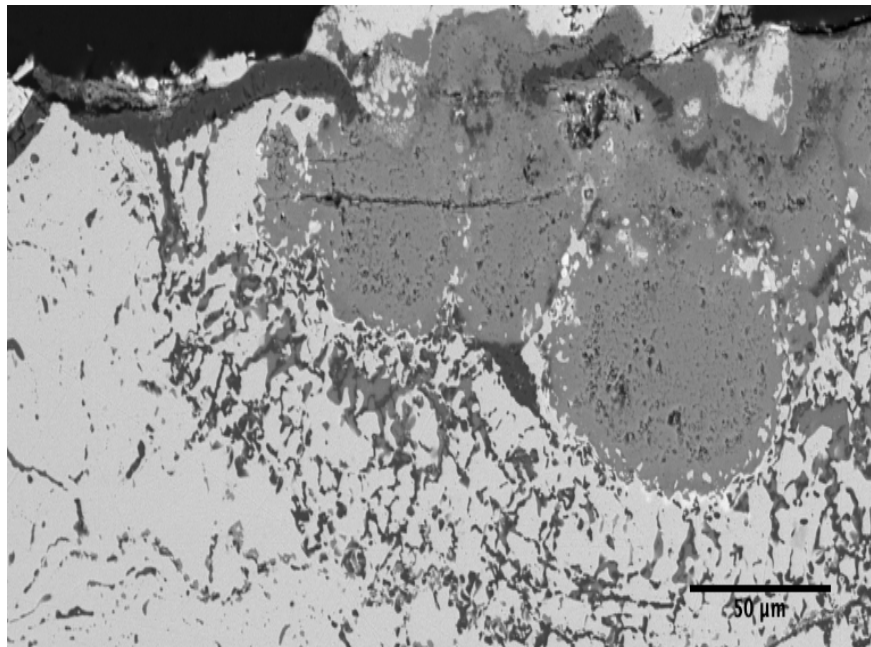
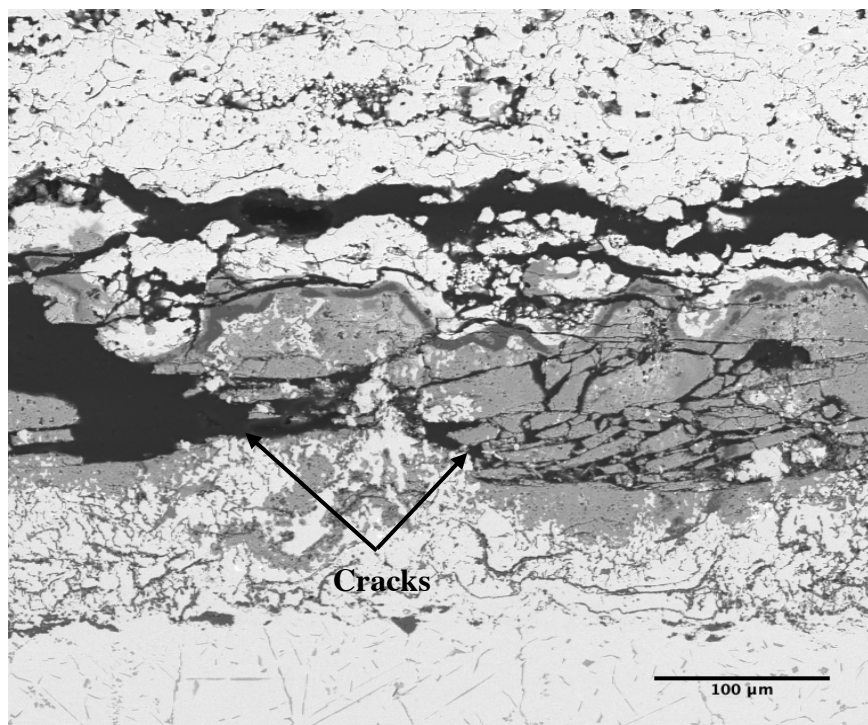


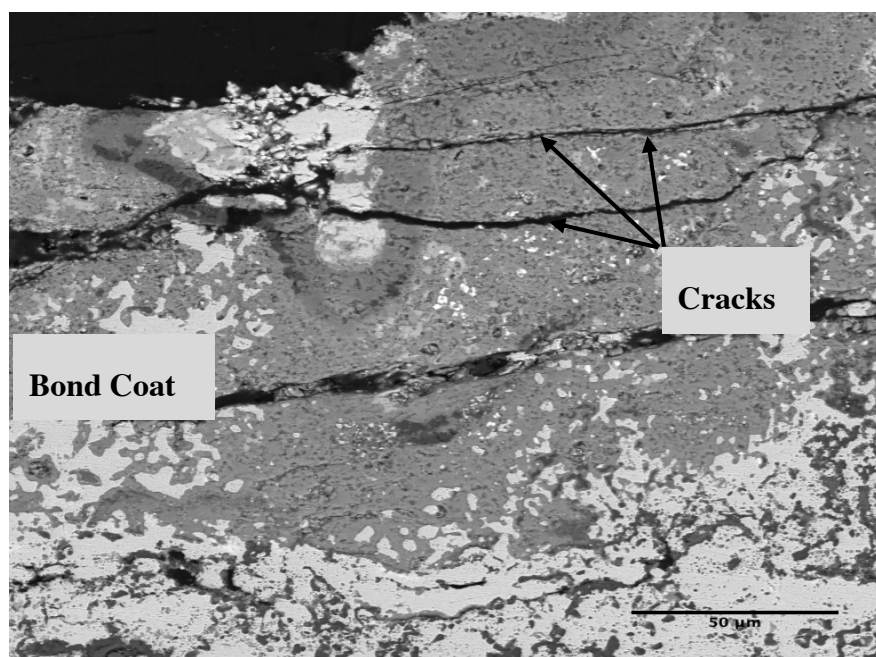
Figure 4.15 SEM micrograph of internal oxides in the bond coat of the TBC specimen oxidized at 1150°C for 360 h.

The association of the bond coat internal oxidation with the top coat spallation indicated that the inward internally grown oxides had a non-negligible effect on the performance of the ABS TBC under isothermal oxidation. It was recognized that most of the failed specimens showed internal oxidation and damage by the cracks that cut the thick TGO.

Figure 4.16 shows the SEM micrograph of the failed specimens at oxidation temperatures of 1050°C and 1100°C. Multiple cracks inside the thick TGO across the detrimental oxides can be clearly observed. This type of cracking behavior was dominant and observed for all the TBC specimens, exhibited severe inward oxidation at different exposure temperatures, indicating that the failure of the TBCs by the formation of internal oxides such as chromia or Cr (Ni, Co) oxides, accompanied with Al depletion, could eventually occur.



(a)



(b)

Figure 4.16 SEM micrograph of the specimen oxidized at (a) 1050°C and (b) 1100°C, showing multiple cracks inside thick TGO across detrimental oxides.

4.3.3 Oxidation Kinetics of TGO

For predicting the lifetime of TBCs, it is important to evaluate the oxidation performance of the TGO at high temperatures. Therefore, the thickness growth of the TGO layer in the TBC specimens was investigated in dependence on exposure time at different oxidation temperatures in this research. The oxidation kinetics of the TGO was then determined for three oxidation temperatures (1050°C, 1100°C, and 1150°C) based on the increase in the TGO thickness. The data of the average thickness of the TGO layer in the TBC specimens were obtained from the oxidation tests at 1050°C, 1100°C, and 1150°C, as summarized in **Table 4.1**, along with the standard deviation for error analysis. The reported data were taken from 70 measurements per specimen.

Table 4.1 TGO thickness data from oxidation tests.

Oxidation Time (h)	Average TGO Thickness (μm)		
	1050°C	1100°C	1150°C
100	2.65 ± 0.31	4.20 ± 0.63	6.94 ± 1.56
200	3.77 ± 0.27	6.11 ± 0.68	9.45 ± 1.36
360	5.42 ± 1.19	8.57 ± 1.17	11.32 ± 3.8
700	7.01 ± 0.62	10.27 ± 1.79	
970	8.68 ± 1.07	12.01 ± 2.49	
1500		14.97 ± 1.86	
1970	11.28 ± 1.4		

It is clear that the standard deviation increased with increasing exposure time and temperature. This may be attributed to nonuniformity in TGO growth due to the formation of mixed oxides when the oxidation time and temperature were increased.

The TGO thickness data were plotted against exposure time for different oxidation temperatures in **Figure 4.17**.

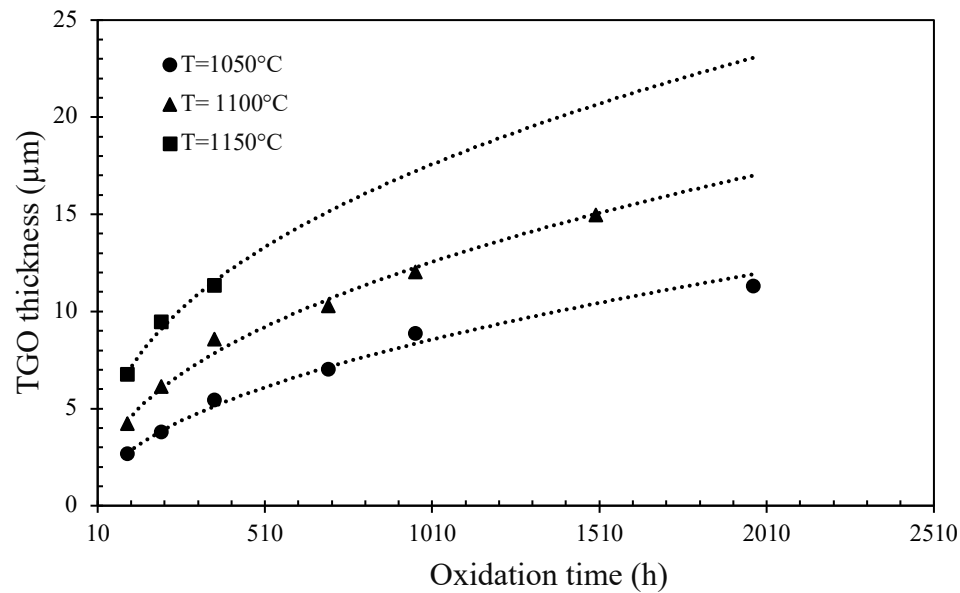


Figure 4.17 Variation of TGO thickness with exposure time as a result of isothermal oxidation at high temperature.

The oxidation kinetics for the TBC system is assumed to follow a parabolic relation, which is given as [39]:

$$h = (K_p t)^{\frac{1}{n_o}} \quad (4.1)$$

where t denotes time, h is the thickness of the oxide layer, K_p represents parabolic rate constant, and n_o is the oxidation constant and equals two if the growth kinetics tends to be parabolic.

Log/log plots of the increase in oxide thickness against exposure time at each temperature provides the time exponent, n_o , by taking the inverse of the slopes. The oxidation kinetics of the APS TBC system tested in the present work at $T=1050^{\circ}\text{C}$ showed a parabolic growth rate while the specimens tested at $T = 1100^{\circ}\text{C}$ and 1150°C showed a sub parabolic growth rate with $n_o = 2.2$, and 2.46 for $T = 1100^{\circ}\text{C}$, and 1150°C respectively. However, in order to produce a global temperature invariant equation, the assumption of parabolic behavior was made for the exposure periods in the present oxidation tests. This allowed for the calculation of a predicted oxide thickness at any time and temperature within the test range and the comparison with other published data.

The TGO thickness data obtained for different exposure times at the three temperatures are plotted against the square root of exposure time, showing a nearly linear trend (*Figure 4.18*) indicating that the parabolic growth rate assumption is reasonable. The slopes of the linear trend lines in *Figure 4.18* are proportional to the square root of the parabolic rate constant at each of the exposure temperatures. The obtained values of the parabolic rate constant K_p are reported in *Table 4.2*, which are comparable to the values obtained by other researchers [113], [114].

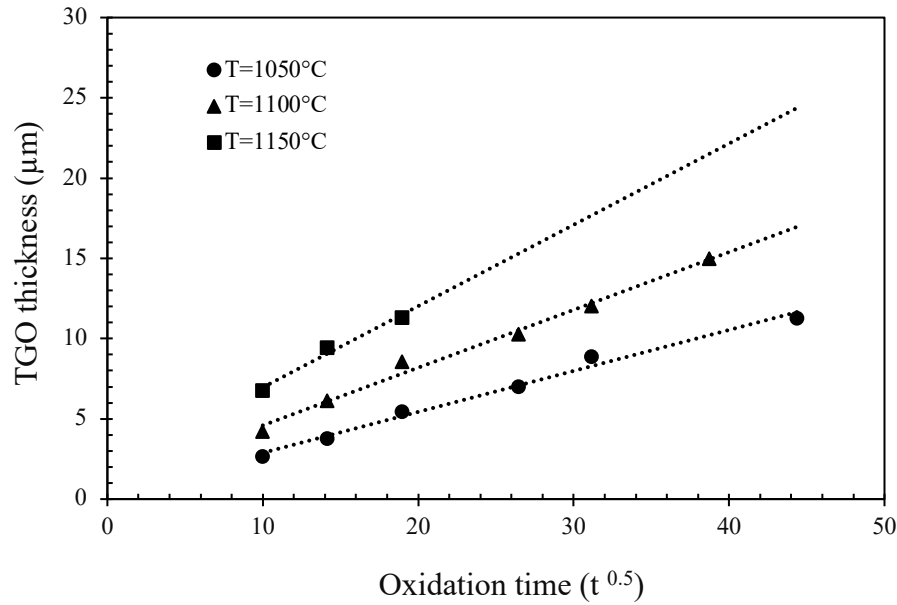


Figure 4.18 Plots for determination of K_p value for each oxidation temperature.

Table 4.2 Experimentally determined parabolic rate constants for TGO growth in oxidized TBC specimens.

Temperature ($^\circ\text{C}$)	Parabolic Rate Constant $K_p(\text{m}^2 \cdot \text{s}^{-1})$
1050	2.71×10^{-17}
1100	3.59×10^{-17}
1150	1.042×10^{-16}

The parameter K_p in Eq (4.1) can be expressed with the Arrhenius equation, dependent of temperature and activation energy [115]. Accordingly, the equation of K_p is given as

$$K_p = K_o e^{\frac{-Q}{RT}} \quad (4.2)$$

where K_o is constant and independent of temperature for thickening of TGO, Q is the activation energy which is effective on TGO growth, R is the universal gas constant, and T is the temperature in Kelvin. The Arrhenius plot gives activation energy for the TGO formation in the APS TBC specimens. By taking the natural logarithm of Eq (4.2) and plotting $-\ln K_p$ vs $(1/T)$ graph for the TGO layer, a best fit straight line is obtained, as shown in **Figure 4.19**. The slope of the straight line corresponds to $\frac{Q}{R}$. The activation energy Q value can be obtained from the slope of the graph with $R = 8.314 \text{ J (mole K)}^{-1}$, which gives $Q = 209.732 \text{ kJ/mol}$. The intercept of the straight line on y -axis gives the value of logarithmic K_o , thus $K_o = 4.47 \times 10^{-9} \text{ m}^2 \cdot \text{s}^{-1}$. Hence,

$$K_p = 4.47 \times 10^{-9} \exp\left(\frac{-209732}{8.314T}\right), \text{ m}^2 \cdot \text{s}^{-1} \quad (4.3)$$

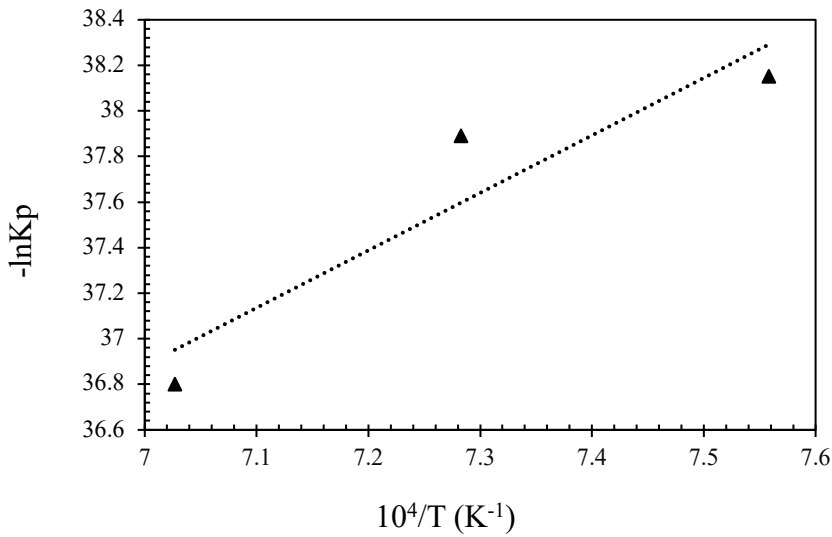


Figure 4.19 Plot for determination of activation energy Q ($-\ln K_p$ vs $1/T$).

It is possible now to create a global temperature invariant equation that allows for predicting the oxide thickness at any time and temperature within the testing range by inserting Eq (4.2) into Eq (4.1) as

$$h^2 = 4.47 \times 10^{-9} \exp\left(-\frac{209737.2}{8.314T}\right) \times t \quad (4.4)$$

Using Eq (4.4) it is possible to predict the oxide thickness for the TBC system at a given exposure time and temperature. **Figure 4.20** presents the comparison between the predicted TGO thickness from Eq (4.4) and the experimentally measured TGO thickness. Hence, this equation can be used to predict the TGO thickness of the TBC system within the ranges of time and temperature investigated in this research

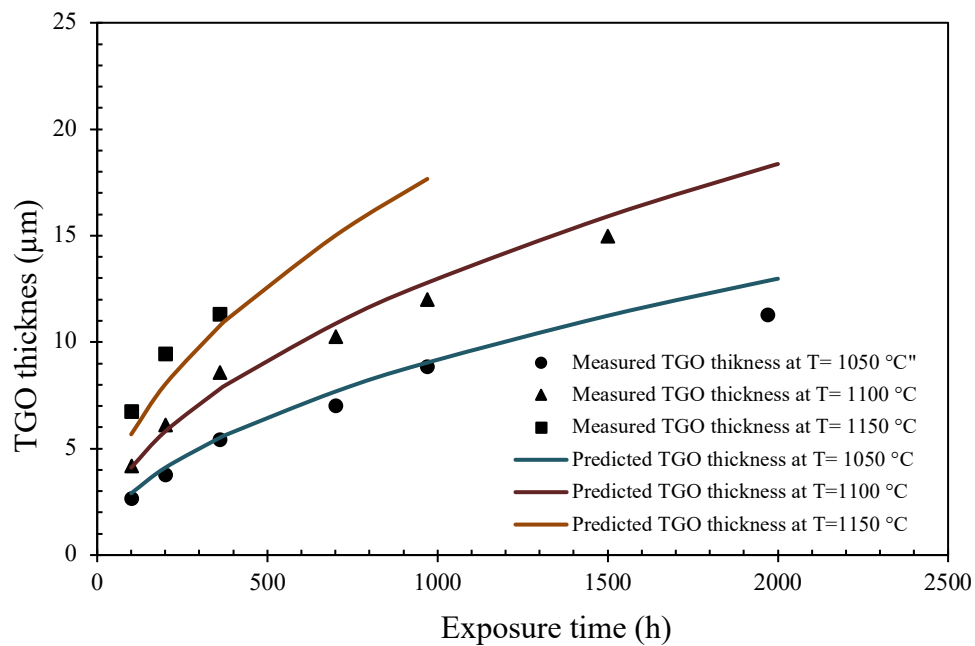


Figure 4.20 Comparison in TGO thickness growing with exposure time at different oxidation temperatures between theoretically predicted values and experimentally measured data.

TGO critical thickness can be considered as a criterion for TBC system failure. When the TGO layer of a given TBC system reaches a critical thickness, the TBC system will fail independent of testing temperature. The data from this research show that the estimated TGO average thickness at TBC failure is approximately 12 μm , which is apparently the critical TGO thickness for the TBC system under isothermal condition at the temperatures of 1050°C, 1100°C, and 1150°C. Thus, with a critical TGO thickness value at a given temperature, the TBC spallation failure time can be predicted using Eq (4.5).

Considering the critical TGO thickness of 12 μm , the time to the TBC spallation can be estimated as follows:

$$t_f = 8.948 \times 10^{-6} \exp\left(\frac{209737.2}{8.314T}\right) \quad (4.5)$$

where t_f is time to failure in hour.

Figure 4.21 depicts the failure times of the TBC under oxidation as a function of oxidation temperature, predicted using Eq (4.5). The dotted line represents the theoretical prediction of the time to produce a 12 μm thick TGO and the discrete points are the experimental data. The predicted failure times and the experimental data agree well in general, showing the trend of the TBC lifetime decrease with increasing exposure temperature, which validates the equation prediction. However, it is noted that the theoretical prediction underestimates the TBC failure time at oxidation temperature 1100°C. On the other hand, this estimation reasonably agrees with the failure times of APS TBC systems obtained from other data sources [44], [116], [117]. Thus, determining the critical thickness of the TBC system

will allow to determine the lifetime of the coating at any temperature within the testing range in this research.

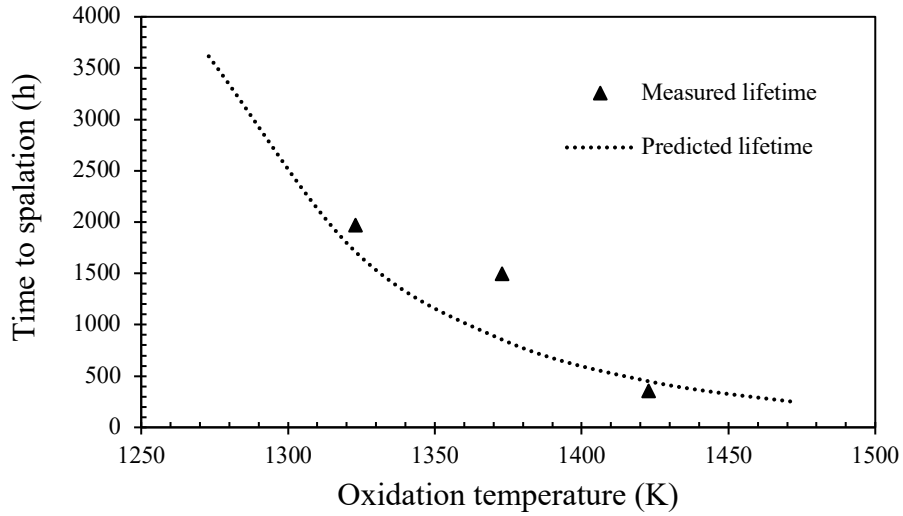


Figure 4.21 Comparison of TBC failure times between theoretical prediction and experimental data.

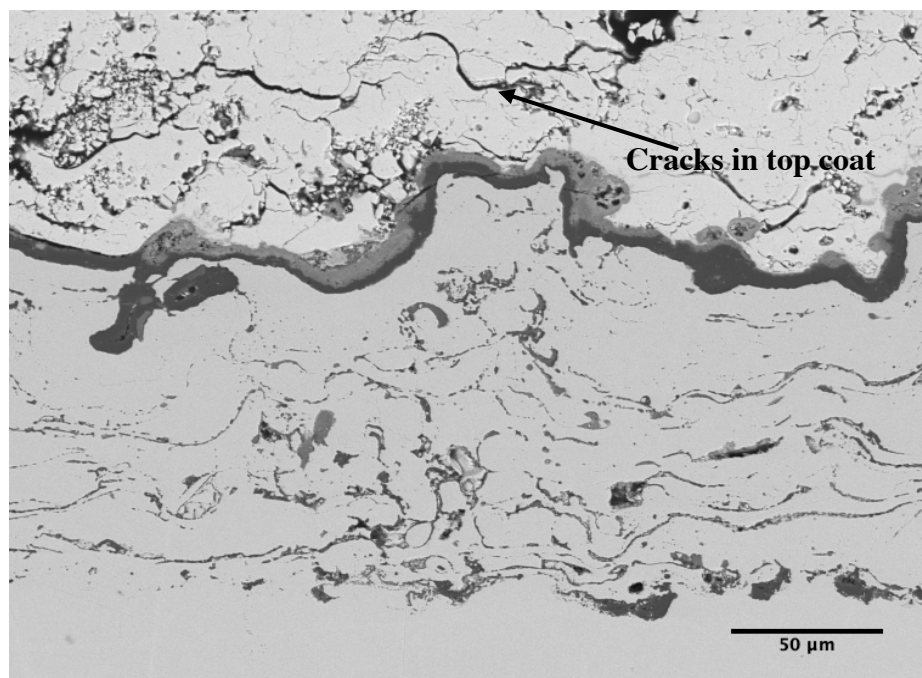
4.4 Cracking and Failure

4.4.1 Crack Formation and Growth

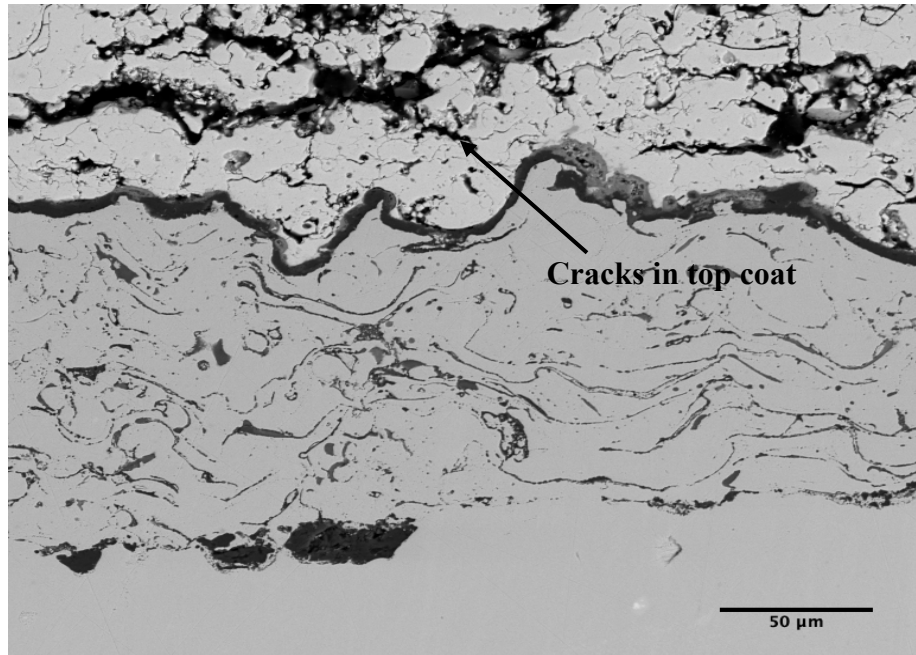
The spallation of the ceramic topcoat is one of the important failure modes that affect TBC system reliability. With the spallation of top coat, the insulating properties of the coating rapidly degrade and hence the bond coat oxidation accelerates [118]. Generally, the failure of APS TBC components is associated with the formation and coalescence of microcracks within ceramic top coat or in TGO or at its vicinity on either interface [119]. Therefore, another main task of this research was to investigate the crack formation and propagation in the TBC when it was exposed to high temperature environments since they were one of

the crucial factors of the TBC failure. Detailed SEM examinations were undertaken on all the TBC specimens to inspect the presence of any cracking.

After isothermal oxidation tested at 1050°C, the TBC specimen experienced a macroscopic failure, but no complete spallation occurred. However, prior to the final failure, microscopic delamination and many microcracks were detected in the TGO and top coat as well as at the TGO/top coat interface. Some of the pre-existing cracks may have already existed in the top coat, as discussed earlier, as a result of the coating deposition process. These cracks could also be formed as a result of in-plane tensile stresses imposed on the ceramic top coat layer during the heating of the TBC components. The presence of these cracks could enhance the strain tolerance of the coating if they were not linked to a major delamination crack. However, it was observed that these cracks extended further with exposure time, as indicated in **Figure 4.22**.



(a)

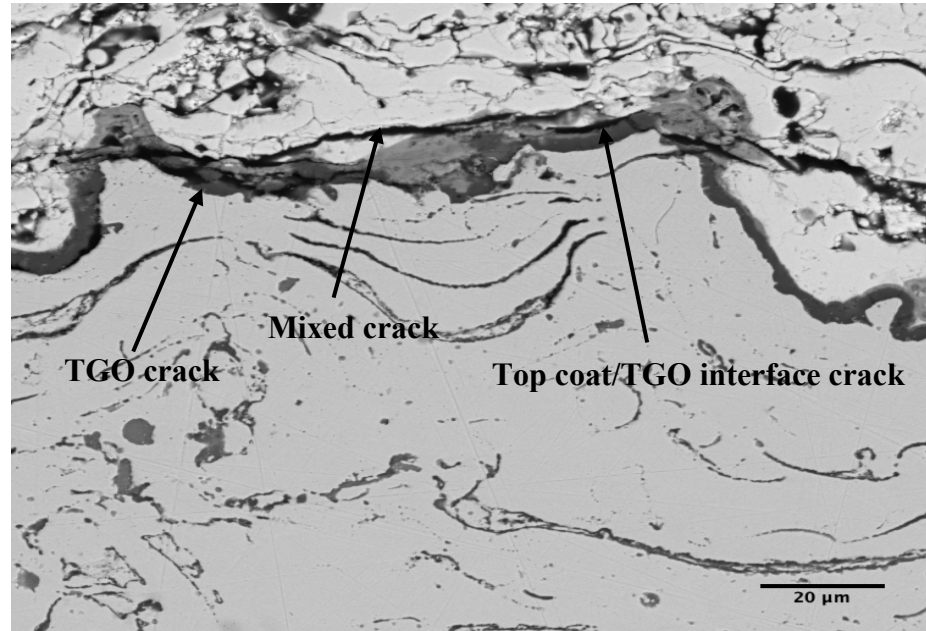


(b)

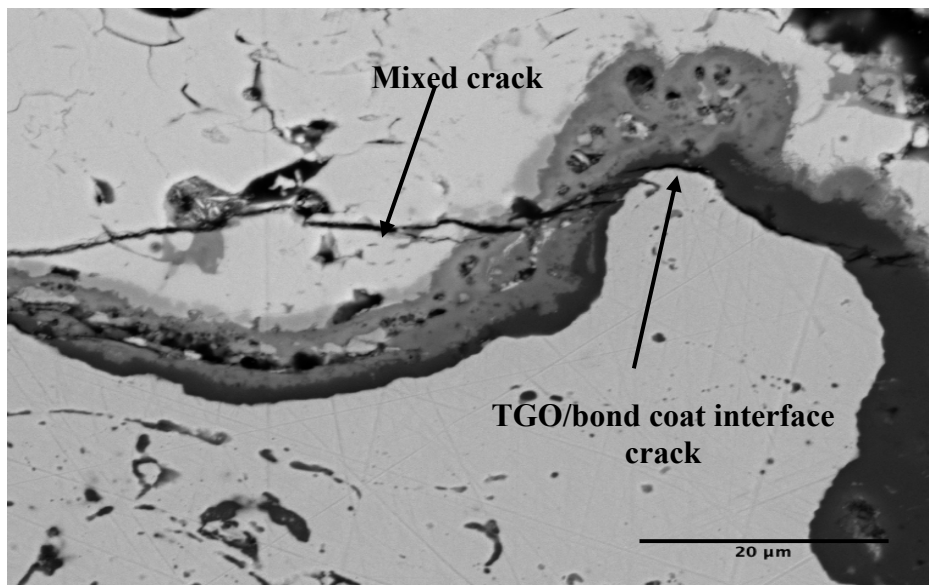
Figure 4.22 SEM examination of cracks in the top coat of the TBC specimen oxidized at 1050°C for (a) 100 h and (b) 360 h.

Furthermore, examining the cross-sections of the TBC specimens oxidized at 1050°C for different exposure times revealed that in addition to the cracks within the topcoat, the cracks that were already formed after 200 h of exposure could also be asserted. The interface cracks between the top coat and TGO, termed top coat/TGO interface cracks, and within the TGO as well, could be distinguished, as shown in **Figure 4.23 a**. There were also cracks that propagated partly in the top coat and partly in the TGO, termed mixed cracks, as shown in **Figure 4.23 a**. After longer exposure times (970 h) crack nucleation occurred at the TGO/bond coat interface, due to thermal expansion mismatch, as shown in **Figure 4.23 b**. Nevertheless, the interface cracks and the cracks associated with the TGO were small compared to the mixed cracks and the cracks that developed in the ceramic top

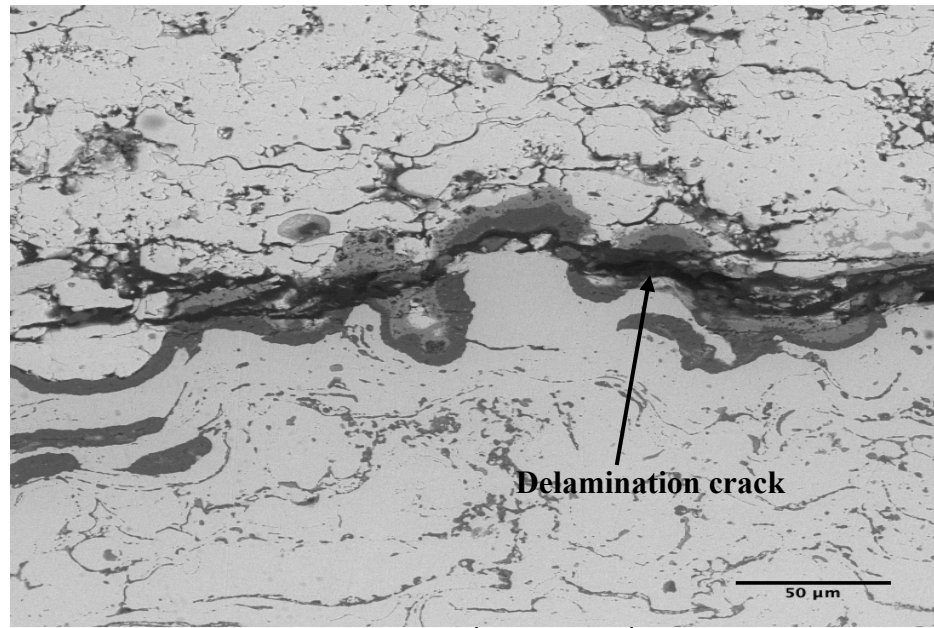
coat. All cracks generated in the TBC specimens were generally parallel to the interfaces between the bond coat, TGO, and top coat. After further exposure at 1050°C, the TBC specimen was found to have the individual cracks linked, forming a delamination crack at the vicinity of the TGO/top coat interface, as shown in *Figure 4.23 c*.



(a)



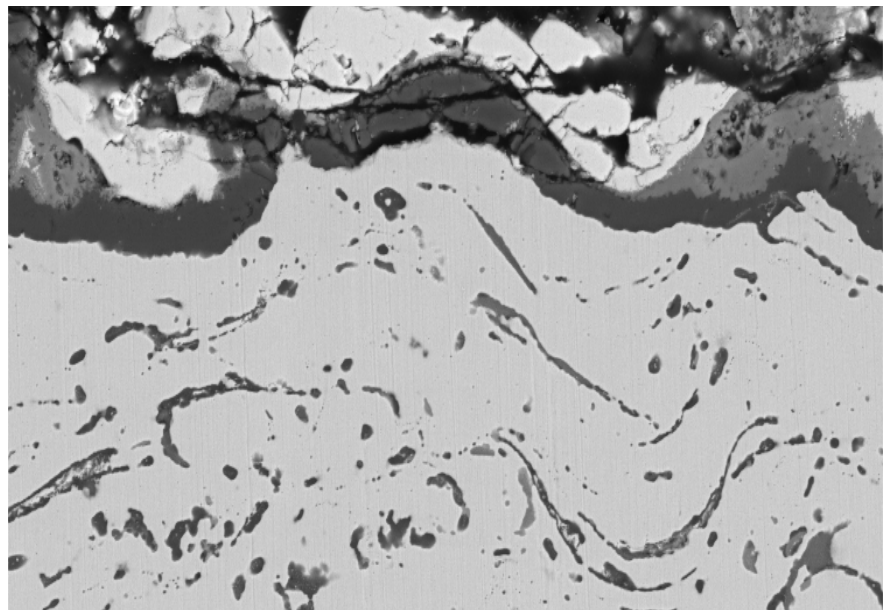
(b)



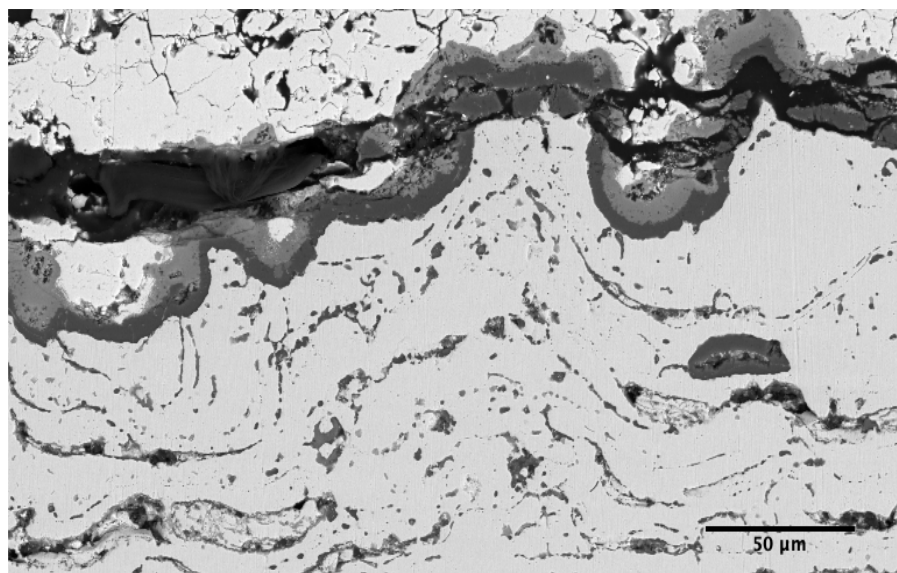
(c)

Figure 4.23 SEM examination of cracks in the TBC specimen oxidized at 1050°C for (a) 200 h, (b) 970 h and (c) 1970 h.

Similar cracking behavior was observed in the TBC specimens oxidized at 1100°C and 1150°C (**Figure 4.24**). However, the size of cracks increased with exposure temperature and time.



(a)



(b)

Figure 4.24 SEM examination of cracks in the TBC specimen oxidized at (a) 1100°C and (b) 1150°C.

On the cross-section of each specimen, crack lengths for all types of crack were measured at more than 10 locations. The averages of the crack sizes with standard deviations are plotted against exposure time in **Figure 4.25**. It can be seen that the longer exposure time resulted in an increase in the size for all types of crack. However, only mixed cracks which propagated partly in the TGO and partly in the top coat (mixed crack), and top coat cracks, had the maximum length and their propagation rates were the higher. The average lengths of other types of cracks showed a minor change with oxidation duration. This indicated that the mixed cracks and top coat cracks may contribute directly to the final failure of the TBCs. However, since the crack that had the maximum length would cause the failure of the TBC, the failure as a result of mixed crack propagation will be dominant at higher oxidation temperatures.

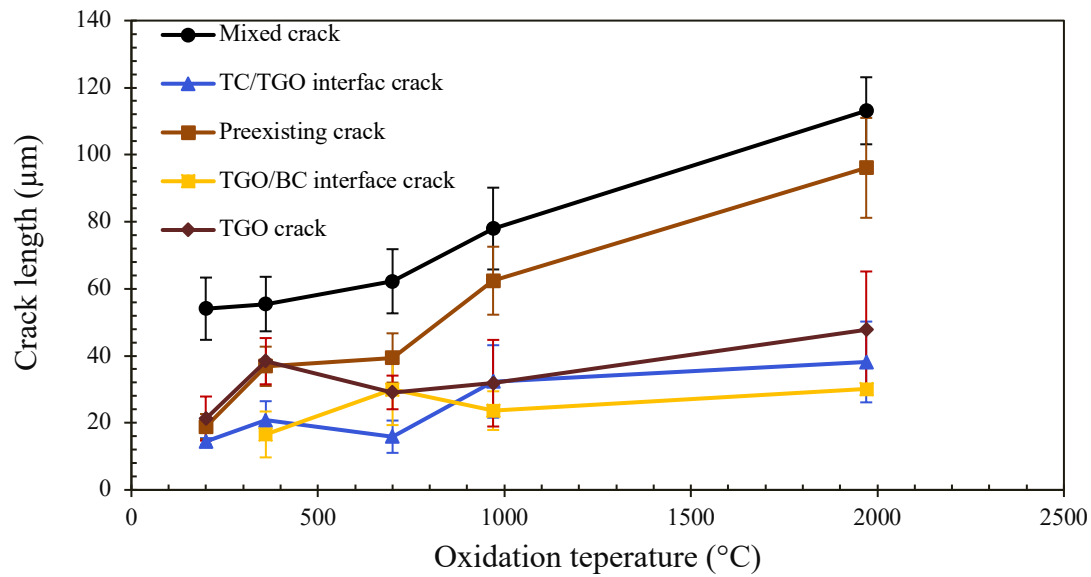


Figure 4.25 Crack sizes versus exposure time for the TBC specimen oxidized at 1050°C.

Figure 4.26 shows the kinetic of the maximum crack length of the mixed crack for temperatures of 1050°C, 1100°C and 1150°C. It can be suggested that the crack length increases with exposure time and temperature.

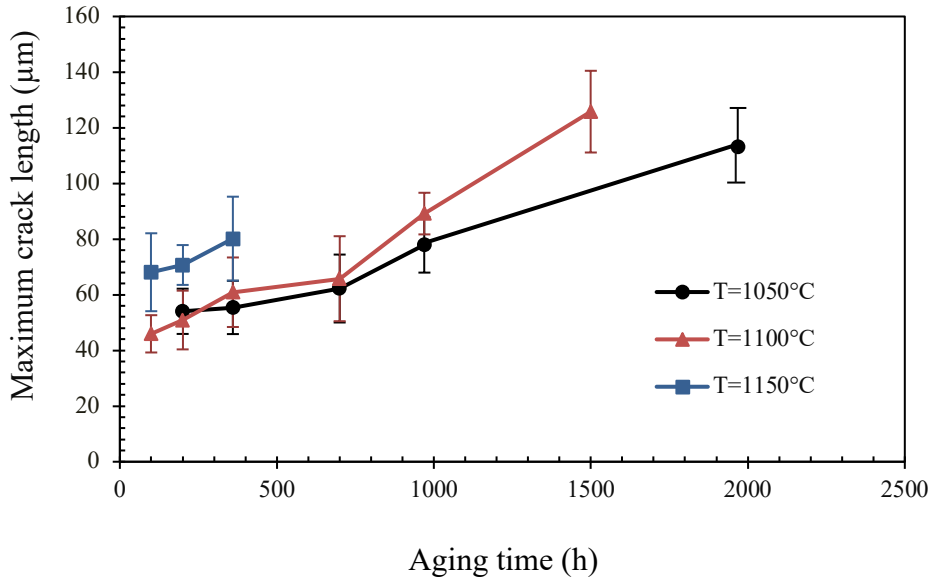


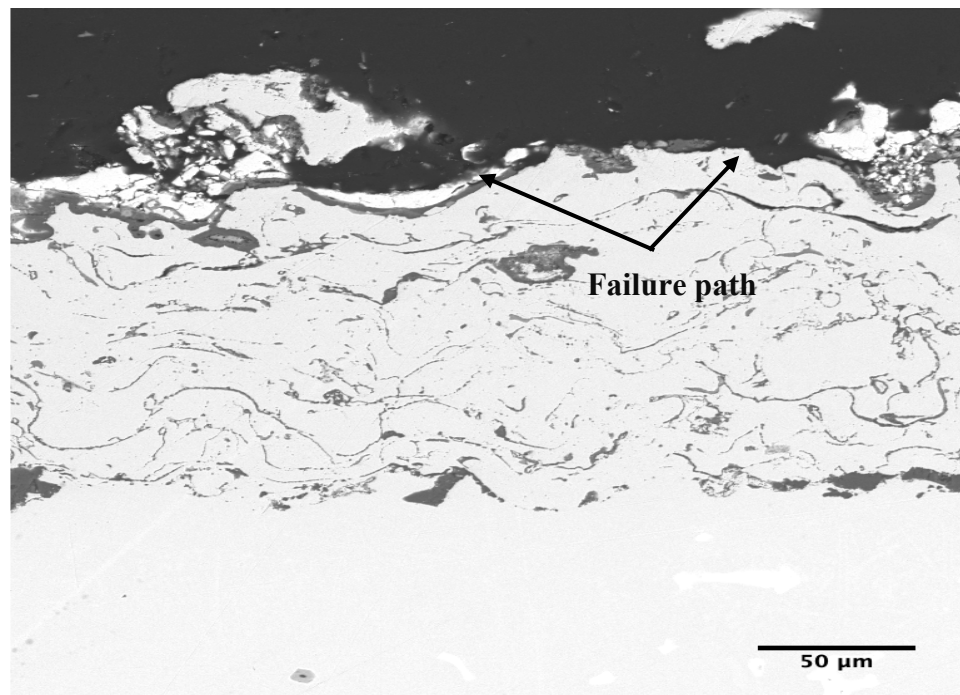
Figure 4.26 Kinetic performance of the maximum crack length of the mixed crack during the TBC oxidation at different temperatures.

4.4.2 Final Failure of TBCs

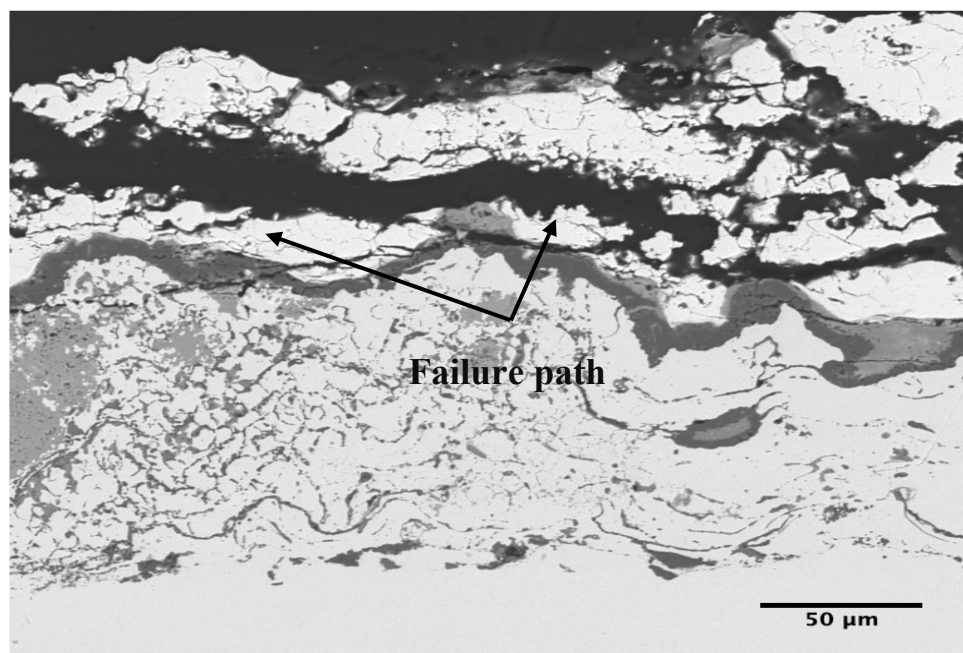
Ultimately, it was the cracking mechanism that led to the spallation of the coating in all cases except at 1050°C where complete spallation of the coating did not occur up to a maximum exposure duration of 1970 h. However, at higher temperatures, 1100°C and 1150°C, the ceramic top coat spalled during cooling, and the final failure occurred at room temperature.

Figure 4.27 shows an example of failure for the APS TBC system after 1970 h isothermal oxidation at 1050°C. Although there was no complete spallation observed and the large

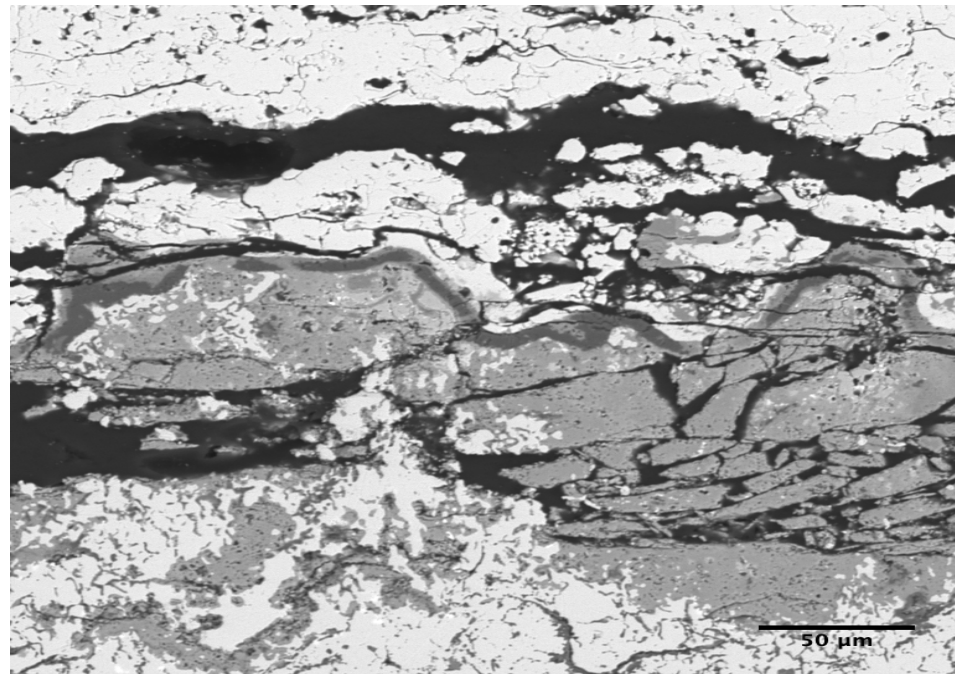
area of the top coating was still attached, cracking was extensive and ran the full width of the specimen, as shown in *Figure 4.23*. The predominant failure crack path was located in the inner part of the top coat near the top coat/TGO interface (*Figure 4.27 a and b*). This explained the white areas of the crack surface shown in *Figure 4.3*, which confirmed occurring of the failure through the ceramic top coat. Other mixing color areas (greyish color) represented the areas where the delamination crack passed through both top coat and TGO [117]. Moreover, this TBC specimen showed a microscopic failure because of severe inward oxidation by the formation of multiple cracking inside the thick TGO (*Figure 4.27 c*) in addition to the type of already formed microcracks, as explained above. The failure by this mechanism must be considered and would be obvious for all the TBC specimens showing severe inward oxide growth associated with Al-depletion in the bond coat during the long-term oxidation. Both mechanical failure of the top coat (TGO growth controlled mechanism at the bond coat/top coat interface) and internal oxide growth failure were observed. However, the failure due to the growth of internally grown oxides was not the main reason for the failure of the TBC, in other words, the failure of the APS TBC system would have happened before there was enough time for internal oxides to become severe due to continuously growing. As an example, *Figure 4.27* depicts that in the case of the TBC specimen oxidized at 1050°C for 1970 h, the failure had already occurred prior to the occurrence of internal oxides (*Figure 4.27 a*), or when only small amounts of inward growing oxide interruptions were formed (*Figure 4.27 b*).



(a)



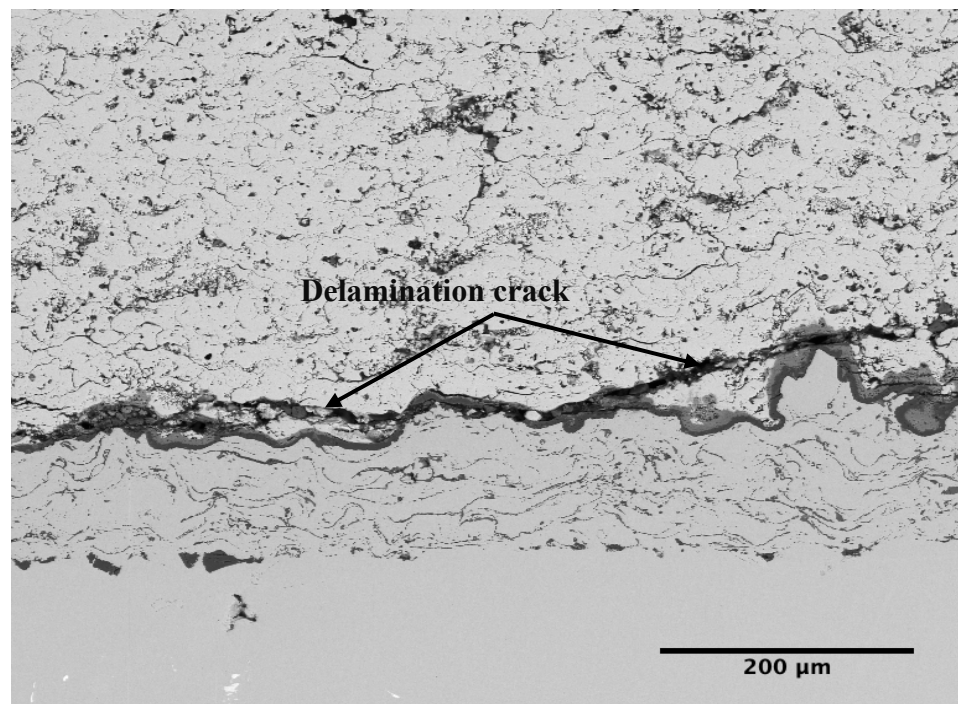
(b)



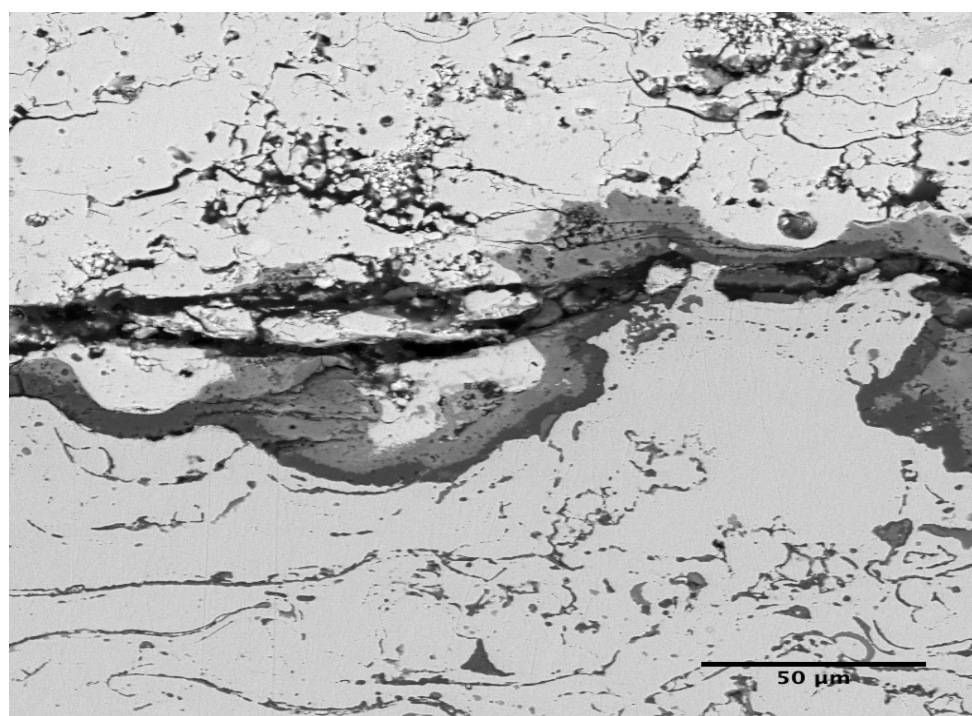
(c)

Figure 4.27 SEM examination of the final failure of the TBC specimen oxidized at 1050°C for 1970 h: (a) and (b) failure path in top coat and (c) cracking within TGO.

At 1100°C oxidation temperature the failure of the TBC was related to the nearing totally delamination and subsequently spallation of the top coat. The investigation of the TBC system after 970 h of oxidations before the final failure showed initial stage of partial delamination effects in the area of the TGO and top coat as a result of crack propagation. It can be clearly seen from **Figure 4.28** that the cracks formed in the TGO in the area of the mixed oxides and subsequently penetrated into the top coat. The examination after 1500 h revealed that the specimen failed due to the decrease in adhesion of the top coat and bond coat interface (top coat spallation) caused by crack propagation. The crack passed partially through the TGO and top coat, as shown in **Figure 4.29**.

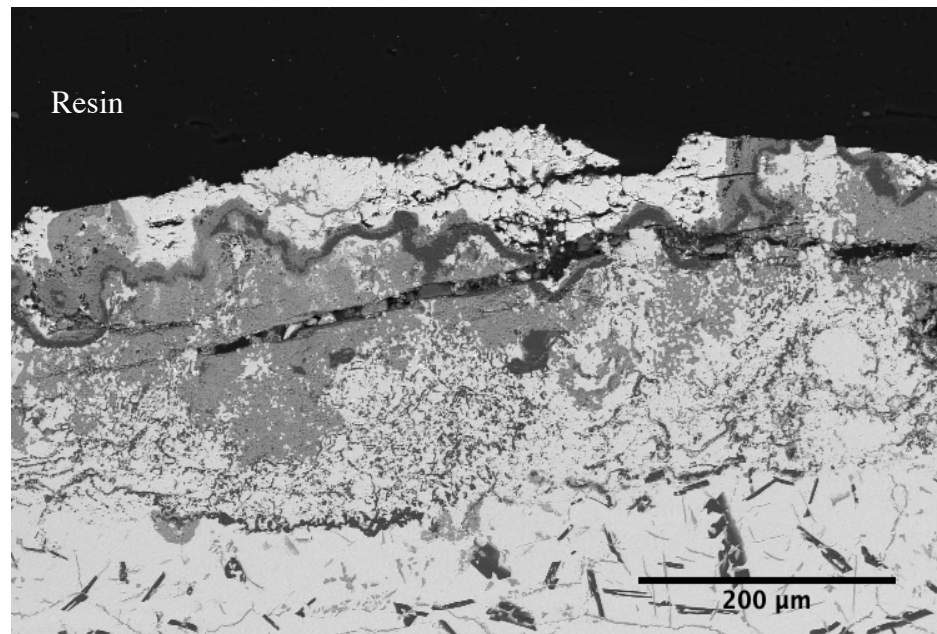


(a)

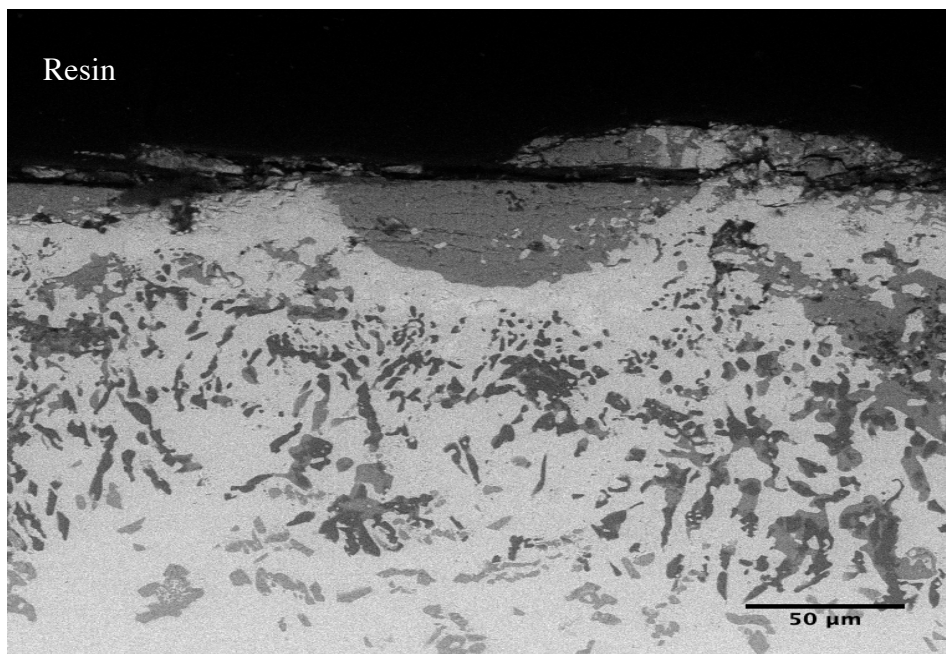


(b)

Figure 4.28 SEM examination of the delamination crack in the TBC specimen oxidized at 1100°C for 970 h: (a) at low magnification and (b) at high magnification.



(a)



(b)

Figure 4.29 SEM examination of the final failure of the TBC specimen after 1500 h oxidation at 1100°C due to spallation of the ceramic top coat.

Upon isothermal oxidized at 1150°C, complete failure of the TBC specimen occurred after only 360 h by the spallation of the top coat. This observation was in agreement with the data reported in literature where the lifetime of APS TBCs ranged from 150 to 400 h at 1150°C [118]. **Figure 4.30** shows an example of the failure of the TBC system after 360 h isothermal oxidation at 1150°C.

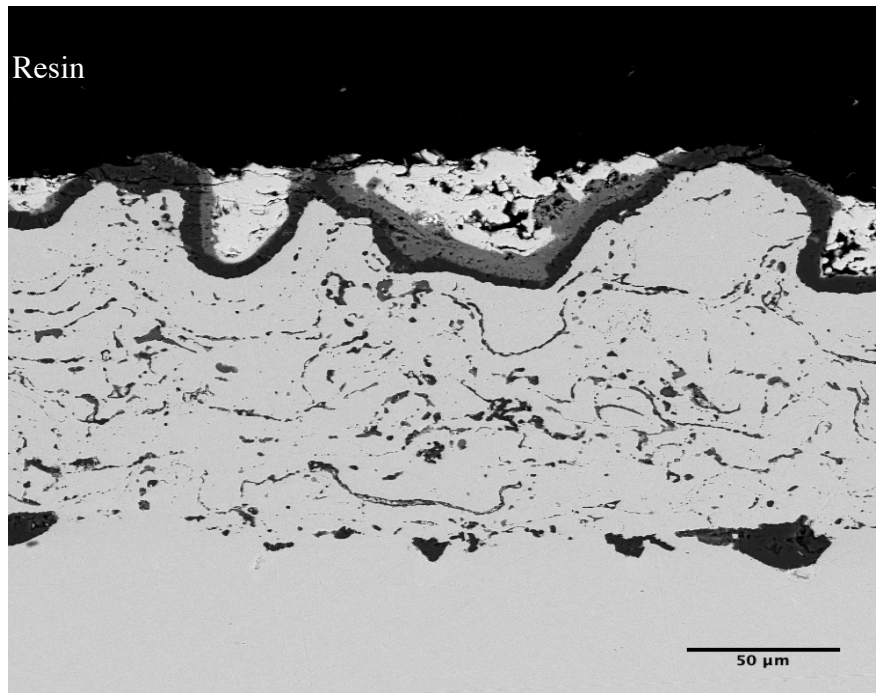


Figure 4.30 SEM micrograph of the TBC specimen after oxidation at 1150°C showing spallation of the top coat.

A possible failure mechanism, which may have led to the observed delamination crack patterns for the TBC system, can be suggested as follows. The TGO growth induced large in-plane compressive stresses during oxidation. Upon cooling, due to the undulation nature of the bond coat in the APS TBC, the geometry imposed the generation of tensile out-of-plane stresses in the TGO at hills of the rough surface. These tensile stresses in addition to

the thermal stresses generated due to the thermal mismatch were the main driving force for the microcrack formation at or near the TGO/ bond coat interface. The formation of microcracks was followed by the propagation of these cracks initially within the hills of the top coat, and then due to the local stress distribution changes, the crack penetrated the TGO and subsequently the top coat and finally linked up to form the delamination cracks that propagated approximately parallel to the bond coat/top coat interface, partly through the TGO and partly through the top coat, leaving the TGO in the valleys unaffected [42].

4.5 Concluding Remarks

The essential design of TBCs consists of a ceramic top coat and a metallic bond coat deposited on a superalloy substrate. The basic function of the top coat is to provide thermal isolation to the underlying layers so that ceramic materials are exclusively chosen because of their low thermal conductivity which can offer thermal insulation function, high melting point to keep the coating structure durable at high temperatures, high thermal expansion coefficient which favors relieving the stresses induced due to the thermal expansion mismatch between the top coat ceramic layer and metallic bond coat layer. To achieve these design goals, the desired case would be that each coating in TBC systems remains fully functional and will not degrade under thermal loading during service, and the interface bonding between the coatings should not deteriorate in the high temperature environment. Therefore, any occurrence during high temperature exposure that affects the functions of the coatings and the bonding between the coatings would degrade the durability and reliability of TBCs. However, from the isothermal tests, it is evident that the TBC materials can be affected seriously by high temperatures, which resulted in the change of the TBC structure.

An in depth and extensive study has been carried out into the oxidation behavior of an APS TBC system consisting of Ni-based alloy substrate, CoNiCrAlY bond coat, and APS applied 8-yttria stabilized zirconia (YSZ) top coat, under isothermal conditions at different temperatures for different exposure times. After isothermal oxidation tests, the APS TBC specimens were analyzed in microstructure using SEM and EDS, focusing on the main factors that affect the TBC delamination, TGO growth, and crack development.

The life of the coatings was found to be strongly dependent on the temperature which the bond coat experienced during oxidation exposure. When the bond coat experienced a temperature higher than 1100°C, the coating life was reduced drastically to 360 h at 1150°C, and this was closely related to the oxidation behavior of the bond coat.

In the light of the bond coat oxidation, which might be the most important factor among others for TBC failure, the TGO layer was formed along the interface of the bond coat and ceramic top layer which contained Al₂O₃ and other mixed oxides. These oxides were believed to decrease the coating life due to oxide growth stresses that were generated rapidly at the top coat side of the coating interface at higher temperatures.

The TGO thickness at the bond coat/TBC interface increased with raising exposure temperature and time. The TGO thicknesses for all tested temperatures and time periods were measured, and the oxidation kinetics studies on the oxidized TBC specimens were carried out. The activation energy required for the development of the TGO layer was found to be about 209.7 kJ /mol.

The depletion of aluminum in the bond coat layer to form the TGO led to the formation of an Al-depleted zone underneath the TGO. This zone increased in size with increasing exposure time at different temperatures. The consequence of Al depletion was the development of fast growing and non-protective oxides such as Co, Ni, Cr oxides. The growth of these oxides in the mechanically constrained environment caused the localized stresses, which consequently must be accommodated by the cracking or spallation of the ceramic layer. In addition, the porous and nonuniform morphology of the TGO provided preferable sites for crack initiation and poor adhesion between the oxide layer and the interfaces, therefore it was considered as a source of weakness that affected the integrity of the APS TBC system during high temperature oxidation. This may motivate further research on the selection of the chemical composition of bond coat material of TBCs to maintain a protective pure alumina TGO layer at high temperature working conditions.

The internal oxidation of the bond coat also played a noticeable role in the degradation of the TBC system. As demonstrated by the oxidation tests, internal oxidation occurred in the region within the bond coat when the TBC specimen was oxidized for longer time. The Internal oxidation of the bond coat started at earlier stage of oxidation as the exposure temperature was raised and the extent of internal oxidation was directly related to exposure time and temperature. The presence of inwardly growing oxide was associated with the damage by the cracks that cut the thick TGO, revealing the non-negligible effect of inward internally grown oxides on the performance of the ABC TBC under isothermal oxidation.

Moreover, it was found that the APS TBC system was dominantly failed by the spallation of the top coat layer due to cracking either within the ceramic top coat or in the TGO or in

their vicinity after cooling from high temperatures. The TGO growth was a crucial factor in the formation of delamination cracks that led to eventual failure of the TBC system. The final failure of the coating system occurred at the bond coat/TGO interface through rapid propagation of the cracks along the interface. The size of the cracks increased with the exposure time and temperature.

The failure of APS TBC system was usually a result of the combination of various mechanisms such as TGO growth, crack formation and propagation, bond coat Al depletion and/or internal oxide growth. All the failure mechanisms that were identified in this study were believed to contribute to the failure of the APS TBC system. However, none of these mechanisms was observed to cause the failure of the TBC by themselves only unless they were very pronounced.

Chapter 5: Results and Discussion of Solid Particle Erosion Test

A typical microstructure of plasma sprayed coating consists of a ‘splat-like’ morphology and a network of microcracks that result from coating deposition process. These microstructural features act to reduce the elastic modulus of the ceramic coating of TBCs and therefore help minimize the stresses that can develop cracks in the coating but make the coating more susceptible to damage by solid particle impaction which is one of the failure modes primarily concerned for TBCs in the state-of-the-art applications. Solid particle erosion can lead to the wear of the coating on turbine blades, vanes, combustors, and other hot section components of aircraft engines. The degradation of the applied coating results in other detrimental effects such as creep, oxidation, and hot corrosion at a temperature even below 1000°C due to local loss of thermal insulation properties [120]. The determination of room temperature erosion behavior of the TBC specimens coated with YSZ is important to gain better understanding about the protection of the TBCs from erosive environments.

In this chapter, the main results of the solid particle erosion tests on the ABS TBC system in as-deposited state and heat-treated conditions are reported. The incremental erosion rates were measured and the effects of impingement angle and impact speed of solid particles on the erosion rates were investigated. Additionally, the influence of isothermal heat treatment on the erosion rate of the APS TBC was also studied. The failure mechanisms of the top coat in as-deposited and heat-treated specimens were analyzed by examining both the coating surface and cross-section of the TBC specimens after the erosion test using SEM.

5.1 Microstructure of TBC Specimen for Solid Particle Erosion Test

SEM micrograph in cross-section of the TBC specimen for solid particle erosion test in as-deposited state is presented in **Figure 5.1**. The thickness and porosity of the top coat were estimated to be about $254 \pm 5.9 \mu\text{m}$ and 17.7 ± 1.7 , respectively.

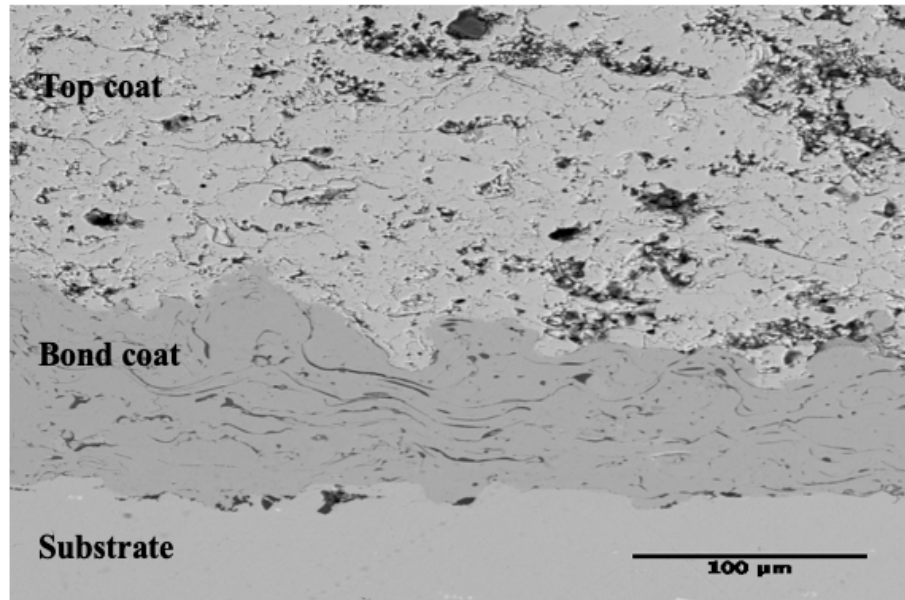


Figure 5.1 SEM micrograph in cross-section of the as-deposited specimen for solid particle erosion test.

Figure 5.2 shows the SEM surface morphology of the top coat in as-deposited state, which exhibits a typical lamellar splats microstructure of APS ceramic coating, in an irregular shape with distinguished boundaries. Inter-splat porosity and a large number of structural defects such as cavities and microcracks are also present in the microstructure, which resulted from the coating fabrication process. The microcracks were beneficial in further reducing the elastic modulus of the ceramic and therefore helped minimize the stresses developed in the coating. However, from an erosion perspective, the presence of microcracks in the top coat makes the coating more susceptible to damage by solid particle

impact. As shown in *Figure 5.2*, various defects such as voids, unmelted particles, cracks, and so on, resulting from the coating deposition process, can be found in the top coat.

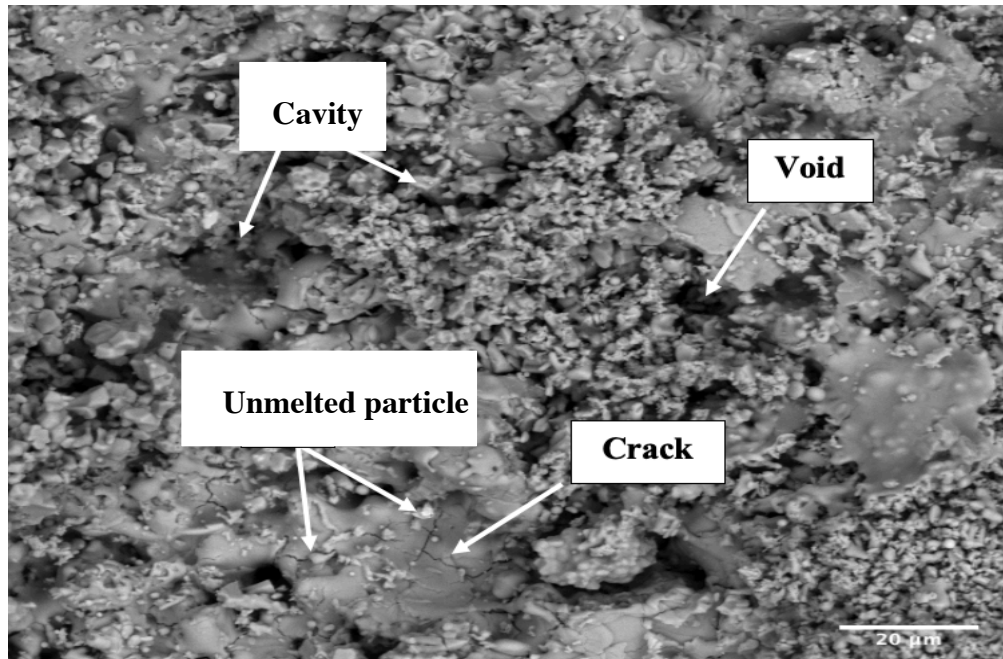


Figure 5.2 SEM surface morphology of the top coat in as-deposited state.

The phase analyses of the top surface in the as-deposited TBC specimen for solid particle erosion test were carried out with XRD. The peaks in the XRD diffraction pattern were identified using JCPDS #48-0224 standard [79]. As shown in *Figure 5.3*, the coating was tetragonal t' phase of partially stabilized zirconia.

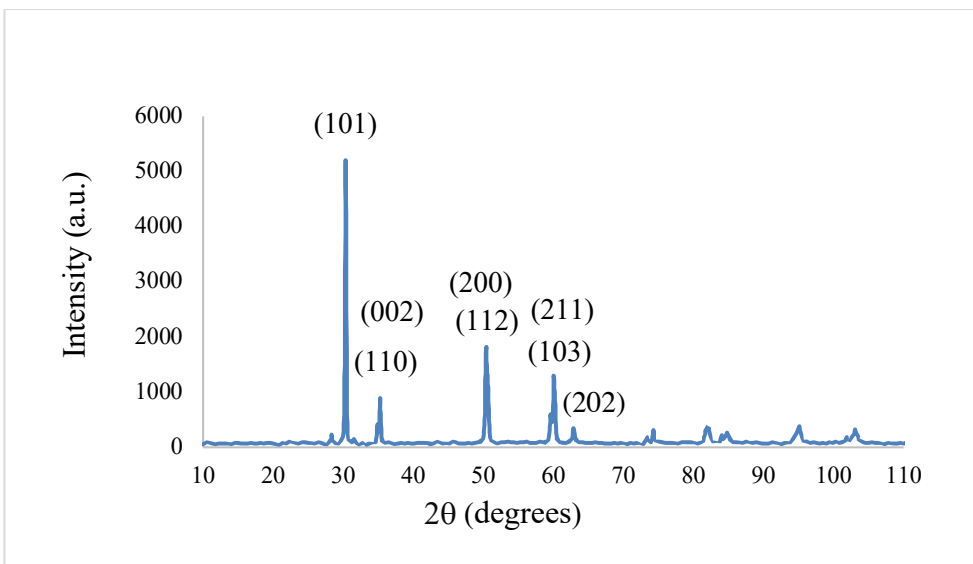


Figure 5.3 XRD diffraction pattern of the top coat in as-deposited condition.

5.2 Erosion Rates

In the erosion tests, the specimens were allowed to erode by the erodent until a steady state erosion rate was attained. The erosion rates then were calculated from a linear regression of ceramic weight loss of the top coat material vs. the mass of erodent consumed. Initial data points include surface contributions such as roughness, and though they are valuable in some cases, they do not represent a steady erosion rate and were not included in this study. As an example, **Figure 5.4** presents a typical erosion curve of the as-deposited TBC specimen under solid particle erosion in room temperature using 50 μm alumina, at a particle impact angle of 30° and particle velocity of 84 m/s. It can be seen that the mass loss of the ceramic material depends linearly on the mass of erodent that had impacted on the top coat surface. The erosion rate was calculated as $0.519 \pm 0.0434 \text{ mg/g}$ representing a relative error of 8.3 %.

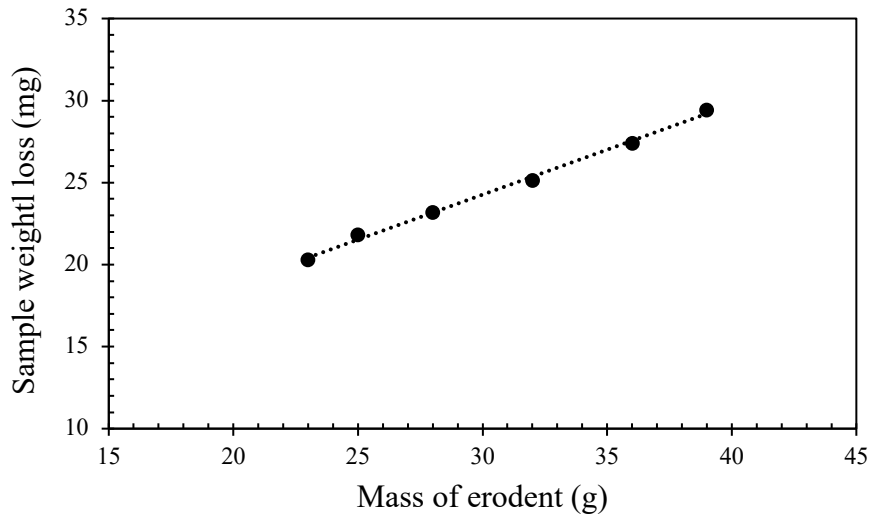


Figure 5.4 Erosion curve of as-deposited TBC specimen under solid particle erosion using 50 μm alumina at 30° impact angle and 84 m/s impact speed in room temperature.

The average erosion rates at different impact velocities and different impingement angles for the APS TBC specimens were determined and reported in **Table 5.1**.

Table 5.1 Average erosion rates (mg/g) of the top coat in as-deposited TBC specimen.

Impingement Angle	Impact Velocity (m/s)	Average Erosion Rate (mg/g)	Standard Deviation
30	84	0.519	0.0434
30	100	0.754	0.0904
30	125	1.0012	0.1002
45	84	0.7814	0.0495
60	84	0.8330	0.115
90	84	1.0203	0.0171

5.2.1 Variation of Erosion Rate with Impingement Angle

Figure 5.5 presents a bar chart of the erosion rates measured in mg/g for the TBC specimen tested in room temperature at impingement angles ranging between 30° and 90° with the particle impact velocity of 84 m/s. The erosion rate was found to increase with increasing particle impingement angles from 30° to 90°. As well known, for ceramics under solid particle erosion the material is removed by fracturing, and the extent of cracking associated with single impact increases with the depth of penetration of the erodent particle, which can be achieved in maximum at 90° impact angle [121]. This in turn means highest effectiveness of the energy transfer of the incident [79]. The erosion rate results obtained are in agreement with the common response of plasma-sprayed TBC coatings impacted by solid particles [122].

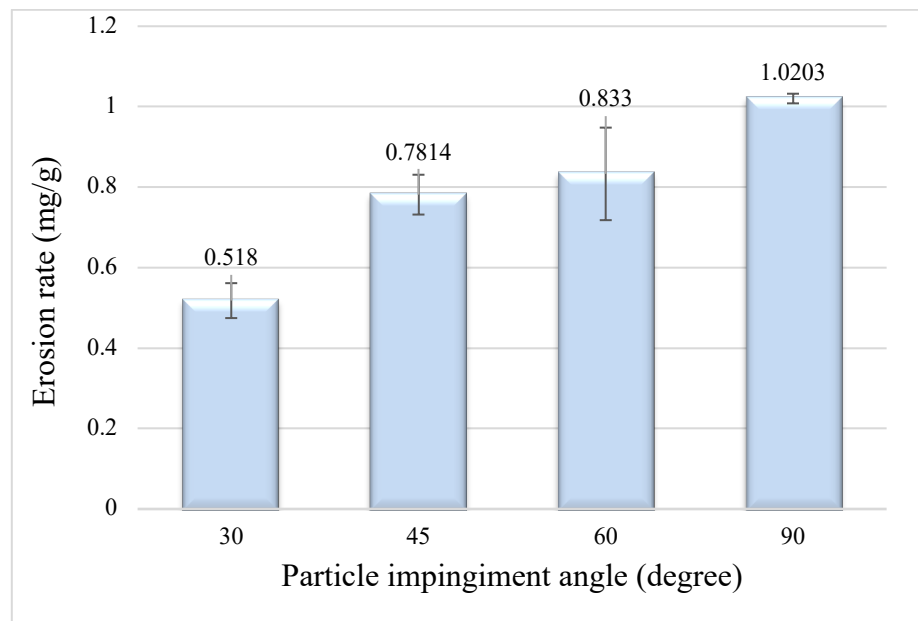


Figure 5.5 Erosion rates of as-deposited TBC specimen tested with particle impact velocity 84 m/s at different particle impingement angles.

5.2.2 Variation of Erosion Rate with Particle Impact Velocity

The experimental results presented in *Figure 5.6* demonstrate the influence of particle impact velocity on the erosion rate of the as-deposited TBC specimen tested at the particle impingement angle of 30° with different impact velocities. The results indicate a general increase in erosion rate with particle velocity.

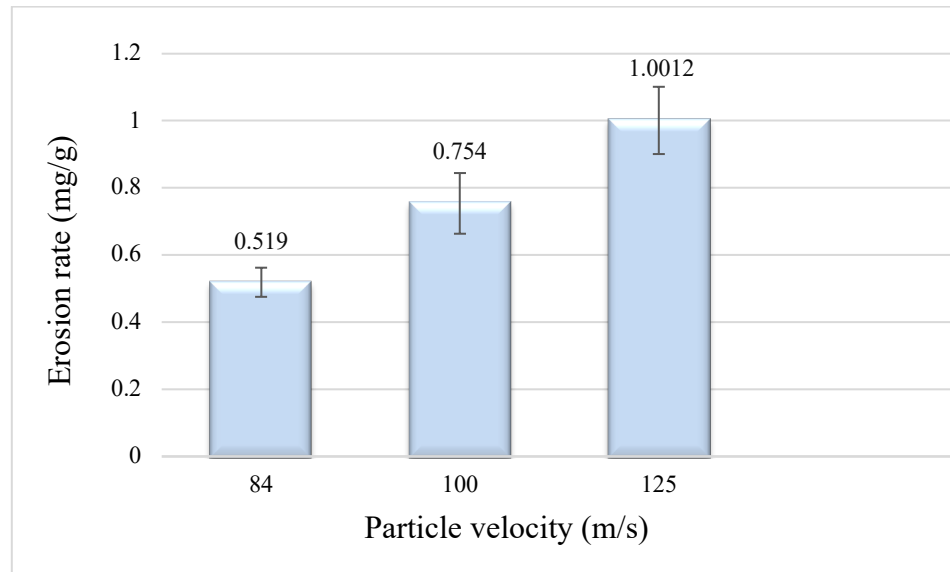


Figure 5.6 Erosion rates of as-deposited TBC specimen tested at particle impingement angle 30° with different particle impact velocities.

A number of studies indicated that the erosion rate can be expressed as a power function of particle velocity [123]. The experimentally measured data of erosion rate E_r are plotted in variation with particle velocity V , as shown in *Figure 5.7*, which can be expressed by the following empirical correlation,

$$E_r = aV^{n_v} \quad (5.1)$$

where n_v is velocity exponent and for brittle materials such as YSZ TBC it takes between 1 and 3 [123], [152]. The value of velocity exponent n_v was measured to be 1.63 and the coefficient a was 0.0004.

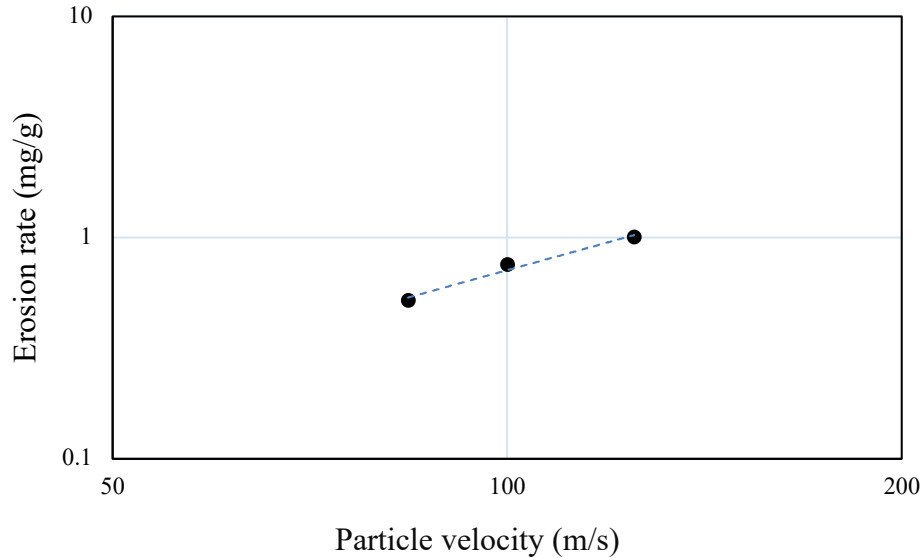


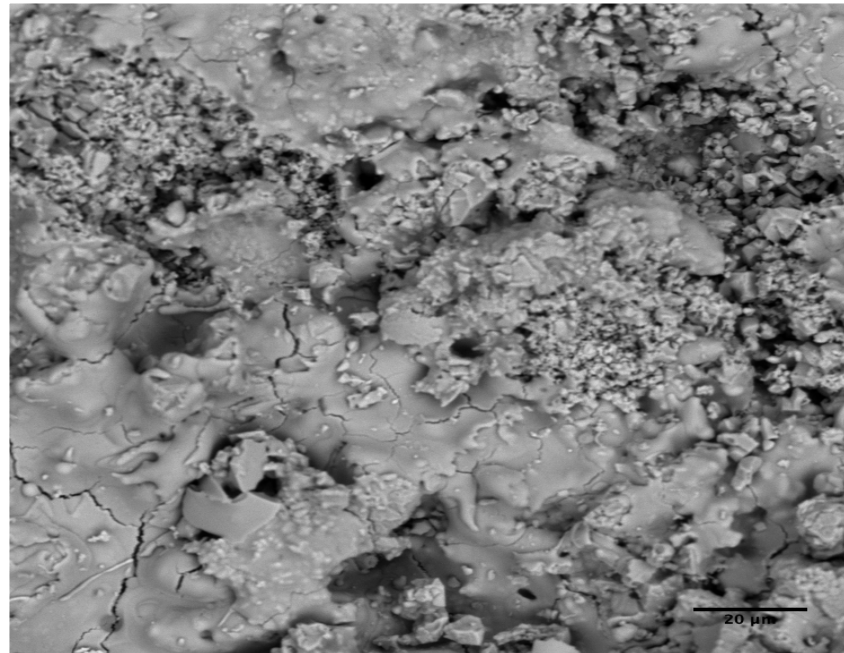
Figure 5.7 Log – log plot of erosion rate against particle impact velocity for as-deposited TBC specimen tested at particle impingement angle 30°.

5.3 Influence of Thermal Aging on Erosion Rate

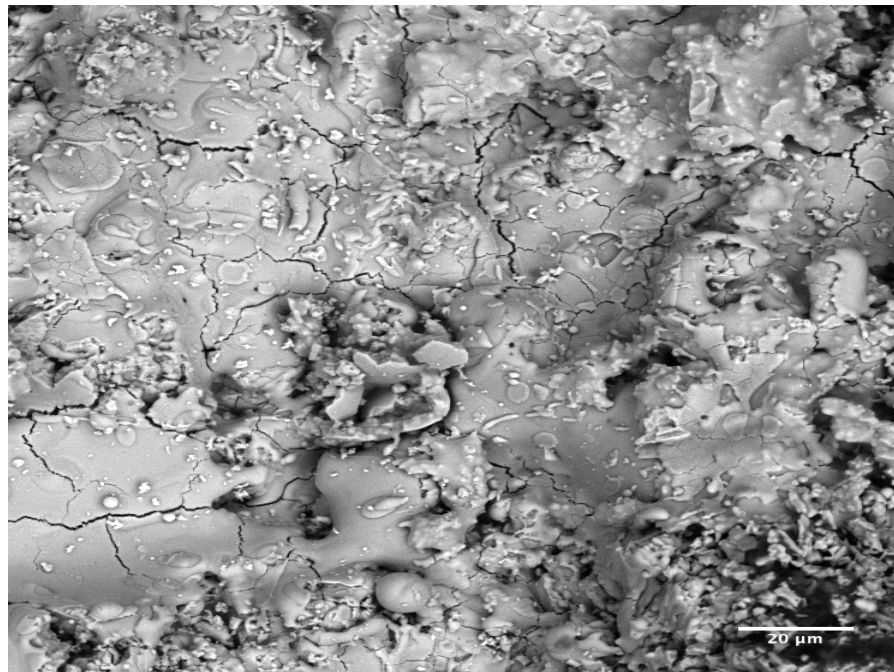
In order to study the influence of thermal aging on the erosion resistance of the TBC, the as-deposited TBC specimens were isothermally heat-treated at 1000°C and 1150°C for 24 h and 72 h. The heat-treated specimens were then erosion-tested using alumina particles with an average size of 50 µm. The particle incidence angle was 30° and the particle velocity was set to 100 m/s.

5.3.1 Surface Morphology of Heat-Treated Specimens

The SEM micrograph in *Figure 5.8 a* and *b* shows the surface morphologies of the coating aged for 72 h at 1000°C and 1150°C, respectively. The top coat that was thermally aged for 72 h at different temperatures showed almost the same microstructure. Both surfaces still exhibited the conventional lamellar structure but more homogenous with larger splats size than that of as-deposited APS TBC specimen (*Figure 5.2*).



(a)

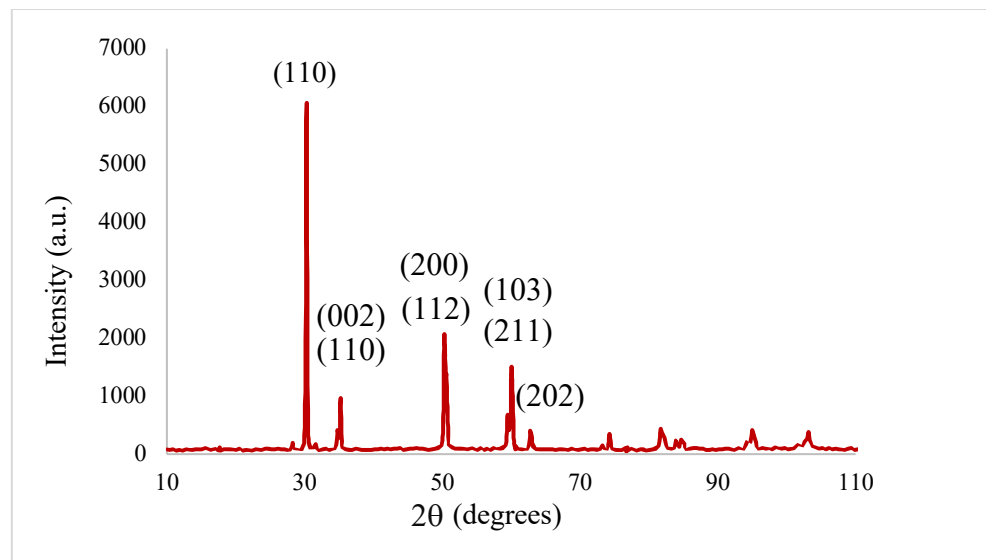


(b)

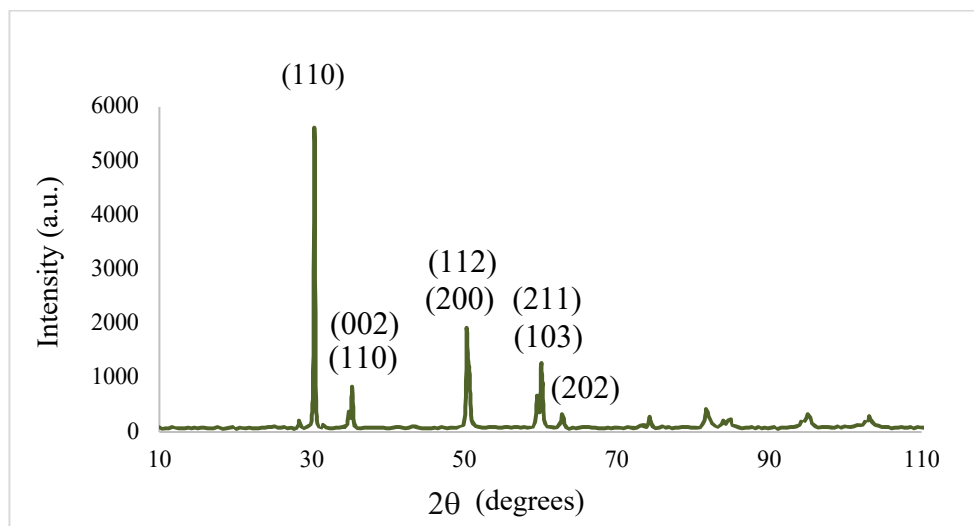
Figure 5.8 SEM surface morphology of the top coat thermally aged for 72 h at (a) 1000°C and (b) 1150°C.

5.3.2 Phase Transformation in Top Coat

To examine if any phase transformations had occurred in the ceramic top coat during the heat treatments, XRD analysis was performed on the as-deposited TBC specimen and heat-treated TBC specimens. As demonstrated by the XRD diffraction patterns in **Figure 5.9**, there was no obvious phase change in the crystallographic nature of the YSZ coat during the thermal aging, compared to the XRD diffraction pattern in **Figure 5.3**. As a result, it can be concluded that phase transformation had no contribution to the top coat degradation.



(a)



(b)

Figure 5.9 XRD pattern of the ceramic top coat in the TBC specimen aged for 72 h at (a) 1000°C and (b) 1150°C

5.3.3 Erosion Rates of Heat-Treated TBC Specimens

The average erosion rates of the top coats in the TBC specimens aged at different temperatures for different durations are given in *Table 5.2*.

Table 5.2 Average erosion rates (mg/g) of the top coats in heat-treated TBC specimens.

Aging Temperature (C°)	Aging Time (h)	Erosion Rate (mg/g)	Standard Deviation
1000	24	0.5265	0.017
1000	72	0.515	0.0078
1150	24	0.4803	0.091
1150	72	0.378	0.032

Figure 5.10 illustrates the effect of thermal treatment on the erosion rate of the TBC specimen. The results indicate a general decrease in the erosion rate with increasing aging temperature and time.

Figure 5.11 illustrates the improvement of the APS ceramic coating, achieved by the thermal treatment. The erosion resistance of the coating after heat-treated at 1000°C for 24 and 72 h was improved by 30% and 36%, respectively. After thermal aging up to 1150°C for 72 h, the improvement increased to 50%. The relative erosion resistance is determined by calculating the decrease in the erosion rate of the specimen as a result of the aging relative to the erosion rate of the as-deposited specimen. The effect of aging temperature

on the improvement of the erosion resistance was more pronounced at aging temperature of 1150°C.

The increase in the erosion resistance of the heat-treated top coat can be attributed to the fact that the heat treatment affected the microstructure of the APS top coat. A typical microstructure of APS coating includes interlamellar pores, voids, and inter splats microcracks that are partially responsible for their low thermal conductivity and low Young's modulus [4]. Under service conditions, however, TBCs are exposed to high temperature condition for an extended time which might affect these properties due to sintering effect. At high temperatures the sintering of the ceramic material of the top coat can cause significant reduction of porosity owing to grain growth, thus enhanced inter-splat bonding which in turn led to the strengthening of the coating structure due to the increase in Yong's modulus, ultimately improved the coating toughness [124] and erosion resistance. The increase in erosion resistance for APS TBCs via heat treatment was also reported by other researchers [107], [125].

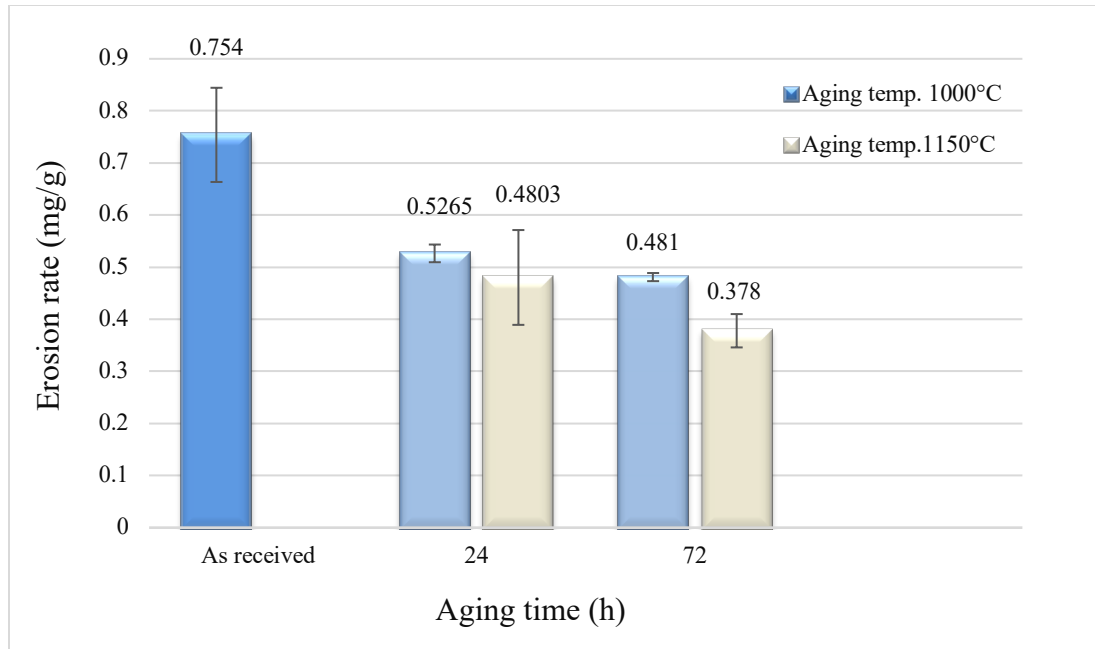


Figure 5.10 Comparison in erosion rate of the TBC specimens aged at different temperatures for different times.

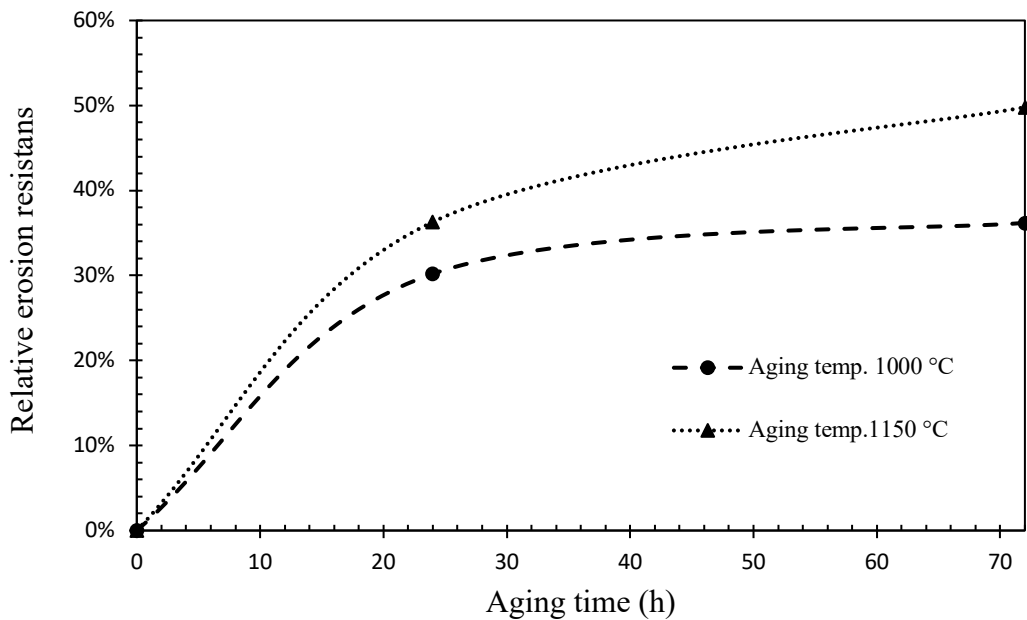


Figure 5.11 Relative erosion resistance of heat-treated TBC specimens. The relative erosion resistance of as-deposited specimen was set to 0 %.

5.3.3.1 Effect of Coating Porosity on Erosion Rate

The porosity of the aged TBC specimens was measured using SEM and Image J software to investigate whether it can be related to the decrease in the erosion rate or not. The measuring results on the TBC specimens heat-treated at different temperatures for different periods showed that the porosity in the top coat decreased to $12.49 \pm 1.328\%$ for coating aged 72 h at 1000°C and $10.767 \pm 0.861\%$ for the coating aged 72 h at 1150°C compared to the porosity in the top coat of the as-deposited TBC specimen. Therefore, the improvement in the erosion resistance of the top coat after the thermal aging strongly depends on the porosity present in the coating. As revealed by McPherson [124], the heat treatment on the ceramic top coat of a TBC system caused the pores to sinter and change their elongated shape into sphere. As a result, the real contact area of the ceramic particles of the top coat increased, which resulted in the change of the mechanical properties of the top coat such as an increase in the elastic modulus [124]. The presence of pores while offering advantages of lowing the thermal conductivity of TBCs [4], can deteriorate the erosion resistance of TBCs due to the reduction of the material strength against plastic deformation or chipping by solid particle impacts [72]. Additionally, the pores in the top coat can serve as stress concentrators and hence reduce the load bearing of the coating surface [121]. The obtained porosity results demonstrated that the porosity present in the top coat was a very important feature influencing the erosion rate and must be considered in the erosion studies of TBCs since they could have a serious impact on the life of TBCs.

5.3.3.2 Effect of Coating Hardness on Erosion Rate

Vickers microhardness test was carried out on the top coat in cross-section of the TBC specimens in as-deposited state and in heat-treated condition, in order to examine if the

coating hardness could affect its erosion resistance. The average hardness values from five tests for each specimen are reported in *Figure 5.12*. It was found that the microhardness of the top coat in the heat-treated TBC specimens increased with increasing aging temperature. This can be attributed to the reduction in porosity of the top coat due to the heat treatments.

The relationship between the erosion rate and hardness for the top coat is illustrated in *Figure 5.13*. It can be seen that the erosion rate decreases with increasing the hardness.

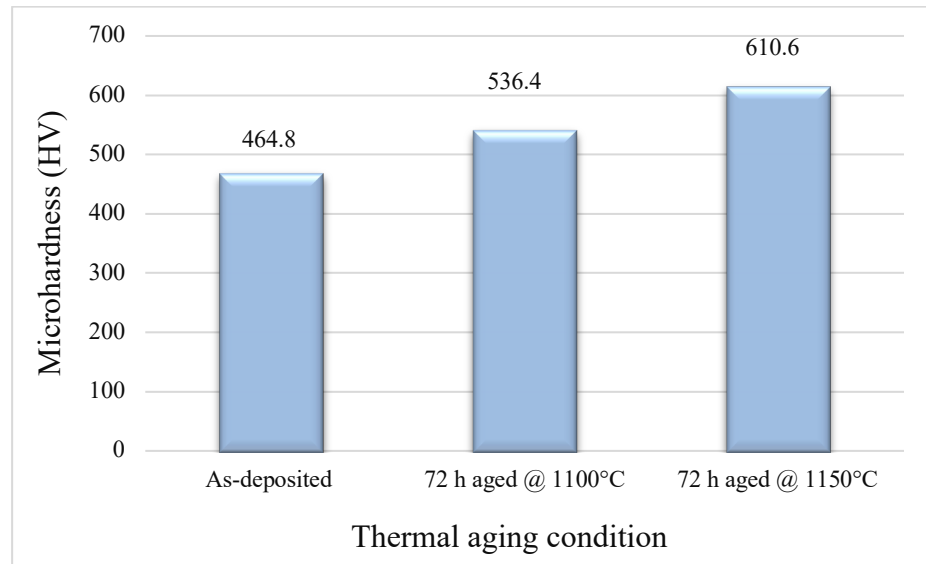


Figure 5.12 Microhardness of the top coat in the TBC specimens.

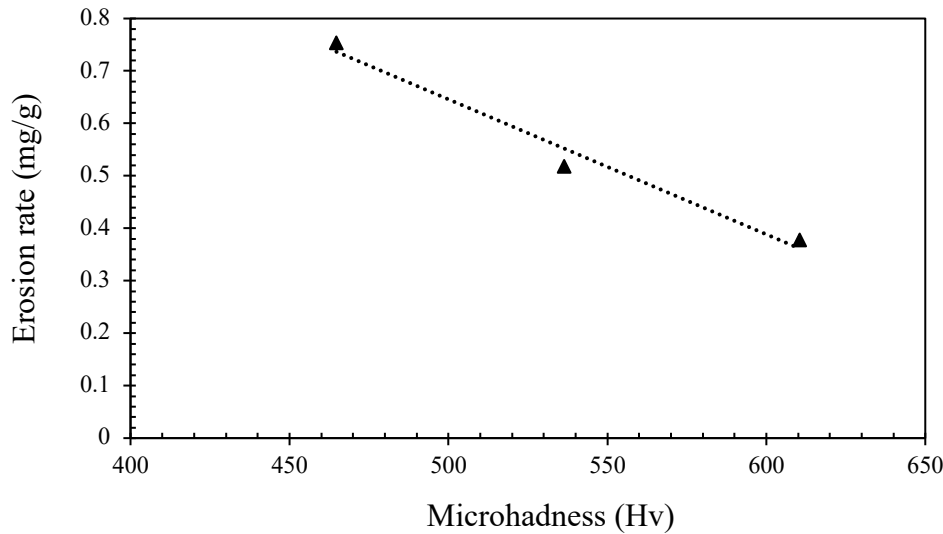


Figure 5.13 Erosion rate versus hardness of the APS top coat in the TBC specimens.

5.4 Erosion Mechanisms of TBCs

5.4.1 Surface Analysis of Eroded TBC Specimens

The mechanism by which material is removed from a coating under erosive conditions may be either ductile or brittle damage. The ductile erosion is distinguished by cutting and deformation mechanism, whereas brittle erosion occurs by cracking and chipping mechanism of the material due to particle impact [126].

To gain more information on the solid particle erosion of the APS TBC system, surface microstructural analysis was performed on the eroded specimens in conjunction with the erosion tests. The eroded surfaces of the as-deposited and heat-treated TBC specimens were examined using SEM. The influence of particle impingement angles on the erosion mechanisms and damages such as scratch and removal of the top coat material can be

deduced from the SEM analyses. The SEM morphologies of the eroded surfaces of the TBC specimens tested at 30°, 45°, 60°, and 90° particle impingement angle with 84 m/s particle impact velocity are presented in **Figure 5.14**. As shown in **Figure 5.14 a**, most of the splats in the top coat seemed possibly damaged. The scars on the coated surfaces were caused by the impacts of the sharp-edged alumina particles. From the erosion test results, the erosion rate was the least at 30° particle impingement angle and the most at 90° particle impingement angle (**Table 5.1**), which indicated that the top coat exhibited erosion in a brittle manner, as most of ceramics-based coatings did [126]. At 45° impingement particle angle, the erosion damage became severe, characterized by the deeper and wider craters that were formed because of particle impacts (**Figure 5.14 b**). Moreover, in addition to the damage created by each impact, the cracks that propagated around and through the splats were pronounced, leaving the coating controlled by fracture. Further increase in particle impingement angle to 60° and 90°, the surfaces appeared more severely damaged and featured by deep and large cracks formed, as shown in **Figure 5.14 c** and **d**. From the solid mechanics point of view, with particle impingement angle increased, the normal component of the impact force to the target surface increased, at the extreme angle of 90°, the total impact force was normal to the target surface thus provided higher breaking force on the brittle ceramic coating, resulting in serious cracking of the coating surface.

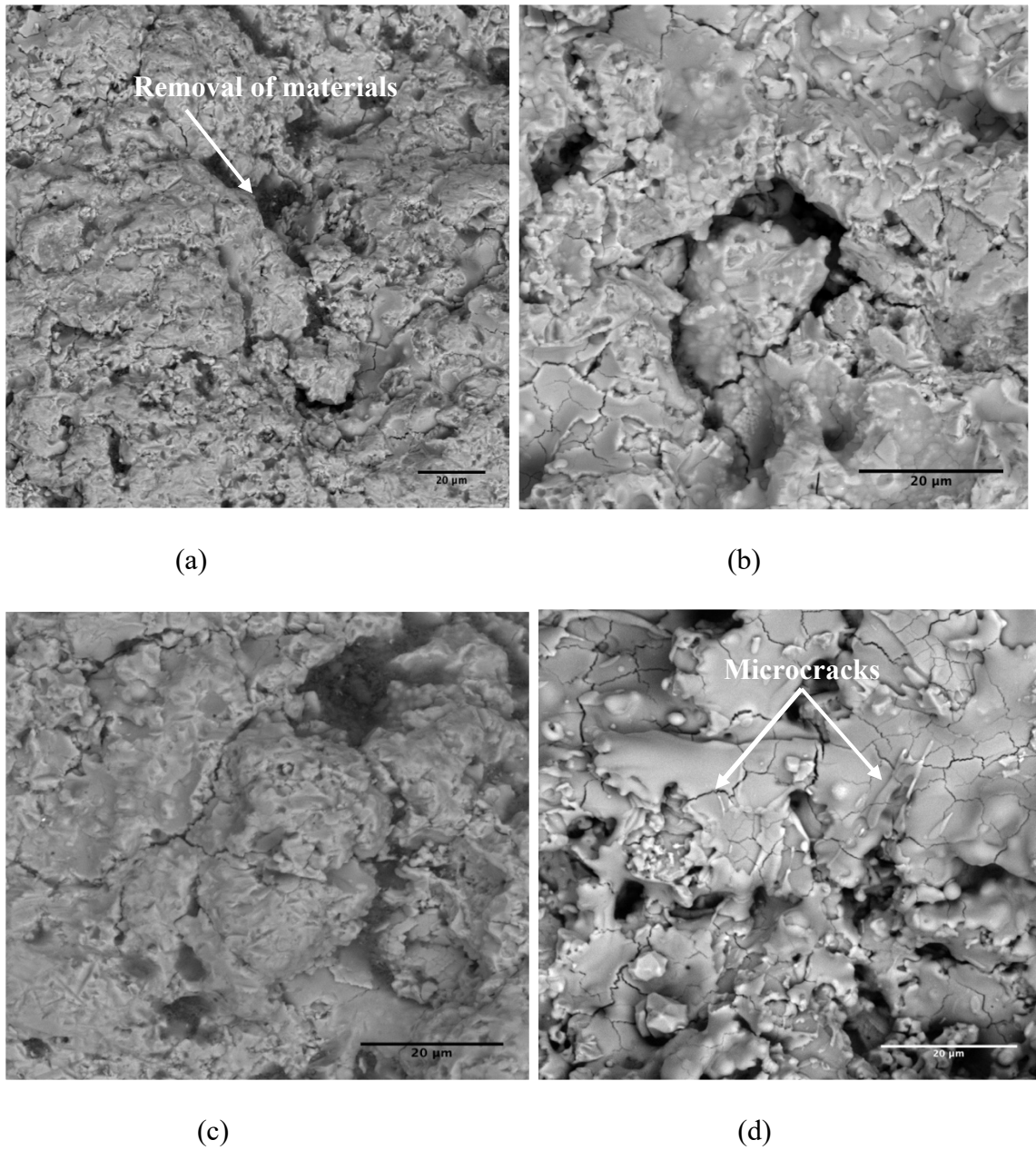


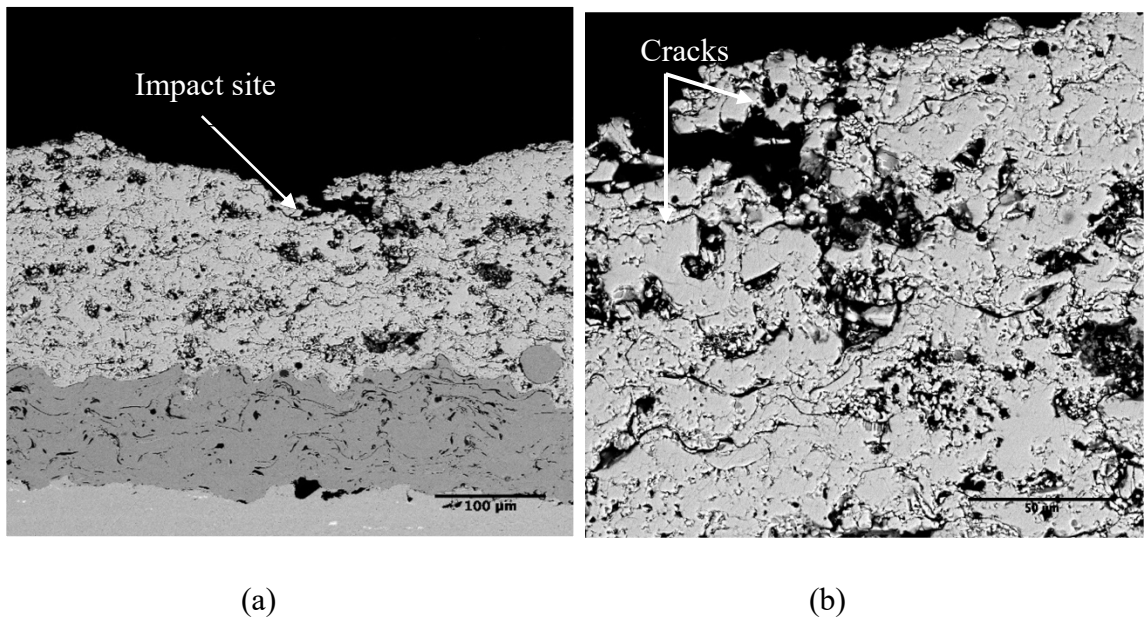
Figure 5.14 SEM eroded surface morphology of the top coat under solid particle erosion at impact angle of (a) 30°, (b) 45°, (c) 60°, and (d) 90°.

It also should be pointed out that even though the erosion rate increased with increasing particle impact angle, it is apparent that there was no remarkable difference in the surface morphology of the top coat eroded at 30°, 45°, and 60° particle impact angle. This in turn,

means that the erosion occurred at different particle impact angles by the same mechanisms that could relate to the material removal through crack propagation along the splats boundaries.

5.4.2 Cross-Sectional Analysis

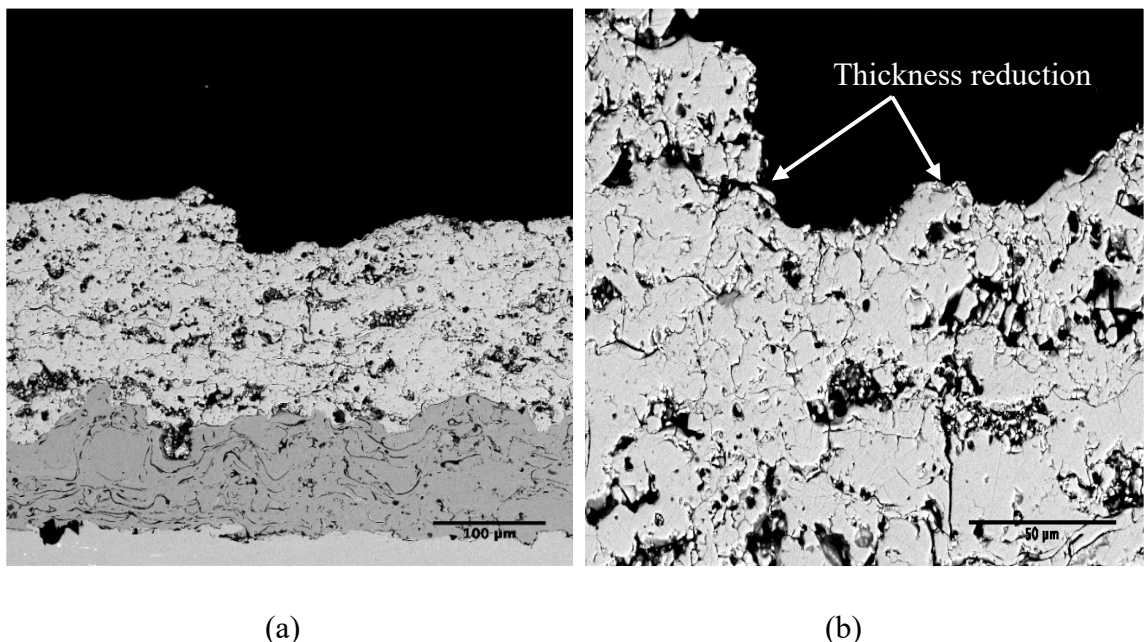
Figures 5.15 to 5.18 present the microscopic images of the cross-sections of the as-deposited TBC specimens eroded at four different impingement angles. It is evident that at all the impact angles the top coat was severely cracked and fractured by the attack of the solid particles. Additionally, as the impact angle was enlarged, the crater depth generated by the particle impact increased, thus resulting in thickness reduction of the topcoat layer. The thickness of the top coat reduced to 78 μm when impacted at 30° and to 63.57 μm at the impact angle of 90° . Moreover, at 90° particle impact, i.e., when the solid particles impinged normally on the top coat surface, many large, deep, connected cracks were generated in the top coat (*Figures 5.18 b*) due to larger impact force. However, it was interesting to note that although serious cracking and fracturing occurred in the top coat during the solid particle erosion process, no obvious damage was found in the bond coat and the interface with the top coat under all the test conditions. This implied that the failure of the TBC under solid particle erosion would be a result of top coat removal by the cutting and smashing of the solid particles layer by layer, rather than the debonding of the top coat, which differed from the failure mechanism of the TBC under isothermal oxidation. Since the thickness reduction of the top coat strongly depended on particle impingement angle, the erosion behavior of the TBC was governed by particle impact condition. Certainly, at the same particle impingement angle, higher particle impact velocity would expedite the removal of the top coat, leading to shorter service life of the TBC.



(a)

(b)

Figure 5.15 Cross-section microscopic images of as-deposited TBC specimen eroded at particle impact angle 30°: (a) at low magnification and (b) at high magnification.



(a)

(b)

Figure 5.16 Cross-section microscopic images of as-deposited TBC specimen eroded at particle impact angle 45°: (a) at low magnification and (b) at high magnification.

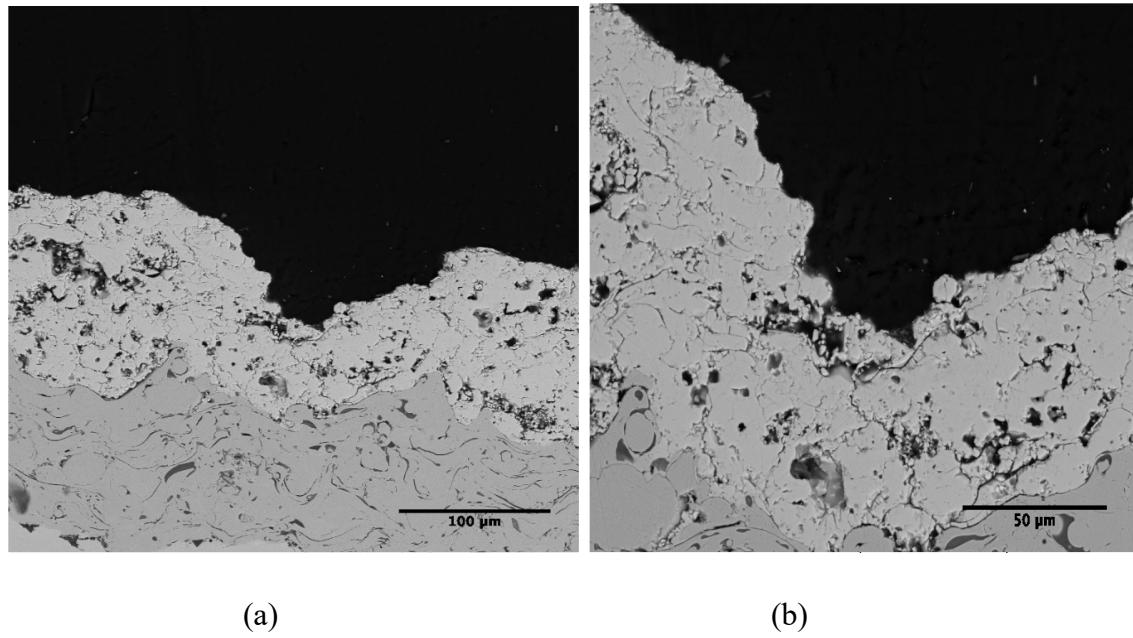


Figure 5.17 Cross-section microscopic images of as-deposited TBC specimen eroded at particle impact angle 60°: (a) at low magnification and (b) at high magnification.

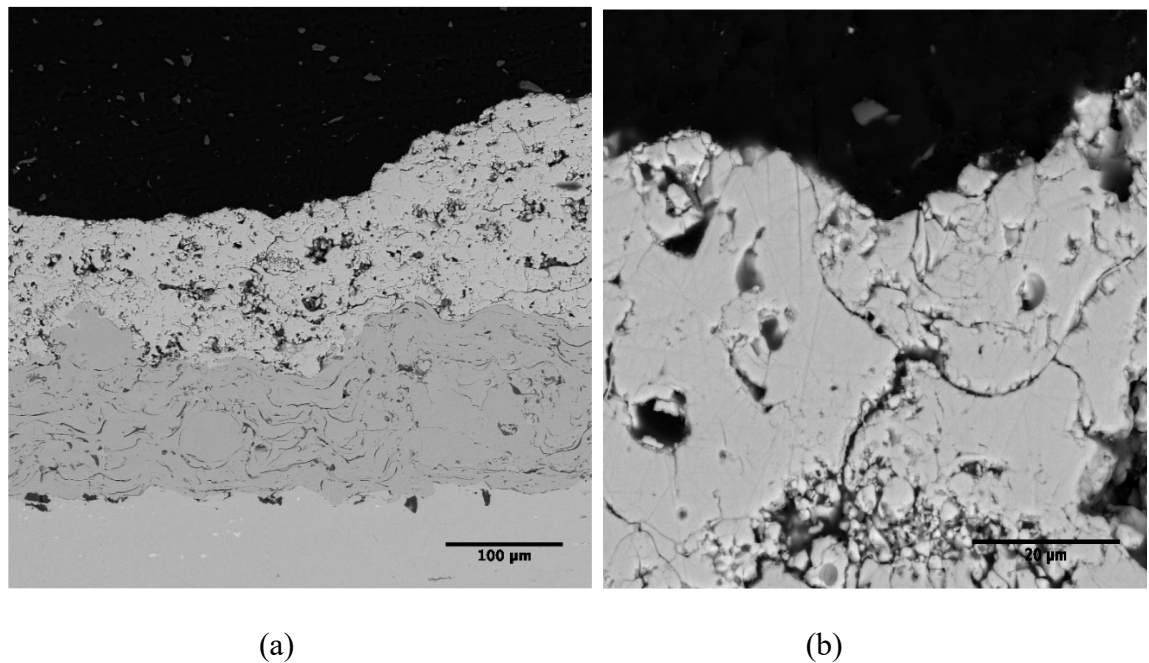


Figure 5.18 Cross-section microscopic images of as-deposited TBC specimen eroded at particle impact angle 90°: (a) at low magnification and (b) at high magnification.

These SEM images confirm that for all the APS ceramic top coats eroded by solid particles at different impact angles the damage mechanism appeared the same and was related to single or multiple splat removal through crack propagation along the boundaries of single splat or cluster of splats. Although these cracks can provide a degree of strain tolerance, they made a larger contribution to the erosion damage of the top coat because they served as stress concentrators and can easily “link-up” to create large cracks or connect splat boundaries, resulting in increased erosion. The fragmentation of the splat tops and the microcrack network within the YSZ close to the area of particle impact were observed in the top coat (*Figure 5.15* to *Figure 5.18*). The propagation of microcracks caused the debonding at the splat boundaries and consequently successive removal of the splats.

Eaton and Novak [75] conducted detailed studies of particulate erosion on plasma sprayed ceramics and other different materials. For porous ceramics, they characterized three different erosion mechanisms. The first mechanism was associated with the presence of primary impact scars (low erosion rate). The second mechanism was associated with fracture, caused by erodent particles, in the region of the target surface around the impact site (moderate erosion rate). The third mechanism was related to the formation of tunnels on the top coat surface (high erosion rate). In the present work, moderate levels of erosion probably best apply to the APS TBC specimens under solid particle erosion test.

Figures 5.19 and **Figure 5.20** show the microscopic cross-sectional images of the eroded TBC specimens at particle impingement angle 30° and particle impact velocity 100 m/s, which were previously heat-treated for 72 h at 1000°C and 1150°C. It appeared that while the heat treatment reduced the erosion rates, the solid particle erosion mechanism and

behavior remained unchanged for the APS top coat. This can be seen in the SEM images, which show that the erosion of the top coat occurred due to the removal of the coating material by chipping and cracking, as a result of the particle impacts but the bond coat and the coating interface seemed undamaged by the erosion attack. Comparing the heat treatment at the two different temperatures, the higher temperature (1150°C) definitely favored the erosion resistance of the top coat, as seen in the high magnification images (**Figures 5.19 b** and **Figures 5.20 b**). The cracks and fracture in the top coat aged at 1150°C are apparently smaller and less than that in the top coat aged at 1000°C . This difference can be attributed to the microstructural improvement of the top coat with larger reduction of porosity after the heat treatment at higher temperature.

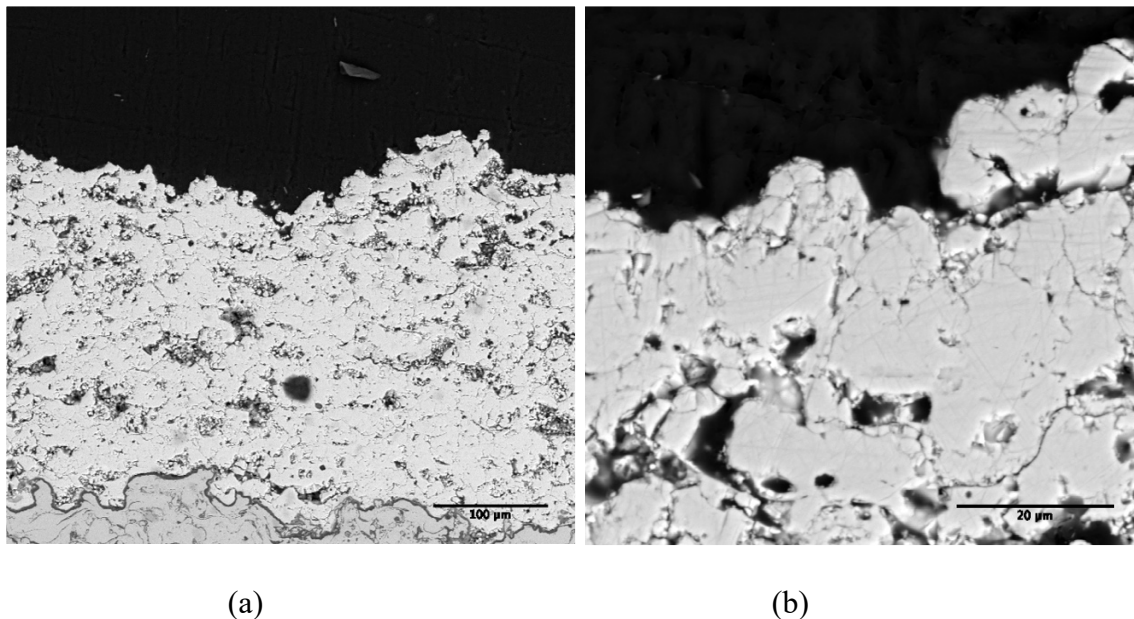


Figure 5.19 Cross-section microscopic images of eroded TBC specimen at impingement angle 30° and particle velocity 100 m/s : (a) at low magnification, (b) at high magnification. The specimen was previously heat-treated for 72 h at 1000°C .

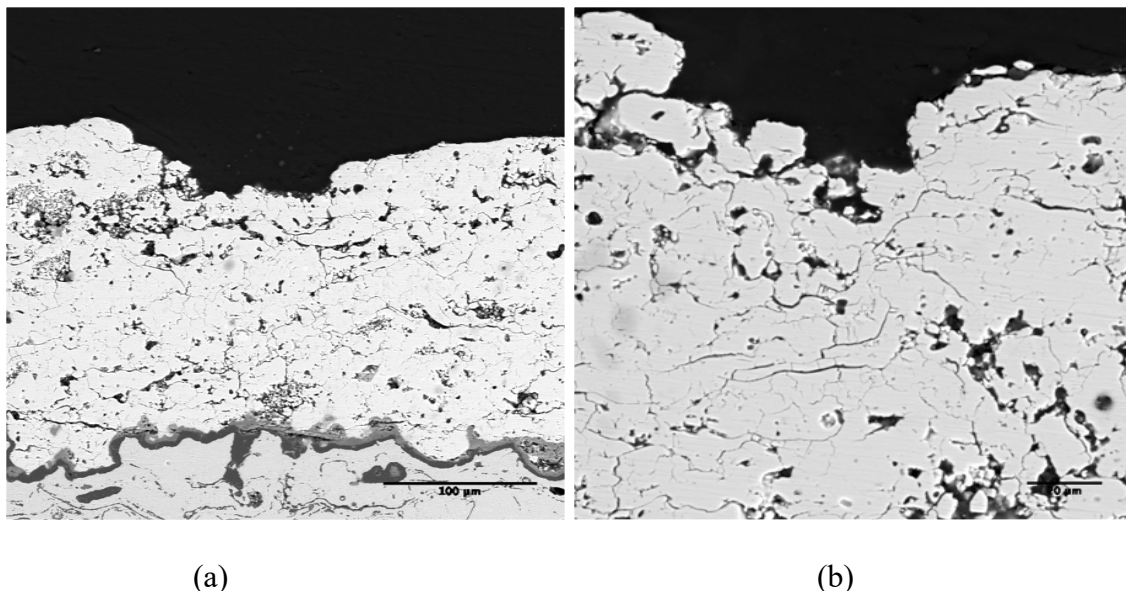


Figure 5.20 Cross-section microscopic images of eroded TBC specimen at impingement angle 30° and particle velocity 100 m/s: (a) at low magnification, (b) at high magnification. The specimen was previously heat-treated for 72 h at 1150°C .

5.5 Concluding Remarks

The solid particle erosion behavior of the TBC system consisting of CoNiCrAlY bond and YSZ top coat produced via APS process was investigated under the erosion test at varying particle impingement angles of 30° , 45° , 60° , and 90° and with different particle impact velocities from 84 m/s, 100 m/s to 125 m/s in room temperature environment. Both as-deposited TBC specimen and the TBC specimens heat-treated at 1000°C and 1150°C for 24 h and 72 h were investigated under solid particle erosion test. The erodent material was alumina particles with an average size of 50 μm .

The experimental results showed that the erosion rate of the top coat increased with increasing particle impingement angle and particle impact velocity. The maximum erosion rate occurred at 90° impingement angle which corresponded to brittle erosion behavior of

the ceramic top coat. Thermal aging can enhance the erosion resistance of the top coat. This was attributed to the onset of the sintering effect at high temperatures, which minimized the porosity in the microstructure and hence increased the hardness of the top coat. Correlation was found between the coating hardness and structure (porosity) and erosion rate as well. The erosion rate decreased with increasing the hardness and reducing the porosity of the top coat.

The eroded TBC specimens were examined under SEM by focusing on both the top coat surface and the coating cross-section, in order to reveal the erosion mechanism of the TBC. It was shown that although the particle impingement angle predominated the cracking and fracturing of the top coat, the erosion mechanisms of the TBC at different particle impingement angles were the same. The erosion damage was limited to the near surface region of the top coat; the bond coat and the interface with the top coat were not affected noticeably by the erosion attack. The failure of the TBC due to solid particle erosion would be caused by the material removal of the top coat layer by layer, as a result of crack propagation and fracture within the top coat. Accordingly, the erosion of the top coat was controlled by crack propagation along the interface bonding of the splats.

Chapter 6: Interfacial Fracture Toughness Model for TBC Systems

The contents of this chapter have been published in the journal *Surface and Coatings Technology* in 2019 [153].

6.1 Investigation of TBC Failure

6.1.1 Failure Mechanism of TBCs

The failure mechanisms of TBCs in high temperature service are overly complex. At the initial stage, i.e., in the as-deposited state, TBCs can be well-bonded to the substrate. However, as the coating system is exposed to operating temperatures, its adherence degrades. Poor adhesion can lead to developing debonding or spallation of the coating, which is driven by residual thermal compressive stresses. Many studies have been conducted to understand the failure mechanisms of TBC systems in order to improve their durability, but they are still not completely understood because of the complexity of TBCs which comes from the multilayer structure, highly coupled failure mechanisms.

Recently, the interfacial fracture toughness of TBCs has received substantial attention as one of the most design parameters that assess the thermal barrier reliability and durability, as discussed in the preceding chapters. Since the crack initiation and growth in TBCs occur in severe conditions such as cyclic thermos-mechanical stresses due to hot gas flow or mechanical loading, it is crucial to quantify the influence of temperature exposure on the TBC interface strength to have a better understanding of the failure mechanisms of TBCs. However, due to the limitation of the existing techniques, the high temperature interfacial fracture toughness of TBCs has been rarely studied. Therefore, the present work was aimed at developing a temperature-dependent fracture toughness model for TBCs.

6.1.2 Fracture Toughness Assessment of TBCs

Fracture toughness approach which accounts for interior coating defects is recommended as a conservative measurement for the debonding characteristics of TBCs [85]. There are several methods that have been devised to evaluate the fracture toughness of TBCs, including experimental, analytical, numerical approaches. Since the data of TBC fracture toughness from different experiments are usually inconsistent due to the different loading modes used in the experiments [87]. For instance, The Vickers indentation fracture test exhibits mode I loading normal to the interface [127]. Four-point bending interfacial fracture test is based on mode II shear loading along the interface [128], [129]. However, actual TBC delamination has mixed-mode nature at the interface [130]. For more accurate evaluation of the fracture toughness of TBCs, an interfacial fracture test method for measuring the interfacial fracture toughness of TBCs in the mixed loading over a range of mode mixity was developed [94], [95]. Meanwhile, considering the actual service environment of TBCs, interfacial fracture toughness tests of TBCs were also conducted at high temperatures [84], [98].

In addition to experimental methods, analysis and numerical approaches have also been applied to the studies of the fracture toughness of TBCs. Although numerical methods such as finite element analysis (FEA) have many advantages in analyzing the stresses and strains in TBCs [131], [132], [133], [134], they cannot accurately include the influence of material defects, for example, crack and pores, in the computation of the fracture toughness. Therefore, the more popular approach to determining the fracture toughness of TBCs is the combination of analytical modeling with the experimental investigation [135], [136]. However, among the models reported in literature, none of them has capacity in predicting

the interfacial fracture toughness of TBCs showing temperature and exposure time dependence as well as mode mixity of loading characteristic.

To this end, the present research was aimed to develop a temperature-dependent interfacial fracture toughness model for TBCs that utilized the Arrhenius equation and microcrack formation theory. In characterizing the crack initiation and propagation in TBCs, the concepts of microcrack formation in a coating caused by the dislocation movement of atoms in the deformation zone were employed. The model proposed in the present research was developed based on a temperature-dependent fracture toughness model for the brittle coating/ductile substrate system [137]. In their model, vertical through thickness cracks across the coating layer were considered. The interface in the present proposed model refers to the interface between the ceramic top coat and the metal bond coat. It is assumed that cracks stay within the interface or near the interface such that the fracture resistance can be characterized by fracture mechanics.

6.2 Theory of the Proposed Model

6.2.1 Critical Energy Release Rate

When an interfacial crack is propagating along the interface of a TBC, the fracture toughness can be described by the critical energy release rate G_c or the critical stress intensity factor K_c if the small-scale yield (SSY) condition ahead of the crack tip can be satisfied [94]. One of the most important characteristics of the interface crack is the mixed mode nature of the near-tip singularity field. Even under far-field tension, the shear loading due to the mismatch in elastic properties will exist in the region of the crack tip [84]. Interfacial mode mixity is defined as the relative proportions of shear to normal tractions ahead of the crack tip. Therefore, it is more descriptive and convenient to use the energy

concept, termed as critical energy release rate G_c , instead of critical stress intensity factor of either Mode I or Mode II to quantify the fracture toughness of TBCs [84]. The nature of the stress field for an interfacial crack between two different isotropic linear elastic media has been discussed in Chapter 2. The energy release rate G_e for a unit area of an interface to decohere is given by Eq (2.12). The critical condition for an interface crack to propagate is therefore given by the fracture criterion $G_e = G_c(\psi)$, where $G_c(\psi)$ is the fracture toughness of the interface, representing the maximum loading amplitude that the interface can withstand without fracture [93], [138].

6.2.2 Formulation of Proposed Model

The coating system considered in this work represents a typical ceramic-metal system and the entire materials of the TBC system are considered isotropic and linearly elastic. The bond coat and substrate are usually made of metal-based materials and can deform plastically before failure. Most solid materials develop plastic strains when the yield strength is exceeded in the region at the crack tip. In fact, inelastic deformation such as plasticity in metals leads to relaxation of the crack tip stress caused by the yielding phenomenon at the crack tip. This yielding will cause the local stress field to deviate from the singular stress form given by Eq (2.5) [88], [139]. However, when SSY exists, i.e., the plastic zone is much less than the characteristic dimension of the crack and the stresses within the plastic zone can be determined by the linear elastic solution [93], [139] as discussed in Chapter 2. The plastic zone size r_p is defined as the distance from the crack tip to the elastic boundary [140]. The fracture toughness of the interface between two dissimilar materials strongly depends on the mode of loading, and the increase in mode mixity may contribute to the increase in plastic work dissipation in the TBC layers [95].

This suggests that the plasticity or SSY plays an important role in the interfacial fracture toughness evaluation under the mixed mode loading conduction. The solutions for interface cracks in the presence of finite deformation are bounded by the length scale (plastic zone size) r_p , and crack tip opening displacement (CTOD) $\delta CTOD$. The solution for the plastic zone size is given as [140]

$$r_p = \frac{1}{3\pi} \left(\frac{|K|}{\sigma_y} \right)^2 \quad (6.1)$$

where σ_y is the yield stress of the weaker material. The CTOD is given by [141]

$$\delta_{CTOD} = \frac{4\sqrt{2}}{\pi\sqrt{1+4\varepsilon^2}} \frac{J}{\sigma_y} \quad (6.2)$$

For linear elastic behavior, J -integral is identical to strain energy release rate G_e , and both are related to the stress intensity factor K as follows:

$$J = G_e = \frac{K^2}{E} \text{ for plane stress, and } = \frac{K^2}{E}(1 - \nu^2) \text{ for plane strain [142].}$$

Under the hypothesis of SSY, a plastic zone (limited plasticity at the crack tip), containing microstructure defects such as dislocations and voids, are formed. The effect of dislocation shielding on the interface crack initiation and growth in metal/ceramic layered structures was studied by Mao et al. [143]. In their study, an analytical solution was derived to investigate the role of mixed mode loading in terms of dislocation shielding. They assumed that the interface crack tip would be blunted due to the dislocation emission from the crack tip. The interface separation would occur when normal and shear stresses ahead of the

blunted crack tip exceeded the strength of the interfacial atomic bond. Once rupture occurred, crack propagation continued by the repeated process. In this case, an atomically sharp tip propagated until the interactions with other slip sources allowed arrest by a new blunting event [143].

For a crack tip under SSY condition, J_c integral at fracture is given by [144]

$$J_c = J_s + J_D \quad (6.3)$$

where J_s is elastic work which equals to $2\gamma_s$ and γ_s is surface energy, and J_D is the plastic dissipation energy per unit area of crack extension.

Chan [144] in his work suggested that the fracture toughness was controlled by dislocation mobility and incorporated the temperature effect into the fracture toughness of the materials based on the Arrhenius equation and control theory. He assumed that the motion of dislocation away from the crack tip was thermally activated and the plastic dissipation attained per unit area when all activated sites were activated, and the P-N barriers were overcome was given by

$$J_D = J_o \exp \left[-\frac{b^2(\gamma_f + U_{P-N})}{K_B T} \right] \quad (6.4)$$

$$J_o = \rho \pi h_p^2 \left(\frac{K_B T}{b^2} \right) \quad (6.5)$$

where b is Burgers vector, γ_f is generalized stacking fault energy, h_p is the dimension of the plastic zone, UP_{-N} is (P–N) barrier energy, ρ is dislocation density, T is absolute temperature, K_B is the Boltzmann constant, and γ_f is generalized stacking fault energy.

Eq (6.5) represents the maximum work done by plastic deformation. J_o is described by the dislocation density ρ , the dimension of the plastic zone h_p , and the thermal activation energy per unit length of dislocation motion $\frac{K_B T}{b^2}$.

It is known that the microcrack initiation process is related to the accumulation of local microscopic deformation through the dislocation motion [145]. Therefore, the fracture toughness can also be evaluated with the microcrack density and the energy for microcrack formation. When deformation occurs in the material, the atoms in a certain area may deviate from their equilibrium positions, leading to energy change in the bonds between atoms. The bonds are broken when the force or energy exceeds a critical value. Microcracks are initiated and propagate due to the atomic deviation and the absence of connection between atoms. In other words, dislocation density ρ characterizes indirectly the cracking behaviour in the material. TBC systems fail by the propagation and coalescence of interface microcracks that are initiated along or near the interface between the top coat and bond coat. They extend laterally as the system thermally cycles. Eventually, a few adjacent microcracks coalesce and propagate into a crack large enough to exhibit large-scale buckling and spallation. Therefore, the fracture toughness can also be characterized by microcrack density and the energy for microcrack formation.

Based on the essence of the Arrhenius equation, the temperature-dependent interfacial fracture toughness model for TBC systems in terms of the strain energy release rate is proposed as follows:

$$G_D = G_o \exp \left(-\frac{\frac{G_c}{n} \left(\frac{\delta_{CTOD}}{m} \right)^2}{K_B T} \right) \quad (6.6)$$

$$G_o = m r_p \rho_c \frac{K_B T}{\left(\frac{\delta_{CTOD}}{m} \right)^2} \quad (6.7)$$

Substituting the Eqs (6.1) and (6.2) into Eq (6.7) gives

$$G_o = m \frac{1}{3\pi} \left(\frac{|K|}{\sigma_y} \right)^2 \rho_c \frac{K_B T}{\left(\frac{\frac{4\sqrt{2}}{\pi\sqrt{1+4\varepsilon^2}} \frac{J}{\sigma_y}}{m} \right)^2} \quad (6.8)$$

G_o can be interpreted as the maximum plastic dissipation attained per unit area of crack extension. G_c is the critical strain energy release rate which defines the fracture toughness of the interface at room temperature. ρ_c is the interfacial or near interfacial microcrack density and it represents the number of microcracks per unit length. Thus $r_p \rho_c$ represents the number of microcracks in the region length around the plastic zone of the crack tip. The physics behind this term is that the initially generated microcracks prior to linking to larger-size cracks are capable of releasing local residual stress around the crack tip [35] and thus

reduce the stress intensity, leading to an increase in toughness. It is well known that microstructural features such as cracks and porosity are deliberately engineered into the top coat to alleviate the stresses arising from the thermal expansion mismatch between the ceramic top coat and underlying layers, making the coating highly compliant and strain tolerant. Therefore, the presence of microcracks can improve the fracture toughness of TBCs. With increasing high temperature exposure time however, the microcracks propagate and link together into larger cracks. Consequently, the microcrack density drops and the toughness decreases during thermal cycling [4], [146]. $\frac{K_B T}{\left(\frac{\delta_{CTOD}}{m}\right)^2}$ is the thermal activation energy in the unit of J/m².

The parameters n and m are the scale linking parameters. The parameter n is introduced to relate the macro strain energy release rate for crack propagation to the micro level energy which must be overcome by dislocation motion. It can be determined by equating the strain energy release rate at room temperature to the strain energy release rate evaluated using Eq (6.6) at room temperature. The parameter m is the correlation factor that represents the relation between the crack size and Burgers vector. It has been reported that the net Burgers vector of all dislocations within the plastic zone and the crack plane is equal to the CTOD where the elastic-plastic boundary crosses the crack plane [147]. Thus, they can be related by a parameter m as $mb = \delta_{CTOD}$.

6.3 Determination of Model Parameters

The strain energy release data at room temperature are given by Deng et al. [95]. In the TBC, the YSZ top coat, which was atmospheric plasma sprayed on Ni-based superalloy, was tested. Their experiment procedure is detailed in Chapter 2. **Table 6.1** gives the

mechanical properties of the substrate, bond coat, and top coat materials of the TBC system used in their study. Utilizing the research results of Deng et al in *Figure 2.22*, four pairs of critical energy release rates versus mode mixity are selected using the Graphclick software tool for the present study, as presented in *Table 6.2*.

Table 6.1 Mechanical properties of the TBC system [95].

Material	Young's Modulus (GPa)	Poisson's Ratio	Shear Modulus (GPa)
Substrate Component	130.70	0.363	47.945
Bond Coat (NiCoCrAlY)	152.4	0.311	58.123
Top Coat (YSZ)	41	0.07	19.158

Table 6.2 Selected data of critical energy release rate versus mode mixity [95].

Mode Mixity ψ (degree)	Critical Energy Release Rate G_c	Parameter (m)	Parameter (n)
19.775	13.29	1.007×10^3	352.608
21.379	22.018	1.6696×10^3	1.0638×10^3
76.41	24.293	1.8420×10^3	1.2880×10^3
77.765	36.368	2.7820×10^3	6.1201×10^3

Substituting the critical energy release rate data (**Table 6.2**) into Eq (2.12) for G_e when $G_e = G_c$, the complex stress intensity factor K can be calculated. Upon determining the stress intensity factor K , the plastic zone size r_p can be calculated according to Eq (6.1) with the yield stress $\sigma_y = 164$ MPa [148] for the bond coat material. The crack tip opening displacement δ_{CTOD} is calculated using Eq (6.2), where the parameter ε is calculated using Eq (2.9), and J -integral is identical to strain energy release rate G_e and the data can be found in **Table 6.2**. The microcrack density ρ_c can be obtained from the experimental data of previous research [149] when the exposure time is zero.

To obtain the parameter m , the Burgers vector b of dislocation for the top coat material, cubic zirconia, needs to be determined. It was reported to be of type $\frac{1}{2} \langle 110 \rangle$ with the lattice parameter $a = 0.513$ nm [150], [151]. Thus the Burgers vector b was calculated to be 3.63×10^{-10} m, then m can be obtained with $mb = \delta_{CTOD}$. The calculated m values at four mode mixity phase angles are reported in **Table 6.2**. To fit the scaling parameter n , the critical strain energy release rate, G_c , at room temperature, given in **Table 6.2**, is set to equal to the high temperature energy release rate in Eq (6.6) at $T = 298$ K (room temperature). Then the scale parameter n can be determined accordingly for the four selected mode mixity phase angles in **Figure 2.11**, which are presented in **Table 6.2**.

6.4 Solution for Interfacial Fracture Toughness

The calculated interface fracture toughness versus temperature at the four selected mode mixity phase angles is illustrated in **Figure 6.1**. It is shown that the interfacial fracture toughness of the TBC increases with temperature, which coincides with other studies

reported in literature [87]. Moreover, at a given temperature, the interfacial fracture toughness of the TBC ascends with mode mixity.

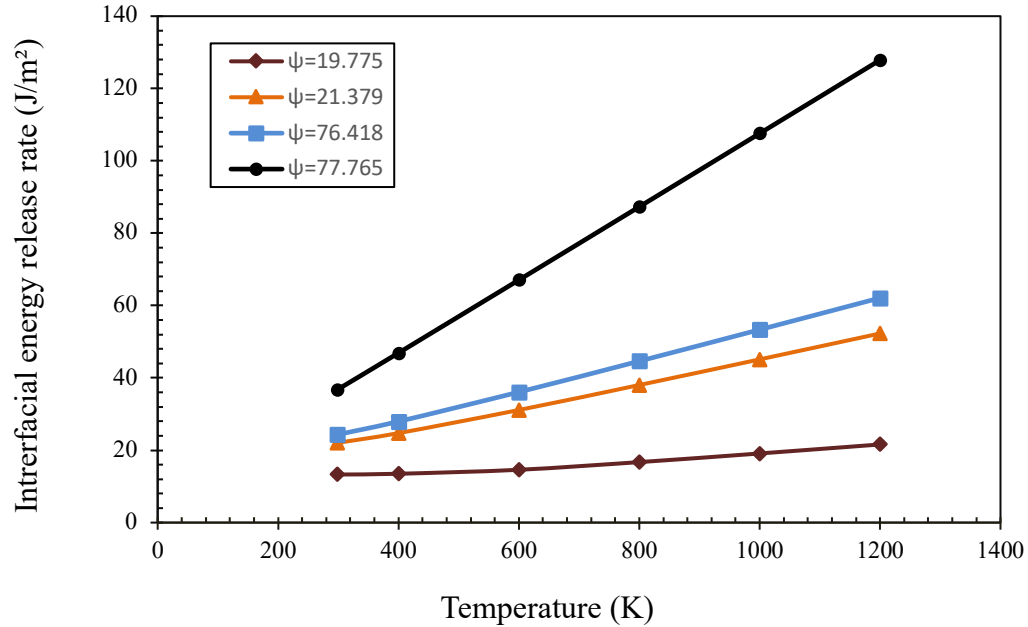


Figure 6.1 Variations of interfacial energy release rate with temperature for different mode mixites.

As revealed from the isothermal test results in the present work, the spallation of the TBC was a result of the crack propagation through the ceramic coating near the interface under high temperature exposure. Additionally, from the erosion test results, the porosity level of the top coat decreased with exposure temperature due to an increase in cohesion of splats boundary (onset of sintering effect). This strengthening mechanism inside the top coat and near the coating surface will hinder the propagation of the crack through the splats. Therefore, the interfacial fracture toughness increased with exposure temperature. However, after long exposure time at high temperatures, the stresses due to the TGO

growth will impose significant effect on reducing the interfacial fracture toughness and hence failure of the coating, as explained in Chapter 4.

Moreover, one of the important parameters that define the present proposed model is the crack density ρ_c . Since it varies with exposure time at high temperatures, high-temperature interfacial energy release rate with exposure time can also be described using the variation of microcrack density with exposure time. The microcrack density of plasma-sprayed ZrO₂-based TBC system at 1050°C was investigated experimentally for selected exposure times [149] and the microcrack density results are provided in **Figure 6.2**. It is shown that the microcrack density initially increased with exposure time, and then reached the maximum density at a certain time followed by a rapid drop due to crack coalescence.

The polynomial fit of the experimental data points in **Figure 6.2** provides the following equation for describing the crack density as a function of isothermal temperature exposure time:

$$\rho_c = -9 \times 10^{-12}t^4 + 4 \times 10^{-8}t^3 - 5 \times 10^{-5}t^2 + 0.036t + 24.962 \quad (6.9)$$

where t is exposure time. With varying crack density ρ_c at different exposure times, the variation of the interfacial fracture toughness of the TBC at 1050°C with exposure time can be predicted using the proposed model, as illustrated in **Figure 6.3**. It is shown that the interfacial energy release rate increases with exposure time and then decreases after reaching 2000 h of exposure time at 1050°C. Therefore, by introducing the microcrack density ρ_c , the dynamic response of the interfacial fracture toughness of TBCs to exposure time at 1050°C can be attained using the proposed model. Certainly, if the experimental

data of the crack density for other temperatures are available, the values of the interfacial fracture toughness of the TBC against exposure time at these temperatures can also be determined from this model.

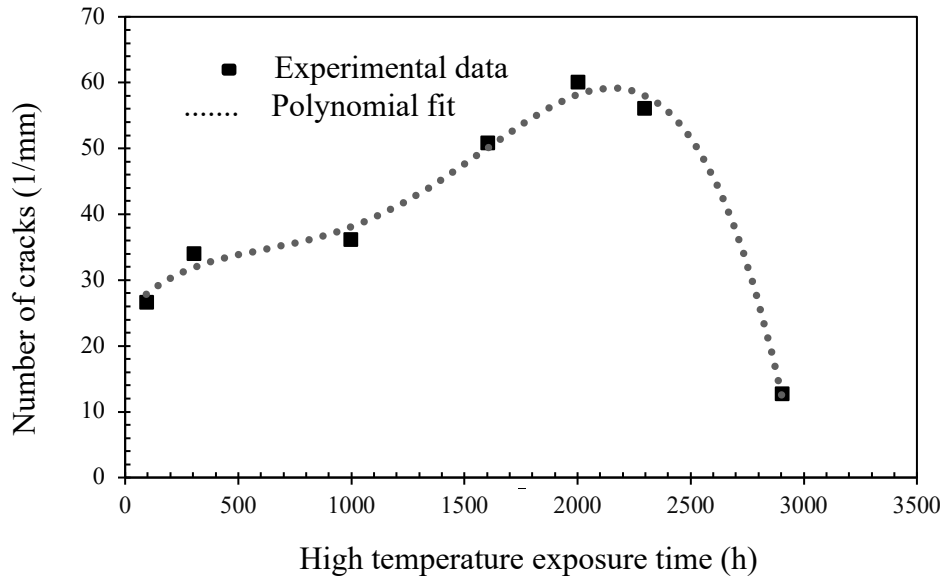


Figure 6.2 Variation of crack density vs isothermal exposure time at 1050°C.

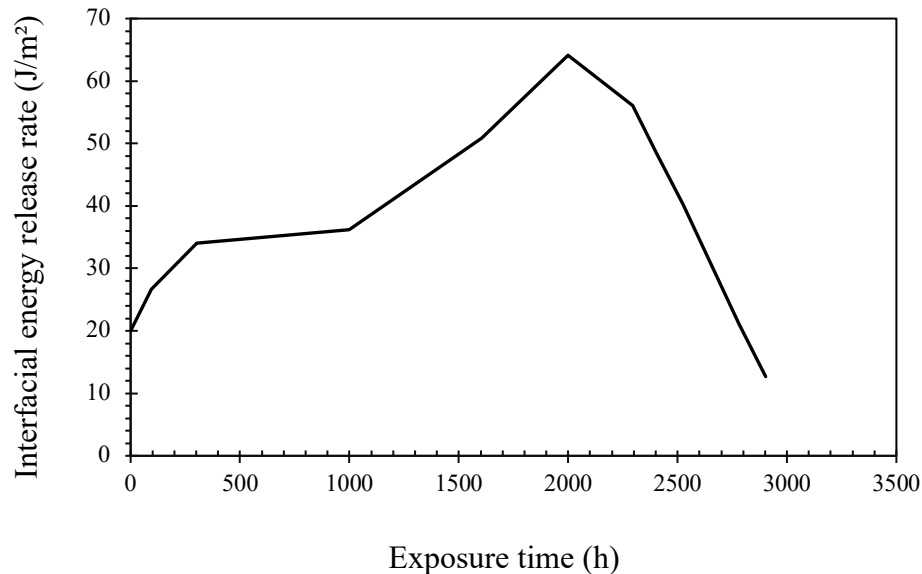


Figure 6.3 Variation of the interfacial energy release rate with exposure time at 1050°C.

The increase in the interfacial energy release rate, despite the increase in the number of cracks (*Figure 6.3*), can be attributed to the fact that the presence of cracks alleviates the stresses arising from the thermal expansion mismatch between the ceramic top coat and underlaying layers, making the coating highly compliant and strain tolerant. Therefore, the presence of microcracks can improve the coating fracture toughness. After 2000 h of exposure at 1050°C, the interfacial release rate decreases to the lowest value indicating the occurrence of the spallation of the TBC system. The reduction of the fracture toughness after reaching a critical time is related to the decrease in the crack density which indicates the coalescence and propagation of microcracks into a large crack as a result of high temperature effects, as delineated in Chapter 4. The propagation of the cracks continues until macroscopic failure occurs. This result is in good agreement with the findings of other studies on TBCs [129], [87], showing that the energy release rate increased with the thermal aging time until reaching the critical time and then decreased to its lowest value.

6.5 Concluding Remarks

A temperature-dependent interfacial fracture toughness model is proposed for APS TBC on Ni-based superalloy in terms of the microcrack formation theory. The energy release rate at room temperature and associated stress intensity factor are considered. The temperature effect is modeled based on the Arrhenius equation and growth control theory. Two scale linking parameters m and n are introduced in this model. The former is introduced to relate the macro strain energy release rate for crack propagation to the micro level energy which must be overcome by dislocation motion, and the latter is the correlation factor that relates the growth of the microcracks in terms of CTOD to the Burgers vector. The near crack tip field at the coating interface is described by the mixed mode singularity

field which is characterized by the parameter, mode mixity ψ , introduced in the model. High-temperature interfacial fracture toughness can be effectively predicted once the coating material properties are available.

The proposed model includes the temperature and exposure time dependent microcrack density, which allows predicting the fracture toughness of TBCs at a given temperature for any exposure time. In principle, the proposed model is capable of predicting the high interfacial fracture toughness for APS TBCs, owing to the utilization of the Arrhenius equation, once the coating material properties at high temperatures are available. However, it should be pointed out that although the proposed model exhibits temperature-dependence, the high-temperature material properties of TBCs are usually difficult to obtain due to experimental limitations. Thus, using room-temperature elastic properties to fit the model parameters would result in a certain deviation in the interface fracture toughness evaluation. Moreover, due to the lack of experimental data of the high-temperature fracture toughness of TBCs, the proposed model is not validated by the experimental data.

Chapter 7: Conclusions and Future Work

7.1 Summary of the Present Research

In this research, the behavior and performance of an APS TBC system under high temperature oxidation and solid particle erosion were studied experimentally, to simulate the real working condition of TBCs on gas turbine components of aerospace. To assess the durability of TBCs under the practical service scenario, an interfacial fracture toughness model for TBCs, which stemmed from the linear elastic fracture mechanics and utilized the experimental data published in literature, was developed based on the Arrhenius-type equation and microcrack density, including the effects of temperature and exposure time. The TBC system used in the isothermal oxidation test and solid particle erosion test consisted of single crystal Ni-based superalloy Inconel 718 substrate, CoNiCrAlY (Praxair CO-211) bond coat and 8 wt% yttria partially stabilized zirconia (YSZ) top coat that was deposited on the superalloy substrate via a plasma thermal spray process.

One of the main concerns associated with the reliable use of TBCs is their stability at high temperature working conditions. Therefore, in the present study, isothermal oxidation behavior and kinetics of the APS TBC system were investigated at three high temperatures, 1050°C, 1100°C, and 1150°C for various exposure times, up to approximately 2000 h. After the oxidation tests, the cross-sections of the oxidized specimens were examined using SEM/EDS, with the focus on the integrity of the coatings, the formation, growth and composition of thermally grown oxide (TGO), internal oxidation of the bond coat, and various cracks developed in the TBC specimens during the exposure periods.

Solid particle erosion is considered as a significant factor in the durability of TBCs under

their operating conditions. In the highlight of failure mechanisms of APS that are related to the degradation of the ceramic coating itself, solid particle erosion test was carried out on the TBC to evaluate the performance and address the failure of the APS TBC system as a result of erosion damage. The erosion test was performed on both the as-deposited and heat-treated TBC specimens, to simulate the actual high temperature working scenario of TBCs, at various particle impingement angles (30° , 45° , 60° , and 90°) with different particle impact velocities. The erosion mechanism of the TBC system was analyzed by examining the eroded specimens under SEM. The influence of heat treatment on the erosion performance of the TBC was investigated by comparing the erosion rate and the microstructure of the eroded top coat between the as-deposited and heat-treated TBC specimens.

As the most crucial factor for the assessment of TBC integrity, interface fracture toughness, describes the efficiency of a TBC system in resisting the crack propagating near the coating interface, which can lead to delamination, spallation and eventually the failure of TBC systems. Therefore, accurately assessing the interfacial fracture toughness of TBCs can effectively predict the service life of TBCs. Hence, an interfacial fracture toughness model that enables the estimate of the interface toughness of TBCs at high temperatures was proposed. The energy release rate at room temperature and associated stress intensity factor were considered in the model formulation. The temperature-dependence was modeled based on the Arrhenius-type equation. The near crack tip field at the interface was described by the mixed mode singularity field in this model. The proposed model was applied to a TBC system, determining the model parameters by utilizing the experimental data reported in literature. The interfacial fracture toughness was then determined at selected mode

mixity phase angles for the TBC system, showing the temperature-dependent relation and the variation with exposure time at a given temperature.

7.2 Conclusions from the Present Research

From the experimental work, associated SEM/EDS analyses, and interfacial fracture toughness modelling as well as the discussion on the testing and modeling results, the following conclusions can be derived from the present research.

1. For the current state-of-the-art TBC system consisting of YSZ top coat and CoNiCrAlY bond coat on Ni-based superalloy Inconel 718, the oxidation of the bond coat did occur during isothermal testing at 1050°C, 1100°C, and 1150°C in air condition.
2. The isothermal oxidation test results revealed that the life of the TBCs strongly depended on the temperature that the bond coat experienced during oxidation exposure and tended to decrease as a temperature of exposure increased.
3. The growth rate of the TGO increased dramatically with temperature and time of exposure. Additionally, the development of TGO had a close relationship with the stability of the bond coat.
4. The formed TGO layer was inhomogeneous, consisting of a dense protective Al₂O₃ layer and a nonprotective mixed oxide layer containing various oxides such as (Ni, Cr, Co) oxides which were formed as a result of Al depletion in the bond coat and the reaction of oxygen with other components in the bond coat. The depletion of Al content and the increase in oxide layer thickness occurred at remarkably higher levels at the highest temperature of 1150°C.
5. The growth of mixed oxides can create stresses which can lead to the formation of

cracks, these cracks can grow and eventually cause the failure of the TBC.

6. Large amounts of internal oxides were formed within the bond coat which were believed to have non-negligible effect on the TBC failure during isothermal oxidation.
7. The studies of oxidation kinetics of the APS TBCs were performed after the isothermal oxidation test. The TGO thicknesses formed at all oxidation temperatures for different exposure times were measured with SEM and consequently, the growth coefficients of the TGO were calculated. The activation energy required for the TGO development was found to be 209.7 kJ/mol. Hence, the global temperature invariant equation, which allows for the prediction of the oxide thicknesses at any time and temperature within the testing range, was determined. Moreover, the prediction of the APS TBC spallation failure time based on the measured critical TGO thickness was performed.
8. The final failure of the TBC systems under isothermal condition was associated with the spallation of the top coat through the rapid propagation of cracks along the coating interface. The size of the cracks increased with exposure time and temperature.
9. The crack propagation in the APS TBCs during the isothermal exposure appeared to be controlled by the TGO growth.
10. All the failure mechanisms that were identified in this study are believed to contribute to the failure of the TBC system, but none of them was observed to cause the failure of the TBC by themselves only unless they were very pronounced.
11. Under solid particle erosion, the erosion rate of the top coat increased with increasing

the angle of impingement and velocity of erodent particles. The maximum erosion rates occurred at 90° impingement angle which corresponded to brittle erosion behavior of the ceramic top coat.

12. The erosion resistance of the APS TBCs increased when the TBC specimen was thermally aged at 1000°C and 1150°C, owing to the onset sintering effect on the top coat, which resulted in the reduction of porosity and increase of hardness of the top coat.
13. The erosion of APS top coat occurred through the fracture at the poorly bonded splat boundaries, which resulted in material fragments being removed from the top coat with continuous particle impact.
14. The adherence at the top coat/bond coat interface was not affected noticeably by particle impacts under the erosion test; the damage (cracking and fracturing) by the solid particle attack was limited to the top coat domain only.
15. The results obtained from the exposure time-dependent high-temperature interfacial fracture toughness model for a TBC showed that the interfacial fracture toughness of a TBC system had a strong dependency on exposure temperature. The interfacial fracture toughness of the TBC increased with temperature.
16. The exposure time-dependent of high-temperature interfacial fracture toughness model of TBCs was obtained by introducing the microcrack density parameter which is exposure-time-dependent at a given temperature. The interfacial energy release rate for the TBC increased with exposure time and then decreased after reaching 2000 h of exposure time at the oxidation temperature of 1050°C.
17. Although the proposed model can more realistically evaluate the interfacial fracture

toughness of TBCs, compared to the existing models, the application of this model has certain difficulties in that the model parameters such that Young's moduli, Poisson's ratio, and CTODs should be temperature-dependent but they are usually unavailable.

7.3 Significant Contributions

Owing to the vital need of aerospace gas turbines for TBCs, many research activities have been reported in literature that involve analytical, experimental, and numerical studies of the performance of TBCs. However, there are still some problems that are not well understood, which affect the life prediction of TBCs and hinder their optimal design. The general expectation of higher gas turbine efficiency in future demands in depth understanding of all factors affecting TBC failure and lifetime. The outcomes of the present research through the experimental and modeling efforts have significantly contributed to a better understanding of these factors, which affect the mechanical behavior of TBCs, and will be important in the ceaseless life prediction work, which will, in the long run, contribute to higher reliability of TBC systems in gas turbines.

For the oxidation of TBCs, this research has more systematically investigated the oxidation behavior of the bond coat by oxidizing the TBC specimen at three different high temperatures, and then examined the oxides formed in the specimens at certain exposure times. As a result, the oxidation kinetics equation of the TGO growth has been derived. With this equation, once the TBC working temperature is known, the TGO thickness and the lifetime of the APS TBC based on measured critical TGO thickness can be predicted.

This information is favorable for the composition control of the bond coat material to ensure the functionality of the top coat at high temperatures.

Previous erosion studies on TBCs only considered the damage of top coat surface and the TBC specimens were all in an intact state or as-deposited state. However, in the real working condition, erosion and oxidation occur concurrently on TBCs. In the present research, a solid particle erosion test was performed on both the as-deposited and aged TBC specimens, thus more likely to represent TBC practical application although the erosion test was not performed in high temperature environment due to the unavailability of the testing facilities. Moreover, by examining both the coating cross-section and the coating surface of the eroded specimens using SEM, the TBC failure mechanism under solid particle erosion was evidently revealed.

Although accurately predicting the fracture toughness for TBCs via modeling is difficult due to the complicity of TBC systems, an analytical model that evaluates the interfacial fracture toughness of the APS TBC system at high temperatures was created. The model effectively assesses the high temperature interfacial fracture toughness of TBCs based on the experimental data available in literature, thus solves the problem of the difficulty in directly measuring the interfacial fracture toughness of TBCs experimentally at high temperatures. Moreover, the proposed model enables the interfacial fracture toughness prediction to be not only temperature-dependent, but also exposure time-dependent by introducing the microcrack density factor that varies with the exposure time at an oxidation temperature.

7.4 Future Work

The present research has shown that there is much about the isothermal oxidation behavior of APS TBCs, which still has to be researched. From the present research results, the failure mode is governed by crack formation and propagation, which is in turn governed by the microstructure of the TBC system. Further research on how to optimize the microstructure of the bond coat that promotes the formation of TGO with a stable Al_2O_3 layer, which is more protective, is needed in order to extend the lifetime and improve the durability of APS TBCs.

The erosion mechanisms of TBCs can be quite complex, therefore, further work is important to further understand the erosion behavior of TBCs. Performing high-temperature erosion testing on TBCs is essential in order to be more representative of their actual working condition. The present research results have highlighted the effect of aging condition on the increase of erosion resistance of the TBC due to the onset of the sintering effect of the top coat at higher temperatures. Hence, focusing on the changes of the microstructure due to aging and sintering by conducting the aging test at higher temperatures than those used in the present research is necessary.

The temperature dependent interfacial fracture toughness model for TBCs was proposed in this research. The parameters used in this model such as Young's modulus, yield strength, and critical energy release rate in room temperature for the TBC were obtained from literature and the changes of these properties at high temperatures are not taken into consideration due to the limitations of the existing testing facilities and methodologies. To further improve and validate this model, this issue needs to be considered and the related

model parameters should be defined accordingly.

In general, optimization of bond coat properties as well as the mechanical properties and microstructure of the Top coat by manufacturing, offers a potential for lifetime extension and improvement of life- time reproducibility of APS-TBC-coatings.

References

1. M. P. Boyce, “An overview of gas turbines,” *Gas Turbine Engineering Handbook*, pp. 3–88, 2012.
2. B. Seth, “Superalloys: the utility gas turbine perspective,” *Superalloys 2000 (Ninth International Symposium)*, pp.3-16, 2000.
3. R. A. Miller, “Current status of thermal barrier coatings — an overview,” *Surface and Coatings Technology*, vol. 30, no. 1, pp. 1–11, 1987.
4. N. P. Padture, M. Gell, and E.H. Jordan, “Thermal barrier coatings for gas-turbine engine applications,” *Science (280)*., vol. 296, no. 5566, pp. 280 –284, 2002.
5. D. R. Clarke, M. Oechsner, and N. P. Padture, “Thermal barrier coatings for more efficient gas-turbine engines,” *MRS Bulletin*, vol. 37, no. 10, pp. 891–898, 2012.
6. A.G. Evans, D. R. Clarke, and C.G. Levi, “The influence of oxides on the performance of advanced gas turbines,” *Journal of the European Ceramic Society*, vol. 28, no. 7, pp. 1405–1419, 2008.
7. M.F. Hussain and W. Tabakoff, “Dynamic behaviour of solid particles suspended by polluted flow in a turbine stage”, *Journal of Aircraft* 10, 434-440,1973.
8. W. Tabakoff, A. Hamed and B. Beacher ‘Investigation of gas particle flow in an erosion wind tunnel”, *Wear* 86, 73-88,1983.
9. R. G. Wellman and J. R. Nicholls, Some Observations on the Erosion Mechanism of EB-PVD TBCs. *Wear* 242, 89-96, 2000.
10. M. Matsumoto, H. Takayama, D. Yokoe, K. Mukai, H. Matsubara, Y. Kagiya, andY.Sugita, “Thermal cycle behavior of plasma sprayed La₂O₃, Y₂O₃ stabilized ZrOcoatings,” *Scripta Materialia*, vol. 54, no. 12, pp. 2035–2039, 2006.
11. A. Cahit, K. Ogawa, A. Turk, and I. Ozdemir, “Thermal shock and cycling behavior of thermal barrier coatings (TBCs) used in gas turbines.” In the *Progress in Gas Turbine Performance*, 2013.
12. G. Witz and H. Bossmann, “Determination of thermal barrier coatings average surface temperature after engine operation for lifetime validation,” *Journal of Engineering for Gas Turbines and Power*, vol. 134, no. 12, 2012.
13. J. R. Brandon and R. Taylor, “Phase stability of zirconia-based thermal barrier coatings part II. Zirconia-ceria alloys,” *Surface and Coatings Technology*, vol. 46, no. 1, pp. 91–101, 1991.
14. H. Xu and H. Guo, *Thermal barrier coatings*. Oxford: Woodhead Pub Ltd, 2011.
15. A. J. Allen, J. Ilavsky, G.G. Long, J. S. Wallace, C. C. Berndt, and H. Herman, “Microstructural characterization of yttria-stabilized zirconia plasma-sprayed deposits using multiple small-angle neutron scattering,” *Acta Materilia*, vol. 49, no. 9, pp. 1661–1675, 2001.
16. U. Schulz, K. Fritscher, C. Leyens, and M. Peters, “Influence of processing on microstructure and performance of electron beam physical vapor deposition

- (EB-PVD) thermal barrier coatings," *Journal of Engineering for Gas Turbines and Power*, vol. 124, no. 2, pp. 229–234, 2002.
- 17. D. D. Hass, P. A. Parrish, and H. N. G. Wadley, "Electron beam directed vapor deposition of thermal barrier coatings," *Journal of Vacuum Science & Technology A: Vacuum, Surfaces, and Films*, vol. 16, no. 6, pp. 3396–3401, 1998.
 - 18. R. Wellman and J. Nicolls "On the effect of ageing on the erosion of EB-PVD TBCs," *Surface and Coatings Technology*, vol. 177-178, pp.80-88, 2004.
 - 19. J. Haynes, M. Ferber, and W. Porter, "Thermal cycling behavior of plasma-sprayed thermal barrier coatings with various MCrAlX bond coats," *Journal of Thermal Spray Technology*, vol. 9, no. 1, pp. 38–48, Jan. 2000.
 - 20. C. Zhu, A. Javed, P. Li, F. Yang, G. Liang, and P. Xiao, "A study of the microstructure and oxidation behavior of alumina/yttria-stabilized zirconia (Al₂O₃/YSZ) thermal barrier coatings," *Surface and Coatings Technology*, vol. 212, pp. 214–222, 2012.
 - 21. W. Soboyejo, P. Mensah, R. Diwan, J. Crowe, and S. Akwaboa, "High temperature oxidation interfacial growth kinetics in YSZ thermal barrier coatings with bond coatings of NiCoCrAlY with 0.25% Hf," *Materials Science and Engineering: A*, vol. 528, no. 6, pp. 2223–2230, 2011.
 - 22. J. Haynes, B. Pint, Y. Zhang, and I. Wright, "Comparison of the cyclic oxidation behavior of β -NiAl, β -NiPtAl and γ - γ' NiPtAl coatings on various superalloys," *Surface and Coatings Technology*, vol. 202, no. 4-7, pp. 730–734, 2007.
 - 23. Z. Yu, K. Dharmasena, D. Hass, and H. Wadley, "Vapor deposition of platinum alloyed nickel aluminide coatings," *Surface and Coatings Technology*, vol. 201, no. 6, pp. 2326–2334, 2006.
 - 24. E. J. Felten and F. S. Pettit, "Development, growth, and adhesion of Al₂O₃ on platinum-aluminum alloys," *Oxidation of Metals*, vol. 10, no. 3, pp. 189–223, 1976.
 - 25. M. Farrell, D. Boone, and R. Streiff, "Oxide adhesion and growth characteristics on platinum-modified aluminide coatings," *Surface and Coatings Technology*, vol. 32, no. 1-4, pp. 69–84, 1987.
 - 26. R. Swadźba, M. Hetmańczyk, J. Wiedermann, L. Swadźba, G. Moskal, B. Witala, and K. Radwański, "Microstructure degradation of simple, Pt- and Pt Pd-modified aluminide coatings on CMSX-4 superalloy under cyclic oxidation conditions," *Surface and Coatings Technology*, vol. 215, pp. 16–23, 2013.
 - 27. M. Saremi, A. Afrasiabi, and A. Kobayashi, "Microstructural analysis of YSZ and YSZ/Al₂O₃ plasma sprayed thermal barrier coatings after high temperature oxidation," *Surface and Coatings Technology*, vol. 202, no. 14, pp. 3233–3238, 2008.
 - 28. M. Daroonparvar, M. Yajid, N. Yusof, S. Farahany, M. Hussain, H. Bakhsheshi-Rad, Z. Valefi, and A. Abdolahi, "Improvement of thermally grown oxide layer in thermal barrier coating systems with nano alumina as third layer," *Transactions of Nonferrous Metals Society of China*, vol. 23, no. 5, pp. 1322–1333, 2013.

29. B. Panicaud, J. Grosseau-Poussard, and J. Dinhut, “On the growth strain origin and stress evolution prediction during oxidation of metals,” *Applied Surface Science*, vol. 252, no. 16, pp. 5700–5713, 2006.
30. A. Evans, D. Mumm, J. Hutchinson, G. Meier, and F. Pettit, “Mechanisms controlling the durability of thermal barrier coatings,” *Progress in Materials Science*, vol. 46, no. 5, pp. 505–553, 2001.
31. D. R. Clarke, “Stress generation during high-temperature oxidation of metallic alloys,” *Current Opinion in Solid State and Materials Science*, vol. 6, no. 3, pp. 237–244, 2002.
32. A. Rabiei and A. Evans “Failure mechanisms associated with the thermally grown oxide in plasma-sprayed thermal barrier coatings,” *Acta Materialia*, vol. 48, no. 15, pp. 3963–3976, 2000.
33. H. Hindam and D. P. Whittle, “Microstructure, adhesion and growth kinetics of protective scales on metals and alloys,” *Oxidation of Metals*, vol. 18, no. 5-6, pp. 245–284, 1982.
34. S. Kuroda and T. Clyne, “The quenching stress in thermally sprayed coatings,” *Thin Solid Films*, vol. 200, no. 1, pp. 49–66, 1991.
35. R. Prescott and M. J. Graham, “The formation of aluminum oxide scales on high-temperature alloys,” *Oxidation of Metals*, vol. 38, no. 3-4, pp. 233–254, 1992.
36. F. Stott and G. Wood, “The mechanism of oxidation of Ni-Cr-Al alloys at 1000°–1200°C,” *Corrosion Science*, vol. 11, no. 11, pp. 799–812, 1971.
37. W. Chen, X. Wu, B. Marple, R. Lima, and P. Patnaik, “Pre-oxidation and TGO growth behaviour of an air-plasma-sprayed thermal barrier coating,” *Surface and Coatings Technology*, vol. 202, no. 16, pp. 3787–3796, 2008.
38. E. Shillington and D. Clarke, “Spalling failure of a thermal barrier coating associated with aluminum depletion in the bond-coat,” *Acta Materialia*, vol. 47, no. 4, pp. 1297–1305, 1999.
39. D. Monceau and B. Pieraggi, “Determination of parabolic rate constants from a local analysis of mass-gain curves,” *Oxidation of Metals*, vol. 50, no 5 – 6, pp. 477-493, 1989.
40. H. Evans and M. Taylor, “Oxidation of high-temperature coatings,” *Proceedings of the Institution of Mechanical Engineers*, vol. 220, no.1, pp.1-10, 2006.
41. D. Naumenko, B. Gleeson, E. Wessel, L. Singheiser, and W. Quadakkers, “Correlation between the microstructure, growth mechanism, and growth kinetics of alumina scales on a FeCrAlY Alloy,” *Metallurgical and Materials Transactions A*, vol. 38, no. 12, pp. 2974–2983, Jan. 2007.
42. E. Busso, J. Lin, and S. Sakurai, “A mechanistic study of oxidation-induced degradation in a plasma-sprayed thermal barrier coating system.,” *Acta Materialia*, vol. 49, no. 9, pp. 1529–1536, 2001.
43. R. Eriksson, “Thermal barrier coatings durability assessment and life prediction,” dissertation, 2013.
44. J. A. Haynes, M. K. Ferber, W. D. Porter, and E. D. Rigney, “Characterization of alumina scales formed during isothermal and cyclic oxidation of plasma-

- sprayed TBC systems at 1150°C,” *Oxidation of Metals*, vol. 52, no. 112, pp. 31–76, 1999.
- 45. K. Yuan, “Thermal and mechanical behaviors of high temperature coatings,” dissertation, 2013.
 - 46. F. A. Golightly, F. H. Stott, and G. C. Wood, “The influence of yttrium additions on the oxide-scale adhesion to an iron-chromium-aluminum alloy,” *Oxidation of Metals*, vol. 10, no. 3, pp. 163–187, 1976.
 - 47. G. H. Meier, M. J. Stiger, J. R. Blachere, F. S. Pettit, C. Sarioglu, R. Janakiraman, E. Schumann, and A. Ashary, “The adhesion of alumina films to metallic alloys and coatings,” *Materials and Corrosion*, vol. 51, no. 5, pp. 358–372, 2000.
 - 48. G. H. Meier, F. S. Pettit, and J. L. Smialek, “The effects of reactive element additions and sulfur removal on the adherence of alumina to Ni- and Fe-base alloys,” *Materials and Corrosion*, vol. 46, no. 4, pp. 232–240, 1995.
 - 49. H. M. Tawancya and N. M. Abbasa, “Role of Y during high temperature oxidation of an M-Cr-Al-Y coating on an Ni-base superalloy,” *Surface and Coating Technology*, vol. 69, pp. 10–16, 1994.
 - 50. P. Niranalumpong, C. B. Ponton, and H. E. Evans, “Failure of protective oxides on plasma-sprayed NiCrAlY overlay coatings,” *Oxidation of Metals*, vol. 53, no. 3, pp. 241–258, 2000.
 - 51. M. K. Gupta, “Design of thermal barrier coatings: a modelling approach,” dissertation, 2014.
 - 52. H. E. Evans and A. T. Donaldson, “Mechanisms of breakaway oxidation and application to a chromia-forming steel,” *Oxidation of Metals*, vol. 52, 1999.
 - 53. X. Chen, J. W. Hutchinson, M. Y. He, and A. G. Evans, “On the propagation and coalescence of delamination cracks in compressed coatings: with application to thermal barrier systems,” *Acta Materialia*, vol. 51, no. 2003, pp. 2017–2030, 2017.
 - 54. Y. R. Takeuchi and K. Kokini, “Thermal fracture of multilayer ceramic thermal barrier coatings,” *Journal of Engineering for Gas Turbines and Power*, vol. 116, no. 1, pp. 266–271, Jan. 1994.
 - 55. P. Wright and A.G. Evan, “Mechanisms governing the performance of thermal barrier coatings,” *Current Opinion in Solid State and Materials Science*, vol. 4, no. 3, pp. 255–265, 1999.
 - 56. D.Zhu, L.J. Ghosn, and R.A. Miller, “Effect of layer-graded on edge stress concentration and oxidation behavior of thermal barrier coatings,” *Nasa/Tm*, 1998.
 - 57. W. Chen, X. Wu, B. Marple, D. Nagy, and P. Patnaik, “TGO growth behaviour in TBCs with APS and HVOF bond coats,” *Surface and Coatings Technology*, vol. 202, no. 12, pp. 2677–2683, 2008
 - 58. P.L. Cao, B.C. Liu, K. Yin, and Z.-P. Zhang, “Optimization design and residual thermal stress analysis of PDC functionally graded materials,” *Journal of Zhejiang University-Science A*, vol. 7, no. 8, pp. 1318–1323, 2006.
 - 59. C.-H. Hsueh and E. R. Fuller, “Residual stresses in thermal barrier coatings: effects of interface asperity curvature/height and oxide thickness,” *Materials Science and Engineering: A*, vol. 283, no. 1-2, pp. 46–55, 2000.

60. M.P. Bacos, J.M. Dorvaux, O. Lavigne, R. Mévrel, M. Poulain, C. Rio, and M.H. Vidal Sétif “Performance and degradation mechanisms of thermal barrier coatings for turbine blades : a review of onera activities,” Aerospace Lab, pp. 1-11, 2011.
61. D. R. Clarke and C. G. Levi, “Materials design for the next generation thermal barrier coatings,” *Annual Review of Materials Research*, Vol.33 no. 1, pp. 383-4217, 2003.
62. E. P. Busso and F. A. Mcclintock, “Thermal fatigue degradation of an overlay coating,” *Materials Science and Engineering: A*, vol. 161, no. 2, pp. 165–179, 1993.
63. V. Lugh, V. K. Tolpygo, and D. R. Clarke, “Microstructural aspects of the sintering of thermal barrier coatings,” *Materials Science and Engineering: A*, vol. 368, no. 1-2, pp. 212–221, 2004.
64. W. Braue, U. Schulz, K. Fritscher, C. Keyens, and R. Wirth, “Analytical electron microscopy of the mixed zone in NiCoCrAlY-based EB-PVD thermal barrier coatings: as-coated condition versus late stages of TBC lifetime,” *Materials at High Temperatures*, vol. 22, no. 3, pp. 393–401, 2005.
65. H. M. Tawancy, A. I. Mohamed, and N. M. Abbas, “Effect of superalloy substrate composition on the performance of a thermal barrier coating system,” *Journal of Material Science.*, vol. 38, no. 18, pp. 3797–3807, 2003.
66. D. R. Clarke, V. Sergo, and M. Y. He, “Precursor to TBC failure caused by constrained phase transformation in the thermally grown oxide,” *Elevated Temperature Coatings Science Technology lii*, pp. 67–78, 1999.
67. M. W. Chen, M. L. Glynn, D. Pan, K. T. Ramesh, K. J. Hemker, R. T. Ott, and T. C. Hufnagel, “Influence of martensitic transformation on the durability of TBC Systems (*Invited*),” *American Society of Mechanical Engineers, Aerospace Division*, vol. 68, pp. 489–495, 2003.
68. M. Kaplan, M. Uyaner, E. Avcu, Y. Y. Avcu, and A. C. Karaoglanli, “Solid particle erosion behavior of thermal barrier coatings produced by atmospheric plasma spray technique,” *Mechanics of Advanced Materials and Structures*, vol. 26, no. 19, pp. 1606–1612, Aug. 2018.
69. E. Bousser, L. Martinu, and J. Klemburg-Sapieha, “Solid particle erosion mechanisms of protective coatings for aerospace applications,” *Surface and Coatings Technology*, vol. 257, pp. 165–181, 2014.’
70. P. Kulu, I. Hussainova, and R. Veinthal, “Solid particle erosion of thermal sprayed coatings,” *Wear*, vol. 258, no. 1-4, pp. 488–496, 2005.
71. M. Stack, B. Jana, and S. Abdelrahman, “Models and mechanisms of erosion–corrosion in metals,” *Tribocorrosion of Passive Metals and Coatings*, 2011.
72. J.R. T. Branco, R. Gansert, S. Sampath, C. C. Berndt, and H. Herman, “Solid particle erosion of plasma sprayed ceramic coatings,” *Materials Research*, vol. 7, no. 1, pp. 147–153, 2004.
73. J. R. Nicholls, Y. Jaslier, and D. Rickerby, “Erosion and foreign object damage of thermal barrier coatings,” *Materials Science Forum*, vol. 251-254, pp. 935–948, 1997.

74. R. Wellman and J. Nicholls, "Erosion, corrosion and erosion-corrosion of EB PVD thermal barrier coatings," *Tribology International*, vol. 41, no. 7, pp. 657–662, 2008.
75. H. Eaton and R. Novak, "Particulate erosion of plasma-sprayed porous ceramic," *Surface and Coatings Technology*, vol. 30, no. 1, pp. 41–50, 1987.
76. R. G. Wellman and J. R. Nicholls, "A review of the erosion of thermal barrier coatings," *Journal of Physics D: Applied Physics*, vol. 40, no. 16, 2007.
77. F. Cernuschi, L. Lorenzoni, S. Capelli, C. Guardamagna, M. Karger, R. Vaßen, K. V. Niessen, N. Markocsan, J. Menuey, and C. Giolli, "Solid particle erosion of thermal spray and physical vapour deposition thermal barrier coatings," *Wear*, vol. 271, no. 11-12, pp. 2909–2918, 2011.
78. R.G. Wellman, M.J. Deakin, and J. Nicholls, "The effect of TBC morphology on the erosion rate of EB PVD TBCs," *Wear*, vol. 258, no. 1-4, pp. 349–356, 2005.
79. R. S. Lima, B. M. H. Guerreiro, and M. Aghasibeg, "Microstructural characterization and room-temperature erosion behavior of as-deposited SPS, EB-PVD and APS YSZ-based TBCs," *Journal of Thermal Spray Technology*, vol. 28, no. 1-2, pp. 223–232, Apr. 2018.
80. R. Swar, A. Hamed, D. Shin, N. Woggon, and R. Miller, "Deterioration of thermal barrier coated turbine blades by erosion," *International Journal of Rotating Machinery*, vol. 2012, pp. 1–10, 2012.
81. E. Tzimas, H. Müllejans, S. Peteves, J. Bressers, and W. Stamm, "Failure of thermal barrier coating systems under cyclic thermomechanical loading," *Acta Materialia*, vol. 48, no. 18-19, pp. 4699–4707, 2000.
82. D. Liu, M. Seraffon, P. Flewitt, N. Simms, J. Nicholls, and D. Rickerby, "Effect of substrate curvature on residual stresses and failure modes of an air plasma sprayed thermal barrier coating system," *Journal of the European Ceramic Society*, vol. 33, no. 15-16, pp. 3345–3357, 2013.
83. X. Wang, C. Wang, and A. Atkinson, "Interface fracture toughness in thermal barrier coatings by cross-sectional indentation," *Acta Materialia*, vol. 60, no. 17, pp. 6152–6163, 2012.
84. G. Qian, T. Nakamura, C. Berndt, and S. Leigh, "Tensile toughness test and high temperature fracture analysis of thermal barrier coatings," *Acta Materialia*, vol. 45, no. 4, pp. 1767–1784, 1997.
85. W. Han, E. F. Rybicki, and J. R. Shadley, "An improved specimen geometry for ASTM C633-79 to estimate bond strengths of thermal spray coatings," *Journal of Thermal Spray Technology*, vol. 2, no. 2, pp. 145–150, 1993.
86. D. Marshall, B. Lawn, and A. Evans, "Elastic/plastic indentation damage in ceramics: the lateral crack system," *Journal of the American Ceramic Society*, vol. 65, no. 11, pp. 561–566, 1982.
87. M. Arai and K. Kishimoto, "Influence of high-temperature exposure on interfacial fracture toughness of thermal barrier coating," *Journal of Solid Mechanics and Materials Engineering*, vol. 1, no. 8, pp. 1005–1016, 2007.
88. M. D. Drory and J. W. Hutchinson, "Measurement of the adhesion of a brittle film on a ductile substrate by indentation," *Proceedings of the Royal Society of*

- London. Series A: Mathematical, Physical and Engineering Sciences*, vol. 452, no. 1953, pp. 2319–2341, 1996.
89. A. Vasinonta and J. L. Beuth, “Measurement of interfacial toughness in thermal barrier coating systems by indentation,” *Engineering Fracture Mechanics*, vol. 68, no. 7, pp. 843–860, 2001.
 90. W. Mao, J. Wan, C. Dai, J. Ding, Y. Zhang, Y. Zhou, and C. Lu, “Evaluation of microhardness, fracture toughness and residual stress in a thermal barrier coating system: a modified vickers indentation technique,” *Surface and Coatings Technology*, vol. 206, no. 21, pp. 4455–4461, 2012.
 91. Y. Yamazaki, M. Arai, Y. Miyashita, H. Waki, and M. Suzuki, “Determination of interfacial fracture toughness of thermal spray coatings by indentation,” *Journal of Thermal Spray Technology*, vol. 22, no. 8, pp. 1358–1365, 2013.
 92. J. Lesage and D. Chicot, “Role of residual stresses on interface toughness of thermally sprayed coatings,” *Thin Solid Films*, vol. 415, no. 1-2, pp. 143–150, 2002.
 93. A. Evans, M. Rühle, B. Dagleish, and P. Charalambides, “The fracture energy of bi- material interfaces,” *Metallurgical Transactions A*, vol. 21, no. 9, pp. 345–364, 1990.
 94. M. Arai, Y. Okajima, and K. Kishimoto, “Mixed-mode interfacial fracture toughness for thermal barrier coating,” *Engineering Fracture Mechanics*, vol. 74, no. 13, pp. 2055–2069, 2007.
 95. H. Deng, H. Shi, H. Yu, and B. Zhong, “Determination of mixed-mode interfacial fracture toughness for thermal barrier coatings,” *Science China Physics, Mechanics and Astronomy*, vol. 54, no. 4, pp. 618–624, Feb. 2011.
 96. L. Qian, S. Zhu, Y. Kagawa, and T. Kubo, “Tensile damage evolution behavior in plasma-sprayed thermal barrier coating system,” *Surface and Coatings Technology*, vol. 173, no. 2-3, pp. 178–184, 2003.
 97. D. Wu and Y. C. Zhou, “Interface fracture toughness of TBCs at high temperature,” *11th International Conference on Fracture*, pp. 976-1981, 2005.
 98. S. Choi, D. Zhu, and R. Miller, “Fracture behavior under mixed-mode loading of ceramic plasma-sprayed thermal barrier coatings at ambient and elevated temperatures,” *Engineering Fracture Mechanics*, vol. 72, no. 13, pp. 2144–2158, 2005.
 99. J. I. Bluhm, “Fracture Mechanics,” *SAE Technical Paper Series*, Jan. 1963.
 100. C. H. Wang, “Introduction to fracture mechanics”, Vic.: *DSTO Aeronautical and Maritime Research Laboratory*, 1996.
 101. A. Agrawal and A. M. Karlsson, “Obtaining mode mixity for a bimaterial interface crack using the virtual crack closure technique,” *International Journal of Fracture*, vol. 141, no. 1-2, pp. 75–98, 2006.
 102. J.-S. Wang and Z. Suo, “Experimental determination of interfacial toughness curves using Brazil-nut-sandwiches,” *Acta Metallurgica et Materialia*, vol. 38, no. 7, pp. 1279–1290, 1990.
 103. J. Dollhofer, W. Beckert, B. Lauke, and K. Schneider, “Fracture mechanical characterization of mixed-mode toughness of thermoplast/glass interface,” *Computational Materials Since*, vol. 19, no 1-4, pp. 223-228, 2000.

104. M. L. Williams, "The stresses around a fault or crack in dissimilar media," *Bulletin of the Seismological Society of America*, vol. 49, no. 2, pp. 199–204, 1959.
105. J. R. Rice, Z. Suo, and J.-S. Wang, "Mechanics and thermodynamics of brittle interfacial failure in bimaterial system, *Metal–Ceramic Interfaces*, vol. 4, pp. 269–294, 1990.
106. T. Hille, S. Turteltaub, and A. Suiker, "Oxide growth and damage evolution in thermal barrier coatings," *Engineering Fracture Mechanics*, vol. 78, no. 10, pp. 2139–2152, 2011.
107. R. G. Wellman and J. R. Nicholls, "A review of the erosion of thermal barrier coatings," *Journal of Physics D: Applied Physics*, vol. 40, 2007.
108. X. Song, F. Meng, M. Kong, Z. Liu, L. Huang, X. Zheng, and Y. Zeng, "Relationship between cracks and microstructures in APS YSZ coatings at elevated temperatures," *Materials Characterization*, vol. 131, pp. 277–284, 2017.
109. H. Herman and, S. Sampath, "Metallurgical and ceramic protective coatings," *Stern, K.H., ED.; Chapman & Hall: London. UK*, pp. 263, 1996.
110. W. Tillmann, O. Khalil, and M. Abdulgader, "Porosity characterization and Its effect on thermal properties of APS-sprayed alumina coatings," *Coatings*, vol. 9, no. 10, p 206, 2019.
111. B. Song, M. Bai, K. T. Voisey, and T. Hussain, "Role of oxides and porosity on high-temperature oxidation of liquid-fueled HVOF thermal-sprayed Ni50Cr coatings," *Journal of Thermal Spray Technology*, vol. 26, no. 3, pp. 554–568, 2017.
112. S. Zhou, Z. Xiong, J. Lei, X. Dai, T. Zhang, and C. Wang, "Influence of milling time on the microstructure evolution and oxidation behavior of NiCrAlY coatings by laser induction hybrid cladding," *Corrosion Science*, vol. 103, pp. 105–116, 2016.
113. R. D. Jackson, M. P. Taylor, H. E. Evans, and X.-H. Li, "Oxidation study of an EB-PVD MCrAlY thermal barrier coating system," *Oxidation of Metals*, vol. 76, no. 3-4, pp. 259–271, Jul. 2011.
114. X. Liu, T. Wang, C. Li, Z. Zheng, and Q. Li, "Microstructural evolution and growth kinetics of thermally grown oxides in plasma sprayed thermal barrier coatings," *Progress in Natural Science: Materials International*, vol. 26, no. 1, pp. 103–111, 2016.
115. A. C. Karaoglanli and A. Turk, "Isothermal oxidation behavior and kinetics of thermal barrier coatings produced by cold gas dynamic spray technique," *Surface and Coatings Technology*, vol. 318, pp. 72–81, 2017.
116. D. Renusch, H. Echsler, and M. Schütze, "The role that interacting failure mechanisms have on the lifetime of APS-TBC under oxidizing conditions," *Materials Science Forum*, vol. 461-464, pp. 729–736, 2004.
117. H. Echsler, D. Renusch, and M. Schütze, "Bond coat oxidation and its significance for life expectancy of thermal barrier coating systems," *Materials Science and Technology*, vol. 20, no. 3, pp. 307–318, 2004.

118. K. Schlichting, N. Padture, E. Jordan, and M. Gell, "Failure modes in plasma-sprayed thermal barrier coatings," *Materials Science and Engineering: A*, vol. 342, no. 1-2, pp. 120–130, 2003.
119. D. Naumenko, V. Shemet, L. Singheiser, and W. J. Quadakkers, "Failure mechanisms of thermal barrier coatings on MCrAlY-type bondcoats associated with the formation of the thermally grown oxide," *Journal of Materials Science*, vol. 44, no. 7, pp. 1687–1703, 2009.
120. B. Janos, E. Lugscheider, and P. Remer, "Effect of thermal aging on the erosion resistance of air plasma sprayed zirconia thermal barrier coating," *Surface and Coatings Technology*, vol. 113, no. 3, pp. 278–285, 1999.
121. N. Krishnamurthy, M. Murali, B. Venkataraman, and P. Mukunda, "Characterization and solid particle erosion behavior of plasma sprayed alumina and calcia-stabilized zirconia coatings on Al-6061 substrate," *Wear*, vol. 274–275, pp. 15–27, 2012.
122. P.C. Tsai, J.H. Lee, and C.L. Chang, "Improving the erosion resistance of plasma-sprayed zirconia thermal barrier coatings by laser glazing," *Surface and Coatings Technology*, vol. 202, no. 4-7, pp. 719–724, 2007.
123. A. W. Ruff and S. M. Wiederhorn, "Erosion by solid particle impact.," *Treatise Materials Science and Technology*, vol. 161, pp. 69–126, 1979.
124. R. Mcpherson, "A review of microstructure and properties of plasma sprayed ceramic coatings," *Surface and Coatings Technology*, vol. 39-40, pp. 173–181, 1989.
125. C.J. Li, G.J. Yang, and A. Ohmori, "Relationship between particle erosion and lamellar microstructure for plasma-sprayed alumina coatings," *Wear*, vol. 260, no. 11-12, pp. 1166–1172, 2006.
126. H. S. Sidhu, B. S. Sidhu, and S. Prakash, "Solid particle erosion of HVOF sprayed NiCr and Stellite-6 coatings," *Surface and Coatings Technology*, vol. 202, no. 2, pp. 232–238, 2007.
127. N. Demidova, X. Wu, and R. Liu, "A fracture toughness model for brittle coating on ductile substrate under indentation loading," *Engineering Fracture Mechanics*, vol. 82, pp. 17–28, 2012.
128. S. Howard, A. Phillipps, and T. Clynn, "The interpretation of data from the four-point bend delamination test to measure interfacial fracture toughness," *Composites*, vol. 24, no. 2, pp. 103–112, 1993.
129. Y. Yamazaki, A. Schmidt, and A. Scholz, "The determination of the delamination resistance in thermal barrier coating system by four-point bending tests," *Surface and Coatings Technology*, vol. 201, no. 3-4, pp. 744–754, 2006.
130. M. Frommherz, A. Scholz, M. Oechsner, E. Bakan, and R. Vaßen, "Gadolinium zirconate/YSZ thermal barrier coatings: mixed-mode interfacial fracture toughness and sintering behavior," *Surface and Coatings Technology*, vol. 286, pp. 119–128, 2016.
131. P. Seiler, M. Bäker, T. Beck, M. Schweda, and J. Rösier, "FEM simulation of TBC failure in a model system," *Journal of Physics: Conference Series*, vol. 240, p. 012069, 2010.

132. S. Nusier and G. Newaz, "Growth of interfacial cracks in a TBC/superalloy system due to oxide volume induced internal pressure and thermal loading," *International Journal of Solids and Structures*, vol. 37, no. 15, pp. 2151–2166, 2000.
133. T. Sadowski and P. Golewski, "Experimental and numerical investigations of TBC behaviour after aging, subjected to tension and bending," *Solid State Phenomena*, vol. 216, pp. 128–133, 2014.
134. M. Jinnestrånd and S. Sjöström, "Investigation by 3D FE simulations of delamination crack initiation in TBC caused by alumina growth," *Surface and Coatings Technology*, vol. 135, no. 2-3, pp. 188–195, 2001.
135. M. Ali, S. Nusier, and G. Newaz, "Mechanics of damage initiation and growth in a TBC/superalloy system," *International Journal of Solids and Structures*, vol. 38, no. 19, pp. 3329–3340, 2001.
136. E. A. Ogiriki, Y. G. Li, and T. Nikolaidis, "Prediction and analysis of impact of thermal barrier coating oxidation on gas turbine creep life," *Journal of Engineering for Gas Turbines and Power*, vol. 138, no. 12, 2016.
137. Y. Gu, K. Chen, R. Liu, M. X. Yao, and R. Collier, "Indentation modeling study of temperature-dependent fracture toughness of brittle coating on ductile substrate based on microcrack formation theory," *Surface and Coatings Technology*, vol. 309, pp. 536–544, 2017.
138. J. Beuth and N. Klingbeil, "Cracking of thin films bonded to elastic-plastic substrates," *Journal of the Mechanics and Physics of Solids*, vol. 44, no. 9, pp. 1411–1428, 1996.
139. T. Becker, J. Mcnaney, R. Cannon, and R. Ritchie, "Limitations on the use of the mixed-mode delaminating beam test specimen: effects of the size of the region of K-dominance," *Mechanics of Materials*, vol. 25, no. 4, pp. 291–308, 1997.
140. V. Tvergaard and J. W. Hutchinson, "The influence of plasticity on mixed mode interface toughness," *Journal of the Mechanics and Physics of Solids*, vol. 41, no. 6, pp. 1119–1135, 1993.
141. E. Zywicz and D. Parks, "Small-scale yielding interfacial crack-tip fields," *Journal of the Mechanics and Physics of Solids*, vol. 40, no. 3, pp. 511–536, 1992.
142. S. Park, Z. Tang, and S. Chung, "Temperature effect of interfacial fracture toughness on underfill for Pb-free flip chip packages," *2007 Proceedings 57th Electronic Components and Technology Conference*, 2007.
143. S. Mao and M. Li, "Effects of dislocation shielding on interface crack initiation and growth in metal/ceramic layered materials," *Journal of the Mechanics and Physics of Solids*, vol. 47, no. 11, pp. 2351–2379, 1999.
144. K. S. Chan, "Relationships of fracture toughness and dislocation mobility in intermetallics," *Metallurgical and Materials Transactions A*, vol. 34, no. 10, pp. 2315–2328, 2003.
145. N. G. Meyendorf, P. B. Nagy, and, S. I. Rokhlin, "Nondestructive materials characterization: with applications to aerospace materials, *Perlin: Spring*, pp. 2004, 2004.

146. A. C. Karaoglanli, A. Turk, and I. Ozdemir, "Effect of sintering on mechanical properties of cold sprayed thermal barrier coatings," *Surface Engineering*, vol. 32, no. 9, pp. 686–690, 2016.
147. J. Weertman, "Dislocation based fracture mechanics," Singapore: *World Scientific*, 1996.
148. M. Hasegawa and Y. Kagawa, "Microstructural and mechanical properties changes of a NiCoCrAlY bond coat with heat exposure time in air plasma-sprayed Y₂O₃–ZrO₂ TBC systems," *International Journal of Applied Ceramic Technology*, vol. 3, no. 4, pp. 293–301, 2006.
149. T. Beck, R. Herzog, O. Trunova, M. Offermann, R. W. Steinbrech, and L. Singheiser, "Damage mechanisms and lifetime behavior of plasma-sprayed thermal barrier coating systems for gas turbines — Part II: Modeling," *Surface and Coatings Technology*, vol. 202, no. 24, pp. 5901–5908, 2008.
150. N. Shibata, "Structure of [110] tilt grain boundaries in zirconia bicrystals," *Journal of Electron Microscopy*, vol. 50, no. 6, pp. 429–433, 2001.
151. R. H. J. Hannink, "Growth morphology of the tetragonal phase in partially stabilized zirconia," *Journal od material Science*, vol. 13, no. 11, pp. 2487–2496, 1978.
152. D. Shin and A. Hamed, "Influence of micro-structure on erosion resistance of plasma sprayed 7YSZ thermal barrier coating under gas turbine operating conditions," *Wear*, vol. 396-397, pp. 34–47, 2018.
153. S. K. Essa, R. Liu, and M. X. Yao, "Temperature and exposure-dependent interfacial fracture toughness model for thermal barrier coatings," *Surface and Coatings Technology*, vol. 358, pp. 505–510, 2019.

